Exploring storm time ring current formation and response on the energy input

by

Raluca Ilie

A dissertation submitted in partial fulfillment
of the requirements for the degree of
Doctor of Philosophy
(Space and Planetary Physics)
in The University of Michigan
2010

Doctoral Committee:

Associate Professor Michael W. Liemohn, Chair
Associate Professor John E. Foster
Associate Professor Aaron Ridley
Research Scientist Gábor Tóth

© Raluca Ilie 2010
All Rights Reserved

For Cosmin

ACKNOWLEDGEMENTS

At this point of finishing my thesis, I can certainly picture numerous people I am indebted to, and here I should thank them all with my sincere heart. I owe my deepest gratitude to my advisor, Prof. Michael Liemohn for his mentoring, teaching, encouragement and support over the years. He showed me an example of a great scholar and advisor, whose patience and professionalism always motivated me. The depth and breadth of his knowledge are a precious resource and I am fortunate for having first hand access to it. Needles to say, without his guidance and persistent help this dissertation would not have been possible.

I would like to thank the professors of my dissertation committee, Gabor Tóth, Aaron Ridley and John Foster for their detailed review, constructive criticism and excellent suggestions during the preparation of this thesis.

I would like to show my gratitude to Dr. Gabor Tóth for always being the voice of cautious optimism. Through countless hours of discussions, he always challenged me to look for solutions to problems rather than focus on the problem. He has constantly given me honest feedback and discussions I had with him always enlightened me.

My sincere thanks also go to Prof. Aaron Ridley, for his insightful comments and advise that have been of great value for my studies. I am also grateful for his help with various computational tools.

A great deal of thanks also goes to the CSEM team for all their support computational issues. Many thanks go to all faculty and staff at AOSS who contributed to my research through teaching, administrating, encouraging and answering my questions.

There were also many friends who have made my graduate student life memorable. I am grateful for getting to know the former students Ofer Cohen, Alex Glocer, Noe Lugaz, Valeriy Tenishev and Jichun Zhang, with whom I shared joyful discussions, for their kindness and their help in my early years at Michigan. Special thanks go to Erika Roesler and to my very good friend Oana Catu for their constant encouragement and advise. To Dalal Najib, Rona Oran and Martin Rubin for all the ups and downs we shared together during this adventure. I cannot pass without saying thanks my fellow students, Amanda Brecht, Dave Pawlowski, Arnaud Valleille, Yiqun Yu to name a few, for their friendship and encouragements over the years.

Finally, I would like to thank my family. To my husband, Cosmin, for continuing to believe in me even when I did not. Everything I have and am is due to him. Without his presence besides me, without his tremendous love and sustained support, I could have never gone this far. To my parents for their endless love and support. To my brother for having so much confidence in me.

TABLE OF CONTENTS

LIST OF FIGURES

Figure

LIST OF TABLES

Table

LIST OF ABBREVIATIONS

ACE Advanced Composition Explorer

AMIE Assimilative Mapping of Ionospheric Electrodynamics

AMPTE Active Magnetospheric Particle Tracer Explorer

AU Astronomical Unit

BATS-R-US Block Adaptive Tree Solar-wind Roe-type Upwind Scheme

CIR Corotating Interaction Region

CME Coronal Mass Ejection

HEIDI Hot Electron and Ion Drift Integrator

HSS High Speed Streams

IMF Interplanetary Magnetic Field

ICME Interplanetary Coronal Mass Ejection

IS Interplanetary Shock

Kp Planetary K

LANL Los Alamos National Laboratory

MC Magnetic Cloud

MPA Magnetospheric Plasma Analyzers

RAM Ring current - Atmosphere interaction Model

RCM Rice Convection Model

SAR Stable Auroral Red

SSC Storm Sudden Commencement

SYM-H Symmetric disturbance field in H

SWMF Space Weather Modeling Framework

ABSTRACT

Exploring storm time ring current formation and response on the energy input

by

Raluca Ilie

Chair: Michael W. Liemohn

While extensive research has been made over the last decades regarding the storm time dynamics, there are still unanswered questions on ring current formation and plasmasphere evolution, specifically on ring current response on the energy input. Large-scale data analysis projects and global magnetospheric simulations provide complementary alternatives for exploring highly complex coupling of the solar wind-ionosphere-magnetosphere system. This issue is addressed by examining the production, transfer, storage and dissipation of energy across the entire magnetosphere using these two analysis methods.

As a first study, the influence of the epoch time choice when doing Superposed Epoch analysis on intense magnetic storms at solar maximum using observations from Advanced Composition Explorer (ACE) and Los Alamos National Laboratory (LANL) geosynchronous satellites is investigated. Seven distinct epoch times throughout the storm were selected. The results indicate that a distinct time stamp is needed in order to resolve certain solar wind features. On the other hand, when it comes to hot proton at geosynchronous orbit, the choice of reference time primarily matters to accurately describe the size of peaks, while the presence and time evolution is

unaltered by it.

While spacecraft and ground based measurements are nowadays widely available, understanding the energization processes that dominate this region is still a difficult problem to tackle using only observations. Consequently, global magnetospheric simulations provide an excellent alternative for investigating the large scale coupling of the solar wind-ionosphere-magnetosphere system.

With the help of the Space Weather Modeling Framework (SWMF), which couples together different numerical models describing separate regions of space, we were able to examine the role the transient spikes in the solar wind parameters play in the development of magnetic storms. For this study we coupled the Global Magnetosphere/Block Adaptive Tree Solar-wind Roe-type Upwind Scheme (BATS-R-US), Inner Magnetosphere/Rice Convection Model (RCM) and Ionosphere Electrodynamics/Ridley Ionosphere Model. We find that changes in the energy input produce a nonlinear response of the inner magnetosphere as opposed to the linear response the empirical models predict. Moreover, our model results show that smoothing the solar wind input results in a two phase, fast then slow, recovery, even though this feature was not seen in the data for the selected storm. In the same time, removing all noise with a window greater than 1 hour changes the entire magnetosphere, dramatically reducing the plasma sheet density and pressure.

While initial increases in the energy input enhance the magnetospheric response, we observe that as the power transferred to the system is increased, the growth of the ring current is stalled and a saturation limits sets in. A threshold in the energy input is necessary for the ring current to develop, while the short time scale fluctuations in the solar wind parameters did not have a significant contribution. Such findings imply that the ions drift to the dayside is not the only loss process that contributes to the decay of the ring current but also the existence of an internal feedback mechanism as the magnetosphere acts as a low-pass filter of the interplanetary magnetic field.

This effect will limit the energy flow in the magnetosphere.

In addition, numerical simulations are performed to study the role of Interplanetary Magnetic Field (IMF) Bz fluctuation periodicity in the transfer of solar wind mass and energy to the magnetosphere. We find that the most important characteristic in determining the transfer of periodicity seen in IMF Bz to the inner magnetosphere is the peak signal to noise ratio in the power spectrum of the input parameter. A peak in the input power spectrum at least twice larger than the background noise is needed in order to trigger a similar periodicity in the magnetosphere response, even though most of the signal energy is contained at a certain frequency.

Finally, it is prudent to explore these issues with an alternative inner magnetosphere drift physics model. Theoretical and numerical modifications to an inner magnetosphere - Hot Electron Ion Drift Integrator (HEIDI)-model were implemented, in order to accommodate for a non-dipolar arbitrary magnetic field. While the dipolar solution for the geomagnetic field during quiet times represents a reasonable assumption, during storm activity this assumption becomes invalid. HEIDI solves the time dependent, gyration and bounced averaged kinetic equation for the phase space density of one or more ring current species. This model is different than the RCM model in that it resolves the pitch angle distribution of the hot ions in the inner magnetoshere. With HEIDI now fully incorporated into the SWMF, an examination of model sophistication on our scientific findings can be explored. A few initial simulations have been conducted and the results are discussed.

CHAPTER I

Introduction

1.1 Space Weather

Similar to the the changes in temperature, rainfall and winds that define the tropospheric terrestrial weather, space weather is due to variable conditions in space between the sun and the Earth and its upper atmosphere. The interaction between the space environment and the modern, technologically complex systems can have significant repercussions on our everyday life. Figure 1.1 presents an illustration of Earth's space environment affected by space weather.

The terrestrial environment is protected by the Earth's magnetic field, which acts as a radiation shield. However, during space weather storms, enough radiation reaches the orbiting satellites to make them vulnerable to electrical charging and increased atmospheric drag, shortening their life span. Also, changes in the ionosphere can alter long-distance radio signals and as well as Global Position Systems (GPS). Strong magnetic fields can induce electrical currents at ground level that can damage electrical power distribution grids and increase corrosion in pipelines (e.g. Alaska oil pipeline). Furthermore, the same conditions can diminish the accuracy of compasses and even cause homing pigeons to go astray. Radiation poses a hazard to astronauts and even commercial airlines face new risks as the passengers and crew on board of high latitudes flights can be exposed to higher than normal levels of radiation.

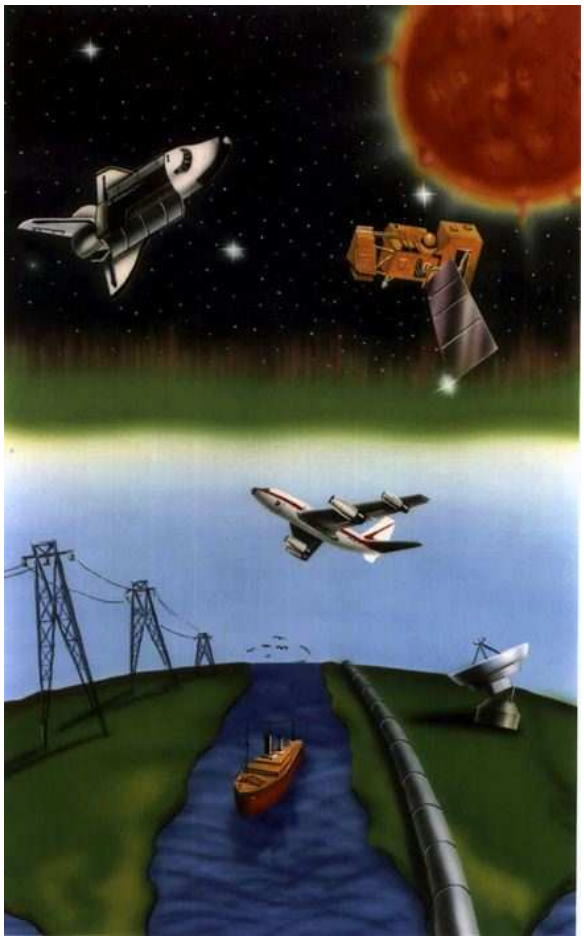

Figure 1.1: Illustration of the terrestrial space environment affected by space weather. Picture courtesy of National Oceanic and Atmospheric Administration.

However, the effects of space weather are not only harmful but they can be beautiful as well. When radiation from a space weather storm impacts the Earth's atmosphere, it can create spectacular displays of aurora, which can be seen at latitudes as low as Ann Arbor, if the conditions are extreme.

Increased dependence on space-borne intelligence systems makes space weather a topic that provides strong motivation for research in magnetospheric space sciences.

1.2 Solar Wind and the Earth's Magnetosphere

The most important source of plasma in our solar system is the Sun. Hot plasma, known as solar wind, is accelerated from the solar surface to supersonic speeds into

Solar Wind Parameter	Value
Flow Speed	450 km/s
Proton Density	6.6 cm^{-3}
Electron Density	7.1 cm^{-3}
He^{++} Density	0.25 cm^{-3}
Proton Temperature	1.2×10^5 K
Electron Temperature	1.4×10^5 K
Magnetic Field	7 nT
Time of arrival to Earth	$\sim$ 4 days

Table 1.1: Typically properties of the solar wind at 1 AU. Table adapted from *Kivelson and Russell* (1995).

the heliosphere (*Parker*, 1958). The solar wind is a turbulent, radially streaming magneto-fluid with the ratio of thermal to magnetic pressure larger than unity. This ratio controls whether particle thermal processes or magnetic processes dominate the behavior of the plasma and is referred to as the plasma *beta parameter*:

$$\beta = \frac{n_p K \left(T_e + T_p\right)}{\frac{B^2}{2\mu_0}} \tag{1.1}$$

where the subscript T_e (T_p) designates the electron (proton) temperature, n_e (n_p) designates the electron (proton) number density, B is the magnetic field, K is the Boltzmann constant and μ_0 is the magnetic permeability of vacuum.

The fact that the β parameter is greater than unity for all solar wind conditions means that the magnetic field is relatively weak and is carried along with the flow. Typical values of the solar wind properties near Earth's orbit are shown in Table 1.1, adapted from *Kivelson and Russell* (1995).

The Earth has an internal dipole magnetic moment created by a magnetic dynamo deep inside the planet in the fluid, electrically conducting core. This produces a magnetic field strength at the equator on the Earth's surface of about 30,000 nT. The magnetic field of Earth poses an obstacle to the oncoming solar wind and therefore carves out a region dominated by the magnetic field of the Earth called the magnetosphere.

When the solar wind interacts with the magnetic field of the Earth, a shock front forms in front of the magnetosphere called the bow shock and acts to slow down the solar wind so that plasma can flow around the magnetosphere. As the solar wind passes through the shock, it is decelerated, heated, and diverted around the Earth in a region called the magnetosheath. This region has a thickness of about 3 Re near the sub-solar point but increases rapidly in the downstream direction. After being decelerated by the bow-shock, the heated solar wind plasma is accelerated again from subsonic to supersonic flow as it moves around the Earth. The boundary between the region of solar wind plasma and the terrestrial magnetic field marks the magnetopause, a thin region of about 100 km thickness. The location of the magnetopause can be calculated by requiring that the total pressure upstream equals the total pressure downstream of this boundary. That is, the magnetic pressure in the magnetosphere balances the thermal and magnetic pressures in the magnetosheath. Since at this location the magnetic field changes both in strength and direction, an extensive current flows around the magnetopause primarily from dawn to dusk on the dayside (*Chapman and Ferraro*, 1929). This current is acting as a separator between the solar wind magnetic field and the magnetic field of the Earth. The magnetopause currents that bound the magnetosphere are sensitive to the square root of the solar wind dynamic pressure ($P_{dyn} = \rho v^2$). When the dynamic pressure of the solar wind changes, these currents increase as the magnetosphere shrinks and, at the same time increasing the magnetic perturbation at the Earth's surface.

The magnetosphere is populated by thermal plasma and energetic charged particles of both solar wind and terrestrial origin. Direct entry of the solar wind plasma occurs on the dayside in the vicinity of the polar cusp. The overall shape of the near-sun (dayside) magnetospheric field resembles the shape of a pure dipole field, although somewhat compressed and distorted. The magnetospheric size is controlled by the solar wind dynamic pressure. Under typical conditions the sub-solar magne-

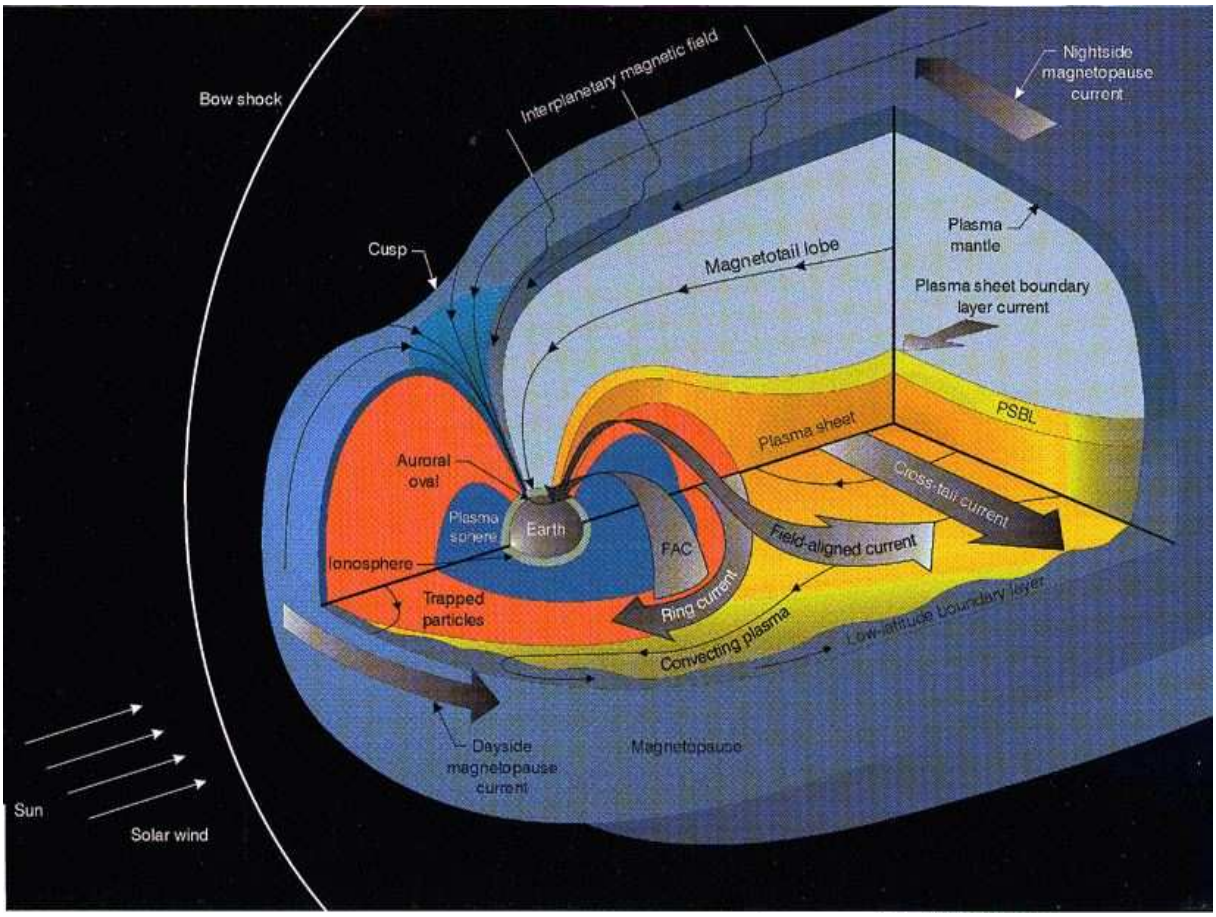

Figure 1.2: Illustration of the terrestrial magnetosphere showing locations of various regions and particle populations. In this diagram, the Sun is to the left. Picture by J. Burch, Southwest Research Institute, San Antonio, USA.

topause location is about 10 Re from the Earth, but when the solar wind density is at its extreme observed values it can be as close as 5 Re (*Shue et al.*, 1998) or as distant as 20 Re. An illustration of the various regions of the magnetosphere is presented in Figure 1.2.

The inner magnetosphere region contains three major overlapping particle populations: the Van Allen radiation belts, the ring current particles, and the plasmasphere. Inner magnetospheric field lines are closed, in the sense that both foot-points are in the ionosphere. Close to the Earth is the plasmasphere (essentially an upward extension of the ionosphere), which is a torus shaped volume that surrounds the Earth and

contains relatively cool ($\sim$ 5000 K) and high density ($\geq$ 100 cm^{-3}) plasma, whose source is the upper atmosphere of the Earth's atmosphere, the ionosphere (*Horwitz and Singh*, 1991). The plasma in this region corotates with the Earth, but it can also flow along geomagnetic field lines from one hemisphere to another. In the equatorial plane, the plasmasphere extends out to a radius of about 4 Re, but its relative volume is magnetic activity dependent. A large and sharp decrease in the plasma density as one leaves the plasmasphere marks the location of the plasmapause, the boundary between the plasma that corotates with the Earth and the plasma that is influenced by the electric field.

Overlapping this region we find the radiation belts and the ring current. The drift of the lower energy particles (10 - 300 keV) results in a large-scale ring of current that encircles the Earth, called the ring current. The population of the ring current and the radiation belts are high-energy particles that bounce back and forth between the northern and southern hemispheres. These trapped high-energy electrons and protons (and at times a significant number of oxygen ions) also drift in the azimuthal direction around the Earth due to gradients in the geomagnetic field, with the electrons and ions drifting in opposite directions. There is no clear distinction between these populations, but it is customary to treat ring current particles as those with keV energies and radiation belt particles as those with 100's of keV to MeV energies (*Kivelson and Russell*, 1995). The ring current prevents the dynamo-generated electric fields at high latitudes from penetrating to middle and low latitudes. Specifically, in response to the penetrating high latitude electric fields, the electrons and protons in the ring current polarize and set up an oppositely directed electric field that effectively cancels the penetrating high latitude electric field.

The ultimate source of the ring current and outer radiation belts particles is the plasma sheet and the ionosphere. The plasma sheet is populated primarily by solar wind particles along with particles that have escaped the upper atmosphere

and have convected to the tail. These particles have an order of magnitude higher energies than the ones found in the magnetosheath and up to two orders of magnitude lower densities. While these particles are not trapped, they have direct access to Earth's upper atmosphere on the night side along magnetic field lines that connect to the auroral ovals. As the plasma sheet particles stream towards the Earth along geomagnetic field lines, they are accelerated and then collide with the Earth's upper atmosphere, producing the aurora.

A large scale current flows across the plasma sheet from dawn to dusk. Known as the neutral current sheet, this current acts to separate two regions of oppositely directed magnetic field in the magnetospheric tail. The magnetic field is toward the Earth above the neutral current sheet (northern hemisphere) and away from the Earth below the current sheet. These stretched magnetic field lines extend deep into the magnetospheric tail and near the magnetopause they get connected to the magnetic field embedded into the shocked solar wind. This magnetic connection acts to generate voltage drops across the magnetospheric tail that can be larger than 100,000 volts and the potential drop maps down to the polar cap. The generated electric field is in the dusk-ward direction across the polar cap. The polar cap potential drop characterizes the total strength of the convection and can also be considered to represent the rate of transport of magnetic flux.

The coupling between the solar wind magnetosphere - ionosphere system sets up large-scale magnetic field-aligned currents (FACs), known as Birkeland currents. Field-aligned currents couple ionospheric currents at high latitudes with magnetospheric currents. The main FAC systems are the region 1 and 2 currents, flowing from the magnetosphere into, across and then out of the ionosphere. The region 1 currents are connected to the magnetopause current while the region 2 system closes through the ring current. These currents attempt to force the flow in the ionosphere to follow the flow in the magnetosphere. When the stress in the magnetosphere in-

creases, the distortion of the magnetic field increases and the current flow along the field lines increases. Since the FACs flow through the resistive ionosphere and produce electric fields that map along magnetic field lines into the ionosphere, it is known that these currents drive the ionospheric convection.

The terrestrial magnetosphere is a complicated system, acting as a buffer and an agent between the variable solar wind and the Earth's ionosphere. The dynamic variations in the Earth's magnetosphere have several causes: the solar conditions, (i.e. the dynamic structures in the sun), the presence of geoeffective structures in the solar wind (Interplanetary Coronal Mass Ejections, high speed streams, shocks), the location of the Earth in the heliosphere as well as the orientation of Earth's magnetic dipole. While we do not have a complete understanding of all the processes in the magnetosphere, the majority of the physical processes derive their energy from the solar wind through the reconnection process. In the sections that follow we discuss the stresses on and in the magnetosphere and their effects along with the transport of energy into the magnetosphere.

1.3 Energy Transfer between Solar Wind and Magnetosphere

Energy transport from the interplanetary plasma to Earth's inner magnetosphere occurs over a range of time scales and efficiencies, varying with radial geocentric distance and magnetic activity. This indicates that the energy and mass transport involve many processes with overlapping ranges.

It is often hypothesized that magnetospheric dynamics are mainly controlled by two external drivers: the solar wind plasma and the interplanetary magnetic field (IMF). Historically, the concept of reconnection was first introduced to magnetospheric physics by *Dungey* (1961). *Dungey* (1961) and *Dungey* (1963) were the first studies to propose that the solar wind energy input into the Earth's magnetosphere is controlled by the solar wind plasma and the IMF, which in turn determines the

dayside reconnection rate. A few years later a statistical study by *Fairfield and Cahill* (1966) demonstrated strong correlation between the direction of the IMF and the intermittent magnetospheric activations observed during substorms. The reconnection process is responsible for enhancing the mass and magnetic flux transport from the dayside magnetosphere to the magnetotail when the IMF is southward. During times when the IMF is in the same direction as the geomagnetic field, the plasma convection at high latitudes is more complex, and the transport of magnetic flux can be from the magnetotail to the dayside. The acceleration of particles from the magnetotail toward the inner magnetosphere was first addressed by *Speiser* (1965) and showed that particles are efficiently accelerated and that some of them are ejected from the neutral sheet along the ambient magnetic field lines.

The physics underlying reconnection occurs on the sub-gyroscale where the ions and eventually the electrons encounter magnetic structure that demagnetizes the charged particles so that they no longer are tied to the magnetic field and drift across it. This process allows field lines from different plasma regimes to connect. Figure 1.3 shows a sketch of this process.

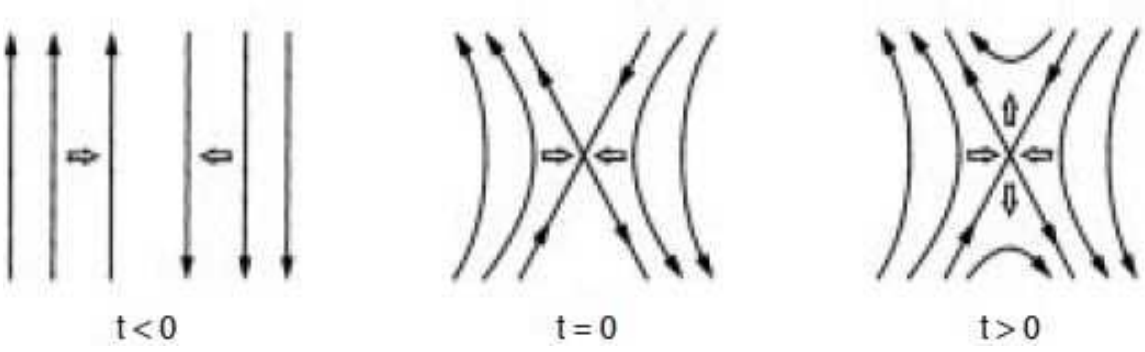

Figure 1.3: Schematic representation of magnetic field reconnection. Figure from *Gombosi* (1999).

When the solar wind and magnetospheric plasmas become linked, the solar wind plasma can cause day-to-night flows over the polar cap and magnetic energy can be

stored in the tail. This transport is strongly dependent on the southward component of the interplanetary magnetic field. When the magnetic field is antiparallel to the geomagnetic field the reconnection rate is strong and when it is all parallel, the reconnection rate is weak. However, this is true only when we consider magnetopause reconnection at the sub-solar point. Since the magnetopause has regions of quite diverse field directions, there is always a component of the Earth's magnetic field that is antiparallel with the IMF B_z, therefore reconnection can take place in a variety of locations. For instance, when the interplanetary magnetic field is horizontal or northward, the antiparallel fields that promote reconnection occur near the polar cusp (*Song and Russell*, 1992). An illustration of northward versus southward MF reconnection sites is presented in Figure 1.4. The location of the reconnection site it is actually an important factor in determining how the mass and energy transport takes place. Reconnection during intervals of strongly southward field transfers magnetic flux to the tail. Reconnection above the cusp during intervals of strongly northward field can add more magnetic flux to the dayside while removing it from the tail. Furthermore, different IMF orientations will result in very different ionospheric potential patterns as well as different plasma flow patterns (e.g. *Luhmann et al.*, 1984; *Coleman et al.*, 2001; *Sandholt and Farrugia*, 2003).

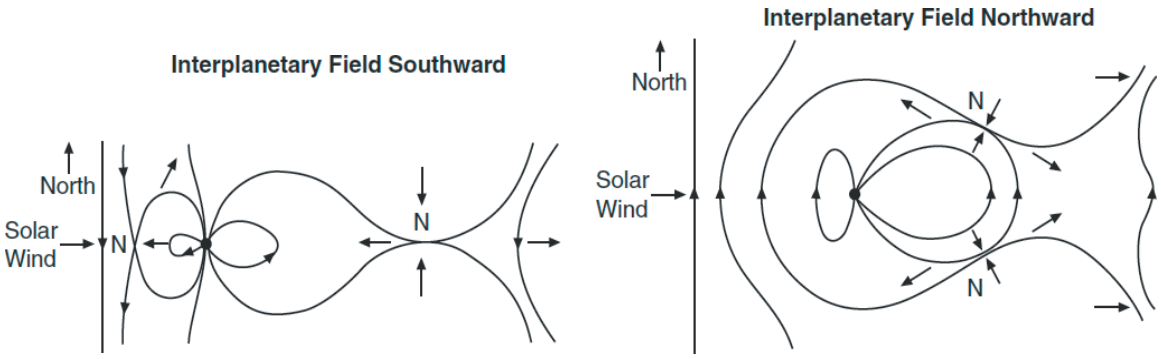

Figure 1.4: Left: Schematic diagram of reconnection sites for southward IMF (left) and northward IMF (right).

Energy flows into the ring current from the solar wind at a rate proportional to the interplanetary electric field in the dawn-dusk direction, but not when the electric field is in the dusk-dawn direction. The dawn-dusk electric field E_y, which represents the product of the solar wind velocity and the north-south field, is the rate of transport of the flux of southward magnetic field carried toward the magnetosphere.

An alternative scenario for the energy transfer between the solar wind and the magnetosphere was proposed by *Axford and Hines* (1961). This suggests that viscous interactions between the solar wind and the flank magnetospheric plasma could result in the transfer of momentum across the boundary. Flank plasma is then drawn to the night side, where an increase in pressure would force a return flow, imposing a dawn-dusk motional electric field similarly to the one created by reconnection. An interesting outcome of this scenario is that this type of driving only produces a single convection pattern, as opposed with several different convection patterns, dependent on the orientation of the IMF when considering reconnection. Nevertheless, *Kivelson and Russell* (1995) reports that only $10 - 20\%$ of energy transferred from the solar wind to the magnetosphere is done through viscous interaction.

There are many mechanisms that are responsible for the particle energization in the inner magnetosphere but the two most important are the ionospheric electric potential and the properties of the near-Earth plasma sheet. The formation of an intense ring current requires significantly high values of both of these drivers (*Kozyra and Liemohn*, 2003), while a decrease in any of them will lower the amount of energy entering the ring current, independent of the nature of the driver (*Kozyra et al.*, 2002; *Liemohn and Kozyra*, 2005).

It has been reported on a variety of different physical mechanisms that might be responsible for the transfer of solar wind energy and momentum into the inner magnetosphere. Studies by *Chen et al.* (1993, 1994) showed that spikes added to the magnetospheric convection produce enhancement of the ring current, due to an

increase in diffusive transport of ions with energies over 160 keV. *Ganushkina et al.* (2000, 2001) suggests that the short lived intense electric fields are responsible for the observed ion flux enhancements inside the plasmapause during storms. Furthermore, inner magnetosphere simulations (*Khazanov et al.*, 2004) using time averages of the electric potential shows that temporal resolution higher than 5 minutes is needed in order to correctly estimate the energization and injection of the high energy plasma sheet electrons. Similarly, *Ganushkina et al.* (2006) found that the short-lived pulses in the near-Earth electric field had a profound influence on the enhancement of the energetic tail of the ring current ion population.

Conversely, many studies have shown that there is a time delay of few minutes between the time that the IMF reaches the magnetopause and the time when the ionosphere starts to react (e.g. *Ridley and Clauer*, 1996; *Ridley et al.*, 1998; *Ruohoniemi and Greenwald*, 1998; *Slinker et al.*, 2001; *Lu et al.*, 2002). Further, the ionospheric potential takes 10 to 20 minutes to fully change from one state to another. *Goldstein et al.* (2003) found that the electric potential response time from the solar wind to the inner magnetosphere is around 30 minutes. *Tsurutani et al.* (1990) describes the magnetosphere as a low pass filter, based on the existence of a break in the IMF B_z - AE coherence spectrum at about 5 hours period. The statistical study of *Murr and Hughes* (2007) suggests that the ionosphere is insensitive to frequencies higher than 0.8 mHz ($\sim$ 21 minutes) in the IMF, meaning that the magnetosphere-ionosphere system naturally acts as a low pass filter of the interplanetary magnetic field. Similarly, *Takalo et al.* (2000) show that the low frequencies in the AE index are correlated to the low frequencies in the rectified eastward component of the interplanetary electric field, while the high frequencies are associated with the intrinsic dynamics of the magnetosphere. However, the exact mechanisms of transport and energization of magnetospheric plasma are still open issues.

1.4 Ring Current: Formation and Decay

The result of a magnetic storm is the formation of an intense, westward toroidal electric current that encircles the Earth centered on the equatorial plane (e.g. *Tsurutani and Gonzalez*, 1997). This ring current occupies geospace from 2 to 9 Earth Radii and is formed through convective transport and azimuthal drift of trapped particles. Although all trapped particles in the inner magnetosphere contribute to the ring current, the main carriers of the storm time ring current are positive ions, mainly H^+ and O^+, with energies ranging from a few keV to hundreds of keV. The contribution from electrons is very little due to their small mass and energy density relative to the protons (*Baumjohann*, 1993). The result is a net charge transport with electrons and ions moving in opposite directions (electrons drift eastward and ions drift westward). Changes in the intensity of this current are responsible for the global decreases in the geomagnetic field.

Charged particles in the presence of a magnetic field undergo three distinct motions: gyration about the magnetic field line, bouncing up and down the magnetic field line, and drifting along isocontours of magnetic field (*Roederer*, 1970).

Thus for example, a particle moving in a magnetic field in the direction perpendicular to the magnetic field vector experiences a Lorentz force in the direction perpendicular to the magnetic field and the velocity vector. This will impose a gyration of the particle around the magnetic field with the gyrofrequency (cyclotron frequency):

$$\Omega_c = \frac{|q|B}{m} \tag{1.2}$$

where q is the electric change of the particle, B is the magnetic field magnitude and m represents the mass of the particle. This motion is referred to as the gyration motion. If the particle's velocity has a component parallel to the magnetic field,

it will move the particle along the magnetic field line. If it moves toward the Earth along a field line, then the magnetic field increases and the particle experiences a force opposite the direction of motion that will act to slow down and eventually stop the field aligned motion, reversing the direction of the particle. The location where the particle's parallel velocity is null is called the mirror point. It will cross the equatorial plane and again mirror as it approaches the Earth in the opposite hemisphere. This is the bounce motion.

During the bounce, the perpendicular energy is proportional to the magnetic field strength, reaching maximum at the location where the total energy is in the perpendicular direction and the magnetic moment

$$\mu_m = \frac{mV_\perp^2}{2B} \tag{1.3}$$

is conserved, under the assumption that the scale length for change in the field is much less than the radius of gyration of the particle or the rate of change of the magnetic field is much less than that for the gyration of the particle around the magnetic field. Conservation of the first adiabatic invariant is what causes the particle to reflect and bounce back and forth along the magnetic field line. The simplest motion is that of particles whose mirror points are located at the magnetic equator and are called equatorially mirroring particles. The pitch angle of these particles (the angle between the particle's velocity and the magnetic field) is 90°.

For particles trapped between two mirror points, another constant of motion is the parallel momentum integrated along the motion path. This is called the second adiabatic invariant and is defined as:

$$I = \oint m v_{||} ds \tag{1.4}$$

If the bounce path shortens, then the parallel energy of the particle increases. This

process is known as Fermi acceleration or acceleration by moving magnetic mirrors. If the magnetic field strength varies with radial distance, the gyrating particle will drift perpendicular to the gradient of the field and the motion is called gradient drift. Furthermore, in the case of a curved field line with the particle moving parallel to the field line, the particle drift is perpendicular to the magnetic field vector and this is called the curvature drift. Both the gradient and curvature drifts are charge and energy dependent. An illustration of these motions is presented in Figure 1.5.

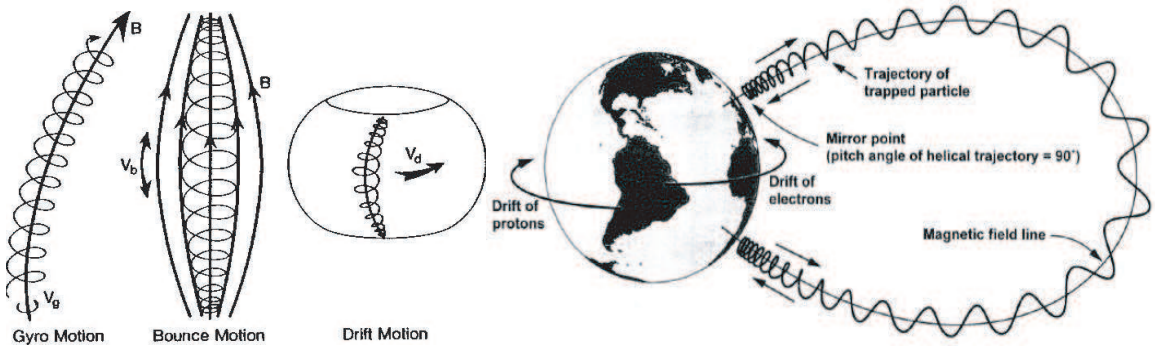

Figure 1.5: Left: Schematic of Gyration, bounce and drift motion. Right: Gyration, bounce and drift motion in the Earth's magnetosphere

Another important drift occurs in the presence of an electric field perpendicular to the magnetic field applied across a plasma. A particle will be accelerated for half of the gyro period and then begins to decelerate. Since the radius of gyration is greatest in the half gyro period that the particle is accelerated, the particles will drift perpendicular to the magnetic and electric fields. The electrons and ions are accelerated in opposite direction but both drift in the direction of the vector product $\mathbf{E} \times \mathbf{B}$ due to opposite directed gyration for electrons and ions. Because electrons and ions drift with the same velocity, there is no current associated with this drift. Therefore, ring current particles undergo drifts due to electric fields as well as drifts due to gradients and curvatures of the magnetic field:

$$\mathbf{v}_{drift} = \frac{\mathbf{E} \times \mathbf{B}}{B^2} + \frac{m}{q} \frac{v_{||}^2 + \frac{1}{2} v_{\perp}^2}{B} \frac{\mathbf{B} \times \nabla B}{B^2} \tag{1.5}$$

Parker (1957) analytically described the currents resulting from these motions in terms of particle perpendicular and parallel pressures relative to the magnetic field. The total current

$$J = J_{drift} + J_{curvature} + J_{gyration} = \frac{\mathbf{B}}{B^2} \times \left(\nabla P_{\perp} + \frac{P_{||} - P_{\perp}}{B^2} (\mathbf{B} \cdot \nabla) \mathbf{B} \right) \tag{1.6}$$

is due to particle drift driven by the magnetic field gradient, the curvature of the magnetic field and the gyration effects within the particle distribution, as defined below.

$$J_{drift} = P_{\perp} \frac{\mathbf{B} \times \nabla \mathbf{B}}{B^3} \tag{1.7}$$

$$J_{curvature} = \frac{P_{||}}{B^4} \mathbf{B} \times (\mathbf{B} \cdot \nabla) \, \mathbf{B} \tag{1.8}$$

$$J_{gyration} = \frac{\mathbf{B}}{B^2} \times \left(\nabla P_{\perp} - \frac{P_{\perp}}{B} \nabla B - \frac{P_{\perp}}{B^2} (\mathbf{B} \cdot \nabla) \mathbf{B} \right) \tag{1.9}$$

The total energy of the ring current during magnetic storms has been proven to be proportional with the disturbance in the equatorial surface magnetic field by *Dessler and Parker* (1959) and *Sckopke* (1966):

$$\frac{\delta B}{B_0} = \frac{2E}{3E_m} \tag{1.10}$$

where B_0 is the average equatorial value of the magnetic field, E represents the total energy contained in the ring current, and E_m is the energy of the Earth's dipole field above the surface. Equation 1.10 is known as the *Dessler-Parker-Sckopke* relation.

The drift path of a ring current particle is not necessarily a closed orbit. The reason is the presence of electric fields in the magnetosphere generated both by the solar wind and the rotation of the Earth. To small geocentric distances, the drift paths are closed and the magnetic drift is the dominant one. At larger distances away from the Earth, the sunward drifting particles are deflected around the Earth and form the partial ring current.

The ring current is a very dynamic population, strongly coupling the inner magnetosphere with the ionosphere, which is an increasingly important source and modulator. Not only IMF B_z but plasma sheet density, ionospheric outflow, substorm occurrence, all have their role in the ring current development and decay.

1.4.1 Sources of Ring Current Particles

The main source populations for the ring current are the plasma sheet and the ionosphere. But since the plasma sheet particle populations are mainly supplied by the solar wind and the ionosphere, it is implied that the ring current has both an ionospheric and solar wind source. While it is well accepted that the ionospheric plasma is the main source of the plasmasphere, its contribution to the plasma sheet and ring current is still unknown. Various studies (see *Denton et al.* (2005) and references therein) indicate the presence of ionospheric origin O^+ in the plasma sheet. The presence of He^{++} in this region implies solar wind source as well (*Lennartsson*, 2001). Since the H^+ ions are found both in the solar wind and the ionosphere, it makes hard to determine where they come from. On the other hand, magnetospheric O^+ is primarily of ionospheric origin. Nevertheless, the contribution of each source as well as the physical mechanisms that control the entry remains an open question.

The plasma sheet is the source of high-energy plasma injected into the inner magnetosphere by strong magnetospheric convection during magnetic substorms and storms, considered responsible for the ring current enhancement during times of high

geomagnetic activity. Plasma sheet density has a direct influence on the strength of the ring current (e.g. *Thomsen et al.*, 1998; *Kozyra et al.*, 1998b). During the main phase of a storm, the plasma sheet can have access to geosynchronous orbit and to the inner magnetosphere (*Friedel et al.*, 2001; *Denton et al.*, 2005). Statistical studies of the plasma at geosynchronous orbit showed that there is a correlation between plasma access and the Kp index (*Maynard and Chen*, 1975; *Korth et al.*, 1999; *Thomsen*, 2004), and it varies with local time and particle energy. *Denton et al.* (2005) performed a superposed epoch analysis of storms in order to correlate the storm phase with the temporal variation of plasma found at geosynchronous orbit and showed that the solar cycle is one of the main controlling factors for the plasma sheet density. Moreover, the ion composition is found to be dependent on the solar cycle (*Young et al.*, 1982) and plasma properties at geosynchronous orbit have been shown to be well correlated with solar wind plasma properties (*Borovsky et al.*, 1998).

For many years the solar wind has been believed to be a significant source for the magnetospheric plasma. The entry of 0.1 to 1.0% of the incident particles into the magnetosphere results in an effective solar wind source for the plasma sheet and therefore ring current populations. Nevertheless, the entry mechanisms, the transport and acceleration processes acting on these particles, before they reach the inner magnetosphere to contribute to the ring current, remain open issues.

On the other hand, *Chappell et al.* (1987), based on ionospheric outflow observations, hinted that the ionosphere alone is able to supply all magnetospheric plasma under any geomagnetic condition. The potential of the ionosphere to act as a source of magnetospheric plasma is the same as the solar wind and is limited as well to various transport and acceleration processes. Although there is controversy whether the dayside cleft or the auroral region are the dominant contributors to the ionospheric outflow, both are significant O^+ ion sources (*Yeh and Foster*, 1990; *Horwitz et al.*, 1992; *Lu et al.*, 1992; *Wing Ho et al.*, 1994). It has been suggested that different mag-

netospheric conditions are regulated by different ionospheric outflow regions (*Daglis and Axford*, 1996). Nevertheless, due to their low energy nature, the acceleration mechanisms that control energization of ionospheric ions from few eV to keV range is still a debatable problem.

Furthermore, the composition of the ring current depends strongly on the magnetic and solar activity. The detailed composition of the ring current was first reported during the Active Magnetospheric Particle Tracer Explorer (AMPTE) mission in the late 1980s during solar min and it was inferred that protons are the dominant ion species in the quiet time ring current, with the contribution of ions heavier than protons being essentially negligible.

Hamilton et al. (1988) reports on the ring current composition during an intense magnetic storm. They find that O^+ is the dominant ion throughout the main phase of a particular storm, mostly found in the inner ring current with a contribution of about 47% of the total energy density, compared with the H^+ 36%. For L shell values larger than 5, the maximum O^+ contribution there was 31%, and H^+ contributing about 51%. Compositional information for the bulk of the ring current ions for the energy range between a few tens of keV to a few hundred keV was also made available from the Combined Release and Radiation Effects Satellite (CRRES) mission (1990 - 1991). Based on these observations, it was inferred (*Daglis*, 1997) that the O^+ content increases with increasing geomagnetic activity, i.e. larger storms display a larger O^+ contribution to the ring current population.

The relative contributions to the ring current content of solar wind and ionospheric ions was summarized by *Daglis et al.* (1999) and the results are presented in Table 1.2.

Ion Source and Species	Quiet Time	Small/Medium Storms	Intense Storms
Total Energy Density (keV/cm^{-3})	~ 10	≥ 50	≥ 100
Solar Wind H^+ (%)	≥ 60	~ 50	≤ 20
Solar Wind He^+ (%)	< 1	< 1	< 1
Solar Wind He^{++} (%)	~ 2	≤ 5	≥ 10
Ionospheric H^+ (%)	≥ 30	~ 20	≤ 10
Ionospheric He^+ (%)	< 1	< 1	< 1
Ionospheric O^+ (%)	≤ 5	~ 30	≥ 60
Solar Wind Total (%)	~ 65	~ 50	~ 30
Ionosphere Total (%)	~ 35	~ 50	~ 70

Table 1.2: Contributions of main ion species to the total energy density at a radial distance of 5 Re, according to composition measurements by the AMPTE and CRRES Missions. Table adapted from *Daglis et al.* (1999).

1.4.2 Loss Mechanisms for the Decay of the Ring Current

The ring current decay during the recovery phase of the magnetic storm leads to the restoration of the surface magnetic field of the Earth and the return of the magnetosphere to its pre-storm state. The long term ring current decay is due mainly to collisions of ring current particles with neutral atoms from the upper atmosphere as well as Coulomb collisions with low energy particles from the plasmasphere. However, during the main phase and the early recovery phase of storms, loss through flow out to the dayside magnetopause can dominate the ring current decay. Since neutralized ring current particles are able to escape the inner magnetosphere trapping region, charge exchange processes act as a major direct loss mechanism for the ring current. Additionally, particle interactions with plasma waves are believed to be responsible for temporary enhancements of particles fluxes.

1.4.2.1 Dayside flow out

While the charge exchange of ring current energetic particles with the cold geocorona hydrogen is the dominant loss mechanism of ring current population during the late recovery phase and the quiet times, the ion flow out on open drift paths

to the dayside magnetopause controls the decay of ring current at times of elevated convection, that is, during the main phase of a magnetic storm and the early recovery phase (*Takahashi et al.*, 1990; *Liemohn et al.*, 1999, 2001b; *Kozyra et al.*, 2002). Due to the long duration of a magnetic storm (ranging from hours to days), the particles that are injected on the nightside are able to drift completely through the inner magnetosphere. This drift is energy and convection dependent and therefore, under times of high convection, it can take only a few hours for the energetic particles moving on open drift paths to reach the magnetopause and to be lost. During this time the ring current is highly asymmetric, and most of its energy (up to 90%) is flowing along open drift paths (*Liemohn et al.*, 2001b; *Kozyra et al.*, 2002). The formation of the symmetric ring current is inhibited by these losses from convection to the dayside magnetopause (*Liemohn et al.*, 1999). *Zong et al.* (2001) estimated that in the course of a magnetic storm the loss rate of O^+ ions to the magnetopause can be as high as 0.61×10^{23} ions/s.

Observations of energetic O^+ ions in the magnetosheath and upstream of the bow shock during times of elevated convection confirms that the ring current is flowing out to the dayside magnetopause at these times (*Moebius et al.*, 1986; *Christon et al.*, 2000; *Zong et al.*, 2001; *Posner et al.*, 2002). *Takahashi et al.* (1990) used a particle trajectory tracing method to quantitatively examine the dayside flow out of ring current particles. The authors suggest that the rapid recovery phase is due primarily to flow out losses while charge exchange losses dominate the slow recovery phase. This study also implies that the energy of the particle along with the length of recovery of the cross polar cap potential control the amount of plasma trapped on the closed field lines.

Kinetic ring current model studies (*Takahashi et al.*, 1990; *Ebihara and Ejiri*, 1998; *Liemohn et al.*, 1999) suggest that dayside ion flow out is the major ring current loss process during the main phase of intense magnetic storms and the eastward

component of the solar wind electric field sets up the time scale for ion loss due to these drifts. Elevated convection corroborated with decreasing plasma sheet density will lead to a gradual replacement of the higher density plasma with the lower density plasma on the open drift trajectories, yielding a significant loss of ring current energy. Conversely, if the plasma sheet density remains high but the convection strength gradually decreases, then newly injected high density plasma will move along open drift paths at higher radial distances. Furthermore, *Liemohn and Kozyra* (2005) show that the former scenario leads to a two phase decay of the ring current, while the latter is producing a single dip storm profile.

An example of a high convection event is presented in Figure 1.6 from *Kozyra and Liemohn* (2003) clearly showing that the ion flow out losses dominate the main phase of the storm while the charge exchange processes are significantly contributing to the ring current decay during the recovery phase. The convection strength controls this loss process, i.e. increasing convection will increase the flow out loss and vice versa.

However, the issue of when flow out loss to the magnetopause is larger than charge exchange loss within the magnetosphere and how these two loss mechanisms relate to the ring current drivers and morphology, is still open to debate. A recent statistical study of intense storms (SYM-H ≤ -100 nT) by *Keika et al.* (2005) used in-situ observations by Geotail/EPIC and showed that the outflowing energy flux is ranging from 10^5 to 10^8 $keV/(cm^2 s)$ during both the main phase and the recovery phase. Furthermore, the authors suggest that not only is the ion outflow better correlated with the square root of the dynamic pressure of the solar wind than the solar wind electric field (and therefore convection), but it has a magnetic local time dependence as well. The outflowing energy fluxes are preferentially higher on the afternoon-side than on the morning-side. They estimate that a minimum of 23% of the total ring current fast decay is due to dayside ion outflow, even in the case of a sudden northward turning of the interplanetary magnetic field which causes a sudden decrease in the

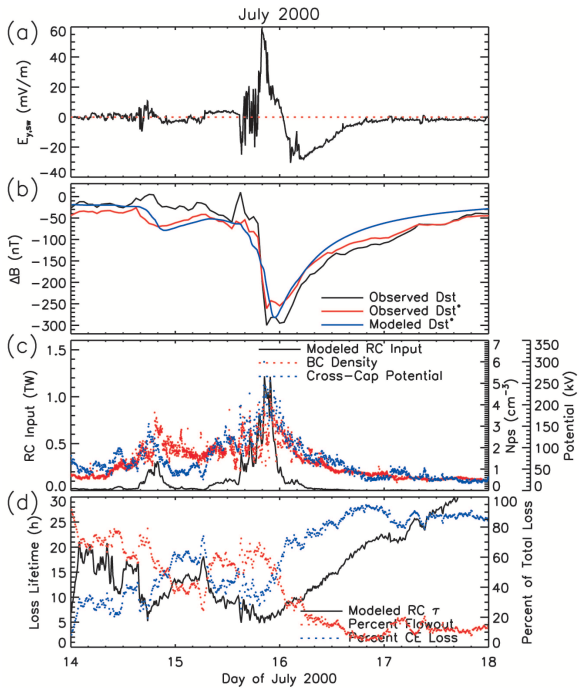

Figure 1.6: Simulation results for the July 14, 2000 magnetic storm. Top panel: eastward component of the solar wind electric field ($E_{y,sw}$ (mV/m)). Second panel: modeled D_{st}s nT (blue line), the observed D_{st} (black line) and observed D_{st}s (red line). Third panel: energy input through the nightside outer boundary (L = 6.75) of the model (black line), plasma density at geosynchronous orbit (red dotted line) and the cross polar cap potential (blue dotted line). Bottom panel: the globally-averaged loss lifetime for the ring current is presented in the bottom panel (black line) along with percentage of loss due to charge exchange (blue dotted line) and flow-out (red dotted line). Figure from *Kozyra and Liemohn* (2003).

convection electric field. However, increased convection will push particles closer to the Earth and therefore charge exchange processes can contribute to the rapid decay of the ring current as well. The spatial configuration of the open drift paths and how deep the particles penetrate into the inner magnetosphere determine whether charge exchange makes a significant contribution to the ring current losses as the ions drift through the inner magnetosphere to the dayside magnetopause region.

1.4.2.2 Charge Exchange

Except during times of high convective drift, the dominant mechanism for the decay of the ring current is the charge exchange of the ring current ions with the geocorona. The geocorona is a halo-like extension of the exosphere out to several Earth radii, consisting of relatively cold ($\sim$ 1000 K), very tenuous neutral hydrogen atoms. Solar far-ultraviolet light is reflected off this hydrogen gas (*Chamberlain*, 1963) and so its abundance has been quantified.

Because the geocorona hydrogen density decreases exponentially with radial distance, at large altitudes down the magnetotail, the collisions with the neutral hydrogen become negligible. However, in the ring current region, these collisions become increasingly important and they account for significant loss of the ring current particles, since magnetospheric H^+ can be easily removed by charge exchange with the neutral exospheric hydrogen.

Singly charged ring current ions can be neutralized after collisions with thermal exospheric hydrogen atoms as described below:

$$H^+ + H_{cold} \rightarrow H + H^+_{cold} \tag{1.11}$$

$$O^+ + H_{cold} \rightarrow O + H^+_{cold} \tag{1.12}$$

$$He^+ + H_{cold} \rightarrow He + H^+_{cold} \tag{1.13}$$

The incident ring current ion picks up the orbital electron of the cold geocorona hydrogen atom resulting in the formation of an energetic neutral atom (ENA). Energetic neutral atoms are not affected by magnetic or electric field forces therefore they are no longer trapped in the geomagnetic field and leave the interaction region in

ballistic orbits in the direction of the incident ion velocity at the time of the impact. If the resulted ENA's velocity exceeds the Earth's gravitational escape field, then it is lost into space or precipitates down into the ionosphere. On the other hand, the low energy ENAs populate the plasmasphere. The existence of energetic neutral atoms was first reported by *Meinel* (1951) based on observations of precipitating energetic neutral hydrogen into the upper atmosphere during auroral substorms. A few years later, *Dessler and Parker* (1959) were the first to suggest the charge exchange between protons and neutral atmospheric hydrogen atoms would effectively contribute to the decay of the ring current, although the effectiveness of ion removal from the ring current through charge exchange processes was previously investigated by *Stuart* (1959) and *Fite et al.* (1958).

However, multiply charged ions allow for multiple charge exchange reactions:

$$He^{++} + H_{cold} \rightarrow He^{+} + H^{+}_{cold} \tag{1.14}$$

The importance of multiple charge exchange collisions was first reported by *Spjeldvik and Fritz* (1978). Their findings indicate that the higher charge states of helium and oxygen ions are increasingly important for energies above 100 keV, while at energies below this cutoff the lower charge states are dominant. *Bishop* (1996) suggests the possibility that that energetic neutral atoms generated in the main ring current traversing the inner magnetosphere can be re-ionized in several ways, converting ENAs back into ring current ions albeit on new L shells, undergoing subsequent charge collisions with geocoronal atoms, generating secondary ENA fluxes that can participate in further ionizing collisions. This mechanism could yield the formation of a secondary ring current close to the Earth, at L shell values of approximately 3, although this is not a large ring current population.

Moreover, low pitch angle ions are subject to additional charge exchange collisions with the oxygen atoms in the upper atmosphere:

$$H^+ + O \rightarrow H + O^+ \tag{1.15}$$

$$O^+ + O \rightarrow O + O^+ \tag{1.16}$$

$$He^+ + O \rightarrow He + O^+ \tag{1.17}$$

$$He^{++} + O \rightarrow He^+ + O^+ \tag{1.18}$$

The mean lifetime for charge exchange interaction of an energetic ion with the cold hydrogen atom, in the equatorial plane as defined by *Smith and Bewtra* (1978) is:

$$\tau_e = \frac{1}{n(r_0)\sigma v} \tag{1.19}$$

where $n(r_0)$ represents the neutral hydrogen density as a function of radial distance in the equatorial plane, σ is the charge exchange cross section of the respective ion and v is the incident ion velocity. The probability of collisions with neutral atoms from the exosphere depends strongly on the energy of the incident particles and is determined by the charge exchange cross sections. Because charge exchange cross sections are both energy and species dependent, different ring current ion species have different charge exchange lifetimes. A compilation of charge exchange cross sections for various ring current ions are found in *Spjeldvik* (1977), *Smith and Bewtra* (1978) and *Orsini et al.* (1998). The neutral hydrogen geocoronal radial profile has been calculated by *Rairden et al.* (1986) based on the observations of the ultraviolet imaging photometer carried on the Dynamic Explorer 1 satellite.

Numerous studies, both based on observations and numerical modeling show that

due to the strong species and energy dependence of the charge-exchange cross sections along with the temporal and spatial dependence of ring current composition, the charge exchange process strongly affects the ring current plasma. Figure 1.7 shows the profile of charge exchange lifetime as a function of energy and species (*Liemohn and Kozyra*, 2005). Moreover, it is inferred that the charge exchange loss processes are predominantly important after initial phase of the ring current decay.

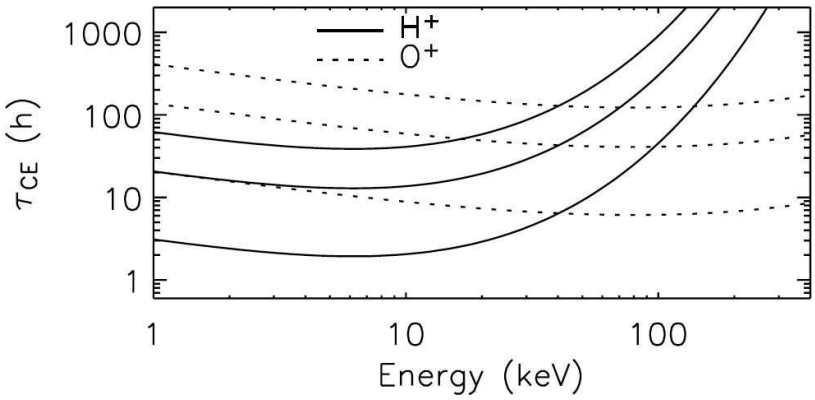

Figure 1.7: The mean lifetime for charge exchange decay as a function of energy for O^+ and H^+ species. Figure from *Liemohn and Kozyra* (2005).

Keika et al. (2003, 2006), based on measurements of energetic neutral atoms (ENAs) made by the High Energy Neutral Atom (HENA) imager on board the Imager for Magnetopause-to-Aurora Global Exploration (IMAGE) satellite, shows that the rate of the charge exchange energy losses is comparable to the ring current decay rate for the intervals of the slow decay, while the loss rate is much smaller than the decay rate in the rapid decay phase in particular for the early stage of a storm recovery. Similarly, *Jorgensen et al.* (2001) shows that during the fast recovery the measured ENAs can only account for a small portion of the total energy loss and the lifetime of the trapped ions is significantly shorter during the fast recovery phase than during the late recovery phase, suggesting that different processes are operating during the two phases. Furthermore *Kozyra et al.* (2002) suggests that charge-exchange losses can be solely responsible for the decay of the ring current during the recovery phase

only if IMF abruptly turns northward at the end of the main phase.

1.4.2.3 Coulomb Collisions

A second loss process, affecting principally low-energy ring current ions, is Coulomb collisions with the thermal plasma of the plasmasphere. Coulomb collisions are collisional interactions between charged particles due to their electric fields.

Ring current particles, moving through the ambient plasmasphere and neutral atmosphere are subject to collisional interactions with coexisting plasmaspheric populations. An energetic charged particle will interact with the electric field of a thermal electron or ion, lose energy, especially due to collision with thermal electrons, and are pitch-angle scattered by both electrons and ions into the loss cone. This interaction will occur whenever the impact parameter is less than the Debye shielding distance.

The angular scattering is important for electrons and low-energy ($\leq$ 10 eV) ions and is usually negligible for high-energy ions (*Wentworth*, 1963). The initial kinetic energies of the particles and the density of the plasmaspheric and atmospheric populations are the primary parameters that determine the loss rate of ring current particles due to Coulomb collisions. The energy transfer rate is maximum when the velocity of the energetic ions and that of the thermal species are comparable (*Fok et al.*, 1993), therefore this implies that most of the energy received by the thermal plasma goes to the electrons. This is illustrated in Figure 1.8 adapted from *Fok et al.* (1993).

Coulomb collisions enable transfer of energy from the ring current to the plasmasphere. It is important to point out that the thermal electrons have significantly larger (by a factor of 4) conductivities compared with the thermal ions. Therefore a small amount of heating from the ring current may produce enhanced ion temperatures comparable to the electron temperatures in the plasmasphere. *Fok et al.* (1993, 1995) reports on such interaction between the ring current ions and the plasmasphere. Coulomb collisions between the low energy ring current population and

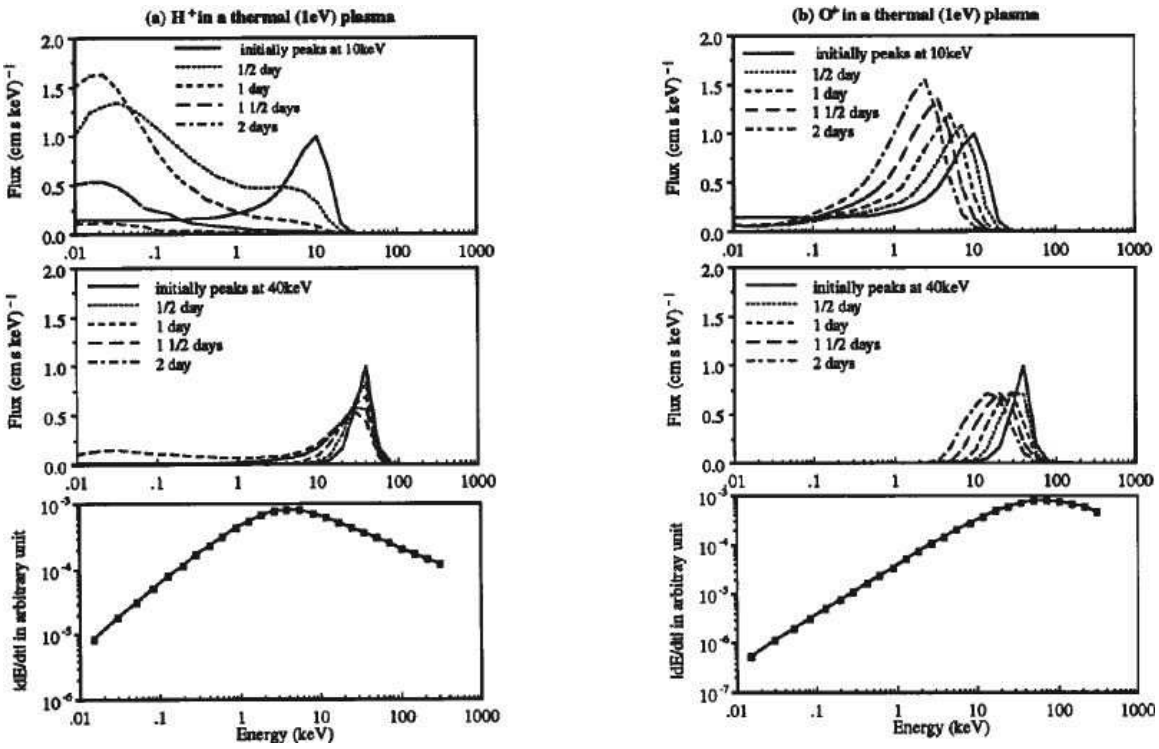

Figure 1.8: Time variations of H^+ (left panels) and O^+ (right panels) fluxes with initial energy peaking at 10 keV (top), 40keV (middle) keV in a background thermal plasma (1eV, $n = 2000$; cm^{-3}) and rate of energy loss as a function of ion energy (bottom). Figure from *Fok et al.* (1993).

thermal plasma are suggested to be responsible for the formation of Stable Auroral Red (SAR) arcs (*Kozyra et al.*, 1997).

The Coulomb lifetime is defined as the time after which only $1/e$ of the particle energy per solid angle at a certain pitch-angle in velocity space remains. Coulomb decay lifetimes for the main inner magnetospheric ion species as a function of energy and thermal plasma density are provided by *Fok et al.* (1991).

Numerical investigations of various loss processes describing the ring current decay (*Jordanova et al.*, 1996) suggest that Coulomb collisions are not negligible at lower energies ($\leq$ 10 keV), especially for heavier ions. It was also shown that Coulomb pitch angle diffusion scatters ions into the loss cone, increasing precipitation at low energies. However, for most geomagnetic conditions, it remains an overall small loss

process for the ring current.

1.4.2.4 Precipitation Losses

An additional non-collisional loss process thought to contribute to ring current decay is the precipitative loss of ring current particles into the atmosphere as a result of wave-particle interactions. If a charged particle gyrating about a magnetic field line with a certain field dependent gyrofrequency encounters an electromagnetic wave that propagates along the same field line and rotates with the same frequency and in the same direction, then the particle can be energized by the electric field of the wave and can be deflected by the magnetic field of the wave. Of course, resonances at frequencies which are multiples of the gyro-frequency can also take place. It is suggested that the ring current particles are affected by waves and irregularities in the magnetic and electric fields within the inner magnetosphere and the subsequent interactions allow for transfer of energy between different components of the ring current, plasmasphere, and radiation belts.

Furthermore, plasma waves can be generated by instabilities within the energetic particle distributions and transfer of energy from the charged particles to the waves becomes possible. There are at least two distinct plasma wave modes present in the magnetosphere that that are able to interact with ring current ions: Electromagnetic Ion Cyclotron (EMIC) and Magnetosonic Whistler waves. EMIC waves are found mostly in the outer magnetosphere, at L shell values larger that 7 (*Anderson et al.*, 1990), while the latter are observed both inside and outside the plasmapause (*Thorne et al.*, 1973).

Resonant pitch angle scattering also has the potential to remove resonant ions on timescales of under one hour. This timescale is therefore much shorter than the loss rate associated with collisional processes (*Feldstein et al.*, 1994). It has been suggested that the the wave particle interaction mechanism is primarily important

during the main phase of the storm (*Gonzalez et al.*, 1989), possibly contributing to the geomagnetic trapping and acceleration of ionospheric ions that are injected during the main phase of a storm. Nevertheless, due to their localized nature (*Jordanova et al.*, 1998), their contribution to the decay of the ring current is small relative to flow out, charge exchange and Coulomb collision losses. The role of this loss process in the evolution of the ring current is still not well understood and is currently the object of many investigations.

In addition, another ring current loss process is the precipitation loss on then nightside due to adiabatic drift into the loss cone as the ions are convected inward (e.g. *Søraas et al.*, 2005). This precipitation loss is actually bigger than the wave scattering because the regional precipitation is larger.

1.5 Magnetic Storm

1.5.1 Geomagnetic Indices

While magnetospheric disturbances are highly complex phenomena, the strength of magnetospheric perturbations is usually described using several ground based geomagnetic activity indices (*Mayaud*, 1980). Different indices emphasize different features of magnetic activity and careful consideration needs to be assumed when selecting an index to highlight certain traits within a data set. Here we describe three of the most used throughout this work: D_{st}**!** (D_{st}**!**) index, Symmetric disturbance field in H (SYM-H) index, and Planetary K (Kp) index.

The D_{st} index is defined as the instantaneous worldwide average of the disturbance of the equatorial horizontal component of the geomagnetic field. This index of geomagnetic activity is based on measurements from ground-based magnetometers placed close to the Magnetic Equator at Honolulu, San Juan, Hermanus and Kakioka, (*Sugiura and Kamei*, 1991) and contains contributions from the magnetopause cur-

rents, both partial and symmetric ring current, magnetotail currents along with Earth induced currents and possibly the substorm current wedge when this current is very strong. In spite of being 'contaminated' by various current systems, numerous studies (e.g. *Greenspan and Hamilton*, 2000; *Siscoe et al.*, 2005) showed that the partial and symmetric ring current are the main contributors to the magnetic perturbation in the horizontal component of the geomagnetic field. This depression in the magnetic field is proportional to the kinetic energy transported by ring current particles (*Dessler and Parker*, 1959). Furthermore, throughout the literature, it has been shown that a strong relationship exists between the variation of the D_{st} index during storms and the energy content of the ring current (e.g. *Jorgensen et al.*, 2001; *Liemohn and Kozyra*, 2003). As an alternative, the contribution from the magnetopause current can be removed from the D_{st} index (*O'Brien and McPherron*, 2000) and a D_{st}**s!** (D_{st}**s!**) is used in order to provide a better measure of the ring current buildup and decay. D_{st}s is defined as following:

$$D^*_{st} = D_{st} - 7.26 \cdot \sqrt{P_{dyn}} + 11.0 \tag{1.20}$$

where P_{dyn} is the solar wind dynamic pressure expressed nPa. Note that from this definition, the magnetopause current is proportional to the square root of the solar wind dynamic pressure. Some studies divide the right hand side of Equation 1.20 by 1.3 in order to remove the signal amplification by induced currents within the Earth (e.g. *Liemohn et al.* (2001b,a)).

Similar to the D_{st} index, the SYM-H geomagnetic index is also an indicator of geomagnetic activity but it has the advantage that it has a 1 minute temporal resolution, compared to 1 hour in the case of D_{st}. However, the D_{st} and SYM-H indices are not only different in time resolution, but also in the number and location of magnetometer stations used. The methods used to calculate and convolve station data into a final index are also different.

Another widely used index is the planetary K-index Kp and it also measures the global disturbance in the horizontal component of the geomagnetic field. Although known as the planetary index, its name is derived from the German word 'Kennziffer', meaning 'characteristic digit'. The time resolution of this index is 3 hours and it is obtained from 13 magnetometer stations located at mid latitudes. Each magnetic observatory has its own perturbation index K, which indicates the range of the maximum perturbation during a 3-hour interval and Kp is an average of the K-indices from all the available stations. Kp is expressed on a scale from 0 to 9. A value of 1 is characteristic of quiet times and a value over 5 is indicative of geomagnetic activity. As Kp is based on mid-latitude observations, it is more more sensitive to high-latitude auroral currents than is the D_{st} index, therefore it includes not only ring current contributions but the contribution from the auroral electrojet as well as the field aligned current system. It is worth mentioning that often there is no one-to-one correlation between the storm strengths given by Kp and D_{st}. A study regarding differences between the Kp and D_{st} responses to different solar wind drivers shows that fast post-shock streams and sheath regions had a relatively stronger effect on the Kp-index, whereas the effects of CMEs are better manifested in the D_{st} index (*Huttunen et al.*, 2002).

In this work we will mainly use the D_{st} index since it provides a good proxy for the ring current build up and decay and the storm intensity and duration are gauged by the D_{st} index as well.

1.5.2 Storm Phases

Geomagnetic storms are major disturbances of the Earth's magnetosphere that occur when the interplanetary magnetic field turns southward and remains southward for a prolonged period of time. Typically, a magnetic storm has three distinct phases: initial phase, main phase and recovery phase.

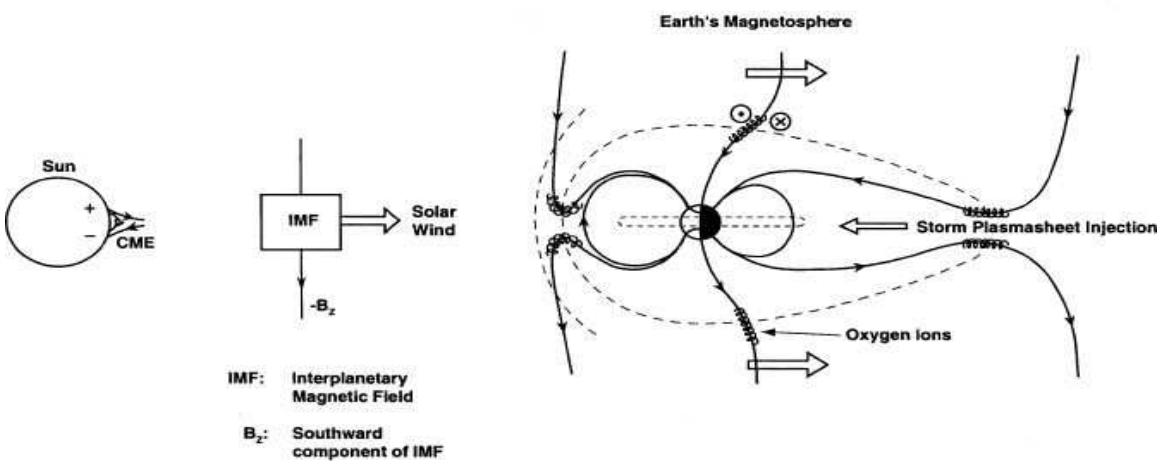

Figure 1.9: Sketch of storm time physical processes. Figure from *Gonzalez et al.* (1994).

The initial phase is characterized by a sudden increase in the magnetic field seen as a raise in the D_{st} index to positive values up to tens of nT. This is the time when interplanetary shockwave, correlated with an actual increase in the solar wind dynamic pressure, impinges into the magnetopause, pushing it inward as much as several Earth radii. The Chapman-Ferraro current intensifies and induces this steep change in the magnetic field, known as the Storm Sudden Commencement (SSC) and marks the beginning of the initial phase of the storm. The initial phase can last from minutes to several hours. However, it is not a necessary feature of the storm.

Following the initial phase, the geomagnetic storm's main phase is defined as the time period when charged particles in the near-Earth plasma sheet are energized and injected deeper into the inner magnetosphere, producing the storm-time ring current. This is a time period of sustained southward IMF. It translates into a great disturbance of the geomagnetic field, an interval of large decrease in D_{st} (D_{st} can reach negative values of hundreds of nT). A typical magnetic storm profile is presented in Figure 1.10. As a result, a strong cross-tail electric field pushes the plasmapause closer to the Earth.

The main phase duration ranges from few hours to as long as several days in the

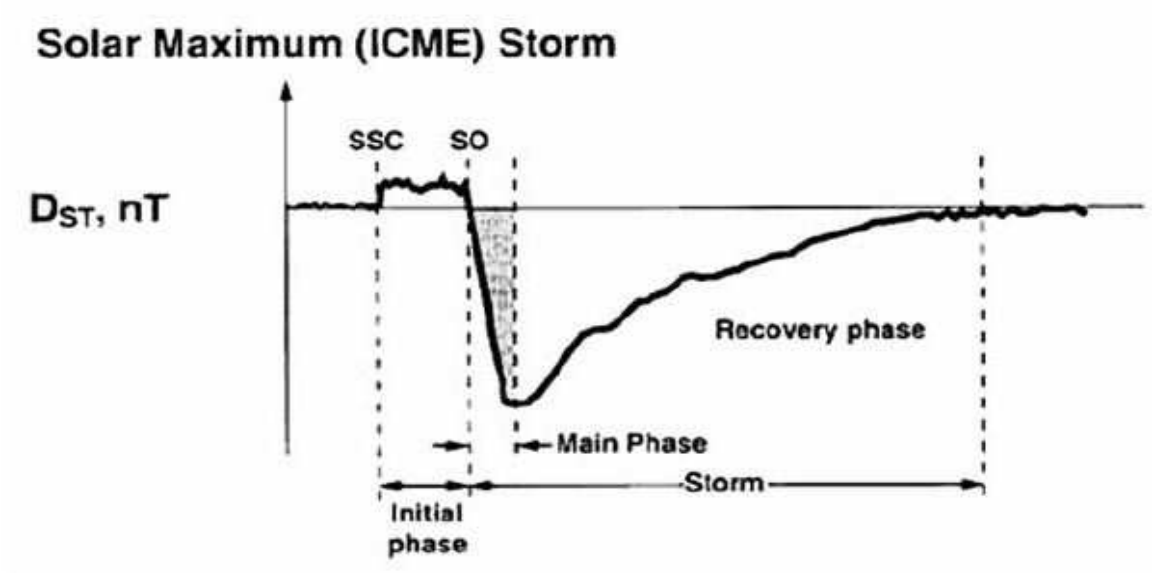

Figure 1.10: Sketch of D_{st} index profile during ICMEs driven storms. Figure adapted from *Tsurutani* (2000).

case of an intense storm. During this time, the main loss mechanism for the ring current particles is the flow-out to the dayside magnetopause (*Liemohn et al.*, 1999, 2001b).

As the southward component of the IMF weakens, the recovery phase begins in several steps. The reconnection rate decreases, leading to weaker electric fields, therefore limiting the injection of fresh plasma sheet particles into the ring current. The rate of plasma energization and inward transport slows and various loss processes start to remove plasma from the ring current. Therefore, the trapped particles in the ring current region start to dissipate through several mechanisms (such as wave-particle interactions, Coulomb scattering) and the D_{st} index slowly returns to its pre-storm condition (*Daglis et al.*, 1999). During this interval, the main mechanism of the ring current decay is charge exchange of ring current energetic ions with cold exospheric hydrogen. The expanding plasmasphere brings cold ionospheric plasma in contact with the ring current, contributing to the scattering of the ring current ions into the loss cone, to become energetic neutral atoms due to charge-exchange with

the cold neutral hydrogen. All these processes result in a gradual decay of the ring current and the magnetosphere gradually returns to its pre-storm state. The recovery phase can last from days to several weeks (*Gonzalez et al.*, 1994).

1.6 Different magnetospheric Storm Drivers

The Sun-Earth system is a complex, electrodynamically coupled system dominated by nonlinear interactions, and geomagnetic storms have their origin in the structure and dynamics of the solar atmosphere. Corotating Interaction Region (CIR), Coronal Mass Ejection (CME) and Interplanetary Shock (IS) are the most typical causes for geomagnetic activity at Earth. Geomagnetic storms are generally classified as recurrent and non-recurrent. Recurrent storms occur every roughly 27 days, corresponding to the Sun's rotation period. They are triggered by the Earth's encounters with the southward oriented magnetic field of the high-pressure regions formed in the interplanetary medium by the interaction of fast and slow solar wind streams co-rotating with the Sun. Non-recurrent geomagnetic storms occur most frequently near solar maximum. They are caused by interplanetary disturbances driven by fast coronal mass ejections and typically involve an encounter with both the interplanetary shock wave and the CME that drives it.

1.6.1 Coronal Mass Ejections

Coronal Mass Ejections are dramatic explosions in the solar atmosphere, originating from the closed field lines regions, characterised by massive ejection of dense solar plasma material into the interplanetary space. The manifestations of the CMEs in the interplanetary medium (after the CMEs are leaving the corona) are referred to as Interplanetary Coronal Mass Ejection (ICME), ejecta, driver gas, clouds or plasma clouds. Their signatures and properties have been extensively investigated and reported throughout the literature (e.g. *Neugebauer et al.*, 1997; *St. Cyr et al.*,

2000; *Gopalswamy*, 2006). ICMES are large scale magnetic structures, characterized by low plasma temperature (*Gosling*, 1990), enhanced magnetic field strength, low variability (smoothness) of the magnetic field (*Burlaga et al.*, 1981). Furthermore, plasma composition displays an increased helium to proton ratio (*Borrini et al.*, 1982; *Galvin et al.*, 1987) along with low plasma beta, decreased density (*Burlaga et al.*, 1981) and low proton temperature when compared to the ambient solar wind. An illustration of a coronal mass ejection is presented in Figure 1.11.

The mass of the CME varies across a few orders of magnitude, from 10^{12} to 10^{16} g, with each CME accounting for an average of 4.4×10^{14}g (*Gopalswamy*, 2006). The CME's velocities can range from few hundred km/s to 3000km/s (*Gopalswamy*, 2006). Often CMEs propagate at speeds greater than 1000 km/s at a few solar radii above the solar surface, speeds exceeding the Alfvén velocities at the same locations, reported to be approximately 800 km/s (*Mann et al.*, 1999). Nevertheless, the average speed has been reported to be solar cycle dependent, the average velocity being twice as large during solar maximum than during solar minimum.

The occurrence of such intense mass and energy releases, often associated with eruptive flares, has been suggested to be highly correlated with the phases of the solar cycle as well. *Gosling* (1990) reports on the occurrence of CMEs as about 4 per day during solar maximum, and down to 0.2 per day during solar minimum.

Fast CMEs with super magnetosonic speeds can drive shocks into the interplanetary medium, which in turn act to accelerate ions to very high energies. This shock can be identified by a sudden rise of the plasma speed, enhancement of magnetic field magnitude, along with density and temperature intensification. The region between the shock and the ICME is called the sheath. A strong correlation between the shock sheath and the CME speeds have been reported (e.g. *Mitsakou et al.*, 2009), suggesting that the coronal mass ejection is the main shock driver at 1 Astronomical Unit (AU).

When the interplanetary coronal mass ejection exhibits a large angle and smooth rotation in the IMF vector, along with low plasma beta values, it is often classified as a Magnetic Cloud (MC) structure. Magnetic clouds represent an important subclass of coronal mass ejections (*Burlaga et al.*, 1981), since they contain the strongest magnetic fields in the solar wind. Magnetic clouds are often interpreted as the signature of a magnetic flux rope (although the flux ropes are the same as magnetic clouds, they are less restricted according to the plasma beta). Typically, ICME flux ropes have their foot-points on the surface of the sun and, due to this closed field characteristic, when the flux rope expands near the sun, both its temperature and density are decreasing, therefore there is a low temperature and density inside the cloud. On average, about a third of ICME ejecta are MCs, although during the quiet phase of the solar cycle this ratio is higher. During the ascending phase of solar cycle 23 almost all ejecta around solar minimum were found to be magnetic clouds, while in the vicinity of the solar maximum the fraction was shown to be below 20% (*Richardson and Cane*, 2003).

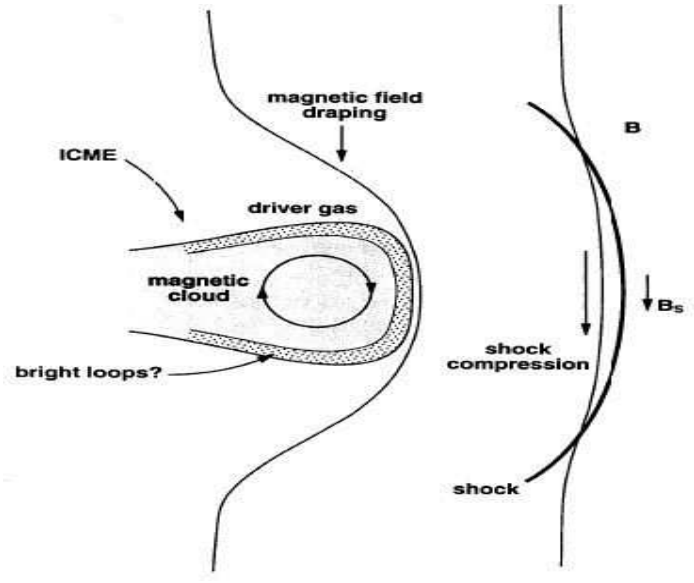

Figure 1.11: Schematic of Coronal Mass Ejection, sun is on the left. Figure from *Tsurutani* (2000).

CMEs are responsible for the major disturbances in the heliosphere such as shocks, interplanetary ejecta, interplanetary radio bursts, and large geomagnetic storms. CME driven magnetic storms are related to long periods of strong southward IMF that allows reconnection with the geomagnetic field and makes possible the transfer of solar wind energy throughout the magnetosphere. Geomagnetic activity is mainly driven by the term $v_x \times B_z$ (*Bargatze et al.*, 1986), where v_x denotes the X component of the solar wind velocity and B_z is the Z component of the interplanetary magnetic field. A typical profile of a ICME driven storm is presented in Figure 1.10.

ICME storms are associated with intense auroral emissions, that extend over all local times. The high speed and the elevated pressure within ICMEs are typically geo-effective enough to perturb the magnetosphere but the southward component of the IMF is the most critical parameter in the development large-scale magnetic storms. Different storm evolutions can take place according to the slow solar wind and the intrinsic characteristics of the interplanetary coronal mass ejections (*Tsurutani et al.*, 1988; *Zhang et al.*, 2004; *Huttunen*, 2005).

1.6.2 Corotating Interaction Region

During the late declining phase of the solar cycle, Coronal Mass Ejection type events become less frequent and the High Speed Streams (HSS) originating in coronal holes (*Gonzalez et al.*, 1999) are the main source of magnetic activity. Coronal holes are confined to the solar poles during the solar maximum phase, but in the descending phase, they expand and move toward the equatorial region (*Hundhausen*, 1972). Unlike the CMEs, which are closed magnetic field structures, these coronal holes are open magnetic field regions which emanate high speed solar wind streams (*Sheeley and Harvey*, 1978). Their velocities are well above the background solar wind velocity, allowing for the formation of an interface region between the fast and slow moving plasma. This flow at different speeds becomes radially aligned at low

heliographic latitudes as the sun rotates. The faster streams are catching up with the slower ones, resulting in a compression of the plasma and the creation of a high pressure region that prevents the mixing of the two flows. Moreover, as the solar wind moves outward, it cools down and it slowly accelerates to supersonic velocities. Therefore the leading edge of the fast stream keeps steepening and eventually a forward and a reverse shock is formed. The shocks are typically formed at large heliocentric distances beyond Earth's orbit. The spiral like structure formed by the slow and fast streams and its interaction region are illustrated schematically in Figure 1.12.

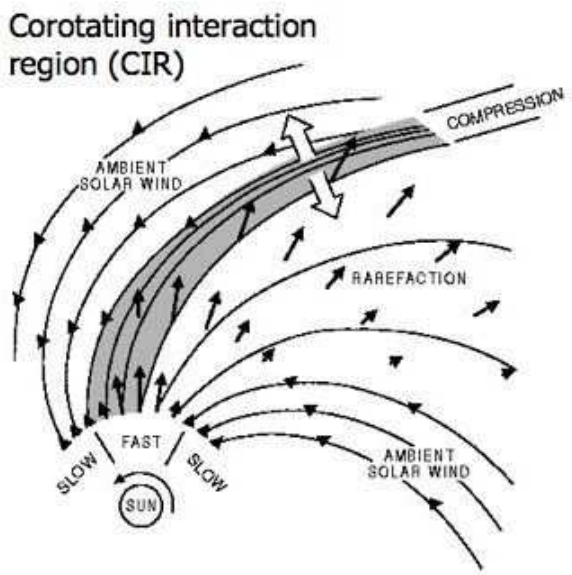

Figure 1.12: Schematic of Corotating Interaction Region.

CIR events have a 27 day periodicity (a consequence of the solar rotation) and they tend to occur mostly in the late declining phase of the solar cycle and solar minimum, as shown by *Mursula and Zieger* (1996). CIRs are typically followed by high speed streams and either the corotating interaction region or the stream can be the driver for geomagnetic activity. While the CIR events are typically associated with modest levels of geomagnetic activity, it was suggested their geoeffectiveness have a seasonal dependence (*Russell and McPherron*, 1973). High speed streams have lower densities

compared to CMEs, but the the eastward component of the electric field is strong, and therefore they can cause strong convection within geospace. An illustration of a corotating interaction region is presented in Figure 1.12.

It is worth mentioning that the pattern of a CIR rotates with the Sun, while the solar wind plasma and associated structures (shocks, magnetic field) propagate nearly radially outward. When such a structure reaches the Earth, it can cause a geomagnetic disturbance. It has been noted that the profile of storms caused by CIRs is somewhat different from that observed in CME storms. Typically, a CIR driven storm exhibits the initial, main and recovery phases, but the initial phase lacks the storm sudden commencement feature and is marked by a gradual increase in the D_{st}. This is caused by the high density plasma region associated with the heliospheric plasma sheet in front of the high speed stream impinging upon the magnetosphere (*Tsurutani et al.*, 1995). A schematic with the typical profile of a CIR storm is presented in Figure 1.13.

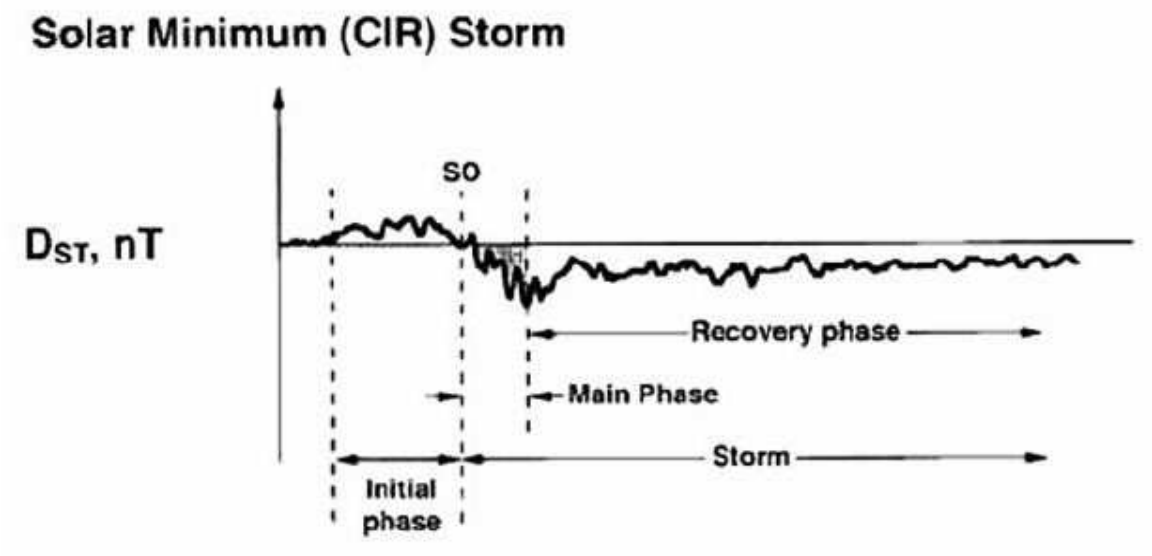

Figure 1.13: Sketch of D_{st} index profile during CIR driven storms. Figure adapted from *Tsurutani* (2000).

During CIR driven events, the reconnection intervals are expected to be inter-

mittent as well as shorter than during CME driven storms, therefore the injection of particles into the magnetosphere may appear to be sporadic. This is due to the fact that the Z component of the magnetic field within a Cororating Interaction Region is highly fluctuating and it was noted that these fluctuations are highly correlated with excursions of the D_{st} index (*Tsurutani et al.*, 2005). *Borovsky and Denton* (2006) explored and tabulated the main differences between CIR and CME driven storms, showing a direct comparison of their input functions and the corresponding responses.

Since CIR recoveries and the events themselves can last much longer than those observed during CME driven magnetic storms (e.g. *Turner et al.*, 2006), due to the southward component of trailing Alfven waves, these events can transfer considerable amounts of solar wind energy to the terrestrial magnetosphere. A comparative statistical study of the geoeffectiveness of the HSS, CMEs and interplanetary shocks (*Lu*, 2006) concluded that the ratio of solar wind kinetic power to the magnetospheric energy is similar for all these drivers. *Turner et al.* (2006) showed that CIRs seem to be more geoeffective in the sense that, on average, the ratio of the energy deposited into the magnetosphere to the energy input to the magnetosphere for high speed streams exceeds the corresponding ratio for the CME case. Further, ring current investigations of HSS/CIR versus CME driven events using numerical models (*Jordanova et al.*, 2006; *Liemohn et al.*, 2008, 2010) show that the ring current response is different for these drivers. CIRs produce smaller D_{st} disturbances compared to the ones produced by CMEs (*Denton et al.*, 2006), indicative of a weaker ring current.

An important aspect of fast streams is that they are embedded with Alfvén waves (*Tsurutani et al.*, 1995). It has been shown that the southward components of the IMF B_z fluctuations (Alfvén waves) within HSS cause sporadic injection of particles into the magnetosphere through magnetic reconnection, due to the the oscillatory nature of the B_z component of the magnetic field, preventing the magnetosphere from fully recovering.

During the prolonged recovery phase of the HSS storms, another type of activity can happen: High Intensity Long Duration Continuous AE Activity (HILDCAA) (*Tsurutani and Gonzalez*, 1987), displaying a strong correlation between the minimum B_z and the maximum AE index. HILDCAA events are being associated with higher speed streams emanating from the coronal holes (*Tsurutani et al.*, 2006), although HILDCAA events can occur after CME storms as well as after CIR storms, or even without any storm occurrence. During this type of geomagnetic activity, the B_z component of the interplanetary magnetic field shows variations in amplitude almost symmetric around zero.

It is important to point out that during the solar cycle declining phase, there is more energy deposited into the magnetosphere than during solar maximum, due to the long duration of the associated occurring phenomena.

To summarize, these different solar wind drivers have different effects on the magnetosphere. That is the southward component of the IMF B_z is higher for CMEs during the main phase of the storm. Solar wind velocity is higher for CIRs, especially during recovery phase and the solar wind density is higher for CIRs during the main phase. CIR type events have less effect on D_{st}, therefore being responsible for less intense storms and weaker ring currents.

Furthermore, different storm types generate different ring current responses: aside from being associated with lower absolute D_{st}, CIRs generally last longer than CMEs. However, their long duration makes them more geoeffective (efficiency of solar wind energy coupling into magnetosphere) (*Turner et al.*, 2006).

There are a few possible causes for the different ring current response: differences in the particle composition, differences in the particle energies, difference in storm lengths, difference in storm strength, difference in convection, diffusion processes, preconditioning of the ions in the magnetotail (this has been associated with CIRs and may be relevant) (*Borovsky and Denton*, 2006).

Corotating interaction regions (CIRs) and interplanetary coronal mass ejections (ICMEs) are the biggest contributors to magnetic disturbances at Earth (*Gosling et al.*, 1991; *Tsurutani and Gonzalez*, 1997). *Feynman* (1980) found that CIRs predominately disturb Kp but not D_{st}, unlike CMEs, which perturb both Kp and D_{st}. *Denton et al.* (2006) showed that geosynchronous plasma responds differently during CME-driven storms than during CIR events; that is, during CME events, the plasma sheet density is one of the parameters that is preferentially enhanced, while CIR-driven storms produce an enhancement in the plasma sheet temperature. Both drivers, CIRs and ICMEs are capable of driving shocks, which in turn, can accelerate charged particles.

1.7 Motivation

Magnetic storms and their solar wind drivers have been extensively investigated throughout the years. Due to the great amount of data available in recent years, a large variety of studies of these space weather events were performed in order to relate solar wind features to the corresponding geomagnetic responses (e.g. *Gonzalez and Tsurutani*, 1987; *Gonzalez et al.*, 1994; *O'Brien and McPherron*, 2000; *Huttunen and Koskinen*, 2004; *Zhang et al.*, 2006a). Plasma observations at geosynchronous orbit are extremely advantageous for the study of storms and, in particular, for studying ring current sources since at this location the transition from plasma sheet to ring current is observed to take place (*Denton et al.*, 2005, 2006).

Understanding how the morphology of the plasmasphere and ring current changes as a function of various factors, processes, source terms, and conditions is critical to our understanding of the geospace domain. While in-situ measurements of the inner magnetosphere broaden our understanding of the dynamic processes that dominate this region, the energization of the system is still a quite difficult issue to examine using observations alone. Consequently, global magnetohydrodynamic (MHD) simulations

provide an excellent alternative for investigating the large-scale coupling of the solar wind-ionosphere-magnetosphere system, especially when such a model is combined with kinetic physics models from various regions of the space where coupling processes are important (like the inner magnetosphere).

The presented work addresses these open issues by investigation of the following outstanding problems:

1. What role does the choice of epoch time play in the description of a magnetic storm when doing Superposed Epoch Analysis?

2. What is the role of transient spikes in the solar wind data in the development of a magnetic storm and how it affects the ring current build-up and decay?

3. What is the response of the ring current to changes in the energy input?

4. What determines the transfer of periodicity seen IMF B_z to the magnetosphere?

5. How well does the Space Weather Modeling Framework simulate an actual event?

We closely studied these questions using both data analysis and numerical simulations of the inner magnetosphere, along with improvement and further development of a new, more reliable ring current model. In Chapter II, the influence of epoch time choice when averaging data from many storm intervals is examined and our results indicate that a distinct epoch time is needed in order to resolve certain storm features. Throughout Chapter IV, Chapter V and Chapter VI we investigate the nature of the relationship between the solar wind energy input and the magnetosphere as well as the capability of SWMF (described in detail in Chapter III) to simulate a magnetic storm. In Chapter VII we discuss initial results involving a modified Hot Electron and Ion Drift Integrator (HEIDI) model. Finally, Chapter VIII summarizes results

from both data analysis and global simulations along and presents suggestions for future work.

CHAPTER II

Statistical study of magnetic storm temporal evolution

2.1 Motivation

Numerous studies have shown that the magnitude and features of magnetic storms depend not only on the values of IMF and solar wind plasma parameters but also on their temporal evolution. The main aim of the statistical study presented in this chapter is to analyze various characteristics of intense geomagnetic storms as well as to better understand the progression of such events.

The tool of superposed epoch analysis was previously used to investigate magnetospheric disturbances, by categorizing the events according to several different characteristics. *Zhang et al.* (2006a,b) and *Liemohn et al.* (2008) examined the features of magnetic storms relative to their intensity and time of occurrence (intense vs. moderate vs. superstorms, solar maximum vs. solar minimum). Distinguishing the events by their solar wind drivers (e.g., CME vs. CIR-driven storms) is another way to categorize them (*Pulkkinen et al.*, 2007; *Denton et al.*, 2006; *Borovsky and Denton*, 2006; *Huttunen et al.*, 2006; *Zhang et al.*, 2007).

Most of the time, for statistical studies, the natural choice of the epoch time seems to be the peak storm intensity (the minimum of D_{st} index) (*Loewe and Prölss*, 1997;

Miyoshi and Kataoka, 2005; *Zhang et al.*, 2006a,b; *Liemohn et al.*, 2008; *Denton et al.*, 2005, 2006). *Pulkkinen et al.* (2007) used the storm onset along with the minimum D_{st} as the epoch time when studying the differences between distinct drivers for magnetic storms, showing that the sheath storms develop faster at the storm onset and the main phase is shorter than in the case of cloud driven events. The storm sudden commencement was used as the epoch time by *Elphic et al.* (1996) as well, to look at the behavior of cold ions at geosynchronous orbit. *Davis et al.* (1997) used the southward turning of the IMF B_z as the time stamp to study the ionospheric response at mid-latitudes to solar wind driving.

It has been acknowledged that in order to describe the temporal variation of certain parameters, the choice of the time stamp might be important, but so far, there has been no systematic examination of the influence of this choice. In this chapter we investigate how the choice of epoch time affects the average behavior of the storm time solar wind and geosynchronous plasma when doing superposed epoch analysis. For this study we selected seven distinct time stamps somewhat evenly distributed throughout the duration of the storm main phase.

2.2 Methodology

2.2.1 Data Coverage

Solar wind IMF and plasma in situ observations are obtained from the ACE spacecraft in orbit around the L1 Lagrange point 1.5 million km upstream of the Earth. The data set, obtained from the National Space Science Data Center, consists of 4-minute interplanetary magnetic field (IMF) data (from the MAG instrument) and 64-second solar wind plasma parameters (from the SWEPAM instrument). The plasma data were then averaged to 4 minutes temporal resolution, taking any 64 seconds value whose start minute fell between the start minute of the IMF data and

4 minutes later. The observations are converted from the GSE to GSM coordinate system and time-propagated from the satellite location to (17 Re, 0, 0), using the minimum variance analysis technique (*Weimer et al.*, 2003; *Weimer*, 2004). Along with the ACE data, the one hour resolution D_{st} index, provided by the World Data Center at Kyoto University, is used to study the geomagnetic responses to solar wind conditions.

For the second half of this work, data are obtained from the Magnetospheric Plasma Analyzers (MPA) on seven Los Alamos National Laboratory (LANL) geosynchronous satellites, which provide good local time coverage for most of the events. Each MPA instrument is a spherical-sector electrostatic analyzer capable of measuring three dimensional distributions of ions and electrons from $1\ eV$ to $45\ keV$, on timescales of $86\ s$. A detailed description of the instrument can be found in *Bame et al.* (1993) and *McComas et al.* (1993). The present study extends the work of *Zhang et al.* (2006a,b). The hot-ion fluxes ranging from 100 eV to 45 keV are used for the moments calculations, and since the MPA measurements do not contain any composition information for the positively charged particles, the calculation of the moments assumes that all ions are protons. For most conditions, this assumption is reasonable to within a factor of 2 since *Young et al.* (1982) showed that, for energies below 17 keV at geosynchronous orbit, n_{O^+}/n_{H^+} is rarely greater than unity. However, during storm times the contribution of O^+ is known to increase substantially. In the case of $n_{O^+}/n_{H^+} >> 1$ the plasma density would be four times higher than would be calculated under the assumption that $n_{O^+}/n_{H^+} << 1$ (*Liemohn et al.*, 1999). Also, due to the fact that MPA measures energy per charge, the temperature measurements are not biased by the all-proton assumption. In the present work we study the average nature of three derived bulk hot-ion parameters: number density (N_{HP}), isotropic temperature ($T_{HP} = (T_{\parallel} + 2T_{\perp})/3$) and entropy density ($S_{HP} = T_{HP}/N_{HP}^{\gamma-1}$, where the polytropic index $\gamma = \frac{5}{3}$). To ensure that the measurements are taken in the

plasma sheet, a limitation is set on the data such that $0.3\ cm^{-3} < N_{HP} < 6\ cm^{-3}$ and $T_{HP,\perp} > 2\ keV$, excluding any measurements from the magnetosheath, low-latitude boundary layer and magnetotail lobes (*Korth et al.*, 1999). The superposed epoch analysis technique enables us to illustrate the dependence of these plasma-sheet parameters on local time and epoch time.

2.2.2 Event Selection

According to the monthly averages of sunspot numbers, for this study we selected intense storms during the last solar maximum, i.e., from July 1999 to June 2002 (see Table 2.1.) The pressure-corrected D_{st} index ($D_{st}{}^{*}$) is used to identify the events as an intense storm, choosing events for which $D^{*}_{st} \leq -100\ nT$. The motivation for using $D_{st}{}^{*}$ instead of the D_{st} index in defining the storms is that the former contains mainly the contribution of the ring current and other near-Earth currents, while the magnetopause current input is removed. To compute the $D_{st}{}^{*}$ we use the formula of *O'Brien and McPherron* (2000):

$$D^{*}_{st} = D_{st} - 7.26 \cdot \sqrt{P_{dyn}} + 11.0 \tag{2.1}$$

where P_{dyn} is the solar wind dynamic pressure in nPa. Out of the 34 events that occurred during this period, only 29 were analyzed in this work; 5 storms were excluded due to lack of solar wind data.

2.2.3 Data Analysis Technique

Superposed epoch analysis (SEA) is a statistical method that combines data from similar but distinct events by defining a reference time (also called epoch time, time stamp and time mark) within each event in order to be used as a mark in the computation of means for each parameter within the selected category. Time marks for each event are chosen in such a way so that $t = 0$ (the so-called epoch time) cor-

Year	Month	Day	Hour	Minimum D^*_{st} (nT)
1999	09	22	23	-178.45
1999	10	22	07	-251.76
1999	11	13	22	-104.01
2000	01	23	03	-105.47
2000	02	12	11	-141.49
2000	04	07	00	-306.42
2000	05	24	08	-147.73
2000	08	12	09	-236.44
2000	09	17	23	-215.12
2000	10	05	13	-192.15
2000	10	14	14	-105.15
2000	10	29	02	-124.29
2000	11	06	21	-168.38
2000	11	29	13	-120.65
2001	03	20	15	-147.82
2001	03	31	08	-401.21
2001	04	11	23	-278.33
2001	04	18	06	-127.62
2001	04	22	15	-103.20
2001	08	17	21	-115.82
2001	10	01	08	-149.97
2001	10	03	14	-164.23
2001	10	21	21	-202.63
2001	10	28	11	-159.92
2001	11	01	10	-102.28
2002	03	24	09	-103.65
2002	04	20	06	-156.91
2002	05	11	19	-102.85
2002	05	03	17	-116.35

Table 2.1: List of events used for this study

responds to some common feature in the superposed data. In the present study we choose seven distinct time references within the development of the storms, ranging from the Storm Sudden Commencement (SSC) to the peak development of the storm (minimum D_{st}). The SSC was defined as the time corresponding to the maximum slope of D_{st} closest to the SSC, except for the cases when there is no obvious jump in solar wind pressure when the SSC time mark was manually chosen to correspond with the southward turning of the IMF B_z component. The slope of the D_{st} index was defined as:

$$D_{st}\ Slope(t_{n+\frac{1}{2}}) = \frac{D_{st}(t_{n+1}) - D_{st}(t_n)}{t_{n+1} - t_n} \tag{2.2}$$

such that the maximum value of the slope corresponds to an increase in the index itself while the minimum value of the slope coincides to the steepest decrease in D_{st}. We choose the slope of the D_{st} index as opposed to the slope of ${D_{st}}^*$ to define our reference times mainly because D_{st} index includes the effect of the dynamic pressure change at the shock associated with the SSC while the storm sudden commencement is removed from the ${D_{st}}^*$ index. The peak enhancement of the ring current was defined as the minimum ${D_{st}}^*$ slope (corresponding to the maximum negative slope). The minimum slope search was performed from the location of the maximum slope to the location of the minimum D_{st} (except 4 events for which it was manually chosen).

Aside from the obvious choice of minimum D_{st} as a reference time and the ones mentioned above, four additional marks were chosen: $Epoch_1$, $Epoch_2$, $Epoch_3$ and $Epoch_4$ defined below:

$$Epoch_1 = \frac{1}{2} \cdot (Time\ of\ Minimum\ D_{st} - Time\ of\ Minimum\ Slope) + Time\ of\ Minimum\ Slope \tag{2.3}$$

$$Epoch_n = \frac{n-1}{4} \cdot (Time\ of\ Minimum\ Slope - Time\ of\ Maximum\ Slope) + Time\ of\ Maximum\ Slope \quad (2.4)$$

for $n = 2, 3, 4$.

To illustrate these choices, Figure 2.1 shows the dynamic pressure (top panel), B_z component of the interplanetary magnetic field (second panel from top), the D_{st} index (black dotted line) along with the pressure corrected $D_{st}{}^*$ (black continuous line), and on the bottom panel the computed slope of the D_{st} index for the April 17, 2001 event. This storm is a typical example of the data set we are studying (but it has a short main phase), given that it shows a clear jump in solar wind dynamic pressure, followed by a southward turning of the IMF B_z, and the maximum slope of D_{st} corresponding to the Storm Sudden Commencement.

To be quantitative, we define the Main Phase as the time interval between the Storm Sudden Commencement (maximum D_{st} slope) and the peak development of the storm corresponding to the minimum D_{st} index. Within the Main Phase we defined the Early Main Phase as the time period starting at the SSC and ending at the location where the ring current has its maximum intensification (minimum slope of D_{st}). The Late Main Phase is defined as the period of time that starts at the peak enhancement of the ring current and ceases where the recovery phase starts (when the D_{st} begins to return to its quiet time value).

For this event, the main phase lasted for 5.5 hours, the early main phase and the late main phase having durations of 3 and 2.5 hours, respectively. The vertical dashed lines in the figure show all the epoch choices for our study. The plots represent 12 hours worth of data.

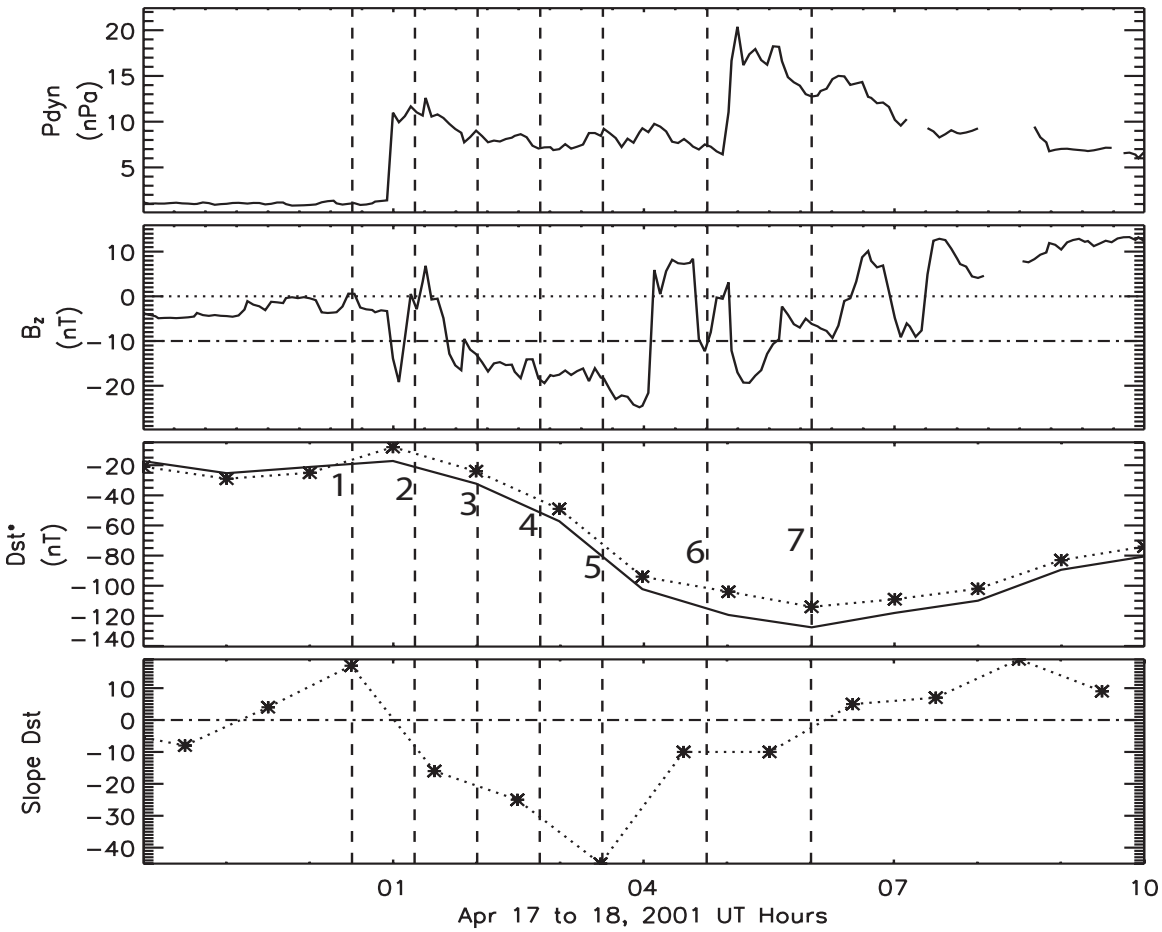

Figure 2.1: Event of April 17, 2001. From top to bottom are plotted the dynamic pressure (P_{dyn}), the z component of the interplanetary magnetic field (B_z), the pressure-corrected D_{st} index ($D_{st}{}^*$) (continuous line) along with D_{st} index (the dotted line) and the slope of the D_{st} index. Vertical lines indicate the position of different epoch time choices: SSC -Maximum Slope of D_{st} index (1), $Epoch_2$ (2), $Epoch_3$ (3), $Epoch_4$ (4), Minimum Slope of D_{st} index (5), $Epoch_1$ (6), and Minimum D_{st} (7). Symbols are added to show the slope and Dst data points.

2.3 Results

2.3.1 Storm Duration

As an initial study for our work, we looked at the average duration of the main phase of the storms. Statistical analysis of these periods (Figure 2.2) of time yielded the following results: the average Main Phase duration of a storm is 13.2 hours with a median (the 50th percentile) of 11.5 hours while the average duration of the Early Main Phase is 7.2 hours with a median of 7 hours. Also the average duration of the Late Main Phase is 6 hours with a median of 4 hours.

Three additional time stamps (equally spaced in time), during the Early Main Phase and of just one during the Late Main Phase were selected for our study. That is, for an average-length storm, the 7 reference times are equally spaced about every 2 hours throughout the main phase.

2.3.2 Solar Wind Data

Superposed epoch means of selected parameters for the 29 storms at solar maximum are presented in Figure 2.3. The top panels show the superposed average values of solar wind dynamic pressure (P_{dyn}), the center panels present the z component of the interplanetary magnetic field (B_z), and the bottom panels show the pressure-corrected D_{st} index (D^*_{st}). The three differently colored lines correspond to the results obtained using distinct time stamps: the red line corresponds to maximum D_{st} slope, i.e., the SSC as the epoch time; the blue line corresponds to the minimum D_{st} slope; and the black line corresponds to minimum value of the D_{st} index. The three plots on the left show the means plotted against the time relative to the epoch time. The vertical dashed line corresponds to the location of the time stamp (zero epoch time). The plots show results for within 1.5 days before and after the epoch time. The horizontal dashed lines in the B_z and ${D_{st}}^*$ panels denote the 80% occurrence level

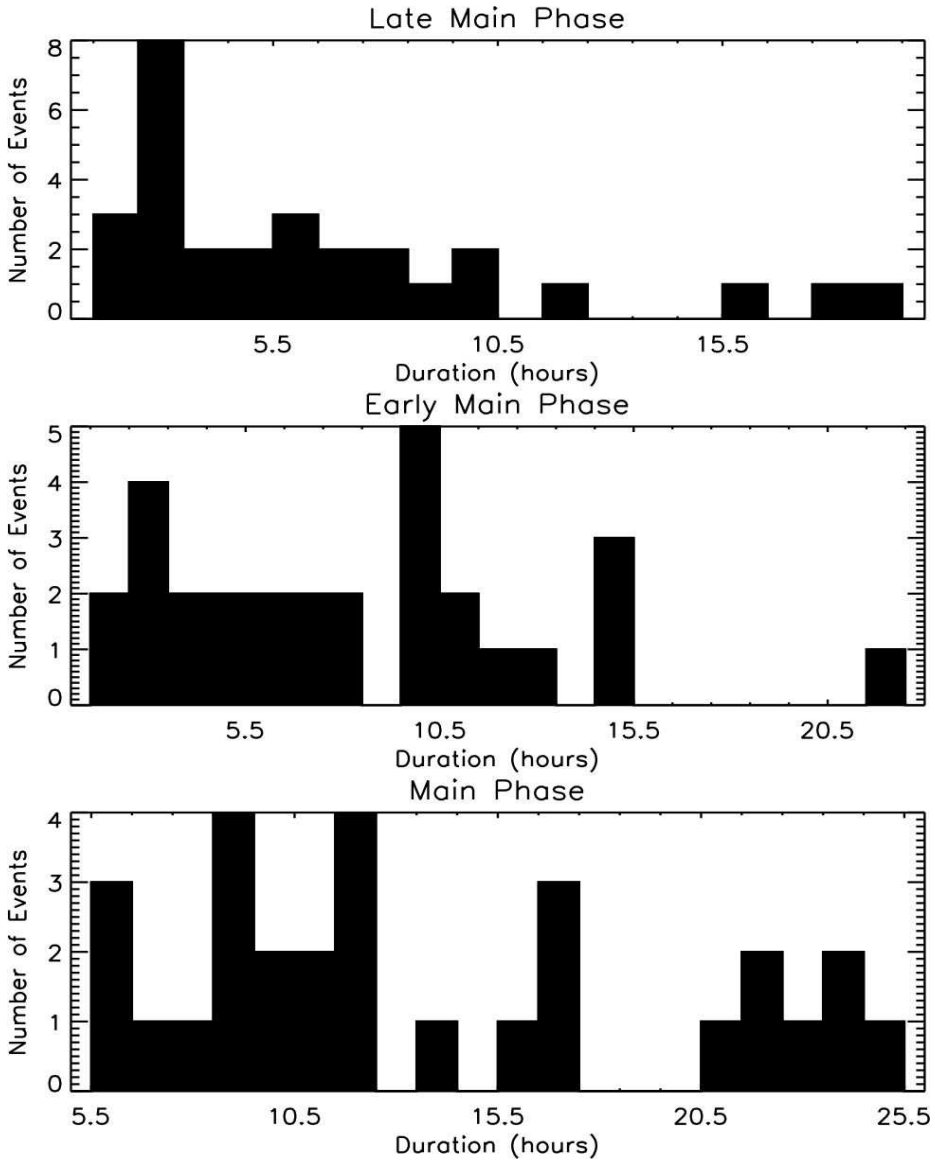

Figure 2.2: Histogram of the Storm Phases Durations: Late Main Phase (top panel), Early Main Phase (middle panel), Main Phase (bottom panel).

thresholds for intense storms (for intense storms with a measured D_{st} less than or equal to $-100nT$, 80% occur when the z component of the interplanetary magnetic field is less or equal to $-10nT$ for a time interval of more than 3 hours) as defined by *Gonzalez et al.* (1994) and *Gonzalez and Tsurutani* (1987). When using Maximum Slope as the Epoch Time (red curves), the SSC-related jump in solar wind dynamic pressure is very well reproduced, with the pressure ramping up and jumping from about 2.25 nPa just before the 0 time to about 8.5 nPa just one hour after. Near the storm peak, however, B_z for this choice of the epoch time does not follow the well-known criterion for intense storms ($B_z \leq -10\ nT$ for more than 3 hours), having values not lower than $-8\ nT$. Note that most of the individual events used in this study were selected to follow this criteria. The averaged D_{st} shows a slow drop, taking about 12 hours until it reaches the minimum value of approximately $-120\ nT$.

When the time stamp is set at the storm peak (black curves), the jump in solar wind dynamic pressure is less distinct (and eventually lost) with the solar wind dynamic pressure gradually increasing, but the standard criterion for B_z is met. The averaged minimum D_{st} for this case is less than $-165\ nT$ and the D_{st} decreases rapidly prior to minimum.

For the situation when the minimum slope of D_{st} is set as the time stamp (blue curves), the superposed means show $B_z \leq -10\ nT$ for more than 3 hours, with a minimum value similar to the previous case. The jump in dynamic pressure is not sharp at all and we see that the superposed ram pressure peaks at the moment when the intensification of the ring current is maximum. This is due to the averaging of a few storms that happened to have a high pressure a few hours after the storm SSC. The D_{st} index shows again a sharp decrease, having a comparable slope as in the previous case, peaking at about $-140\ nT$ this time. Also, the B_z in both situations has similar traits, reaching almost the same minimum value. We note that at the beginning of the storm, the D_{st} averaged relative to the peak of the storm descends

at a slightly slower pace than the one averaged at the peak enhancement of the ring current, mainly because the B_z turns southward in a more gradual manner than in the latter case when the gradient of B_z is higher. Therefore, as previously shown, the controlling factor in the rate of change of D_{st} is the southward component of the IMF (e.g. *Burton et al.*, 1975). On the left figures, the minimum averaged D_{st} occurs at different epoch times for different zero-epoch choices.

The three plots on the right show the same mean values shifted relative to the location of the means when averaged at the D_{st} minimum. The time shift of the blue and red lines relative to the black ones is 4 and 12 hours, respectively. This is in good agreement with our findings regarding the duration of the Main Phase. Note that we only choose one zero-epoch time in our superposed epoch analysis, therefore the means are not normalized with respect to the duration of the storms. Consequently, it is expected that the minimum averaged D_{st} when superposing our data at the minimum D_{st} slope (maximum D_{st} slope) does not occur exactly 6 (13.2) hours from the location of minimum averaged D_{st} when superposing at the minimum D_{st}. This is due to the fact that phase lengths of the individual storms are variable. Please note that the closer to the storm peak the epoch time is selected, the shorter the length of Main Phase gets with the Late Main Phase following the B_z ramp of the storm. Thus, by changing the epoch time in our analysis, not only the average intensity of the set changes but also certain features used to identify the events are no longer reproduced by the superposed data. The *Gonzalez et al.* (1994) criterion to produce an intense storm is met only if the superposition of the data is done in the interval between the $Epoch_4$ (which is, on average, 6 hours before the storm maximum and not shown in Figure 2.3) and storm peak.

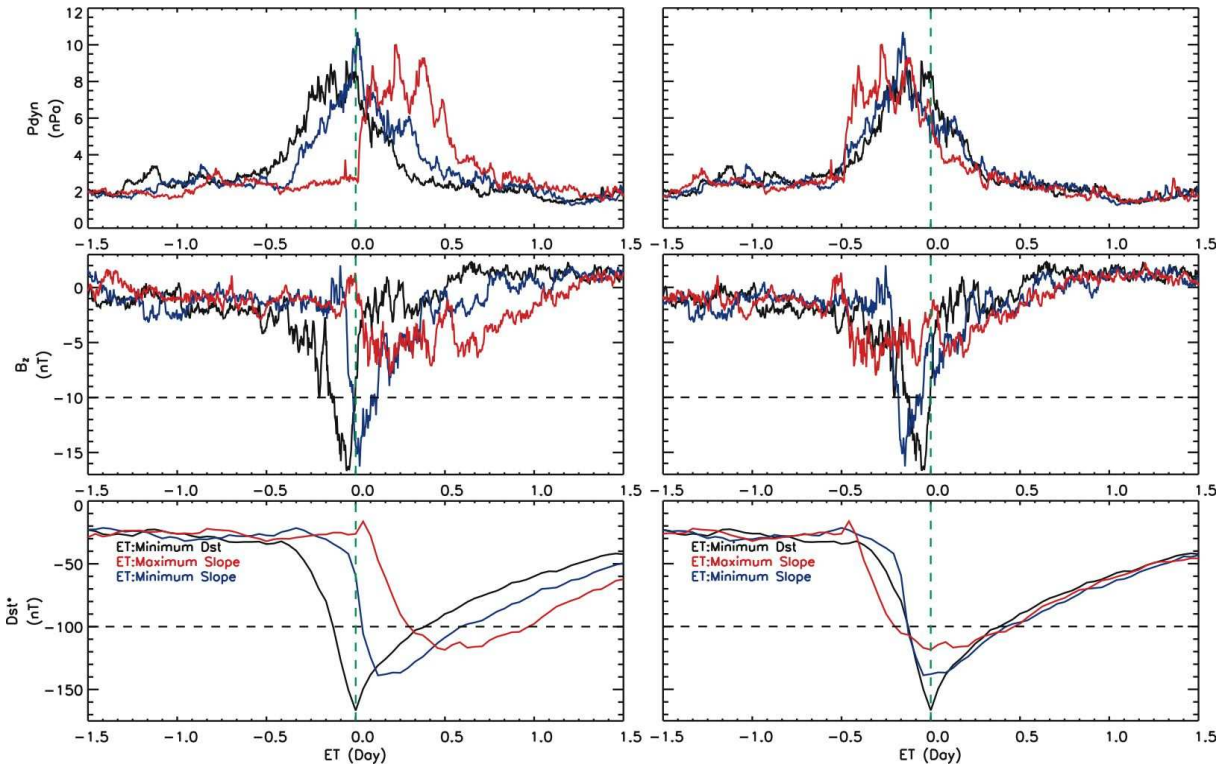

Figure 2.3: Superposed epoch means for 29 Intense storms at solar maximum. From top to bottom are plotted the superposed averaged values for the dynamic pressure (P_{dyn}), the z component of the interplanetary magnetic field (B_z) and the pressure corrected D_{st} index ($D_{st}{}^*$) for three different choices of the time stamp: red line-maximum D_{st} slope, blue line-minimum D_{st} slope, black line-minimum value of D_{st} index. The figures on the left are plotted relative to the epoch time while the ones on the right show the same mean values shifted relative to the location of means when averaged at the D_{st} minimum.

2.3.3 MPA Data

Figure 2.4 presents the superposed epoch analysis of geosynchronous plasma parameters for the 29 intense storms for just three choices of the epoch time (maximum D_{st} slope, minimum D_{st} slope and minimum D_{st}). For each choice of the epoch time, the hot-ion density (N_{HP}), temperature (T_{HP}) and entropy density ($S_{HP} = T_i/N^{2/3}$) (*Birn et al.*, 2006) values, as a function of universal time versus local time, are grouped into bins of 1 hour temporal resolution and averaged essentially in the same manner as described by *Zhang et al.* (2006b). The color scale is linear and showed only on the last column on the right (as in *Zhang et al.* (2006b)). Purple (black) bins correspond to values exceeding the maximum (minimum) value on the color scale. When the time stamp is set at the peak enhancement of the ring current (minimum slope of D_{st}, center column), the density peaks around storm maximum and the entropy density shows a minimum a few hours into the recovery phase on the day side. When the epoch time is chosen at the beginning of the storm (maximum slope of Dst, left column plots), the density at the storm peak is not as high as for the case when the time stamp is set at the peak of the storm (minimum D_{st}, right column plots). An interesting feature is that we see little to no variation in the temperature behavior for all three situations, with a temperature intensification in the afternoon sector in the early main phase of the storm and a minimum at the peak of the storms. We conclude that the late main phase of the storm has the highest concentration of particles, when the ring current is at its peak, while the early main phase is dominated by temperature enhancements.

If no losses to the plasma occurred, then adiabatic convection from the nightside to the dayside during a storm would produce a density increase and a temperature increase with the specific entropy density being constant. As can be seen in all three panels of the third row, before the storm and during the early phase of the storm the entropy density increases from midnight to noon. This is as expected for the flow of

the hot ions from the nightside to the dayside through the hydrogen geocorona, where charge-exchange loss creates an ion distribution that is hotter and less dense on the dayside. As can be seen in the first panel of the third row, during the storm main phase the entropy density increase from the nightside to the dayside is even larger, and the density decrease from the nightside to the dayside is even larger. This may be an indication of pitch-angle-scattering loss of ions to the atmosphere in addition to charge-exchange losses during the storm main phase. During the recovery phase (third panel of third row) the density, temperature, and entropy density trends from the nightside to the dayside are not consistent with adiabatic convection plus charge exchange. In particular, the entropy density is lower on the dayside than it is on the nightside. Future work using computer simulation is needed to determine what produces this entropy density gradient.

The entropy density increases from midnight to the dayside, and the low entropy density in the morning region is a feature seen in all three cases, but the transient, very low entropy density, morning features are captured only when the superposition is done close to the peak of the storm.

To quantitatively investigate these results, Figure 2.5 presents line plots of the average hot-ion density (N_{HP}), temperature (T_{HP}) and entropy density (S_{HP}) for each of the epoch times used in this study. These values were extracted from Figure 2.4 at seven local times. Again, the mean values for all parameters are shifted relative to the location of means when averaged at the D_{st} minimum. In order to reduce the statistical error in our bins, we have smoothed the data for all the MPA line plots by performing running averages with a window of five hours. We see that at different local times, the densities peak at different times during the storm, i.e., at different epoch times, and therefore we observe a motion of the particle peak density from the afternoon sector towards the morningside as the storm progresses. This progression might seem counter-intuitive given the fact that ions drift in the opposite direction.

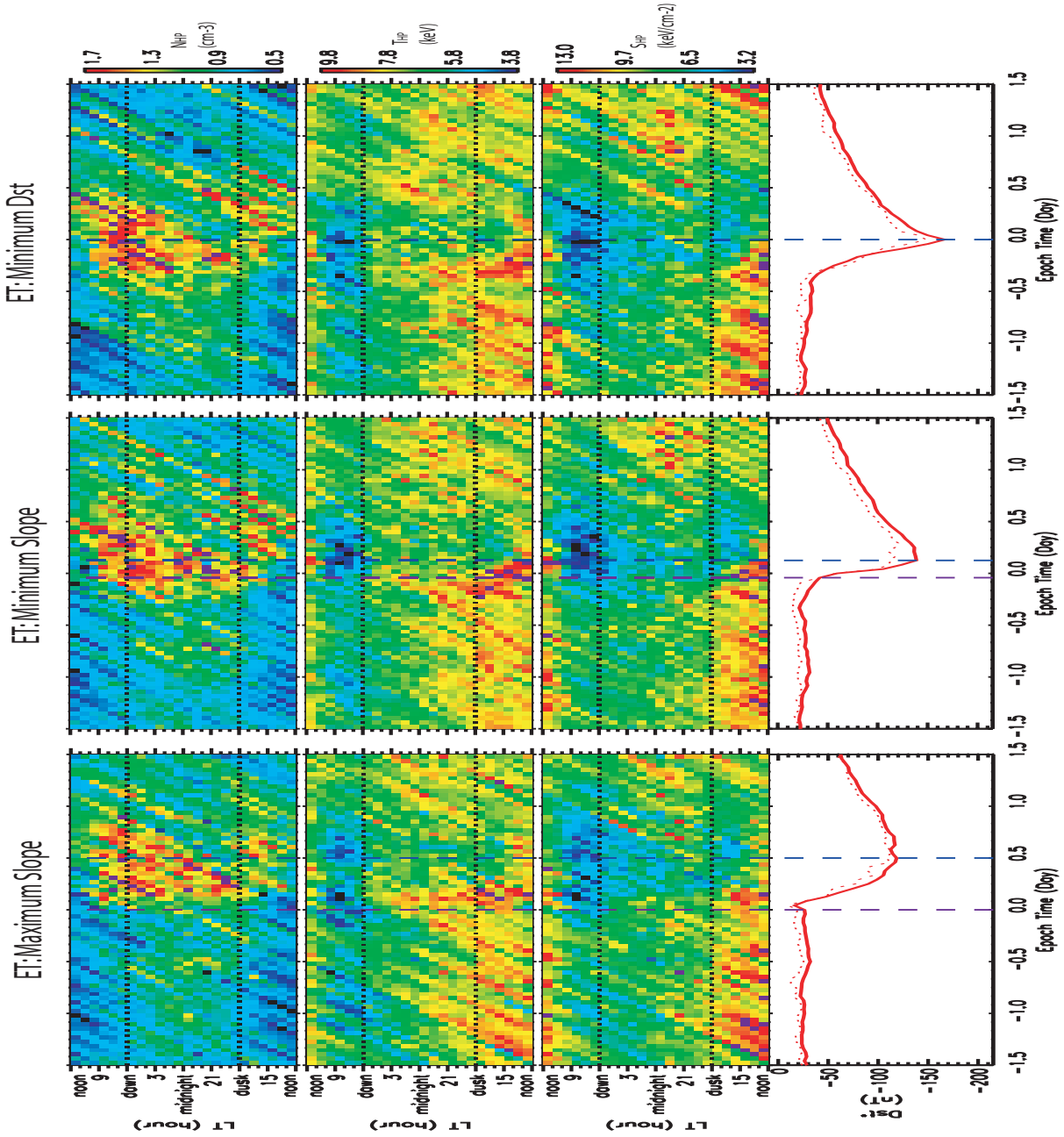

Figure 2.4: Superposed epoch data from the MPA instruments for three distinct epoch times. From left to right, by columns: minimum slope of D_{st} , maximum slope of D_{st} and the minimum D_{st} . The rows show the hot proton density (cm^{-3}), the hot proton temperature (keV), the entropy density ($\frac{keV}{cm^{-2}}$) and the D_{st} (dotted line) and $D_{st}{}^{*}$ (continuous line) indices (nT). The purple dashed vertical line in all plots shows the location of the 0 time while the blue dashed vertical line represents the location of the minimum superposed D_{st} time mark.

Liemohn and Brandt (2005) provide a possible scenario to explain this motion (Figure 2.6): When the hot plasma is moved into the inner magnetosphere, the ion drift around the pressure peaks alters the local flow of material. Subsequent injections generate new vortices and the flow is diverted eastward. This motion accounts for the spatially varying inflow of fresh particles from the plasma sheet.

The averaged temperature, seen in the middle column of Figure 2.5, shows strong temporal variations only in the afternoon sector, with the noon hot-ion temperature having the maximum value at the peak development of the storm while the 15 LT and 18 LT temperatures peak just before the storm maximum. This dayside peak in temperature, seen only with an epoch time early in the main phase of the storm, is an observation of the loss of the pre-storm hot ions out of the inner magnetosphere as they are convected out past geosynchronous orbit. In all the other local times, the temperature is relatively constant. The peak otherwise is lost when the averaging is done using a time stamp later in the storm development. Therefore the flow of the preexisting ring current is seen best with early epoch time choices.

The superposed entropy density, seen in the right column of Figure 2.5, shows minimum values at the epoch time in the afternoon and night sector. The noon and 15 LT entropy density shows some variation with the noon entropy density peaking at the zero-epoch time. This is to be expected since the entropy density is a derived parameter, therefore its behavior is determined by that of density and temperature.

Figure 2.7 shows a presentation similar to that of Figure 2.5, except that each row corresponds to a different zero epoch, and the colored curves correspond to different local times. The 6 LT density peaks at the peak of the storm with a maximum value of 1.65 cm^{-3}, the 3 LT density peaks at $Epoch_1$ with a maximum value of 1.49 cm^{-3}, midnight density peaks somewhere around the minimum D_{st} slope with a maximum value of 1.4 cm^{-3}, the 21 LT peaks at $Epoch_4$ with a maximum value of 1.64 cm^{-3}, the dusk density peaks close to the start of the storm with a maximum value of 1.2 cm^{-3},

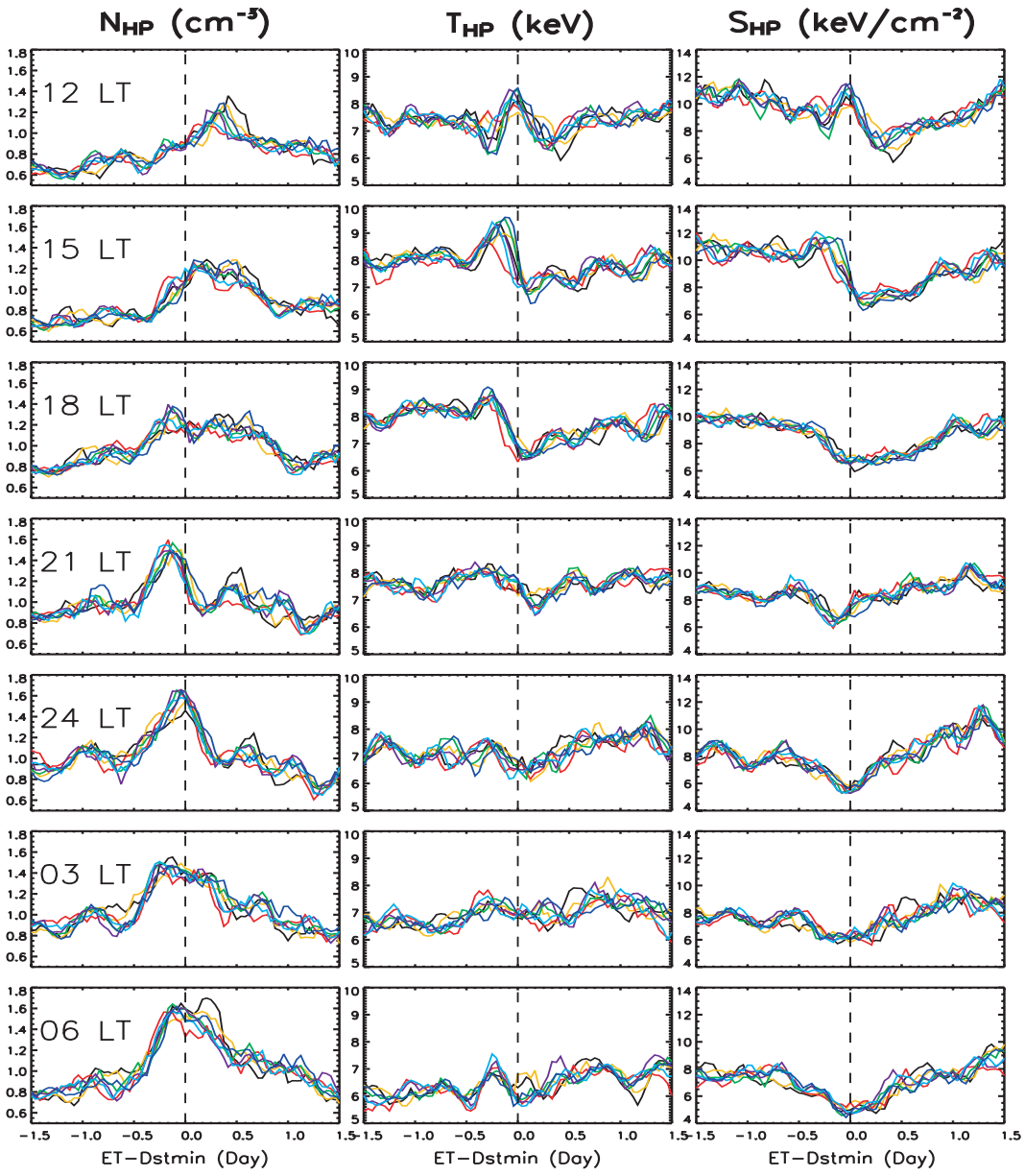

Figure 2.5: Superposed epoch data from the MPA instruments showing Epoch Time profiles extracted from the results in Figure 2.4. From left to right, by columns are presented the hot proton density (cm^{-3}),the hot proton temperature (keV) and the entropy density ($\frac{keV}{cm^{-2}}$) for different choices of epoch time. Each row corresponds to a certain local time while the color lines represent the distinct time marks: Maximum Slope of D_{st} (blue), $Epoch_2$ (light blue), Minimum Slope of D_{st} (red), $Epoch_1$ (yellow), $Epoch_4$ (green), $Epoch_3$ (purple), Minimum D_{st} index (black).

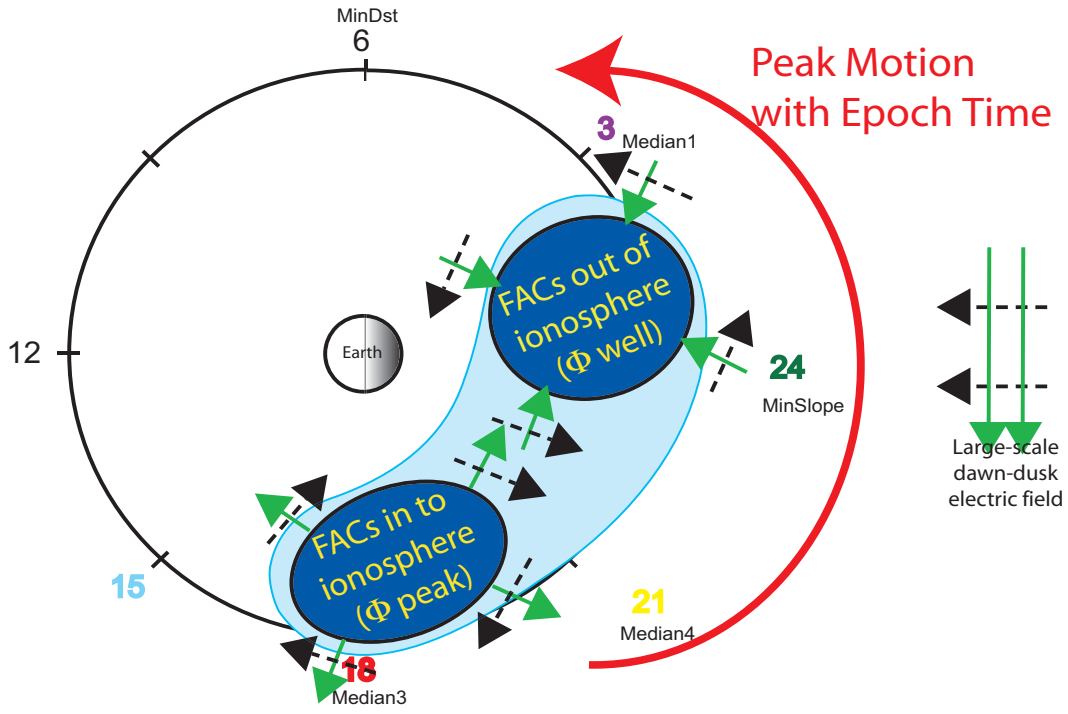

Figure 2.6: Illustration of the motion of density peak during the development of the storm. The view is in the equatorial plane of the Earth, looking down from over the North Pole. The green arrows show the dawn to dusk convection electric fields, and the dashed arrows show the ExB drift. The regions of the Field Aligned Currents (FAC) are denoted by the black sectors. The 'phi peak' and 'phi well' in the figure refer to the potential peak and well that form when plasma from the magnetotail moves towards the inner magnetosphere. The labels Epoch 1-4, MinSlope, and MinDst at various LTs show the location of the peak when the averaging is done using these epoch times.

while the dayside local time densities peak sometime during the recovery phase of the storm. The 12 LT and 15 LT densities are the lowest, independent of the epoch time choice, while the density at dawn shows the highest values. Also, independent of the time stamp, the 6 LT temperature has the lowest values, while the 18 LT and 15 LT hot proton temperatures have the highest values in all seven cases. These findings are in good agreement with *Denton et al.* (2005), who showed that the hot proton density is mostly enhanced on the dawn and dusk side, while the temperature on the dawnside is lower than the temperature on the duskside.

We notice a westward enhancement of the densities, starting with high values at dawn and decreasing peak densities westward through the nightside. This corresponds to an enhancement of the proton density in the morning sector. The nightside temperature (midnight, 21 LT, 3 LT, 6 LT) shows little to no variation while the dayside hot-ion temperature has maximum values during the main phase of the storm, followed by a drop of about 20% of its value at the peak of the storm. Similarly to the temperature, the entropy density has minimum and maximum values on the dayside and almost no variation on the nightside. The average drop in the entropy density is of approximately 17%. This is in agreement with the findings for density and temperature.

In order to quantify the effects of choosing different reference times when doing superposed epoch analysis, it is useful to perform a statistical test on some of the moments values from the different epoch time results. Figure 2.5 is particularly useful for this, in which the averaged moments from the different reference time choices are directly compared. It can be seen that there are certain times and places within the plots of Figure 2.5 when there is a large amount of spread between the moments values. It is these places that will be systematically considered to identify when the reference time choice is important.

Specifically we conducted significance tests for some of the maximum and mini-

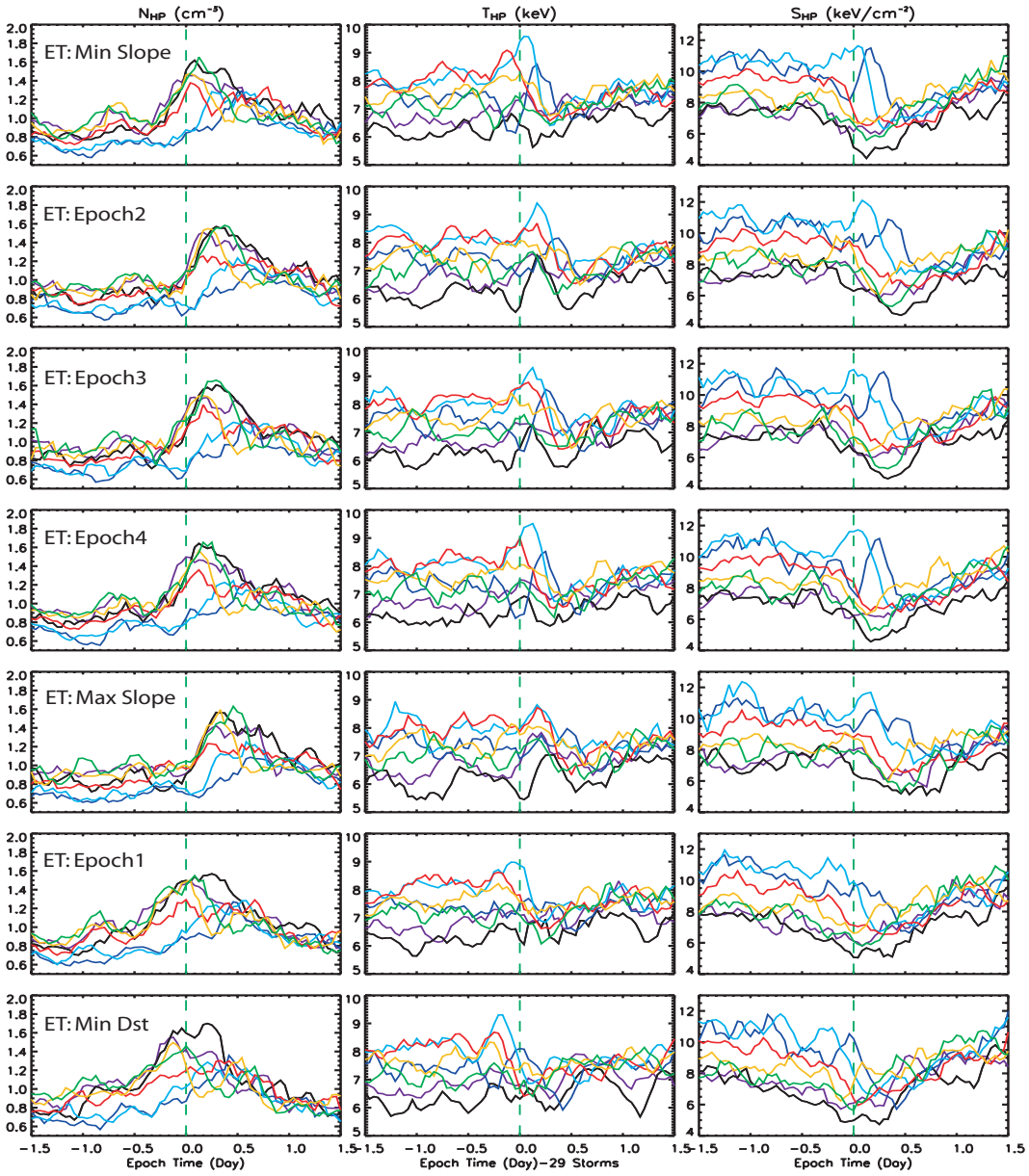

Figure 2.7: Superposed epoch data from the MPA instruments showing Local Time profiles extracted from the results in Figure 2.4. From left to right, by columns are presented the hot proton density (cm^{-3}),the hot proton temperature (keV) and the entropy density ($\frac{keV}{cm^{-2}}$) for different choices of epoch time. Each row corresponds to a certain epoch time while the color lines represent the distinct local times: noon (blue), 15 LT (light blue), 18 LT (red), 21 LT (yellow), midnight (green), 3 LT (purple), 6 LT (black).

mum values within Figure 2.5. For the hot-ion density column, the maximum value within the plot was compared against the minimum value at the same epoch time. That is, a vertical line was drawn straight down from the peak value within any one density panel, and the peak value was compared against the minimum value along that vertical line, from whichever other reference time result is the lowest there. So, for example, for the hot-ion densities at 12 LT (Figure 2.5, left column), the peak value is from the curve for the minimum D_{st} reference time (black curve, 1.35 cm^{-3} at ET=0.4 days), which was compared with the corresponding value from the minimum slope reference time at ET=0.4 days (red curve, 0.95 cm^{-3}). For the hot-ion temperature results in Figure 2.5, again the peak temperature value was found and compared with the minimum temperature at the same epoch time, from whichever reference time result is lowest at that place in the plot. For the entropy density results, the procedure is reversed: the minimum value of each plot was compared with the maximum value at the same epoch time.

Using these values, the Student T-test statistics and significance were calculated for the hot-ion density, temperature and entropy density means using all seven choices of epoch times. T-test statistics T of two populations $x = (x_0, x_1, ..., x_{N-1})$ with mean $\bar{x}$ and $y = (y_0, y_1, ..., y_{M-1})$ with mean $\bar{y}$ is computed in the following way:

$$T = \frac{\bar{x} - \bar{y}}{\sqrt{\frac{\sum_{i=0}^{N-1}(x_i - \bar{x})^2 + \sum_{i=0}^{M-1}(y_i - \bar{y})^2}{N+M-2}} \cdot (\frac{1}{N} + \frac{1}{M})} \tag{2.5}$$

i.e., the ratio of the means difference to the standard error of differences. The series elements are all of the real data that contributed to the average values for the two specific points from Figure 2.5 that are being compared. For example, for the hot-ion densities at 12 LT (Figure 2.5, left column), the two points being compared (from the red and blue curves at ET=0.4days) contain 342 and 303 observations (which are summation ranges N and M in equation 5).

The significance of the T-test represents the probability that the two samples of populations have significantly different means. The significance is a value in the interval [0.0, 1.0], and a small value of less than 0.05 is indicative of the fact that x and y have significantly different means, while a value of 1.0 corresponds to 100% correlation between the samples.

T-test statistics were calculated between the points that make up the maximum value of each averaged quantity and the points that account for the minimum value at the same universal time. The results are shown in Table 2.2. These statistics were calculated using the averaged quantities shown in Figure 2.5. Each of the numbers represents the significance value for different populations. We note that when superposing at maximum D_{st} slope, the peak in noon density is not as sharp as when we superpose the data at minimum D_{st} slope. When the epoch time is chosen close to the start of the storm ($Epoch_2$), we note a peak in the noon temperature, a peak that is lost when the epoch time is set at close to the maximum intensification of the storm, meaning that the numbers that go into the the peak value of temperature are significantly different than the ones that go into the averaging at the minimum D_{st} at the same epoch time. For the 21 LT density and entropy density, 6 LT entropy density and 3 LT temperature, the maximum and the minimum values are not significantly different, meaning that most likely, they come from the same populations. For all the other local times, all parameters have significantly different means. Therefore, the choice of the epoch time matters primarily in accurately depicting the size of the peak in all of the averaged quantities. Qualitatively, the presence and shape of the peaks is unaltered by the time stamp used in the analysis.

2.4 Discussion and Conclusions

We have reported on the importance of epoch time selection when doing statistical studies using the superposed epoch analysis. We have performed the averaging of

LT	N_{MAX}	T_{MAX}	S_{MIN}
1200	$\mathbf{8.9}\times10^{-10}$	$\mathbf{4.8}\times10^{-34}$	$\mathbf{3.8}\times10^{-4}$
1500	$\mathbf{5.0}\times10^{-2}$	$\mathbf{1.7}\times10^{-11}$	$\mathbf{2.6}\times10^{-44}$
1800	$\mathbf{1.9}\times10^{-3}$	$\mathbf{9.2}\times10^{-18}$	0.3
2100	0.1	$\mathbf{4.2}\times10^{-2}$	0.3
2400	$\mathbf{1.4}\times10^{-4}$	$\mathbf{3.5}\times10^{-22}$	$\mathbf{1.4}\times10^{-27}$
0300	$\mathbf{7.2}\times10^{-6}$	0.5	$\mathbf{1.9}\times10^{-9}$
0600	$\mathbf{3.8}\times10^{-15}$	$\mathbf{2.6}\times10^{-5}$	0.7

Table 2.2: Significance values for hot-ion density, temperature and entropy density correlations between data points contained by the maximum and minimum values at the corresponding epoch time. Boldface numbers indicate values below the 5% correlation limit.

29 solar maximum intense storms using both solar wind data from ACE and geosynchronous observations by the MPA instruments from the LANL satellites. The results presented above show clearly that certain parameters require a certain epoch time in order to reproduce an accurate behavior, and others are less sensitive to the epoch time choice when doing superposed epoch analysis, since they exhibit less spatial and temporal variation. The *Gonzalez et al.* (1994) convention commonly used to illustrate intense storm behavior is met by superposed storm profiles, only if the superposition of the data is done at the $Epoch_4$ or later, i.e., no earlier than about 6 hours before the storm peak for an average length storm. In addition, when the zero epoch time is set near the minimum D_{st} index, the storm sudden commencement features are lost.

The average duration of the main phase is found to be 13.2 hours. This result is somewhat in agreement with *Pulkkinen et al.* (2007), who found that the average duration of sheath storms is of about 8 hours while the main phase in the case of cloud storms lasts for about 14 hours. Note that in our study we do not differentiate between the storm drivers and we only study storms that occurred during the solar maximum. However, CME-driven storms occur with predilection during solar maximum (*Richardson et al.*, 2001), so our data set is probably dominated by such storms, thus our claim that our result for the main phase duration is in agreement

with the findings of *Pulkkinen et al.* (2007) is justified. Moreover, the ring current takes about 7.2 hours on average to reach maximum enhancement while the Late Main Phase lasts for approximately 6 hours, in agreement with her CME main phase duration findings of 14 hours.

We have investigated the characteristics and the temporal evolution of geosynchronous plasma parameters as a function of local and epoch time. Our results show an eastward motion of the particle peak density with different local time densities peaking at different moments during the development of the storm. These findings lead us to conclude that this motion describes the inflow of fresh plasma sheet particles into the inner magnetosphere. Conversely, flow-out of the preexisting ring current is seen best with early epoch times. Thus the noon temperature is one of the bulk ion parameters that requires a time stamp closer to the start of the storm in order to be resolved in the averaging.

Furthermore, our findings indicate that a distinct epoch time is needed to accurately resolve certain solar wind features; when looking at the hot protons at geosynchronous orbit, the choice of the epoch time primarily matters in accurately depicting the size of the peak in all averaged quantities while the presence and shape of the peaks is unaltered by the time stamp used in the analysis.

CHAPTER III

Overview of Space Weather Modeling Framework

3.1 The Space Weather Modeling Framework

The Space Weather Modeling Framework (SWMF) is a robust, high-performance numerical tool that can be used or customized to link together Sun to Earth modeling components, capable of simulating physics from the solar surface to the upper atmosphere of the Earth (*Tóth et al.*, 2005, 2007). The SWMF integrates numerical models for numerous physics domains, self-consistently solving the physics within each region of interest and the coupling between them. This includes models of the Solar Corona (SC), Eruptive Event Generator (EE), Inner Heliosphere (IH), Solar Energetic Particles (SP), Outer Heliosphere (OH), Global Magnetosphere (GM), Inner Magnetosphere (IM), Plasmasphere (PS), Radiation Belt (RB), Polar Wind (PW), Ionosphere Electrodynamics (IE), Upper Atmosphere (UA) and Lower Atmosphere (LA) coupled into a complex model. Each domain can be represented with alternative physics models, and the coupling of these modules makes the SWMF a unique and powerful tool in simulations that were not possible with individual physics models. An illustration of the SWMF modules and their coupling is presented in Figure 3.1.

Many of the codes currently part of SWMF are based on first-principle physics, but simpler models, such as empirical codes, are implemented as well. The system is capable of simulating the space environment from the solar atmosphere to the

Earth's atmosphere, involving numerous components of the framework at the same time. Nevertheless, as few as one module can be used at a time, i.e. running a model in stand alone mode. In the following chapters, all simulations are driven by solar wind observations from the ACE satellite orbiting at the Lagrange 1 point on the Sun-Earth line. Three modules will be used: Global Magnetosphere (GM), Ionosphere Electrodynamics (IE) and the Inner Magnetosphere (IM). The models used and the coupling invoked are described in the following sections.

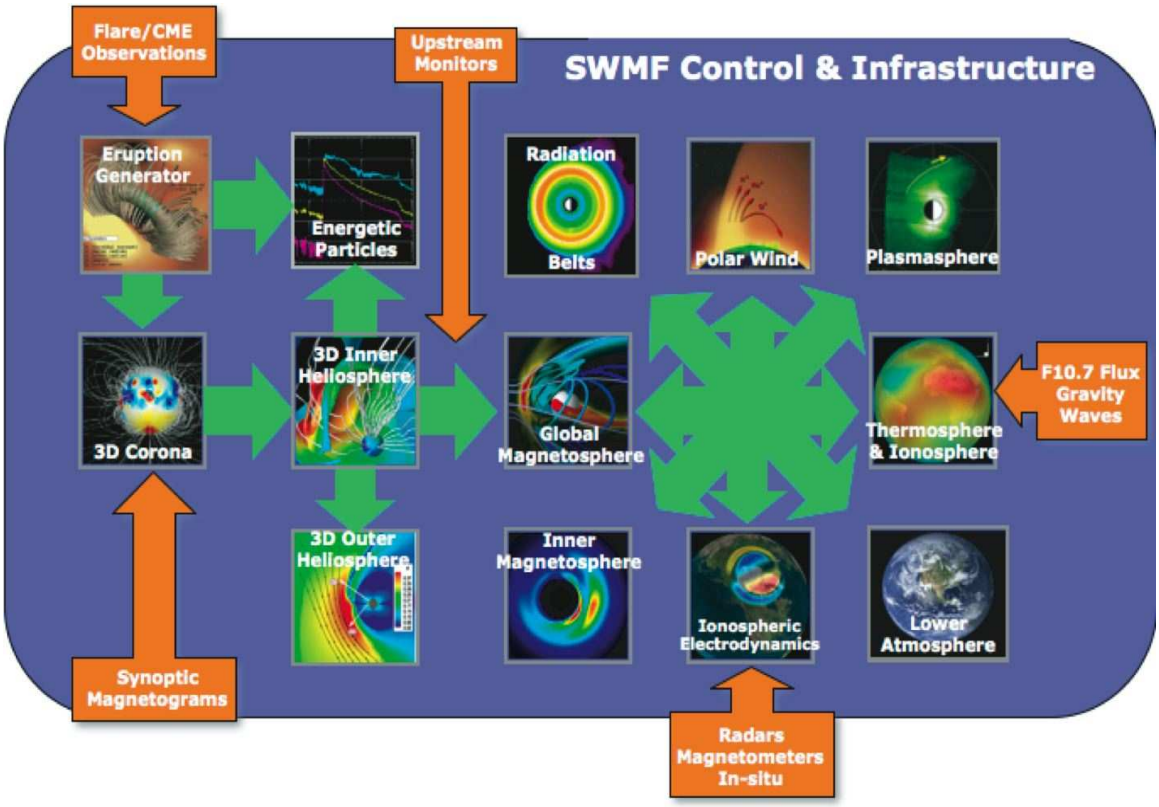

Figure 3.1: Diagram showing various SWMF components. Arrows indicate couplings between modules.

SWMF has been extensively used for scientific studies of the geospace by many authors, e.g. *Toth et al.* [2007], *Zhang et al.* [2007], *Yu and Ridley* [2009]. Below we will briefly describe the domains relevant to this study.

3.1.1 Global Magnetosphere

This domain describes the magnetic field and plasma properties in the outer magnetosphere and encompasses the bow shock, the magnetopause and the magnetotail of the planet. The physics of the global magnetosphere domain is dominated by the magnetospheric convection and the large scale transport of mass and energy from the solar wind to the magnetosphere. There is one model for the global magnetosphere in the SWMF, the Block Adaptive Tree Solar-wind-type Roe Upwind Scheme (BATS-R-US) global magneto-hydrodynamic (MHD) model (*Powell et al.*, 1999; *Tóth et al.*, 2006). This model solves the magnetohydrodynamic equations, everywhere outside an inner boundary near Earth, taken here at 2.5 Re. In the ideal MHD formalism, there are several important assumptions being made: the electron - proton plasma is treated as a single fluid, the pressure is isotropic (the thermal plasma is treated as a scalar), the heat flow is neglected, conductivity is infinite (plasma is perfectly conducting, therefore null magnetic resistivity), and charge neutrality is assumed. For reference, the MHD equations in the conservative form are written as:

$$\frac{\partial \rho}{\partial t} + \nabla \cdot (\rho \mathbf{u}) = 0 \tag{3.1}$$

$$\frac{\partial (\rho \mathbf{u})}{\partial t} + \nabla \cdot \left[\rho \mathbf{u}\mathbf{u} + \left(p + \frac{B^2}{2\mu_0} \right) I - \frac{\mathbf{B}\mathbf{B}}{\mu_0} \right] = \rho \mathbf{g} \tag{3.2}$$

$$\frac{\partial \mathbf{B}}{\partial t} + \nabla \cdot (\mathbf{u}\mathbf{B} - \mathbf{B}\mathbf{u}) = 0 \tag{3.3}$$

$$\frac{\partial \epsilon}{\partial t} + \nabla \cdot \left[\mathbf{u} \left(\epsilon + p + \frac{B^2}{2\mu_0} \right) - \frac{(\mathbf{u} \cdot \mathbf{B})\, \mathbf{B}}{\mu_0} \right] = \rho \mathbf{g} \cdot \mathbf{u} \tag{3.4}$$

In the above equations, the conserved quantities are the plasma mass density ρ, momentum density $\rho\mathbf{u}$, total energy density ϵ and the magnetic field $\mathbf{B}$, while $\mathbf{u}$ is

the plasma velocity, p is the pressure, $\mathbf{g}$ is the gravitational acceleration due to the central body. The total energy density is expressed as the following:

$$\epsilon = \frac{\rho u^2}{2} + \frac{p}{\gamma - 1} + \frac{B^2}{2\mu_0} \tag{3.5}$$

One of the most interesting features of BATS-R-US is that it uses an adaptive Cartesian, block-based grid (see *Powell et al.*, 1999), allowing the user/the code itself to specify/determine the desired spatial resolution. The domain is divided into block tree structures, with each block containing $n \times n \times n$ cells ($n = 8$ for the purpose of the studies within this thesis) and therefore enabling effective parallelization of the model by distributing different blocks to separate processors. Moreover, this architecture allows for easy refinement of blocks, by splitting them into 8 new blocks (division of each block in two for each dimension). Although the resulting block contains the same number of grid points, the resolution is halved (more refined). An example of the block structure used in BATS-R-US is presented in Figure 3.2.

Since the Alfvén velocity ($v_A = \frac{B}{\sqrt{\mu_0 \rho}}$) is not only unbound to the speed of light but it can actually exceed it in locations where the magnetic field is strong enough (near the Earth's magnetic poles for example), this speed can be the one that determines the time step (time step is determined by the fastest wave speed). In this situation, one can use the Boris correction (*Boris*, 1970; *Gombosi et al.*, 2003), which limits the Alfvén speed to the speed of light, and artificially decrease of the light speed by including the displacement current into the Ampere's law and re-deriving the semi-relativistic MHD equations. This correction allows for an increase in the time step.

For simulations of the Earth's magnetosphere, the coordinate system of choice is Geocentric Solar Magnetospheric (GSM), with the X axis pointing radially from the center of the Earth towards the Sun. The Z axis points towards the northern hemisphere such that the terrestrial dipole axis is contained by the X-Z plane, and the Y axis points dusk-ward, completing the right-handed system. The Earth's magnetic

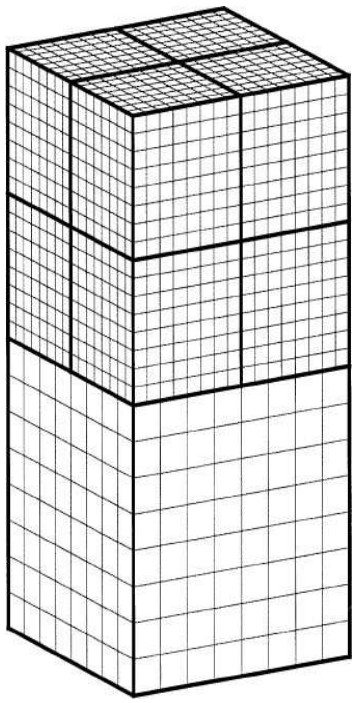

Figure 3.2: An illustration of the block structure. The thick black lines show the boundary between blocks while the thinner lines represent the boundary between grid cells. Figure from *Powell et al.* (1999).

dipole axis is titled away from the rotation axis by 11° and can move as a function of time, so it rotates around the rotation axis each day. The algorithms and numerical schemes are described in detail by *Powell et al.* (1999) and *De Zeeuw et al.* (2000).

The GM module (BATS-R-US) couples to all other modules used in the subsequent studies. In the regions close to the body, where the grid overlaps with that of the Inner Magnetosphere component, the MHD results are nudged toward the IM results (*De Zeeuw et al.*, 2004), while the flux tube volume and ionospheric footprints are passed through couplers to the inner magnetosphere (IM) component. Also, the field-aligned current strength and position are passed to the ionospheric electrodynamics (IE) component, which in turn returns the electric potential at the GM boundary. This value is converted to velocity at the inner boundary. Throughout this thesis, we used as an upstream boundary condition the measurements from the ACE spacecraft. The inner boundary density is set to a fixed value of 28 cm^{-3}, while the temperature

and the magnetic field are continuous through the inner boundary.

3.1.2 Inner Magnetosphere

The physics of the Earth's inner magnetosphere is highly complicated since this region contains overlapping particle distributions over a large range of energies. The motions (gradient and curvature drifts) of these different particle populations are energy dependent, therefore a standard single fluid treatment of this plasma cannot provide an adequate description of the inner magnetosphere. To accurately simulate this closed-field-line region, a kinetic model solving the energy-dependent particle flows of hot ions and electrons is needed. The Rice Convection Model (RCM) (*Harel et al.*, 1981; *De Zeeuw et al.*, 2004) is one of the IM models and it was used for these studies, unless specified otherwise.

The RCM represents the plasma population in terms of multiple isotropic fluids and calculates the dynamic behavior of the inner-magnetospheric particles in a region of the magnetic equatorial plane that extends from just inside the dayside magnetopause to the nightside inner plasma sheet ($\sim$ 10 Re) and $\sim$ 7 Re on the dawn/dusk direction. The inner boundary is 9.86° invariant magnetic latitude. Nevertheless, when coupled with BATS-R-US, the outer boundary is dynamic, following the boundary of the last closed field lines.

In this region, the plasma undergoes slow flow with $v << v_{thermal}$ and $v << v_{Alfven}$ (*Wolf*, 1983), drifting as an action of the co-rotation and electromagnetic fields.

Each fluid is regarded as a volume of phase space, characterized by adiabatic energy invariant λ_k, flux tube content η_k, and charge q_k, whose flux tube averaged characteristics are advected through the magnetosphere. The subscript k describes a given charge, mass and energy invariant λ_k species.

$$|\lambda_k| = W\left(\lambda_k, \mathbf{x}, t\right) V^{2/3} \tag{3.6}$$

where W is the particle kinetic energy, λ_k is conserved along a drift path, and V is the flux tube volume

$$V = \int_{Sh}^{Nh} \frac{ds}{B\left(\mathbf{x}, t\right)} \tag{3.7}$$

Nh and Sh refer to the field line endpoints in the northern and the southern hemispheres, respectively.

The flux tube content η_k is related to thermodynamic pressure P and the plasma distribution function $f_k(\lambda)$ by the following relations:

$$PV^{5/3} = \frac{2}{3} \sum_k \eta_k |\lambda_k| \tag{3.8}$$

$$\eta_k = \frac{4\pi\sqrt{2}}{m_k^{3/2}} \int_{\lambda_{min}}^{\lambda_{max}} \sqrt{\lambda} f_k(\lambda) d\lambda \tag{3.9}$$

Because RCM assumes isotropic particle distributions, the motion of the whole flux tube is used to describe the motion of the plasma. The bounced averaged particle motion in an electric and magnetic field, including the gradient and curvature drifts (*Wolf*, 1983) is obtained by averaging over an isotropic distribution and over a flux tube.

$$\mathbf{v_k}\left(\lambda_k, \mathbf{x}, t\right) = \frac{\left[\mathbf{E} - \frac{1}{q_k}\nabla W\left(\lambda_k, \mathbf{x}, t\right)\right] \times \mathbf{B}\left(\mathbf{x}, t\right)}{B^2\left(\mathbf{x}, t\right)} \tag{3.10}$$

The Rice Convection Model advects each fluid using the following relation:

$$\frac{\partial \eta_k}{\partial t} + \frac{\mathbf{B} \times \nabla\left(\Phi + \Phi_c + \frac{\lambda_k}{q_k} V^{-2/3}\right)}{B^2} \cdot \nabla \eta_k = -Losses \tag{3.11}$$

Φ represents the ionospheric electric potential, where the induction electric field can be neglected, and Φ_c represents the electric potential due to corotational electric

field. The right hand side of Equation 3.11 denotes explicit losses, typically charge exchange for ions and precipitation into a loss cone for electrons (*Wolf et al.*, 1991; *Toffoletto et al.*, 2003) while outflow through the dayside magnetopause is implicit in the RCM solution of the advection equations. However, for our studies, all ions are considered to be protons and charge exchange collisions are not considered explicitly within the RCM domain. More detailed RCM descriptions of the model equations and the numerical techniques can be found in the work of *Sazykin* (2000) and *Toffoletto et al.* (2003).

In the stand alone version, the flow of electric currents along magnetic field lines to and from the conducting ionosphere and the associated electric fields are calculated self-consistently, assuming that the field lines are perfect conductors (*Vasyliunas*, 1970). However, RCM can receive the ionospheric potential from the Ionosphere Electrodynamics (IE) component, creating a self-consistent inner magnetosphere when it is used in conjunction with GM and IE.

Transfer of information from GM to IM is expedited by efficient ray-tracing algorithms in BATS-R-US, as described by *De Zeeuw et al.* (2004). The ray tracing allows field-lines to be quickly traced from one hemisphere to another, yielding flux tube foot points and averaged densities and temperatures. The GM domain also provides the the open/closed field line boundary, and passes it to the IM module on each coupling to update the spatial boundary on a continuous basis. On the other hand, IM computes the density and pressure along those closed field lines and feeds this information to GM in order to correct these values.

3.1.3 Ionospheric Electrodynamics

The magnetosphere and ionosphere are closely coupled due to the flow of magnetospheric currents along the magnetic field lines into and out of the conductive ionosphere, via region 1 (at higher latitudes) and region 2 (equator-ward of region

1) field-aligned currents. The two-dimensional electric potential and auroral precipitation patterns are described within this domain. The SWMF uses an ionospheric model that is a combination of an electric potential solver and a model of the electron precipitation (*Ridley and Liemohn*, 2002; *Ridley et al.*, 2004), and is needed for proper GM and IM domain simulations.

Field-aligned currents are computed at 3.5 Re in the magnetosphere and then mapped down into the ionosphere, where the ionospheric electric potential is calculated. FACs provided by the Global Magnetosphere domain are needed to calculate particle precipitation and conductance patterns. The conductance and field-aligned currents are used to calculate the electric potential.

Since most of the mapping occurs between 2.5 Re (GM inner boundary) and 110 km (known as the 'gap' region), the magnetic field in this region is set to dipolar values and the current is scaled according to the $B_{ionosphere}/B_{3.5Re}$ ratio, where $B_{ionosphere}$ represents the strength of the magnetic field in the ionosphere while $B_{3.5Re}$ is the magnetic field at 3.5 Re in the magnetosphere.

The radial (field-aligned) current J_r at the ionosphere height is used to calculate the electric potential from:

$$J_r(R_e) = \left[\nabla_\perp \cdot (\Sigma \cdot \nabla\Phi)_\perp\right]_{R=R_e} \tag{3.12}$$

where Φ is the ionospheric electric potential, Σ is the height integrated conductance tensor. The closure currents are described by:

$$J_\perp(R_e) = \Sigma \cdot \nabla\Phi \tag{3.13}$$

The conductance tensor includes effects from several sources: solar illumination conductance, nightside starlight conductance, auroral precipitation conductance, and polar cap conductance.

Solar illumination is an important ionization source and thus conductance source on the dayside and is approximated by taking the F10.7 flux (the 10.7cm solar radio flux) as a model input along with the Hall (in the direction perpendicular to both the magnetic and electric fields) and Pedersen (in the direction perpendicular to the magnetic field and parallel to the electric field) conductivities as derived by *Moen and Brekke* (1993):

$$\Sigma_H = F_{10.7}\left(0.81cos(\xi) + 0.54\sqrt{cos(\xi)}\right) \tag{3.14}$$

$$\Sigma_P = F_{10.7}\left(0.34cos(\xi) + 0.93\sqrt{cos(\xi)}\right) \tag{3.15}$$

where ξ is the solar zenith angle, which is 0° at the sub-solar point and 90° at the terminator. The starlight and polar cap conductance effects are included as constants, while the auroral precipitation conductance is accounted for using an empirical relationship based on results from the Assimilative Mapping of Ionospheric Electrodynamics (AMIE) technique (*Ridley et al.*, 2004).

The electric potential is mapped back to the inner boundary of the GM domain. Then the electric field and velocities at the inner boundary are calculated using

$$\mathbf{E} = -\nabla\Phi \tag{3.16}$$

$$\mathbf{v} = \frac{\mathbf{E}\times\mathbf{B}}{B^2} \tag{3.17}$$

and the co-rotation velocity field is added to the ionospheric generated velocity field.

IE provides the electric potential to IM component as well through one way coupling.

3.1.4 Simulations Setup

For all simulations performed, we coupled together the Global Magnetosphere (BATS-R-US), Inner Magnetosphere (RCM) and Ionosphere Electrodynamics (RIM) models. An outline of the simulation setup is presented in Figure 3.3.

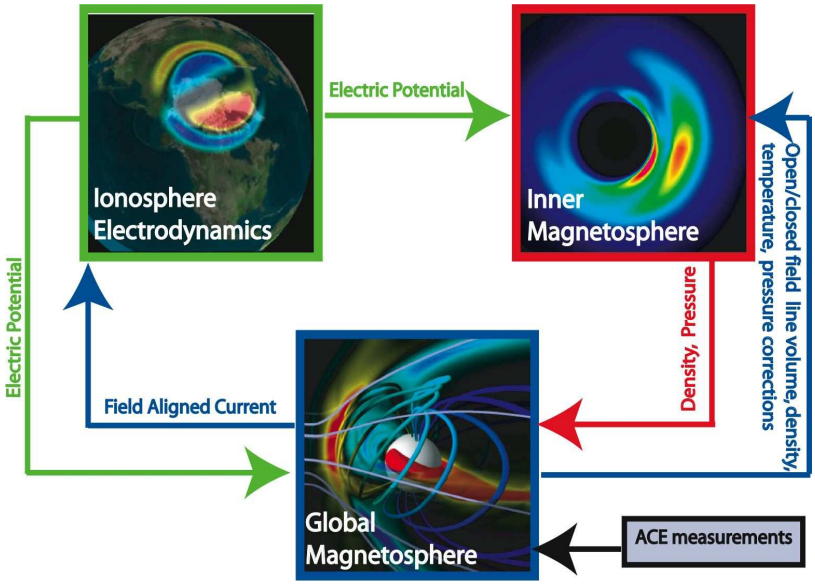

Figure 3.3: Coupling schematic of the GM-IM-IE coupling within SWMF.

The the inner boundary of GM is set at 2.5 Re from the center of the Earth where the flows generated by the ionospheric potential are set. The simulation domain is defined by X with the range [-224Re, 32Re], with Y and Z in the range [-128Re, 128Re]. The IM domain overlaps with the GM domain and changes according to the open/closed field line boundary information provided by BATS-R-US; the IM domain typically extends to 10 Re in X and Y coordinates in the equatorial plane, within the GM region.

We ran the BATS-R-US model with refined spatial resolution, the smallest grid cells being set to 1/8 Re in the shell region from 2.5 to 3.5 Re where the field aligned current calculation is performed. Close to the Earth (X: 16Re, -32Re, Y: -8Re, 8Re, Z: -8Re, 8Re) the resolution was set to 1/4 Re. In the vicinity of the tail and bow shock the resolution was set to 1/2 Re, while everywhere else was 2 Re. Figure 3.4 shows

the BARS-R-US grid resolution in the equatorial plane used for all of our SWMF simulations.

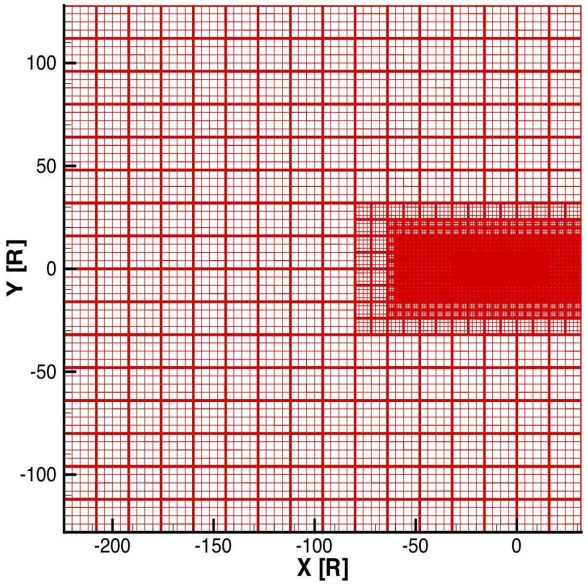

Figure 3.4: Illustration of the grid resolution setup in the equatorial plane. Sun is on the right.

The smallest cells are concentrated closer to the Earth and at the expected locations of the bow shock and the magnetotail. Note that in this simulation the cell spatial resolution is set low (2.0 Re) in the far magnetotail to avoid too much computing time. The Ridley Ionospheric Model (IE) uses a two dimensional spherical grid with 1 degree resolution in latitude and 2 degree resolution in longitude, while the RCM (IM) uses a non-uniform 78 by 48 2D spherical grid.

The simulations were carried out in three stages. In the first stage, the Global Magnetosphere component is initialized and runs for 1500 iterations in order to converge to a steady state solution. After this initial stage, the GM, IM, and IE components start from the GM solution and run for additional 700 iterations to obtain an initial state for all components. The model is driven by the ACE satellite measurements propagated to (32, 0, 0) Re, at the start time of the simulation. These data are applied as the upstream boundary conditions. After that, the time accurate session begins. A Rusanov numerical scheme is used with the less diffusive mc3 (monotonized

central) slope limiter. The Boris correction factor is set to 0.01 (that is, the speed of light is 100 times slower than reality, to allow for larger times steps).

For the purpose of this study, in the IM/RCM model, the protons are the only ions and charge exchange is not explicitly included. In the IE component, on the basis of the observed data, the 10.7 cm solar radio flux (F10.7) expressed in Janskys (Jy) is used as an input parameter for each simulation event. The nightside Pedersen conductance is 1.0 mhos, which dominates on the nightside. The average Pedersen conductance in the polar cap is set at 0.25 mhos.

The GM and IE components are coupled every 5 seconds, meaning that the electric potential from IE and the field aligned currents from GM are updated at this frequency. The IM-GM and IE-IM couplings occur every 10 seconds (2 time steps in RCM). The IM obtains the field topology and plasma information from the GM component, while getting the electric potential from the IE and provides the density and pressure corrections back to GM every 10 seconds. Typically, each BATS-R-US simulation domain contains about 2.5 million cells and the time step is 0.07 seconds (RCM has a 5 seconds time step). Coupling these three components enables passing information back and forth between the GM, IE and IM, allowing a self consistent treatment of the magnetosphere.

CHAPTER IV

Averaged Input Simulations

4.1 Motivation

In Chapter II we took a close look at the average profile of intense storms at Solar Maximum by using the technique of Superposed Epoch Analysis for different choices of epoch times. As a next step, using global magnetosphere modeling, we will investigate whether the averaged solar wind conditions (which smooth out large excursions in the solar wind drivers) will be able to reproduce the average characteristics of a magnetic storm as highlighted in Chapter II. Smoothing, averaging, and/or de-spiking the input data will allow us to determine the role of the transient spikes in the development of magnetic storms. In order to determine the effectiveness of fluctuations in solar wind parameters in triggering magnetic storm, numerical simulations with SWMF, using averaged solar wind upstream conditions, will be performed.

4.2 Methodology

The modules used in the SWMF simulations were the GM (BATS-R-US), IM (RCM), and IE (Ridley Ionospheric Model) and the simulation setup was described in Chapter III, Section 3.1.4. Due to high computational demands (on 64 processors it takes 5 hours to simulate 1 hour of the storm), we restricted our study to only five

storms as opposed to 29 in the previous study. The events were selected according to the pressure-corrected D_{st}, D^*_{st}, being less than $-100\ nT$, similarly to the procedure described in Chapter II. To more accurately carry out this study, each of the five actual intense storms selected occurred at solar maximum and around the equinox, therefore the Earth's tilt axis is relatively the same for all events. Moreover, all of the selected events were CME driven and displayed a sharp gradient in the solar wind plasma pressure. The magnetic storms considered for our study are: September 22, 1999; April 18, 2001; August 17, 2001; October 21, 2001 and October 28, 2001.

To investigate the effectiveness of the fluctuations in the solar wind parameters, averaged solar wind upstream conditions are to be taken as upstream conditions to the SWMF. The averaged input is obtained by doing Superposed Epoch Analyses (SEA) of all five intense, CME driven storms with three distinct locations for the zero epoch time: Dst minimum (the peak of the storm development), the jump in pressure in solar wind parameters (corresponding to Storm Sudden Commencement) and the maximum slope in Dst index (the sharpest decrease in Dst - the peak of Ring Current enhancement).

Each of the 5 actual intense storms will be individually simulated with the SWMF and for one of the five storms selected, we plan to run simulations using the solar wind averaged data as the upstream conditions input. In addition, the superposed epoch technique will be applied to all of the simulation results in order to compare the average profile of the five simulated events with the profile of a storm driven by the averaged solar wind conditions. This study will allow us to examine the nature of the relationship between the solar wind parameters and the formation and decay of the ring current.

Figure 4.1, Figure 4.2, Figure 4.3, Figure 4.4 and Figure 4.5 show the solar wind plasma and interplanetary magnetic field (IMF) parameters, obtained from ACE satellite, for each event. The data is propagated from the satellite location to (32, 0,

0) Re in the GSM coordinate system using the Minimum Variance Analysis method of *Weimer et al.* (2003) and *Weimer* (2004).

During the September 22, 1999 event (Figure 4.1), we note a substantial jump in the particle number density from 19 cm^{-3} to 76 cm^{-3}, happening around noon (12:52 UT) on September 22. At this time the IMF B_z is northward, only to turn southward approximately 7 hours later and stays negative for another 4.5 hours. During the main phase of the storm, the IMF B_z fluctuates between 29 nT and -23 nT while the minimum D_{st} and SYM-H indices reached -173 nT and -166 nT, respectively.

Figure 4.2 shows the ACE observations for April 18, 2001 magnetic storm. Again, we see a steep jump in particle number density, from 23 cm^{-3} to 39 cm^{-3}, in the morning of April 18th, 2001. For this event, the Z component of the IMF turns southward at the same time with the density jump and remains southward for at least 3 hours, displaying large fluctuations between 16 nT and -25 nT throughout the main phase. This produced a disturbance in the geomagnetic field with an observed D_{st} minimum of -114 nT and a SYM-H index of -122 nT.

During the August 17, 2001 storm (Figure 4.3), the particles number density starts increasing at about 14:00 UT from 5 cm^{-3} to 28 cm^{-3}, while IMF B_z is predominantly southward for a period of $\sim$ 10 hours. We note that B_z has large oscillations between 28 nT and -27 nT and the resulting magnetic storm recorded a D_{st} and a SYM-H minimum of ~ -105 nT and -131 nT, respectively.

For the October 21, 2001 storm (Figure 4.4), the solar wind density and IMF B_z displayed similar features as those in the August event. The proton number density is suddenly increasing to double it's pre-storm value (from 18 cm^{-3} to 37 cm^{-3} around 15:00 UT) and IMF B_z is turns southward as soon as the shock reaches the Earth's magnetosphere, fluctuating between 25 nT and -27 nT. This produced a D_{st} minimum of -187 nT and SYM-H index reached -219 nT.

A week later, another CME hits the Earth at 02:00 UT on October 28th (Figure

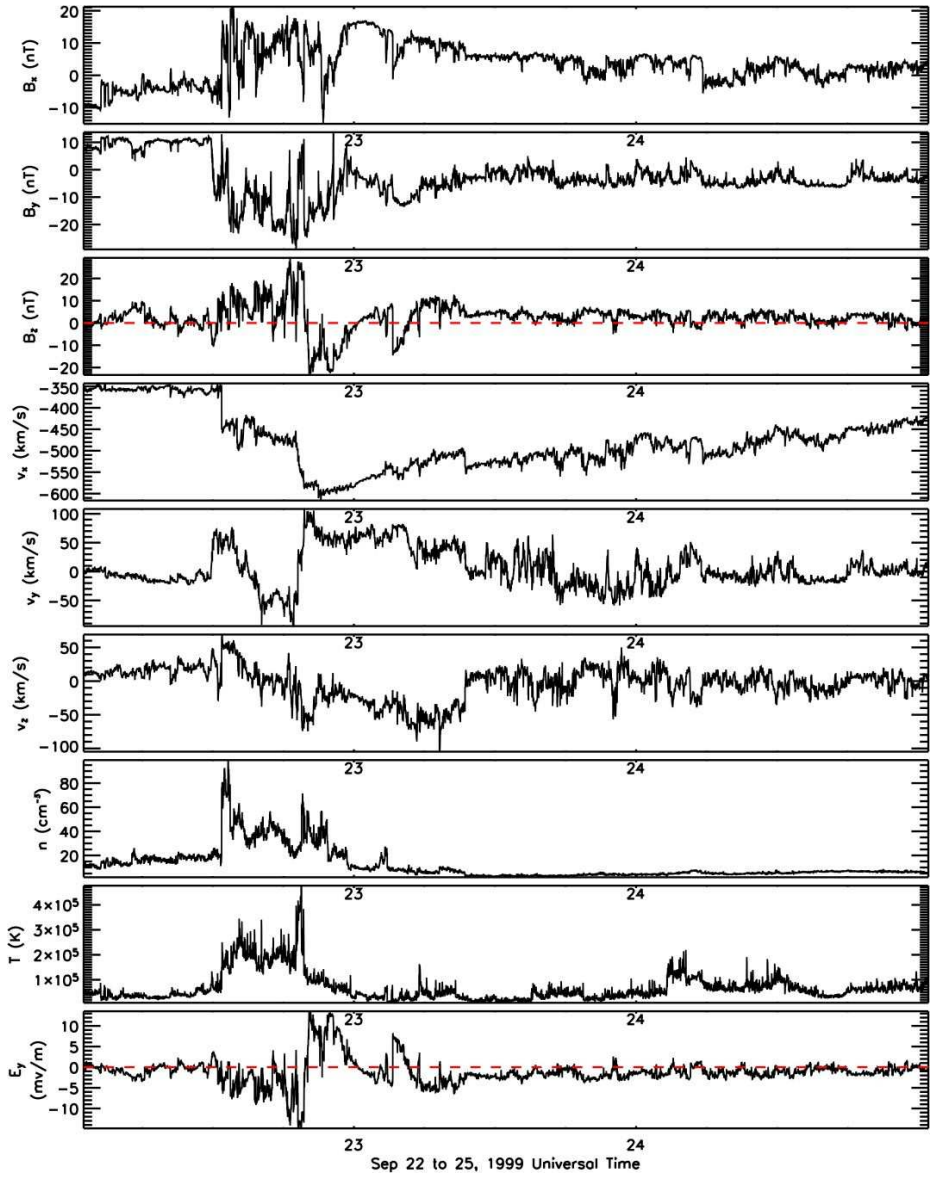

Figure 4.1: September 22, 1999 input parameters. From to to bottom are presented the input parameters: B_x (nT), B_y (nT), B_z (nT), v_x (km/s), v_y (km/s), v_z (km/s), density (cm^{-3}), temperature (K), and eastward component of the electric field E_y (mV/m). The horizontal red dashed line is drawn at zero in the B_z and E_y plots to better identify the northward/southward turning of the IMF B_z field.

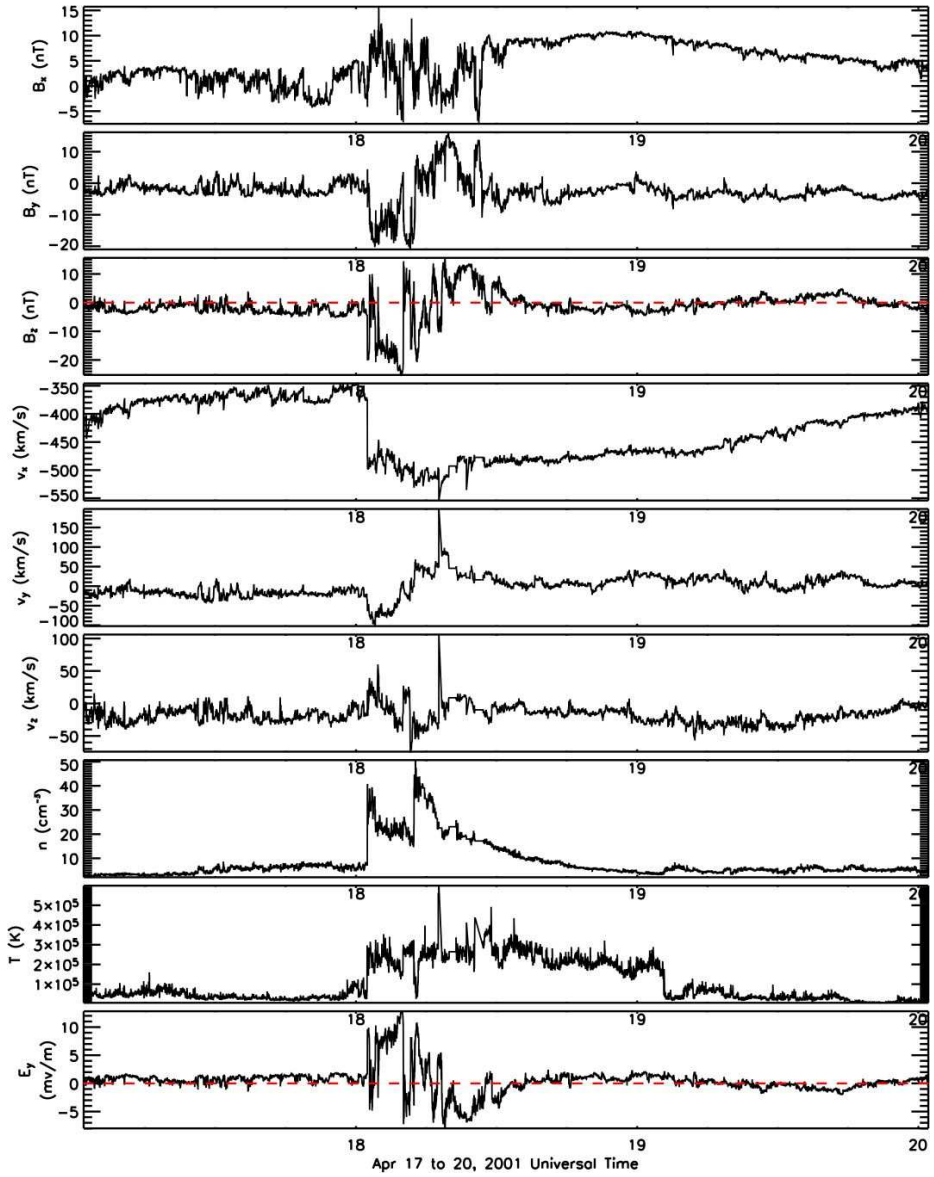

Figure 4.2: April 18, 2001 input parameters. From to to bottom are presented the input parameters: B_x (nT), B_y (nT), B_z (nT), v_x (km/s), v_y (km/s), v_z (km/s), density (cm^{-3}), temperature (K), and eastward component of the electric field E_y (mV/m). The horizontal red dashed line is drawn at zero in the B_z and E_y plots to better identify the northward/southward turning of the IMF B_z field.

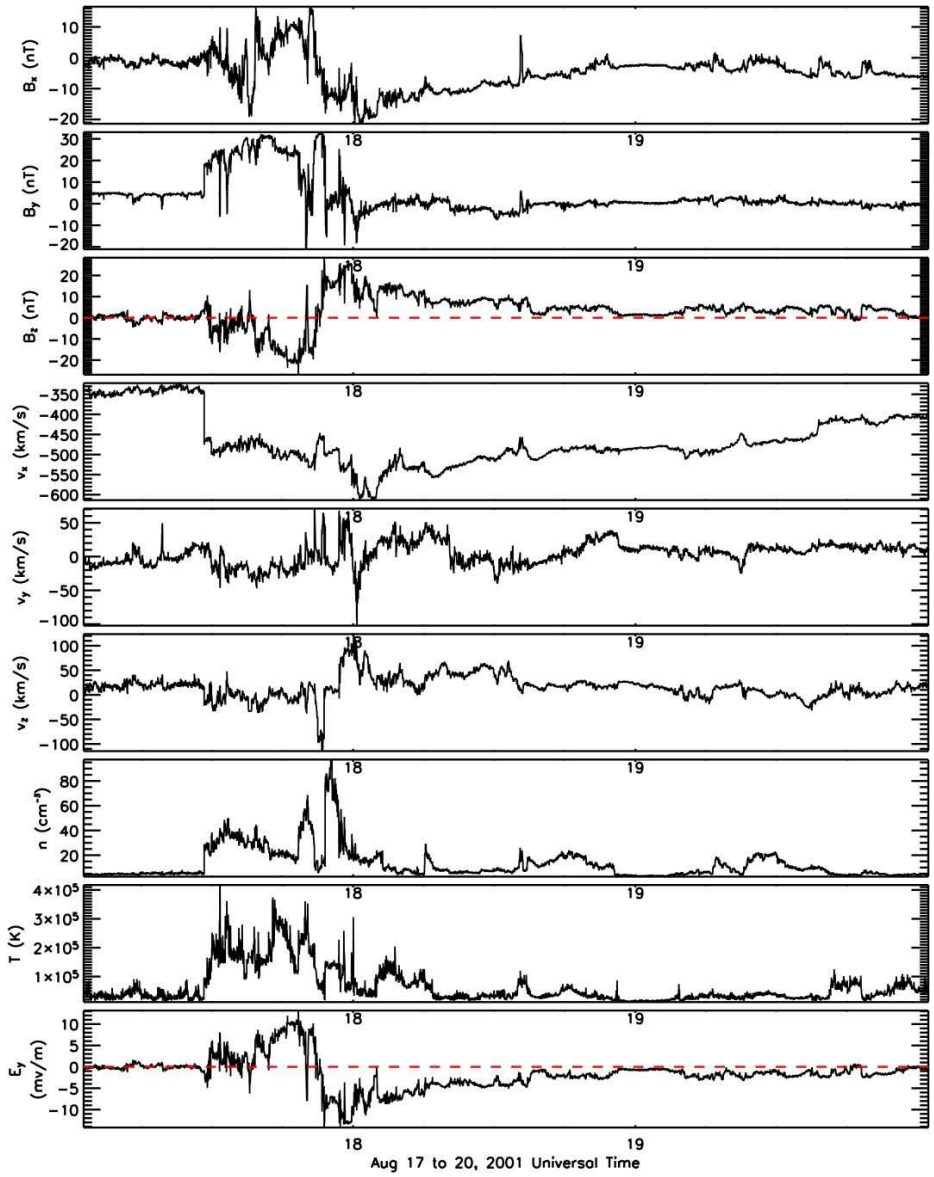

Figure 4.3: August 17, 2001 input parameters. From to to bottom are presented the input parameters: B_x (nT), B_y (nT), B_z (nT), v_x (km/s), v_y (km/s), v_z (km/s), density (cm^{-3}), temperature (K), and eastward component of the electric field E_y (mV/m). The horizontal red dashed line is drawn at zero in the B_z and E_y plots to better identify the northward/southward turning of the IMF B_z field.

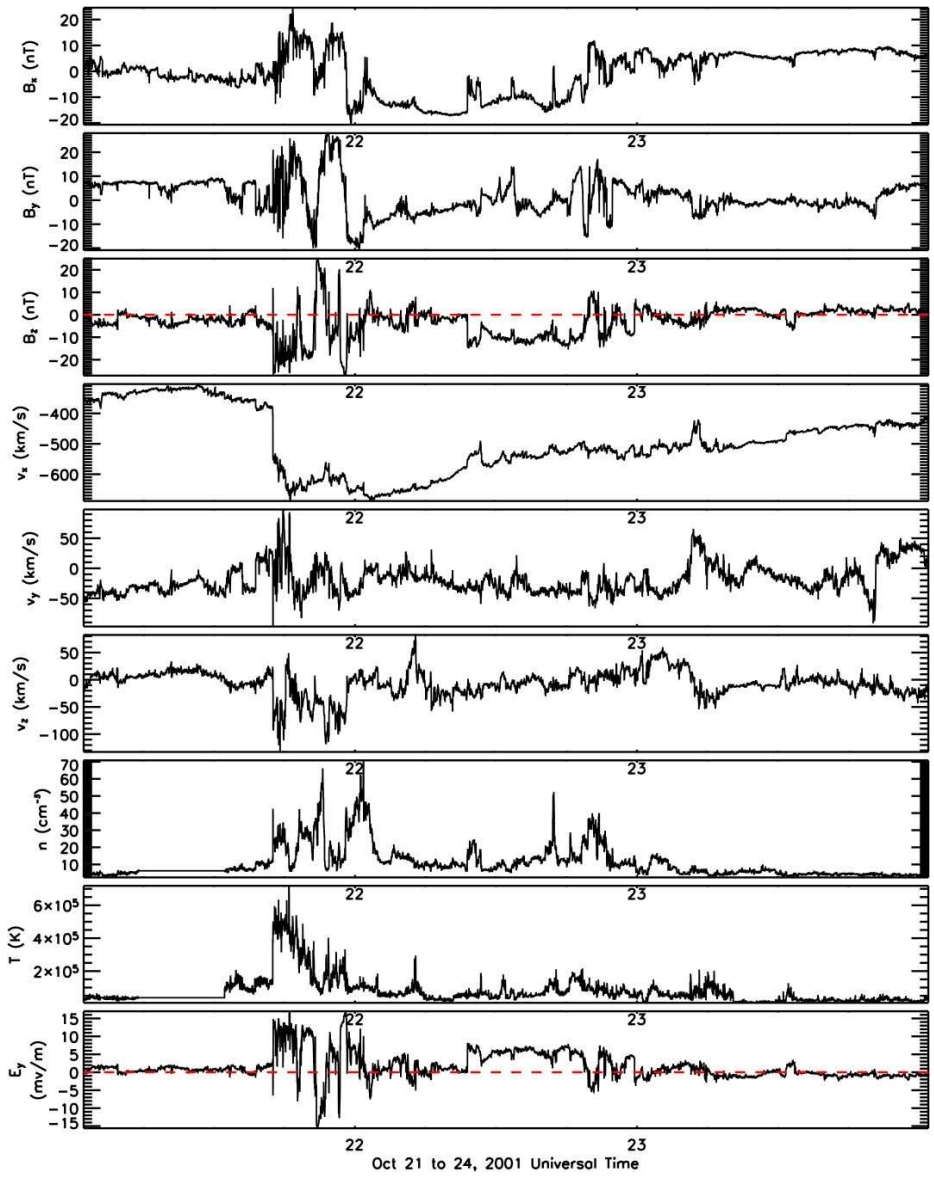

Figure 4.4: October 21, 2001 input parameters. From to to bottom are presented the input parameters: B_x (nT), B_y (nT), B_z (nT), v_x (km/s), v_y (km/s), v_z (km/s), density (cm^{-3}), temperature (K), and eastward component of the electric field E_y (mV/m). The horizontal red dashed line is drawn at zero in the B_z and E_y plots to better identify the northward/southward turning of the IMF B_z field.

4.5), and a storm with a minimum D_{st} of -157 nT and a recorded SYM-H index of -150 nT develops. The density increases about 4 times (from 12 cm^{-3} to 43 cm^{-3}) and the IMF B_z (varies between 9 nT and -20 nT) stays southward for more than 6 hours.

4.3 Results

Figure 4.6 shows the D_{st} results for all the individual events. The black dashed line shows the 1 hour resolution observed D_{st}, the black continuous line presents the 1 minute resolution SYM-H observations and the blue line shows the simulated D_{st} results. From top to bottom are presented the simulation results for September 22, 1999, April 18, 2001, August 18, 2001, October 21, 2001, and October 28, 2001.

We note that for the September 22, 1999 (top panel of Figure 4.6), the simulated D_{st} is lower (with a minimum of -230 nT) than both observed geomagnetic indices (D_{st} and SYM-H), it drops sooner and starts recovering at the time when the observed D_{st} is still progressing toward its minimum. Therefore the model results overestimate the strength of the ring current and indicate a shift in the peak of the storm.

For the case of April 18, 2001, the simulated D_{st} does not go below -62 nT, although it seems to reproduce isolated features during the storm. The Storm Sudden Commencement is well captured, although the timing is delayed by a few minutes. Another interesting feature is that the slight increase in D_{st} at about 05:30 UT is captured as well but the values are completely off. Nevertheless, the simulated D_{st} seems to level with the observed one towards the time the recovery phase takes place.

In a similar way, the isolated features of the D_{st} index are well captured in the case of August 17th, 2001 event, but the D_{st} fails to reach values comparable to the observed ones (modeled $D_{st} = -48$ nT compared with observed $D_{st} = -105$ nT). During the main phase, it does not go below ~ -48 nT and levels up with the observations during the recovery phase. Therefore the simulation does not reproduce

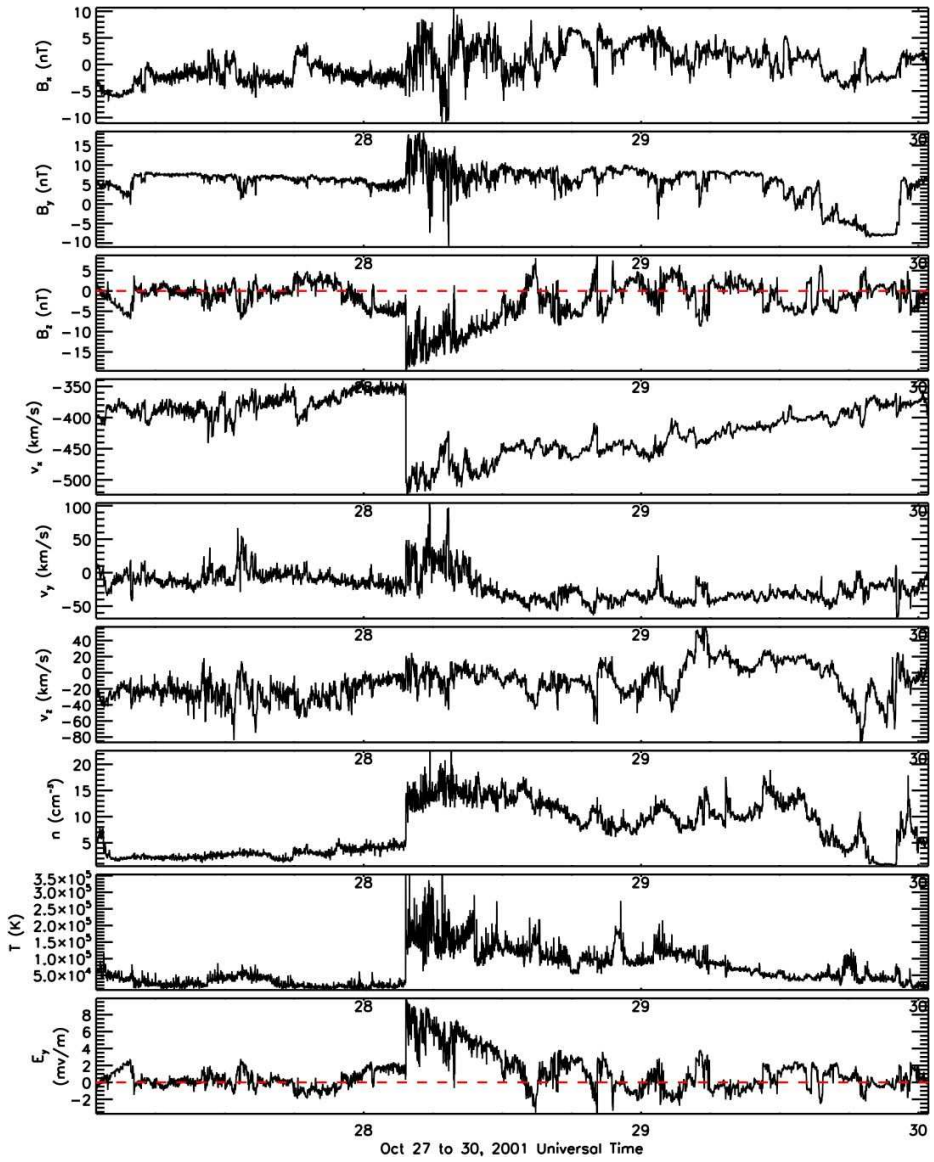

Figure 4.5: October 28, 2001 input parameters. From to to bottom are presented the input parameters: B_x (nT), B_y (nT), B_z (nT), v_x (km/s), v_y (km/s), v_z (km/s), density (cm^{-3}), temperature (K), and eastward component of the electric field E_y (mV/m). The horizontal red dashed line is drawn at zero in the B_z and E_y plots to better identify the northward/southward turning of the IMF B_z field.

the profile of an intense storm at this stage.

For the October 28, 2001 storm, the storm sudden commencement is again well captured, but the timing is a few minutes delayed. Nevertheless, the delay is small and can be due to the propagation of the data to 32 Re. However, throughout the storm, the D_{st} does not decrease at all and is fairly constant, barely reaching ~ -35 nT.

Interestingly enough, the cross polar cap potential is well fitted with the observationally based Assimilative Mapping of Ionospheric Electrodynamics (AMIE) potential routine of *Ridley et al.* (2000). In Figure 4.7 we only show the simulation results for the transpolar potential for August 2001 event. The close profile of the two indicate that the convection electric field is well represented by our model. Nevertheless, the overall ring current behaviour is not well reproduced, except for the September 1999 event. This could be due to too low plasma of a pressure in the inner magnetosphere. We note that one major difference between the 5 events selected, the September event had a very long initial phase, that lasted for several hours, compared to a few minutes for all the other storms.

Please note one event was rerun with different run setups, including different resolutions and different numerical schemes, but the results did not change significantly.

4.4 Conclusions

Even though the events we selected were similar in their nature, that is, were driven by the same solar wind driver, occurred at similar tilt of Earth's axis, during the same solar cycle and with similar intensities, the model was unable to reproduce their profile. Only for the event of September 1999 the simulated D_{st} index reached an 'intense storm-like' value, although the overall intensity of the ring current was overestimated. Therefore, it would be futile to continue the superposed input study. Our goal was to probe the answer to this question: is the average of individual storm

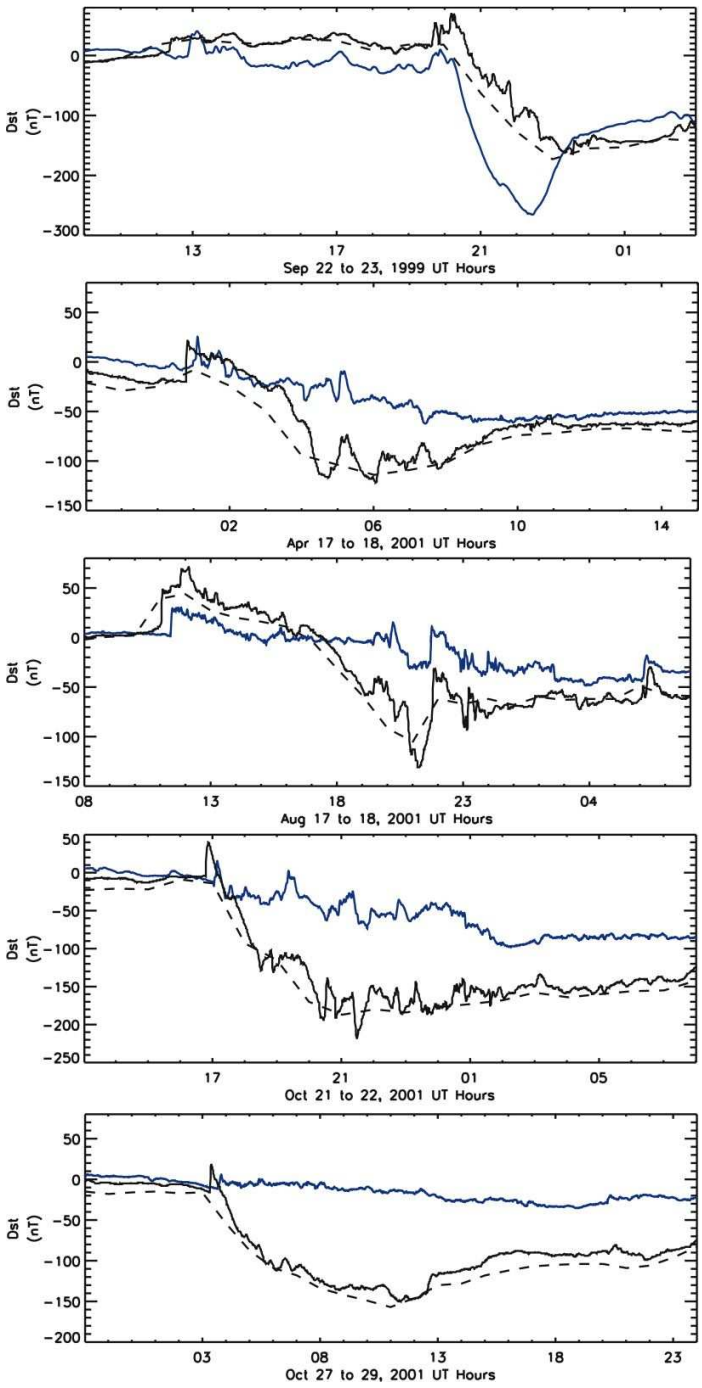

Figure 4.6: D_{st} profiles for all the events. Black dashed line presents the 1 hour resolution observed D_{st}, the black continuous line presents the 1 minute resolution SYM-H observations and the blue line shows the simulated D_{st} results. From top to bottom are presented the results from the simulation of September22, 1999, April 18, 2001, August 18, 2001, October 21, 2001 and October 28, 2001.

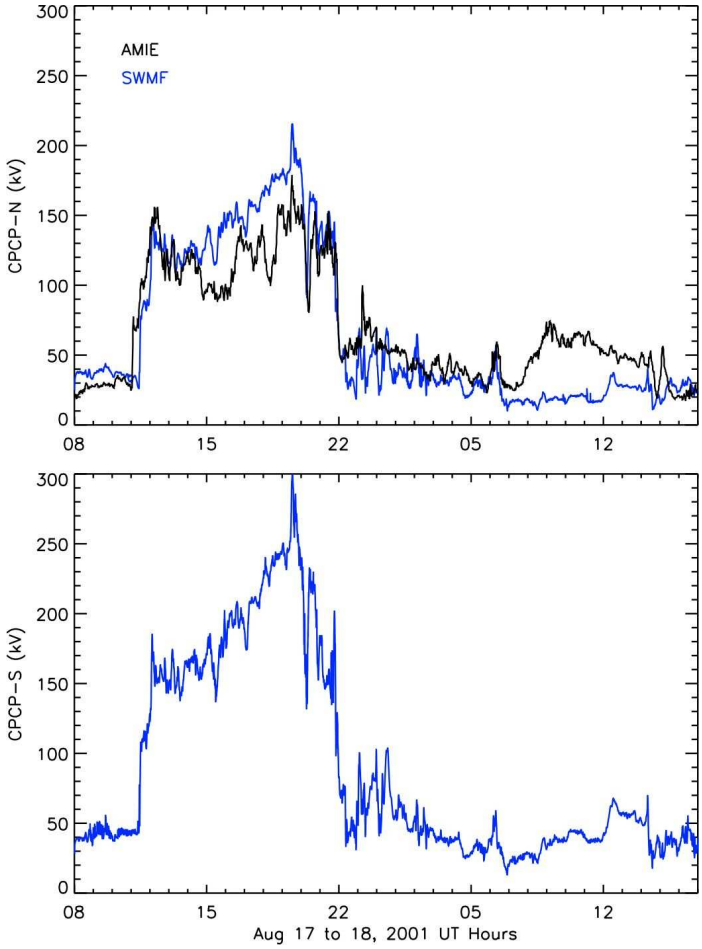

Figure 4.7: Cross polar cap potential (CPCP) profiles for August 17, 2001 events in both the norther (top panel) and southern (bottom panel) hemisphere. Black line presents AMIE potential while the blue lines show the modelled result

simulations the same as a single simulations using the averaged input? This study no longer makes sense when the simulations of the individual storms are so inconsistent with the observed state of magnetic disturbance. It seems that the SWMF produces the correct convective flow in the magnetosphere, so it is most likely not producing the correct near-tail plasma sheet densities and temperatures. The direction of the numerical study needs to be revised to better address the posed question.

In order to examine the role of the transient spikes in the development of a magnetic storm, we can focus our attention on a single event rather than a series of events, and perform smoothing of the input parameters for just that particular storm. This analysis is presented in Chapter V.

Another option would be to not only focus on the same solar wind driver but rather to investigate different types of solar wind drivers and understand the dominant physical processes for each class of storm. Therefore, Chapter VI presents our work on CIR driven storms. As in Chapter V, this study investigates the role of solar wind fluctuations in controlling inner magnetosphere dynamics.

Furthermore, a better model for the inner magnetosphere is important. For storms, the inner magnetospheric drift physics model is one of the key elements of the code. Therefore, it is useful to incorporate a new drift physics model into SWMF. One such endeavour is described in detail in Chapter VII.

CHAPTER V

Non-linear feedback of the solar wind parameters on the ring current

5.1 Motivation

There are still things we don't know about the storm-time ring current and plasmasphere, especially with regard to the ring current's nonlinear response on the energy input. The magnetospheric responses to the solar wind input has been suggested to be highly nonlinear and to produce very different outputs for a slight difference in the input (*Baker and McPherron*, 1990; *Klimas et al.*, 1994).

Non-linear response of the ring current formation and decay to the changes in the plasma sheet density has been reported throughout the literature (e.g. *Ebihara et al.*, 2005). *Palmroth et al.* (2003) used global MHD simulations to investigate the solar wind energy transfer to the magnetosphere. The authors suggested that during the main phase of a magnetic storm, the energy transferred from the solar wind to the magnetosphere is well correlated to the solar wind parameters, implying a linear relationship between driver intensity and the corresponding magnetosphere reaction. Interestingly enough, the correlation is lost as soon as the recovery phase starts. Conversely, *Lavraud et al.* (2006) argue that the proton ring current energy is increasing with increasing plasma sheet density, predicting a linear relationship

between the two.

A time delay of the order of minutes has been reported to exist between the time the IMF reaches the magnetopause and the ionosphere starts to react (e.g. *Ridley and Clauer*, 1996; *Ridley et al.*, 1998; *Ruohoniemi and Greenwald*, 1998; *Slinker et al.*, 2001; *Lu et al.*, 2002). While the ionospheric potential takes 10 to 20 minutes to fully change from one state to another, it takes about 30 minutes for the inner magnetosphere to respond to changes in the the electric potential from the solar wind (*Goldstein et al.*, 2003).

Transient spikes in the solar wind parameters are observed during most magnetic storm events, leading to considerable changes in the convection strength in the Earth's magnetosphere, therefore altering the flow of plasma sheet particles that contribute to the total energy content of the ring current. Spikes added to the magnetospheric convection increase the diffusive transport of ions with energies over 160 keV and therefore produce enhancement of the ring current (*Chen et al.*, 1993, 1994). Moreover, the short lived, intense electric fields during magnetic storms are believed to be responsible for the observed ion flux enhancements inside the plasmapause and to contribute to the enhancement of the energetic tail of the ring current ion population (*Ganushkina et al.*, 2000, 2001, 2006).

Tsurutani et al. (1990) is the first to describe the magnetosphere as a low pass filter. *Murr and Hughes* (2007) suggest that the ionosphere is insensitive to frequencies higher than 0.8 mHz in the IMF (changes on the approximately 21 minutes time scale), meaning that the magnetosphere-ionosphere system naturally acts as a low pass filter of the interplanetary magnetic field. Furthermore, low frequencies in the AE index are suggested to be correlated to the low frequencies in the rectified eastward component of the interplanetary electric field (E_y), and the high frequencies are associated with the intrinsic dynamics of the magnetosphere (*Takalo et al.*, 2000).

The majority of empirical models that provide a prediction for the D_{st} index are

linear with respect to the solar wind parameters (e.g *Burton et al.*, 1975; *O'Brien and McPherron*, 2000; *Temerin and Li*, 2002, 2006). Non-linear dependence on the dynamic solar wind pressure is considered by some models (e.g. *Wang et al.*, 2003), while *Siscoe et al.* (2005) suggest that non-linearity of the system should be based on the eastward component of the interplanetary electric field, rather than the ram pressure.

If the ring current shows a linear response with respect to its drivers, then the presence of the transient spikes alone in solar wind parameters should have no extra contribution to the energization and loss of the ring current population. Smoothing the solar wind plasma and IMF, therefore reducing the solar wind energy transferred to the magnetosphere, should yield a linear response of the inner magnetosphere with respect to the energy input.

The presented work addresses this open issue by examining the event of September 22, 1999 through global magnetosphere simulations using the Space Weather Modeling Framework (SWMF), for a variety of time averaged solar wind inputs.

5.2 Solar wind inputs

Solar wind observations from the ACE satellite, orbiting around the Lagrange 1 point, were used as inputs in the SWMF simulation. The setup of the simulation is described in Section 3.1.4. Note that the data is propagated from the satellite location to (32, 0, 0) Re in the GSM coordinate system using the Minimum Variance Analysis method of *Weimer et al.* (2003) and *Weimer* (2004).

To assess the role of small scale fluctuations in the solar wind plasma, we averaged the input data (4 minutes temporal resolution) with running average windows of 60, 120, and 180 minutes, in this way decreasing the energy input into the magnetosphere. Figure 5.1 shows solar wind plasma and interplanetary magnetic field (IMF) parameters for the September 22, 1999 event. The different colored lines correspond to

different input data: red lines show the 4 min temporal resolution ACE observations, while purple, green, and blue lines correspond to 60, 120 and 180 minute running averages, respectively.

The event chosen for this study is an intense, ICME driven magnetic storm, showing a large disturbance of the geomagnetic field with an observed D_{st} index minimum of $-173\ nT$. A well defined shock is observed in the solar wind, with a four times increase in solar wind particle density at about 12:52 UT, from approximately 19 cm^{-3} to 76 cm^{-3}. B_z is mostly northward until 19:52 UT when it becomes negative and stays negative until 00:32 UT on September 23rd, with a minimum value of approximately $-22\ nT$. When we smooth the data with a window of 3 hours, the shock in solar wind plasma density is not as sharp as before, showing a maximum value of 36.5 cm^{-3}, while the B_z southward turn happens a few minutes earlier than seen in the 4 minutes data and only reaching a minimum of $-13\ nT$. The X component of the solar wind velocity is one parameter for which the effect of averaging is not as significant, mostly because v_x is quite steady (except at the beginning of the storm), showing very little temporal variation.

Geomagnetic activity is powered by the solar wind energy injected into the magnetosphere, therefore we use this quantity as an indication of inner magnetospheric activity. Integration of the rectified eastward component of the interplanetary electric field over the time yields a proxy for the total energy input[1] into the Earth's magnetosphere and it is defined as the following:

$$I_{E_y} = \int_{t_1}^{t_2} E^*_{y,sw} \mathrm{d}t \tag{5.1}$$

where $E^*_{y,sw}$ is:

[1]Throughout this chapter we will refer to this quantity as the *energy input*.

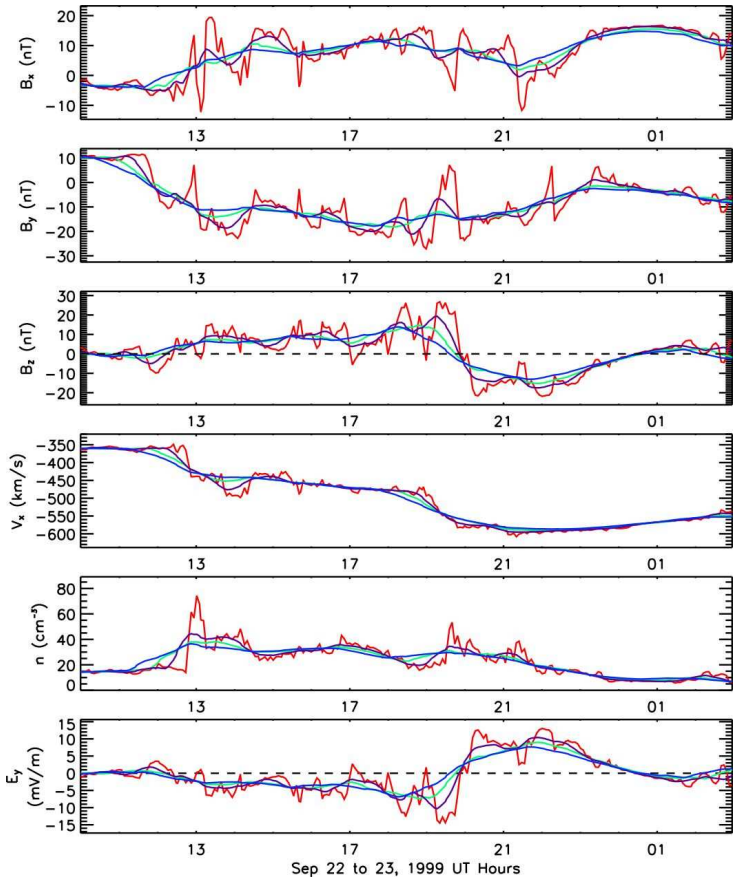

Figure 5.1: Averaged inputs for the September 22, 1999 event. Red lines show the ACE observations with a temporal resolution of 4 minutes, and the running averages with windows of 60 minutes (purple line), 120 minutes (green line), 180 min (blue line). From top to bottom are presented the input parameters: B_x (nT), B_y (nT), B_z (nT), v_x (km/s), density (cm^{-3}) and eastward component of the electric field E_y (mV/m). The horizontal dashed line in the B_z plot indicates the northward/southward turning of the field.

$$E^*_{y,sw} = \begin{cases} 0 & \text{if } B_z \geq 0 \\ -(v_x \cdot B_z) & \text{if } B_z < 0 \end{cases} \tag{5.2}$$

and t_1 corresponds to the start time of the simulation (September 22, 10:00 UT), while t_2 is the end time of the simulation (September 23, 03:00 UT). Note that E_y for all cases was computed using the smoothed values of v_x and B_z and not by smoothing the high resolution E_y time series.

Input Resolution	4 min	60 min	120 min	180min	180 B_z only	N only
I(Vs/m)	120738	106959	92124	82039	83042	120738
Percent Diff	0	12.1	26.9	38.2	36.9	0
D_{st} (nT)	-265	-254	-131	-42	-138	-201
Percent Diff	39.3	35.2	30.4	123.6	25.3	12.1

Table 5.1: Values of the time integrated energy input into the system for different simulations, and the percent difference between the energy input produced by the 4 minute resolution input data and 60, 120, 180 minutes averaged solar wind inputs.

Percent differences were calculated between energy input when the temporal resolution of the upstream solar wind was 4 minutes and energy input for the 60, 120, and 180 minute averaging of the data and shown in the first two rows of Table 5.1. The smoothing of the data diminishes the power input into the system by about 38%, when the averaging is done with a window of 3 hours. It is worth mentioning that the bulk of the energy input is transferred during the storm main phase (from 20:00 UT to 23:00 UT), therefore including the quiet time in our integration of E_y does not change its value significantly (Figure 5.2). As we can see the bulk of energy input is in the time period of 20:00 UT and 24:00 UT, therefore integrating E_y over our simulation time range does not change the total energy input significantly, since the contribution from the quiet time is close to zero.

Row 3 and 4 show the simulated D_{st} index values and percent differences between the observed value and the ones produced by our simulations. We note that the 180 min smoothed-density-only run produces a ring current closest to the observations, while the 3 hour smoothing of all the data produces the weakest D_{st} index.

5.3 Smoothing all input parameters

5.3.1 Magnetospheric Response

The D_{st} index results are shown in Figure 5.3 for the cases in which all of the input parameters were smoothed. The modeled D_{st} index is calculated by solving the Biot-

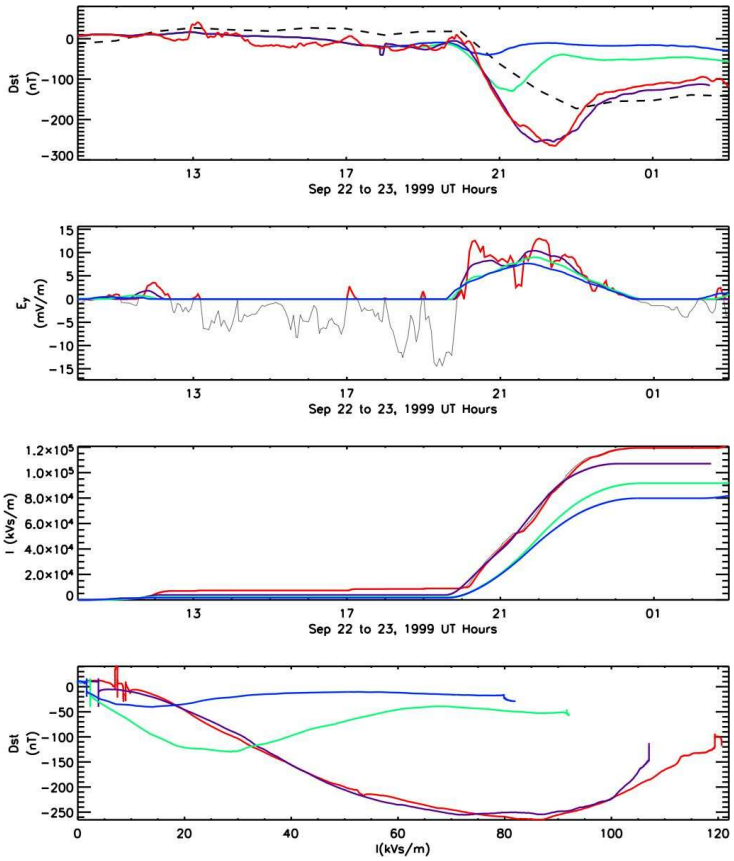

Figure 5.2: From top to bottom: D_{st} vs. time, E_y vs. time, the integrated energy input vs. time and the D_{st} vs. energy input in the bottom panel. The colored lines indicate the observed values (black), 4 minute temporal resolution (red), 60 minute (purple), 120 minute (green) and 180 minute (blue) smoothed input results for all parameters.

Savart integral for all the electric currents encompassed by the BATSRUS simulation domain from the inner boundary outward, and taking the magnetic field disturbance along the Z-axis. Again, the colored lines show the results from the four different temporal resolution inputs: 4 minutes (red), 60 minutes (purple), 120 minutes (green), and 180 minutes (blue), while the black dashed line shows the observed D_{st} and the black continuous line corresponds to the SYM-H index. The comparison with the observed indices provides us with a measure of the ability of the model to accurately represent the inner magnetospheric response. The 60, 120, and 180 minutes averaging runs were started from the same common restart file (obtained from the 120 minute

run) just before 18:00 UT as opposed to 10:00 UT for the case of the 4 minute averaging run. The reasoning behind this was to use less computer resources and it was motivated by the fact that this time was still several hours before the main phase of the storm (during the very quiet pre-storm interval).

When the 4 minute and 60 minute temporally smoothed inputs are used in our simulation, the modeled D_{st} profiles are quite similar, peaking within the same hour and dropping to about the same value, then recovering very fast during the first 2 hours and slower after that. For both of these cases, the simulated D_{st} index is dropping sooner and lower (more intense) than the observed value, indicating a stronger ring current and a shift in the peak of the storm.

For the case when the inputs are smoothed with a window of 2 hours, the D_{st} index is less negative (less intense) than the observed one; it recovers quickly for 2 hours after which the recovery is slow, as noted in the previous cases as well. Similar behaviour is seen in the case of the simulation that used Kp-like (3 hours) averaged input data, only this time the D_{st} index did not go below $-40\ nT$. Please note that the main phase of the September 22, 1999 event only lasted about 3 hours, therefore averaging over 180 minutes, the B_z southward magnitude has been greatly decreased, implying that the magnetic convection will be significantly weaker.

Interestingly enough, for all cases, the D_{st} profile showcases a two-phase recovery. There are a few hypotheses that are trying to explain this fast and then slow recovery phase. *Liemohn et al.* (1999) postulated from numerical simulation results that the fast early recovery phase is due to particle flow-out of the inner magnetosphere toward the dayside magnetosphere. Also, *Jorgensen et al.* (2001) suggested that different processes are responsible for the fast and the slow recovery phase, that is, during the early fast recovery the lifetime of trapped ring current particles is considerably shorter compared with the late slow recovery phase.

Many authors (e.g. *Liemohn et al.*, 1999, 2001b; *Jordanova et al.*, 2003) argued

that charge exchange processes are primarily responsible for the decay of the ring current during the late recovery phase, due to the reaction's slow timescale compared with the loss of ions to the dayside due to large scale plasma convection. In our study, we cannot conclude anything about the charge exchange losses since these losses are not explicitly included into our global magnetospheric simulations. Yet, our simulation results suggest that such behavior is reproducible without the charge exchange mechanism explicitly taken into account.

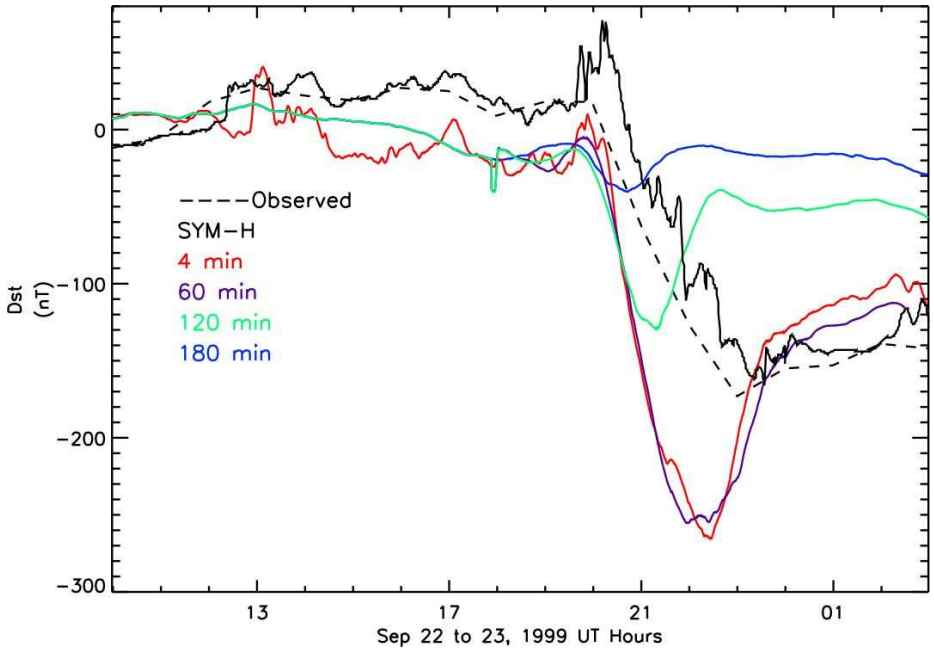

Figure 5.3: D_{st} index simulation results for all the runs using averaged inputs for the September 22, 1999 magnetic storm. Each colored line corresponds to a different simulation results using different time resolution input data: 4 minutes (red line), 60 minutes (purple line), 120 minutes (green line), 180 min (blue line). Black dashed line shows the observe D_{st} index, while the black continuous line corresponds to the SYM-H observations.

Figure 5.4 presents the BATSRUS pressure distribution in the X-Y plane (as modified by RCM) during the development of the storm, for all our simulation runs. Pressure is directly correlated with the current density and provides a good measure of the current distribution. The ring current develops at different times during the storm, depending on the averaging window; the least intense value of the D_{st} index

occurs during the 3-hours averaged input with a ring current that grows and peaks sooner. In the 4, 60, and 120 minutes averaged inputs runs, the current becomes symmetric around 23:00 UT (weaker in the latter case), while for the 180 minutes averaged inputs run, pressure is close to one order of magnitude lower, resulting in a less disturbed geomagnetic field (as seen in Figure 5.3). In the last column of Figure 5.4, the plasma sheet is very weak, while in the first two columns, the plasma sheet shows an intensification during the main phase and decays close to 24:00 UT, at the same time as the start of the slow recovery phase. Similar features are seen in the case of 120 minutes averages, the drop in the near Earth plasma sheet pressure is followed by the slow recovery of the ring current. While the D_{st} decay is mainly modulated by the ring current, the recovery is controlled by both the ring and the tail current systems (*Feldstein et al.*, 2000). A rapid decay of the tail current can cause a sudden recovery in the D_{st} index. On the other hand, *Ohtani et al.* (2001) argues that the contribution of the tail current to the D_{st} is approximately 20-25 % of the total. We can consider then that the two-phase decay seen in the D_{st} index might not be due only to the loss of trapped ring current energy, but also to the early decay of the tail current system.

5.3.2 Midnight Plasma Sheet

The major sources for the ring current population are the ionospheric outflow and the injection of the plasma sheet particles into the inner magnetosphere. Plasma sheet particles are accelerated due to the convection electric fields and become trapped and start gradient-curvature drifting around the earth, forming the ring current. Therefore we investigate the contribution of the plasma sheet density to the energization of the ring current. To do so, we have included 24 virtual satellites in our simulations, located one hour of local time apart at geosynchronous orbit, and extracted values throughout the simulation run times. Our model solves the MHD equations for the

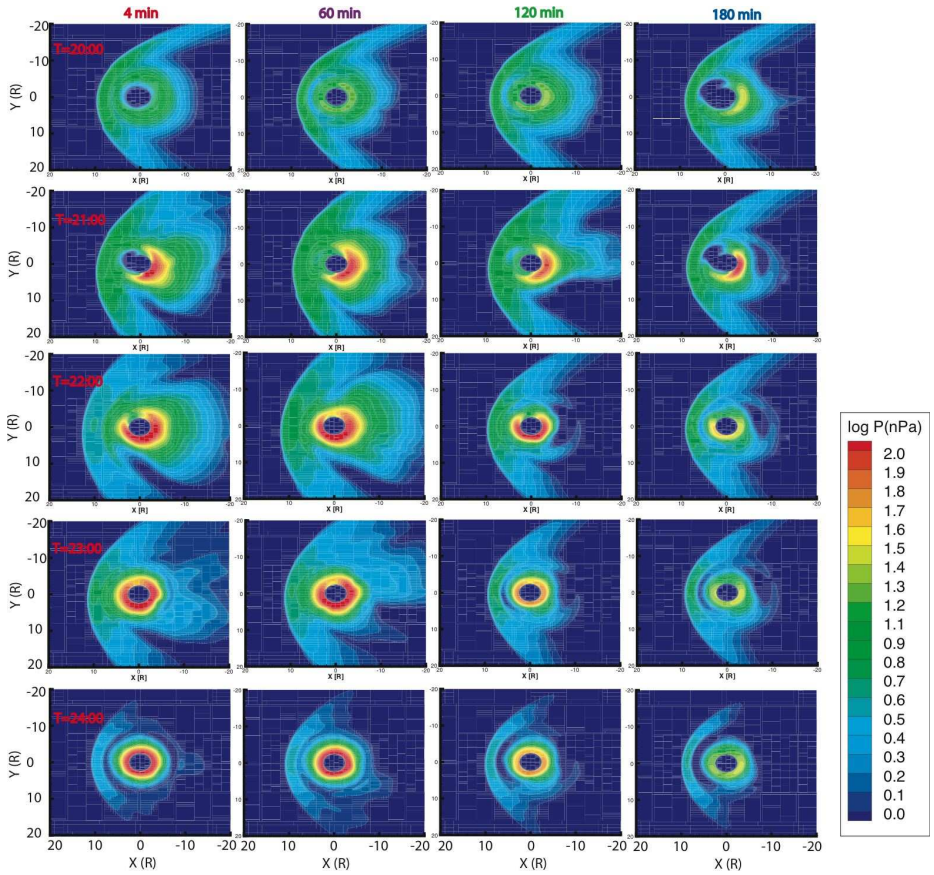

Figure 5.4: Pressure distribution in the X-Y plane for all simulation results. From left to right, each column corresponds to a case study: 4 minutes, 60 minutes, 120 minutes and 180 minutes running averages of input parameters. From top to bottom, we present snapshots of the pressure on a logarithmic scale at five times during the event: 20:00 -24:00 UT on September 22, 1999. The scale of the plot is logarithmic (base 10) and is expressed in nPa.

mass density and it provided us with a measure of plasma sheet population expressed in atomic mass units per cubic centimeter (amu/cm^{-3}). Since compositional information is not available, in order to convert it to number density expressed in units of particles per cubic centimeter, we are using the formulae of *Young et al.* (1982), that is, empirical relationships between the densities of O^+ and H^+ as a function of the Kp index and the solar flux $F_{10.7}$, as described below:

$$n(O^+) = 0.011 \exp\left(0.24Kp + 0.011F_{10.7}\right) \tag{5.3}$$

$$\frac{n(O^+)}{n(H^+)} = 0.045 \exp\left(0.17Kp + 0.010F_{10.7}\right) \tag{5.4}$$

The density provided by our model (n_{SWMF}) was corrected in such a way that accounts for the percentage of both oxygen and hydrogen ions:

$$n_{corrected} = n_{SWMF}\frac{n(H^+) + n(O^+)}{n(H^+) + 16n(O^+)} \tag{5.5}$$

Note that for this event, Kp was fluctuating between 2 and 8, with a maximum of 8 at the storm peak.

Figure 5.5 presents the geosynchronous nightside plasma sheet density (averaged over the 12 nightside virtual satellites), the radial component of the bulk velocity and the sunward particle flux results for 4 minutes temporal resolution and 3 hours averaged solar wind input cases only, used in our study. The radial velocity and the density were averaged across the nightside around the geosynchronous orbit, from 18 LT to 06 LT. For the case of the high resolution solar wind input (red line in Figure 5.5), both the plasma sheet density and the sunward velocity are steady up until 20:00 UT, at which time B_z becomes negative and the plasma sheet density increases and remains at elevated values for most of the duration of the main phase. The radial velocity is considerably enhanced, reaching a maximum of about 80 km/s for the 4 minute simulation while the 3 hour averaged input (blue line in Figure 5.5) yields a maximum velocity of under 30 km/s. Interestingly, we note a sudden drop in the nightside plasma sheet density just before the storm maximum (22:00 UT), from about 4 cm^{-3} to approximately 2 cm^{-3} (red line in Figure 5.5). Similarly, the sunward velocity for the high resolution input data is increasing considerably closer to the storm maximum ($\sim$22:00 UT) only to decrease just before 00:00 UT, at the same time with the start of the slow recovery phase. Therefore, we suggested that fewer plasma sheet particles are accelerated enough to gain access to the inner

magnetosphere and become trapped. The difference in the Earthward particle flux for the two cases is significant. Smoothing the input with a window of 3 hours yields a steady, less dense plasma sheet density on the nightside, along with weaker flux and lower radial velocity. Therefore, removing the transient spikes in the solar wind by smoothing the solar wind input data with a window of 3 hours yields a less dense and less energetic plasma sheet population.

The density drop might explain the rapid recovery of the ring current, since the source of particles is depleted and there are very few additional particles injected into the ring current. Smoothing the input with a 3 hour window produces a steady, low density plasma sheet, showing very little variability. Again, this is explained by the fact that the weak and smooth southward IMF B_z (as shown in Figure 5.1, blue line in the third panel from top) decreases the magnetospheric convection and produces a less variable plasma sheet.

Takahashi et al. (1990) showed that both particle energy and the length of recovery of the cross tail potential control the amount of plasma trapped on closed field lines. These authors propose that the recovery of the D_{st} index is due to a combination of decreased injection and charge exchange of trapped particles. Moreover, they show that the drop in the plasma sheet density during the early recovery phase is the main contributor to the fast recovery of the simulated ring current. In addition, the late slow recovery occurs when the IMF B_z becomes positive. The particle injection rate is strongly dependent on the cross tail potential difference, and therefore the variation in the IMF B_z controls this potential. *Liemohn et al.* (1999) used simulations to examine two distinct events, one during solar minimum and one during solar maximum, considering the different oxygen content during the stormtime injections. They found that the drift losses out to the dayside magnetopause are the major loss mechanism during the main phase of the storms. Their study strengthens the belief that the fast early decay of the ring current is dominated by the "flow out" effect and

not by the collisional losses. *Kozyra et al.* (1998a,b) also show that the ion drift to the compressed dayside magnetosphere is the main loss mechanism that accounts for the fast recovery of the D_{st} index. Moreover, *Liemohn et al.* (2001b) state that changes in the inner magnetosphere plasma sheet density alter the particle open drift paths, and in the case of steady convection, an increase (decrease) in the plasma sheet density produces a more (less) disturbed D_{st} index. A decrease in the cross tail potential will produce a more symmetric ring current that dominates the induced perturbance in the geomagnetic field.

Our findings are also indicative of the fact that the drop in the midnight plasma sheet density (seen in the higher temporal resolution of the solar wind input runs) controls the beginning of the fast recovery phase, since the fast recovery appears to start at the time the plasma sheet density drops considerably. Also, the time when the Z component of the IMF becomes positive corresponds to the time when the ring current decay becomes slow.

The question still lingers: what causes the sudden loss of plasma sheet particles at the storm maximum and what mechanisms are responsible for this? Are the small time scale fluctuations in the solar wind responsible for this sudden decay of the ring current or is it just an artifact of the computer simulation?

Figure 5.6 shows the distribution of density and temperature at geosynchronous orbit, extracted from the virtual satellites locations, as a function of local and universal time. Once again, the density is corrected as previously described. The black bins indicate values lower than the minimum, while the purple bins indicate values greater than the maximum.

For the 4 minutes case (top left panel), the density increases from the dayside to the nightside and shows enhancements at midnight, and at the dayside, during the main phase of the storm. These features are lost when the upstream solar wind input is smoothed with a window of 3 hours (top right panel). The density profiles for both

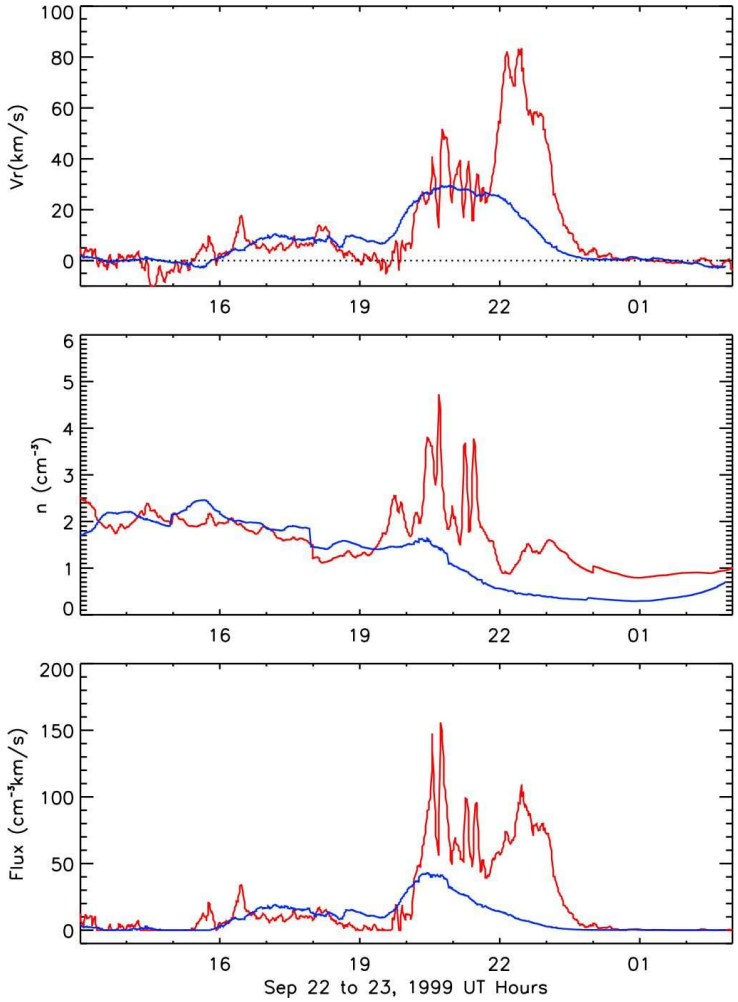

Figure 5.5: Nightside average of plasma sheet density extracted at the geosynchronous orbit (middle panel), radial velocity (top panel) and particle flux (bottom panel) results for the 4 minutes (red line) and 180 minutes (blue line) averaged solar wind inputs.

cases have very similar behaviours in the 12:00 - 18:00 UT time range. Please note that up to 18:00 UT, the density and temperature profiles for the 3 hour input data run were obtained from the 120 minutes averaged input data, since the 180 minutes run was restarted from about 18:00 UT as previously stated. Therefore the change in density after this time, which corresponds to the actual main phase of the storm, is what interests us. During the recovery phase, the 3 hour input produces a significantly lower density in the inner magnetosphere. The particle temperature is enhanced in the morning-afternoon sector for both cases, but the low temporal resolution input

(bottom right panel) reveals an injection of a more energetic particle population on the dawnside, although the density is low. The lower temperatures during this time period throughout the inner magnetosphere are due to the lowered energy input into the system. We note that for both cases, on the nightside, the density is low and the temperature is enhanced during the recovery phase. The dense midnight plasma just before the peak of the storm (22:00 UT) has quite a low temperature, while the dayside counterpart at the same universal time is made up of more energetic particles. Also the dawnside shows a larger depleted density region than the dusk side. Statistical studies (e.g. *Denton et al.*, 2005; *Lavraud et al.*, 2006) reported on the dawn-dusk asymmetries. The authors showed that during the main phase of magnetic storms, a time when both convection and ring current strength are high, the plasma density is enhanced primarily in the dawn region. Moreover, cold dense plasma is observed in the midnight sector, mainly during time periods of northward IMF and associated with a cold dense plasma sheet. Our results also indicate the presence of a cold and dense particle population on the dawn side during the main phase of the September 1999 event. Although the midnight dense and low temperature plasma seen in our high resolution input run occurs during a period of southward IMF, it is because it takes some time for the cold and dense plasma sheet to convect inward during northward IMF but can rapidly move in the inner magnetosphere when the IMF turns southward.

5.3.3 Ionospheric Response

Due to the fact that the magnetic field lines of the inner magnetosphere pass through the mid-latitude ionosphere, the convection patterns and the cross polar cap potential provide a great proxy to evaluate the ring current dynamics.

Figure 5.7 presents the variations in the cross polar cap potentials in both the southern and northern hemisphere predicted by our model over the course of the

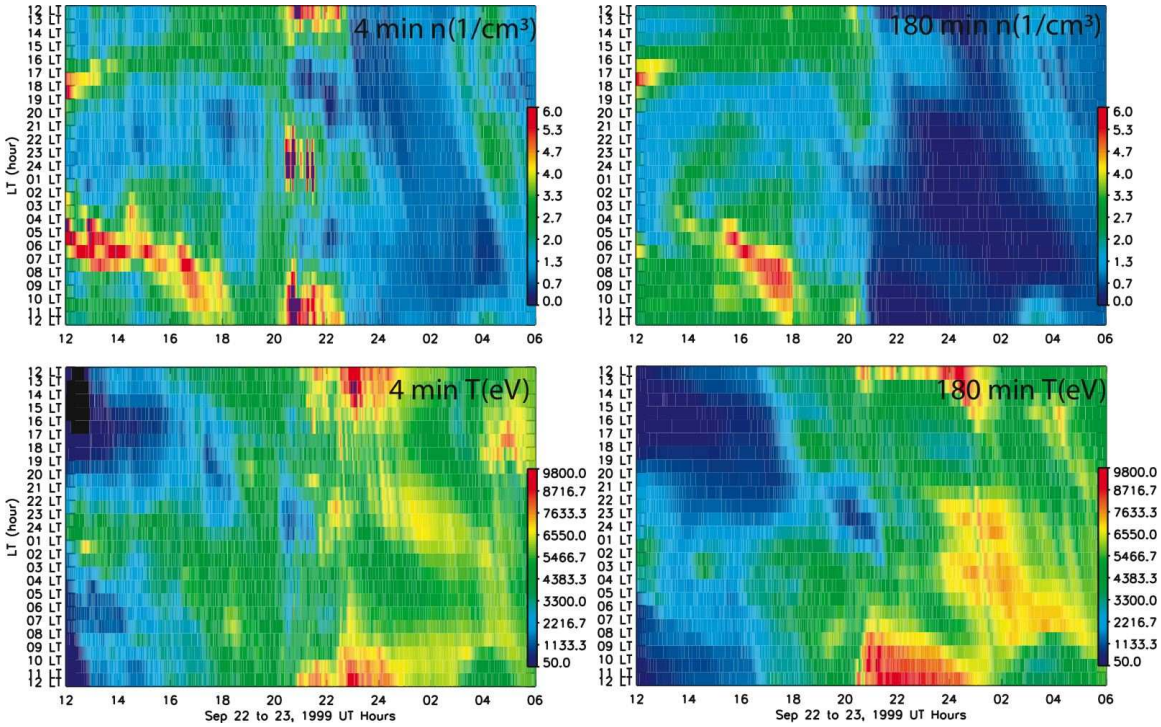

Figure 5.6: LT-UT map of the density (top row) and temperature (bottom row) for the 4 minutes averages (left column) and 180 minutes (right column) averages of the input parameters simulation results. Data was extracted from the virtual satellites included in the simulations at geosynchronous orbit.

September 22, 1999 magnetic storm. Again, the different colored lines correspond to different simulation results using the averaged solar wind input. It is interesting to note that the 120 minutes temporal resolution run produced the highest peak potential for this interval. Nevertheless, we can see that for all cases, the cross polar cap potential has a very similar behaviour. This is indicative of the fact that the small time scale fluctuations in the solar wind parameters do not appear to affect the cross polar cap potential, and so the flow generated by the change in transpolar potential is not altered significantly by the input averaging.

Since the ionospheric convection strength remained approximately constant in all of the simulated cases, the nightside plasma sheet density is the main parameter that controls the differences in the intensity of the simulated ring current. The loss of ring

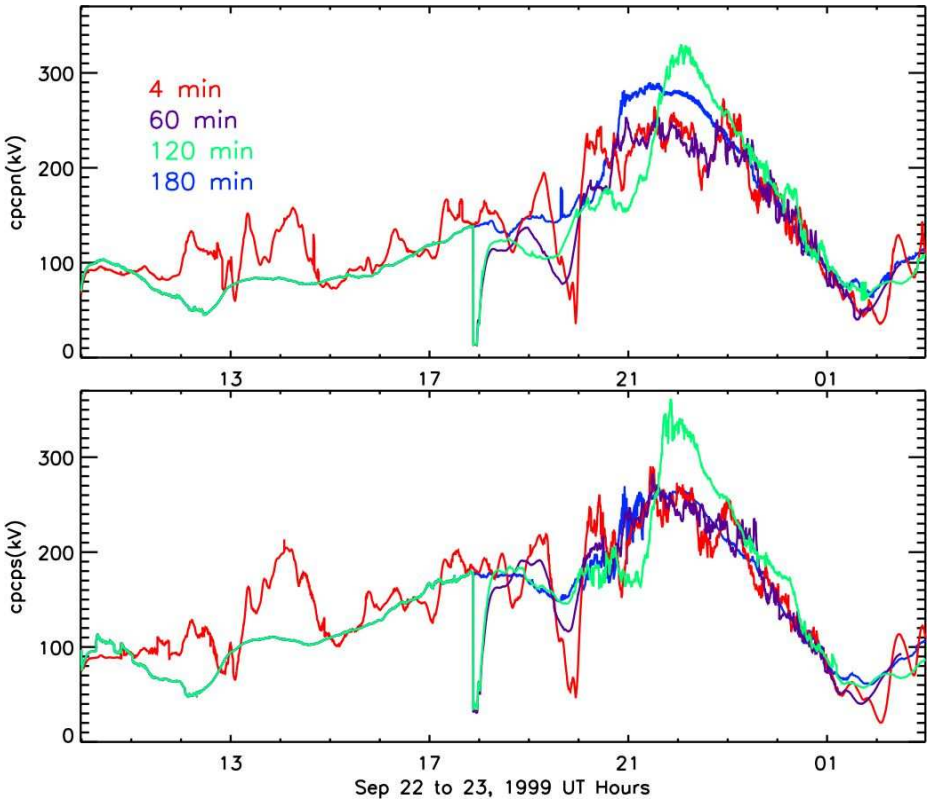

Figure 5.7: Cross polar cap potential simulation results in the northern (top panel) and southern (bottom panel) hemisphere, for all the runs using averaged inputs for the September 22, 1999 magnetic storm. Each colored line corresponds to a different simulation results using different time resolution input data: 4 minutes (red line), 60 minutes (purple line), 120 minutes (green line), 180 min (blue line).

current particles is due to the lower density plasma moving to lower radial distances along the open drift paths. The role of the temporal variations in the nightside plasma sheet inflow in developing a two phase decay of the ring current is also assessed by *Jordanova et al.* (2003). Their study concluded that the fast early recovery of the D_{st} is correlated with the sudden drop in the midnight plasma sheet density. Moreover, the two phase recovery phase results are consistent with the findings of *Liemohn and Kozyra* (2005). In their numerical study, the two phase decay of the ring current energy was found to occur when the plasma sheet density was suddenly reduced while the ionospheric convection was kept constant for a few hours after the density drop. Suddenly reducing both ionospheric convection and plasma sheet density, or

just decreasing the convection first and then the density, produced a one phase slow only recovery profile.

Since, in our simulations, we don't include charge exchange processes that are believed to be the ones responsible for the slow decay of the ring current, we attribute the slow decay phase to the fact that the source of the ring current particles is completely depleted, and along with weaker magnetospheric convection, fewer particles are accelerated (at a less rapid rate) and moved inward to become part of the ring current.

5.4 Smoothing selective input parameters: B_z and N

Averaging all the input parameters might not give us enough information to quantify which of them is primarily responsible for the decay of the ring current. To gain insight into this issue, we smoothed only one parameter at a time: in the first case study, we smooth only the Z component of the IMF with a window of 3 hours and keep all the others parameters at 4 minutes temporal resolution and in the second, we only smooth the solar wind density. The choice of 3 hours averaging seemed reasonable since it showed the most drastic response in the development of the storm. In the B_z smoothed case, the energy input changes only by 1.2% from the case in which all of the drivers are smoothed over a 180 minute window, and 36.9% from the case in which the inputs were 4 minute resolution. In the latter, the energy input is the same as in the case of 4 minutes averages (since E_y only depends on v_x and B_z and not on density).

The effects of smoothing only B_z and only the density are shown in Figure 5.8. The D_{st} profile for the first case is similar with the one for which the input was averaged with a window of 2 hours. The D_{st} minimum in smooth-B_z-only case is $-138\ nT$. The ring current shows more intensification that in the case when all input parameters are averaged over a 3 hour window. Even though the amount of solar wind energy

transferred to the magnetosphere is not significantly higher (as calculated in Equation 5.1), the response of the magnetosphere is definitely greater. Therefore, together all other 7 parameters (v_x, v_y, v_z, B_x, B_y, density and temperature) that constitute the input for our model have a considerable contribution to the energization of the ring current. On the other hand, when we only average density, the D_{st} index drops even lower, peaking at $-201\ nT$, though still higher than in the case of 4 and 60 minutes averages. These results shows us that both IMF B_z and the solar wind density control the energization of the ring current in the SWMF simulations, but the IMF B_z carries most of the contribution.

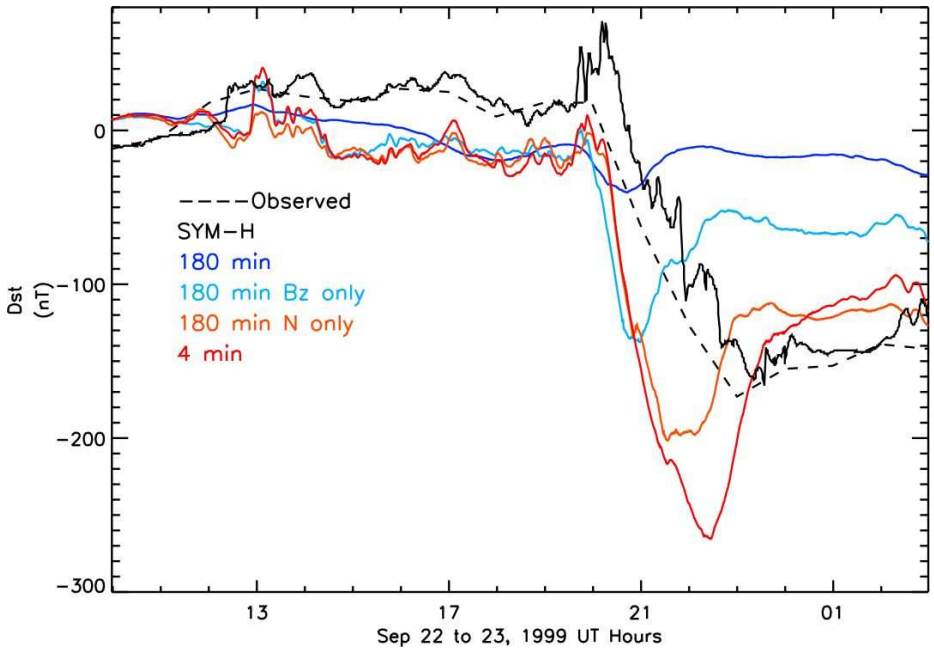

Figure 5.8: D_{st} index simulation results for the runs using averaged B_z only (light blue line), N only (orange line), 4 minutes (red line) and 3 hours averaging of all inputs (blue line) for the September 22, 1999 magnetic storm. Observed Sym-H and D_{st} index are shown in black, and black dashed line respectively.

Looking at the midnight plasma sheet populations (Figure 5.9), the density from the smooth-B_z-only run peaks first, but this time delay seems to be due to the fact that the 3 hour-averaged B_z drops a few minutes before the 4 minute temporal resolution IMF B_z. Therefore this is an artifact of the averaging. Nevertheless, in both cases,

we note the increase during the main phase and the sharp drop just before the slow recovery starts, although the size of the peak is larger for the smoothed-density-only run. The sunward velocity for the smoothed-density-only run is similar to the 4 minute resolution run, but the peak in velocity in the former case is considerably lower. The velocity profile for smoothed-B_z-only run is similar to the case of 3 hour averaged input run. This is indicative of the fact that the Z component of the IMF is the main parameter that controls the particle injection rate. The time the near-Earth tail sunward particle flux starts to decay is well correlated with the start time at the slow recovery phase.

Snapshots of the pressure distribution at five different times during the storm (Figure 5.10) also reveal that when only smoothing the solar wind density, a stronger ring current develops along with a greatly enhanced tail plasma sheet pressure. For the case when only the density is smoothed, the tail plasma sheet pressure starts reducing in intensity at about 23:00 UT, the same time as when rate of decay of D_{st} index becomes less steep. Similar but less distinct features (since the tail plasma sheet pressure seems to be lower) are seen in the case of only smoothing B_z .

5.5 In situ data-model comparison

During this event, the trajectories of the Geostationary Operations Environmental Satellite GOES08 and GOES10 were included in the SWMF simulations and MHD parameters were extracted along these orbit paths. The magnetic field simulation results are compared to flux gate magnetometer measurements aboard these satellites and presented in Figures 5.11 and 5.12. The satellite trajectories are shown in the top two panels (the black disk shows the location of the inner boundary, in our case 2.5 Re), followed by the magnetic field components B_x (nT), B_y (nT), and B_z (nT). Please note that the data is in GSM coordinates and the sun is on the right. A diamond, an asterisk, and a triangle are used to orient the reader as to where the data

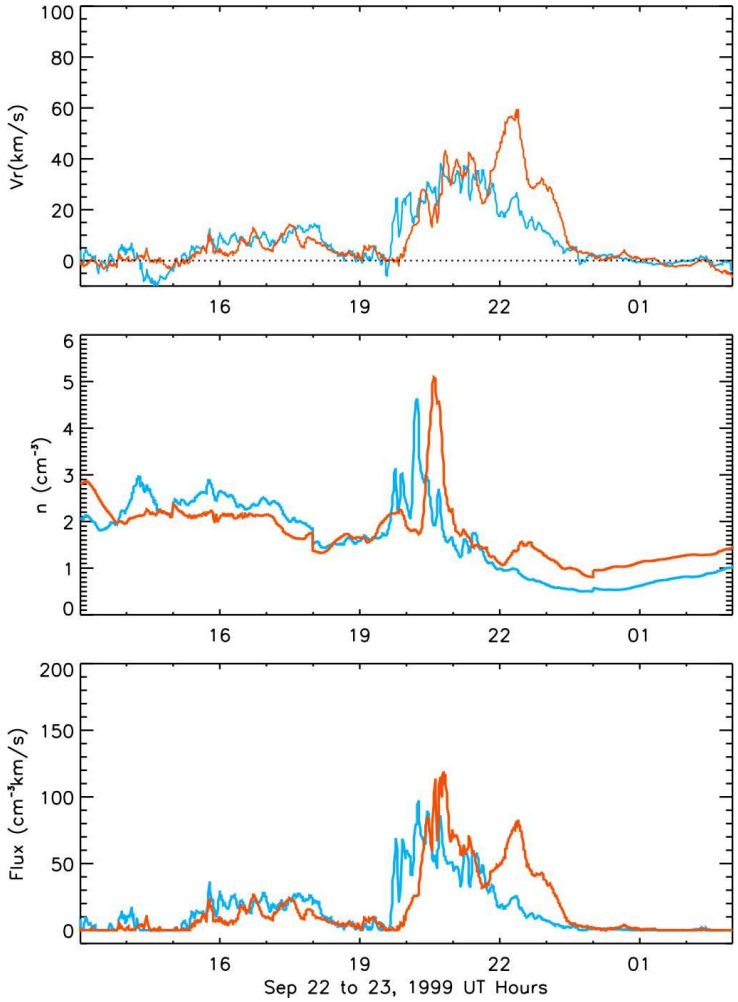

Figure 5.9: Nightside average of plasma sheet density extracted at the geosynchronous orbit (middle panel), radial velocity (top panel) and particle flux (bottom panel) results for the B_z only (light blue line) and density only (orange line) averaged solar wind inputs, extracted at geosynchronous orbit.

is being taken. In all three panels, the black lines show the satellite measurements while the red and blue lines correspond to model runs using 4 minutes and 180 minutes averaged solar wind input, respectively. Figure 5.11 displays the results from GOES08. We note that for this event, the spacecraft is located on the dayside at the storm peak (23:00 UT). For the case of high resolution solar wind input, the magnetic field measurements are reproduced remarkably well, with excellent agreement with respect to overall trends, but there are several discrepancies in the details. The smooth rotation in the Y component of the magnetic field during the main phase (20:00 -

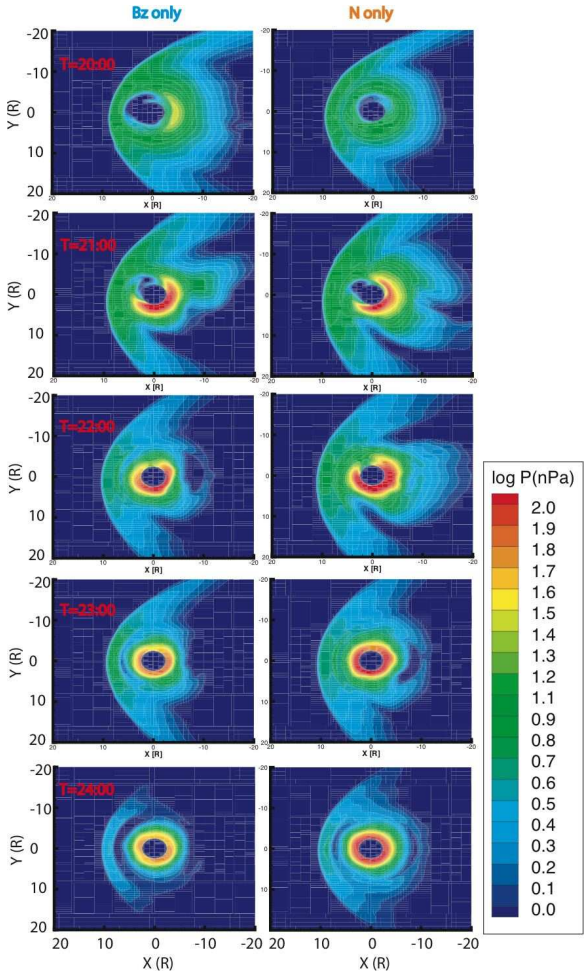

Figure 5.10: Pressure distribution in the X-Y plane for all simulation results. From left to right, each column corresponds to a case study: B_z only and N only 180 minutes running averages of input parameters. From top to bottom, we present snapshots of the pressure on a logarithmic scale at five times during the event: 20:00 -24:00 UT on September 22, 1999

01:00 UT) is well reproduced by our model, a feature that is lost when the input is smoothed with a window of three hours. In this case the magnetic field topology changes greatly, revealing a magnetic field that is less stretched, which in turn is correlated to a weaker ring current. For both simulated cases, B_x is underestimated during the late main phase and early recovery phase, while the other two components of magnetic field vector are overestimated.

Similarly to Figure 5.11, Figure 5.12 shows the magnetic field results for the GOES10 satellite. In this case too, the spacecraft was located on the dayside during

the storm peak. A sharp drop in B_z is observed in the GOES10 data at about 20:00 UT that is very well replicated in our 4 minutes resolution simulation, while the coarser input data fails to completely capture this feature. Similarly, the large scale features of B_y are considerably better represented by the high resolution run. The X component of the magnetic field is again underestimated during the main phase of the storm and even the large scale features are not well represented for both cases. This is because the satellite is popping in and out of the magnetosphere, while the simulated satellite is staying inside the magnetosphere after 21:30 UT.

At 20:00 UT GOES10 goes out of the magnetosphere. In the 4 minute run, this sudden compression of the magnetosphere is well modeled, while in the 3 hour run the satellite comes close to the magnetopause but never crosses it.

We note that considerably reducing the energy input into the magnetosphere by removing the transient spikes in the solar wind also has the effect of changing the magnetic field topology, as is evidenced by the comparison with GOES satellite data. This, in turn, alters the particle energies and trajectories while influencing the particle loss rate.

5.6 Comparison with an empirical model

The geomagnetic effectiveness of the solar wind is a complex problem. Predicting the inner magnetosphere response, i.e., of the D_{st} index, from the solar wind parameters has been extensively investigated and it is usually done by assuming the energy input rate is countered by an empirical ring current loss rate. Most of the energy input functions are dependent on the southward component of the IMF and the solar wind velocity. One such global energy balance model is that of *O'Brien and McPherron* (2000), who determined an empirical expression for the D_{st} index, relating the evolution of this geophysical activity parameter to the solar wind,

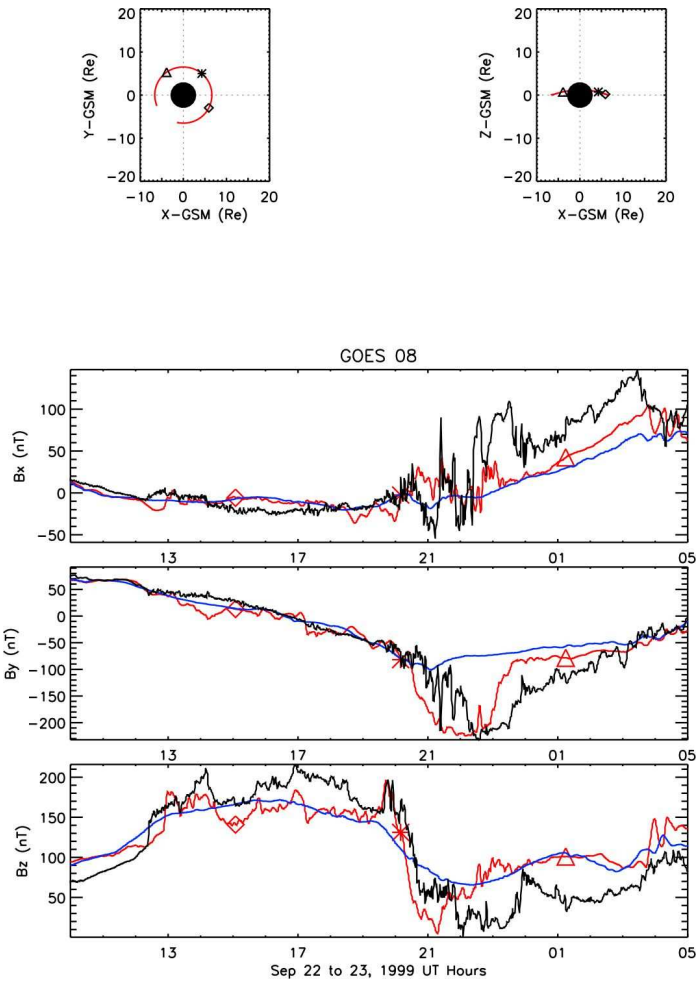

Figure 5.11: Magnetic field components at the GOES 08 satellite. Top 2 panels show the satellite trajectory, while the bottom 3 show each component of the magnetic field in nT. Each colored line corresponds to a different simulation results using different time resolution input data: 4 minutes (red line), 180 min (blue line). Black line shows the observations.

$$\frac{\mathrm{d}D^*_{st}}{\mathrm{d}t} = Q(t) - \frac{D^*_{st}(t)}{\tau}, \tag{5.6}$$

where τ represents the decay time of the ring current and is a function of the interplanetary electric field

$$\tau = 2.4 * \exp 9.74/(4.69 - (v_x \cdot B_z) \tag{5.7}$$

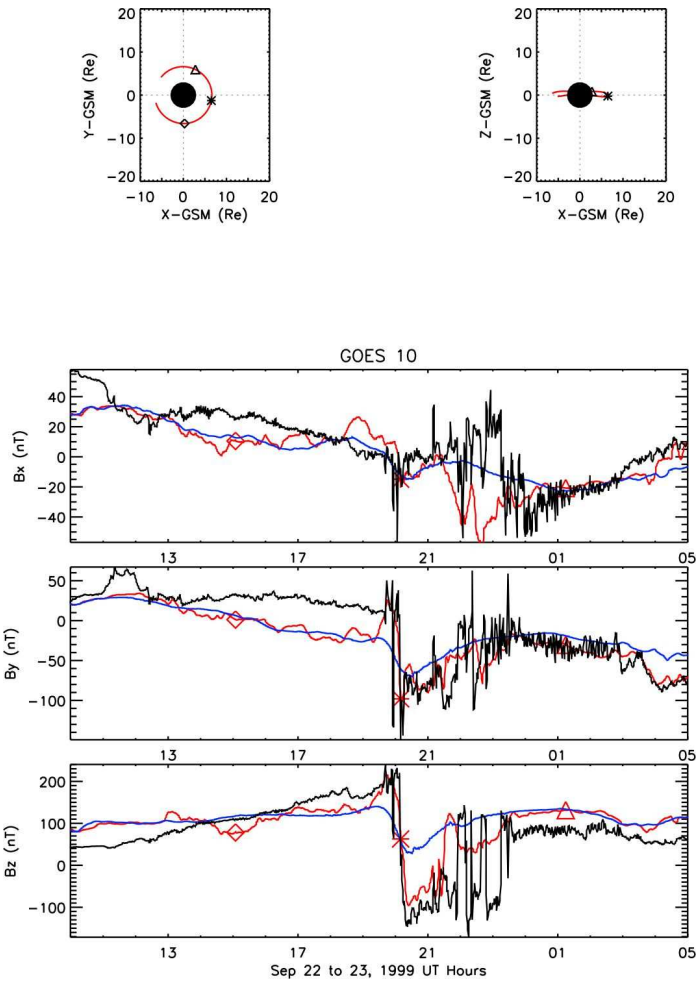

Figure 5.12: Magnetic field components at the GOES 10 satellite. Top 2 panels show the satellite trajectory, while the bottom 3 show each component of the magnetic field in nT. Each colored line corresponds to a different simulation results using different time resolution input data: 4 minutes (red line), 180 min (blue line). Black line shows the observations.

only for negative B_z. The injection function Q is a linear function of the interplanetary electric field:

$$Q(nT/h) = \begin{cases} \alpha(E^*_{y,sw} - E_c) & \text{if } E^*_{y,sw} > E_c \\ 0 & \text{if } E^*_{y,sw} < E_c, \end{cases}$$

where $\alpha = -4.4\ nT/h(mV/m)^{-1}$, $E_c = 0.49\ mV/m$. $E^*_{y,sw}$ represents the energy input function and depends on the strength and the direction of the interplanetary magnetic field and the X component of the solar wind velocity. The contribution

of the ring current, that is D^*_{st}, is calculated by removing from the D_{st} index the contributions from the magnetopause current along with the diamagnetic effects:

$$D^*_{st} = D_{st} - 7.26\sqrt{P_{sw}} + 11nT, \tag{5.8}$$

where P_{sw} represents the solar wind dynamic pressure in nPa. We use this formulation to investigate how well the physics of the storm is represented in our model relative to the empirically based predictions of ${D_{st}}^*$ for this event, for all the solar wind inputs.

Figure 5.13 shows the D_{st} index predicted by the *O'Brien and McPherron* (2000) empirical formulae (Equation 5.6). The colored lines show the predicted D_{st} profile using the 4 different temporal resolution inputs: 4 minutes (red), 60 minutes (purple), 120 minutes (green), and 180 minutes (blue). The black dashed line shows the observed 1 hour resolution D_{st} while the black continuous line corresponds to the measured 1 minute temporal resolution SYM-H index. For this event, minimum D_{st} reached -178 nT, while the SYM-H minimum value was -166 nT. The predicted D_{st} profiles show a linear trend, that is, less solar wind energy input produces less geomagnetic disturbance. The main phase of the storm is quite well reproduced, although the predicted D_{st} shows a lower injection rate compared to the observed profile. Nevertheless, the start time of D_{st} enhancement is well captured in the empirical model results. We see that the observed recovery phase of the ring current is slightly faster than predicted by the *O'Brien and McPherron* (2000) model. We note that the rate of the drop in the predicted D_{st} is increasing with increasing energy input and the 4 minutes input data predicts a rate of ring current injection closest to the observations. Since the injection function Q as described by *O'Brien and McPherron* (2000) is a linear function of E_y, therefore limited to only v_x and IMF B_z (Equation 5.2), it is possible that it is underestimated, which might lead to an underestimation of the ring current build-up and therefore an underpredicted D_{st} .

In the same style as Figure 5.13, Figure 5.14 shows empirical model D_{st} results

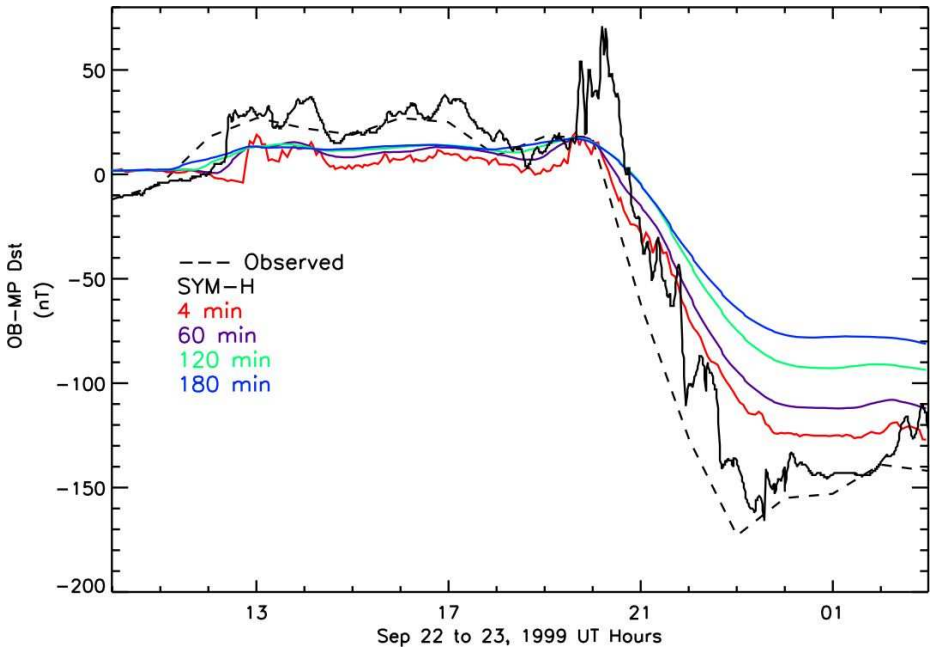

Figure 5.13: Empirical predictions of D_{st} index results for all averaged inputs for the September 22, 1999 magnetic storm. Each colored line corresponds to a different time resolution input data: 4 minutes (red line), 60 minutes (purple line), 120 minutes (green line), 180 min (blue line). Black dashed represents the observed D_{st} while the black continuous line show the observed SYM-H index.

with two additional smoothed inputs: 3 hour averaged B_z-only (light blue) and density only (orange) along with the 4 min (red) and 180 minutes (dark blue) all-input averaged calculations. As expected, there are no notable differences between the red and orange lines or the light and dark blue lines. That is due to the fact that the predicted D_{st} only depends on density via the pressure correction term. The small scale variability in the predicted D_{st} is due to the different time resolution of the inputs.

While the D_{st} index is a direct measure of the disturbance in the geomagnetic field produced by near Earth currents (in particular, the ring current), it is also a good indication of the total kinetic energy of the particles that contribute to this current (*Dessler and Parker*, 1959; *Sckopke*, 1966). Therefore, assessing the relationship between the solar wind energy input and the D_{st} index is well suited for this study.

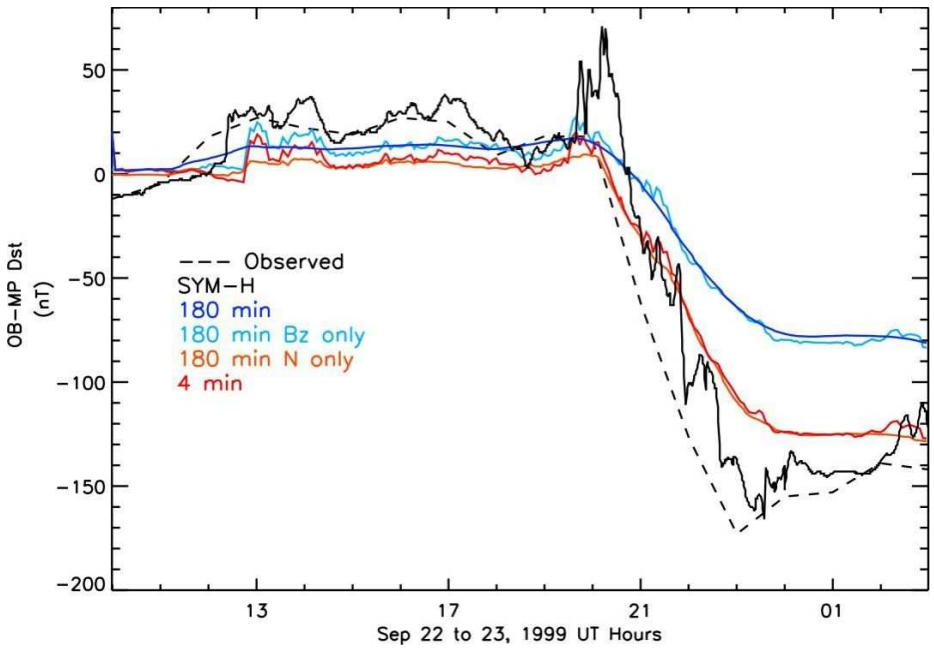

Figure 5.14: Empirical predicted of the D_{st} index results for averaged inputs for the September 22, 1999 magnetic storm. Each colored line corresponds to a different time resolution input data: 4 minutes (red line), 180 min (dark blue line), 180 min smoothed - B_z - only (light blue line), 180 min smoothed-density-only (orange line). Black dashed represents the observed D_{st} while the black continuous line show the observed SYM-H index.

Figure 5.15 presents the minimum D_{st} index, both predicted from the *O'Brien and McPherron* (2000) equations (red line) and simulated from the SWMF (black line) as a function of the energy input (as defined in Equation 5.2). Red triangles represent the predicted value of D_{st} using solar wind input for which only one variable is smoothed (i.e., B_z and density, as described above), while the black diamonds show the complementary simulated results. We note that the empirically predicted D_{st} index shows a linear dependence on the energy input into the magnetosphere, while the simulated D_{st} index appears to be non-linearly correlated with the energy input.

To illustrate this linearity and non-linearity, Figure 5.16 is a repeat of Figure 5.15 but with the X axis extending to zero. The two dashed lines connect the smallest D_{st} value with the origin of the plot. If the empirical (linear) models are propagated back to zero energy input, it is clear that if any energy is added to the system at all,

the D_{st} will respond. In the simulations, as Figure 5.16 illustrates, this is not the case; some threshold amount of energy must be put into the system before there will be any response at all. Further, the global simulations show that if too much energy is added into the system, the D_{st} won't respond either, implying a saturation effect. A possible saturation limit is seen at about 100 kVs/m in the profile of the SWMF simulated D_{st} index for this event.

This non-linear relationship indicates the existence of an internal feedback mechanism that limits the energy flow in the magnetosphere. One possibility is that the outer magnetosphere is acting as a low-pass filter on the oscillations in the upstream solar wind conditions. Magnetic merging on the dayside does not instantly influence convection within the near-Earth tail, but rather there is a significant time delay as the field lines are convected tail-ward and reconnect on the nightside. In a forthcoming study by A. J. Ridley [manuscript in preparation], the SWMF shows a clear decoupling between IMF fluctuations and geospace responses (such as D_{st} and CPCP) for oscillations of less than 30 minutes. This is fairly consistent with the findings of this real-event study, which show that the input power from oscillations of less than 1 hour do not significantly change the resulting D_{st} time series.

5.7 Summary and Conclusions

The September 22, 1999 ICME driven magnetic storm was simulated using the Space Weather Modeling Framework. ACE satellite measurements were used as the upstream boundary conditions. Analysis of the simulated storm focused on the assessment of the role the transient spikes in the solar wind parameters play in the development of the storm. To accomplish this, we reduced the energy input into the magnetosphere by smoothing all solar wind parameters in the input data with windows of 1, 2 and 3 hours. Moreover, just smoothing selective parameters (i.e., IMF B_z and density) allowed us to quantify the role each of them played in the en-

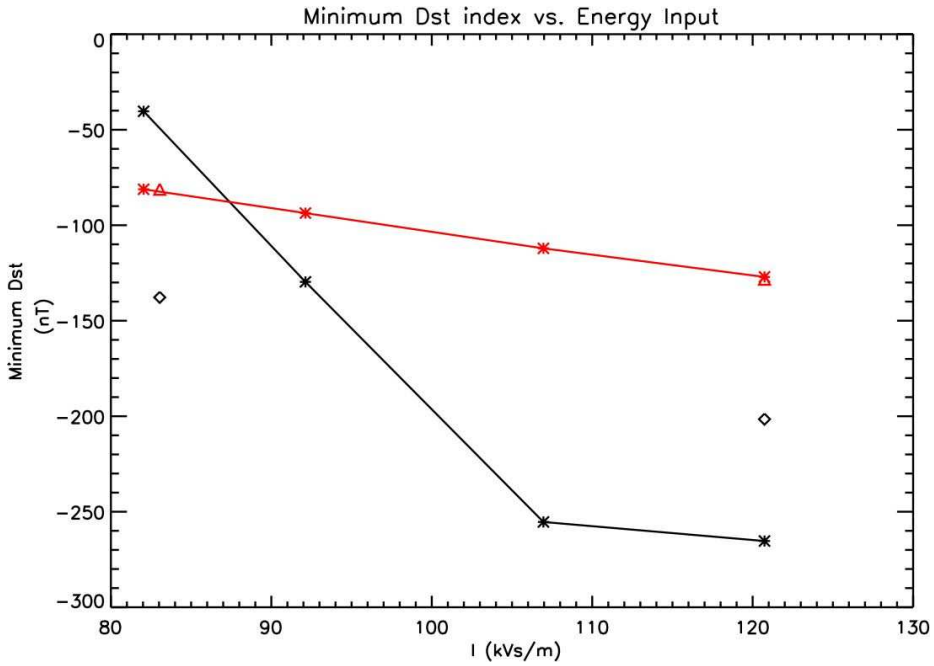

Figure 5.15: Minimum D_{st} vs. Energy Input. Red line shows the empirical D_{st} prediction results while the black line shows simulation results using SWMF. The red triangles (black diamonds) show the 3 hours smoothing of B_z and density using the empirical D_{st} prediction model (MHD simulation).

hancement of the ring current. The results of the simulations were compared against ground-based and satellite-based observations.

Our model produces a two-phase, fast and then slow, recovery phase, in spite of the one phase recovery of the observed event. The fast recovery observed in the simulation results occurs when the actual D_{st} is still decreasing, while the simulated slow recovery matches the observed timing and slope. A large cross polar cap potential combined with a low plasma sheet density is most likely responsible for the rapid initial decay of the ring current, similar to the results of *Liemohn et al.* (1999).

Empirical prediction of the D_{st} index not only shows a linear relationship with the energy input, but also reveals a one phase recovery D_{st} profile. This is to be expected, since the formulation depends linearly on the solar wind parameters. On the other hand, *Feldstein* (1992) suggests that a nonlinear relationship between the energy input and D_{st} is necessary to better predict the growth and decay of the ring

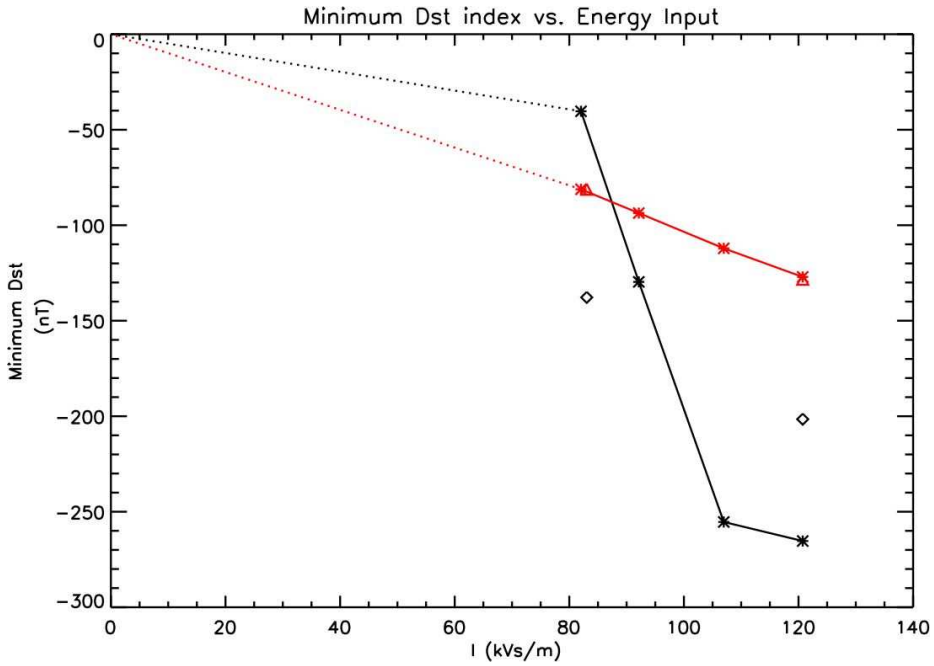

Figure 5.16: Same as Figure 5.15 except with a different x-axis scale (going down to zero).

current.

When reducing the energy input more than 13 % (that is, smoothing the input with a window larger than 60 minutes), a weaker ring current forms, therefore a less intense storm develops. In the same time, the 4 and 60 minute smoothed upstream input data produces an overshoot in the estimation of the D_{st} index. This is can be due to the too dense and too cold plasma sheet the MHD model produces.

Nevertheless, averaging up to 60 minutes changes the plasma sheet variation as well as the entire magnetosphere and reduces the plasma sheet density and pressure. Small scale variations of the electric and magnetic field alter the inner magnetosphere energy density, while rapid small scale variations produce a more dynamic tail.

Since the plasma sheet is the source region of the ring current particles, changes in its density have a great impact on ring current intensifications. The sudden decay of the plasma sheet particle population along with the weakening of the convection electric field due to changes in the Z component of the interplanetary magnetic field

account for the slow recovery phase.

The reconnection rate (modulated by IMF B_z) at the dayside magnetopause controls the ionospheric outflow of particles that will populate the inner magnetosphere. Even though our simulation results indicate no significant differences for CPCP in both hemispheres, for all cases studied, the sharp drop in the midnight plasma sheet density seems to be responsible for the shut down of the fast early recovery. Because our simulations do not explicitly include charge exchange processes, we attribute the late slow decay recovery to the fact that the source region of ring current particles is completely depleted.

Comparison with GOES08 and GOES10 magnetic field measurements indicates that varying the energy input produces variations in the magnetic field topology and strength, which in turn modifies the particle orbit, inducing new loss processes. The reduced energy input runs reveal a magnetic field that is less stretched with a weaker ring current.

Our global simulation results based on this storm in September of 1999 indicate that changes in the energy input change the response of the magnetosphere in a non-linear manner, as opposed to the linear relationship the empirical model predicts. Our results indicate that a threshold in the energy input is necessary for a ring current to intensify, while the short time fluctuations in the solar wind parameters did not have a significant contribution. On the other hand, while initial increases in the energy input enhance the magnetospheric response, we observe that a saturation limit is reached as the power transferred to the system is increased and the growth of ring current is stalled. This implies that not only ion drift loss to the dayside magnetopause is the main loss mechanisms that removes the ring current particles during the early recovery phase, but also the existence of an internal feedback mechanism as the magnetosphere acts as a low-pass filter on the interplanetary magnetic field, that limits the energy flow in the magnetosphere.

CHAPTER VI

Transfer of IMF B_z fluctuation periodicity to the magnetosphere

6.1 Motivation

The orientation and intensity of the interplanetary magnetic field play a central role in the interaction between the solar wind and Earth's magnetosphere. The contribution of the southward component of IMF, whose geoeffectiveness is closely related to the effect of the solar wind electric field, is the most significant among the contributions from all other solar wind parameters such as bulk velocity, density, temperature, and magnetic field strength (*Burton et al.*, 1975; *Akasofu*, 1983; *Baker et al.*, 1981). Solar wind-magnetosphere interaction highly evolves with time and the parameters associated with it often exhibit a variety of transient and periodic fluctuations. The different origins of the solar wind streams and the conditions of their propagation in the interplanetary medium lead to different variations in the solar wind and IMF parameters. Furthermore, variations in the B_z component for different types of the solar wind conditions are different from one another regarding the duration of fluctuation periods and as well as their intensities (*Tsurutani et al.*, 1988).

High-speed stream type events are common during the declining phase of solar cycles and their prominent feature is the wavy fluctuations of the IMF. These fluc-

tuations have large amplitudes during periods of high-speed solar wind (*Tsurutani et al.*, 1995; *Diego et al.*, 2005). Usually during high speed streams, the B_z varies in the form of fluctuations about a zero level, has a period of $\sim$ 60 minutes, and average fluctuation amplitudes of 5 to 6 nT (*Hviuzova et al.*, 2007). Typically, the wave amplitude is largest during the early stage of the streams when the solar wind velocity is increasing, due to the compression of the magnetic field magnitude and the amplification of the waves from stream-stream interactions (e.g. *Pizzo*, 1985; *Tsurutani et al.*, 1995). Conversely, the wave amplitude becomes smaller as the solar wind speed decreases to nominal values.

These Alfvén wave intervals are modestly geoeffective, in the sense that the D_{st} index is disturbed but seldom goes below -50 nT. The origin of the large amplitude Alfvén waves is uncertain, but it has been suggested that they may be locally generated from stream-stream interaction effects or amplified Alfvén waves originating from the coronal hole. *Tsurutani and Gonzalez* (1987) reported on the existence of such Alfvén wave trains that propagate outward from the sun, typically in the trailing portion of high-speed streams.

As opposed to CME driven storms, during CIR driven events, due to the fluctuating nature of the IMF B_z, the reconnection intervals are short and intermittent, leading to sporadic injection of particles into the magnetosphere (*Tsurutani et al.*, 2005). On account of their long duration, these events can transfer considerable amounts of solar wind energy to the Earth's magnetosphere (e.g. *Turner et al.*, 2006; *Lu*, 2006).

In this study, we investigate the geoeffectiveness of IMF B_z fluctuation periodicities during a Corotating Interaction Region driven event (November 10th, 2003) and focus on the high speed stream part of it. Moreover, we examine the role of IMF B_z fluctuation periodicity in the transfer of solar wind mass and energy to the magnetosphere. We will assess the response of the magnetosphere through global

magnetosphere simulations within Space Weather Modeling Framework, using both spacecraft observations and idealized input as upstream boundary conditions.

6.2 Real Event Simulation: Results and Discussion

We study the geomagnetic activity during the event of November 10-12, 2003, a magnetic storm triggered by a classic CIR, representative for this type of solar wind driver. During this time a moderate disturbance of the geomagnetic field was observed with a recorded minimum D_{st} index of $-78\ nT$ and $SYM-H$ index of -67 nT. Solar wind observations from the ACE satellite, orbiting around the Lagrange 1 point on the Sun-Earth line, were used as solar wind upstream boundary conditions for the SWMF simulation. Using the Minimum Variance Analysis method (*Weimer et al.*, 2003; *Weimer*, 2004), data is propagated from the satellite location to (32, 0, 0) R_e in the GSM coordinate system, where X is the direction from the Earth to the Sun. The setup of the simulation is described in Section 3.1.4. Figure 6.1 shows solar wind plasma and interplanetary magnetic field parameters for this event.

A compression in the plasma and magnetic field is seen around 06:00 UT on the first day, when the particle density increases from 6 cm^{-3} to almost double its value. This magnetically compressed region is the Corotating Interaction Region, although its temporal delimitations are not well defined. The IMF B_z fluctuations are largest within the CIR, with frequent northward/southward turnings, with large negative B_z component of the IMF reaching peak values of $-15\ nT$. It has been suggested that the highly fluctuating Z component of the magnetic field in the CIR region is the main parameter responsible for the induced disturbance in the geomagnetic field and the subsequent development of the storm main phase (*Tsurutani et al.*, 1995). For this particular storm, the observed minimum D_{st} occurs outside the CIR region, at about 12:00 UT on November 11th (see Figure 6.2). The High Speed Stream region extends from approximately 06:00 UT on November 11th to beyond November 13th,

when the magnitude of the X component of the solar wind velocity ramps up from $\sim$ 450 km/s to about $\sim$ 700 km/s. During this time the particle density is quite steady with a value of $\sim$ 4 cm^{-3}. The Y component of the electric field is highly fluctuating due to the excessive variability of the IMF B_z, with higher values in the CIR region than in the high speed stream. Even though the velocity is elevated, the B_z values during the stream passage do not exceed 5 nT in magnitude.

The temperature is slowly increasing at the beginning of the interval and remains elevated at approximately 2×10^5 K during the high speed stream. The X component of the solar wind velocity v_x is steady, showing very little temporal variation during the stream passage. The B_y component is roughly positive during the whole time interval except at the beginning of November 11th, when it rotates and changes sign for a period of about 3 hours, while the B_x component is mainly negative during this time.

6.2.1 D_{st} Index and Cross Polar Cap Potential

The results of the global magnetosphere simulation of the November 10 - November 12, 2003 event, using the time shifted ACE observations as the upstream boundary conditions (run #1), are presented in Figure 6.2. The top panel shows Cross Polar Cap Potential (CPCP) model results (blue lines) against the ionospheric potentials from the Assimilative Mapping of Ionospheric Electrodynamics (AMIE) routine of *Richmond et al.* (1998) and *Ridley and Kihn* (2004). The 1 minute temporal resolution AMIE cross polar cap potential was obtained by running AMIE for the time interval of interest, using only magnetometer data from about 128 stations. We note that the simulated CPCP follows closely the observationally based potential obtained from AMIE (black line) in the northern hemisphere, throughout the whole period, although the global simulation overestimates the values of the CPCP. We note the elevated transpolar potential during the main phase of the storm, i.e. during the CIR

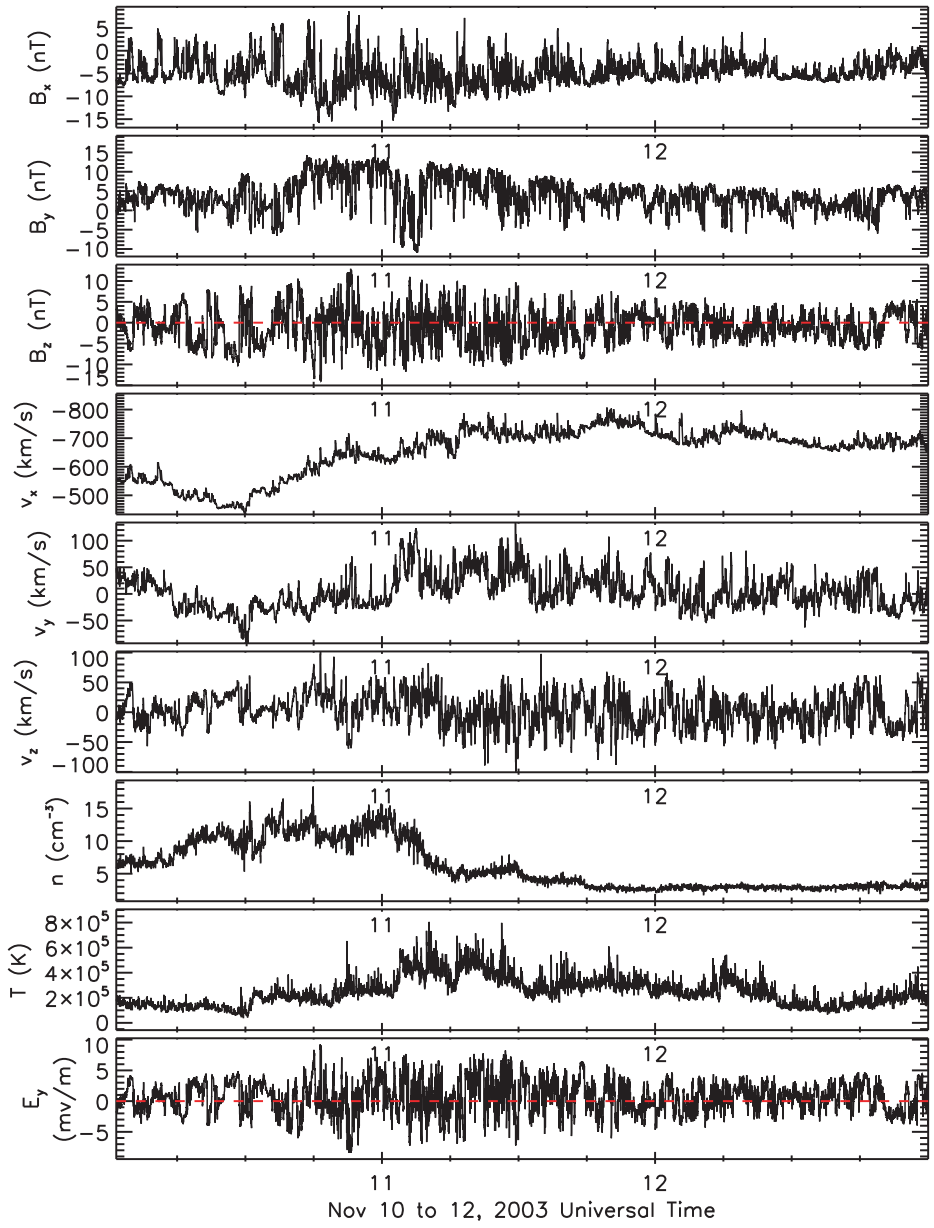

Figure 6.1: ACE observations with a temporal resolution of 4 minutes for the November 10, 2003 event. From top to bottom are presented the input parameters: B_x (nT), B_y (nT), B_z (nT), v_x (km/s), v_y (km/s), v_z (km/s), density (cm^{-3}), temperature T (K) and eastward component of the electric field E_y (mV/m), where $E_y = v_x \cdot B_z$. A horizontal dashed red line is drawn at zero in the B_z and E_y panels to better identify northward/southward turnings.

passage, when the convection electric field is high. During the stream, both the AMIE and SWMF potential show a decrease, due to decreased E_y (decrease in magnitude of the southward component of IMF).

The bottom panel of Figure 6.2 presents the D_{st} index in the same format as above. The modeled D_{st} index (blue line) is calculated by solving the Biot-Savart integral for all the electric currents encompassed by the BATS-R-US simulation domain from the inner boundary outward, and taking the magnetic field disturbance along the Z axis at the origin of the coordinate system. The comparison with the observed indices provides us with a measure of the ability of the model to accurately reproduce the inner magnetospheric response. Note that the observed D_{st} index (black dashed line) is underestimated but the overall trend is captured by the global simulation. Also, there are some discrepancies between the observed Sym-H and D_{st} profiles as well, sometimes showing greater differences than those between the simulated D_{st} and observed Sym-H. To quantify the SWMF performance we use the correlation coefficient and normalized root-mean-squared error (nRMSE) (Equation 6.1 described below) between the modeled D_{st} and the observed D_{st} and Sym-H,

$$nRMSE = \sqrt{\frac{\sum_{i}^{n} (x_i - y_i)^2}{\sum_{i}^{n} x_i^2}} \tag{6.1}$$

where x is the measured value, y is the simulated value, and n is the number of data-model pairs used in the calculation. nRMSE ranges from 0 (model is perfect agreement with the observations) to 1, and a value of 1 indicates that the simulation results are within ± 1 of the measured values means. However, this value can be misleading, therefore the nRMSE values must be paired with the correlation coefficient for a proper interpretation of these statistics. Table 6.1 shows these values for both data-data and data-model comparisons.

Note that for all the data-model comparisons the nRMSE scores are well below 1,

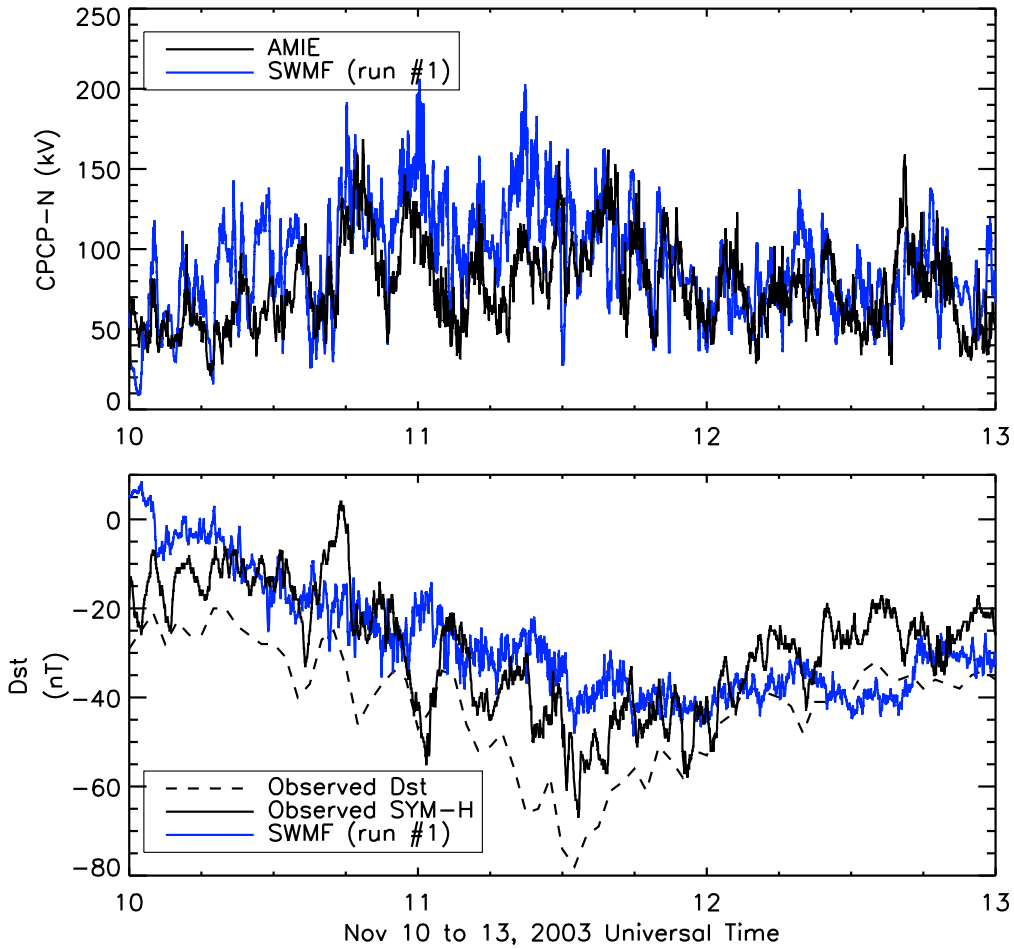

Figure 6.2: D_{st} and CPCP simulation results. Top panel: CPCP (kV). The blue line shows the SWMF simulation results using real data as upstream boundary conditions, while the black line shows the AMIE values. Bottom panel: D_{st}. Again the blue line shows the SWMF real data input simulation results, while the black continuous line shows the 1 minute resolution SYM-H (nT) and the black dashed line displays the 1 hour temporal resolution D_{st} (nT) values.

x	y	nRMSE	Correlation Coefficient
Sym-H	modeled D_{st}	0.36	0.62
D_{st}	modeled D_{st}	0.41	0.61
AMIE CPCPn	modeled CPCPn	0.40	0.51
Sym-H	D_{st}	0.44	0.88

Table 6.1: Normalized root-mean-square-error (nRMSE) and correlation coefficients between the values of observed geomagnetic indices and the corresponding simulation results.

indicating that the model results are closer to the observed values for the corresponding parameters, than the average magnitude of the observations. When comparing the two observationally based indices, D_{st} and SYM-H, the nRMSE has the highest value from all the comparison pairs. However the correlation coefficient, which is a measures of how well the two sample populations vary together, is the highest too. The discrepancies between the two observed geomagnetic indices are due to the fact that even though both indices are designed to measure the disturbance in the equatorial horizontal component of the geomagnetic field, they are are calculated based on slightly different methods of baseline subtraction as well as they are based on observations from different ground stations. The correlations coefficients are all greater than 0.6, except for the modeled CPCP- AMIE potential pair, indicating that the model is reasonably well capturing the trend within the observations. Although the CPCP comparison shows the lowest nRMSE, the correlation coefficient indicates the least correlation between these two quantity. However, this is due to the highly varying potential and if the data is smoothed by applying a running average with a window of 1 hour, the correlation coefficient increases to $\sim$0.7. Therefore, the global magnetospheric model reproduces the observations reasonably well.

6.2.2 Mass Transport

The major sources for the ring current population are ionospheric outflow and the injection of plasma sheet particles into the inner magnetosphere. Convection electric fields accelerate the plasma sheet particles as they move closer to the Earth and then gradient curvature drifts move the particles around the Earth, forming the ring current. We investigate the contribution of the plasma sheet density on the energization of the ring current by including 24 virtual satellites in the simulations. These satellites are located one hour of local time apart at geosynchronous orbit. Plasma and field information from BATS-R-US is extracted at their location.

Figure 6.3 displays the mass flux through the geosynchronous orbit ring. The top panel shows the average flux crossing geosynchronous orbit, and the next two panels separate this net mass flux into its positive (inward) and negative (outward) components (middle and bottom panels, respectively). The average flux was calculated as the mean of all particle fluxes across geosynchronous orbit, while the inward (outward) flux was calculated as the average of all positive (negative) mass fluxes across the geosynchronous orbit.

During the main phase of the storm, we note a large increase in the average particle flux corresponding to injection of particles from the plasma sheet as seen in the middle panel as well. We also note the 'sine wave'-like shape of the average flux, corresponding to inflow then outflow of plasma crossing this boundary.

6.2.3 Periodicity

Hviuzova et al. (2007) suggests that typically, during CIR driven events, the fluctuations in the IMF B_z about a zero level have a periodicity of ~ 60 minutes, with an average fluctuation amplitude of $\sim 5\ nT$. Therefore, for studying periodicities and scaling properties of the input versus the system response, we have used a standard Fourier Transformation (FT) procedure for the Z component of the interplanetary field, the observed SYM-H index, the AMIE derived transpolar potential and the modeled D_{st} from run #1, with a sampling time of 3 days (November 10 - 12, 2003). The results are presented in Figure 6.4. The power spectrum of the IMF B_z (Figure 6.4, top row) reveals that the power is distributed over all frequencies, and lacks any apparent spike that would indicate a preferential frequency as suggested by *Hviuzova et al.* (2007). In addition, the power spectrum of SYM-H shows no indication of one hour periodicity and most of the power is distributed among all frequencies. However, it displays a peak corresponding to a ~ 5 hours periodicity, but the power contained at this frequency is relatively low compared to the background. Similarly

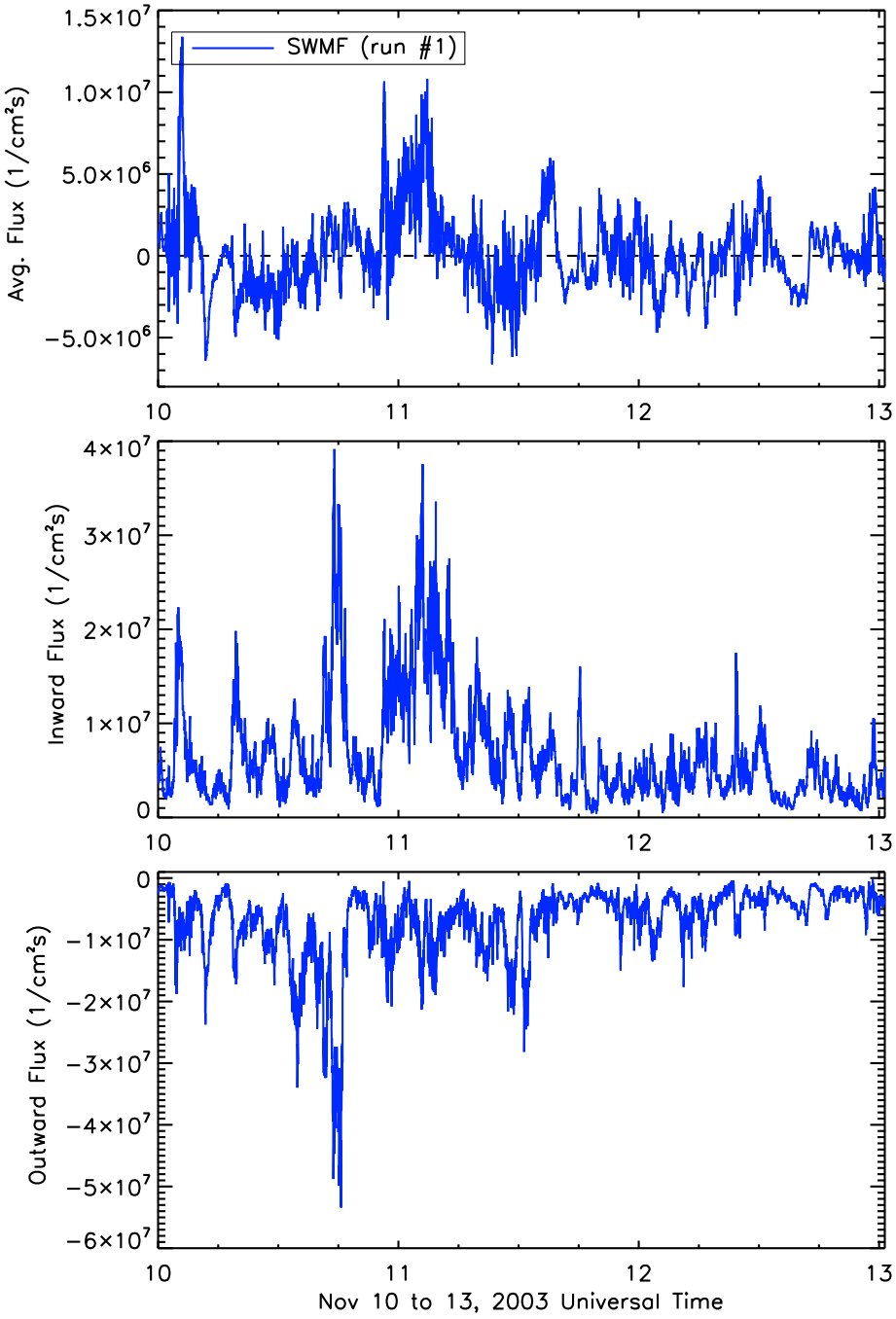

Figure 6.3: Simulation results for mass transport through the geosynchronous orbit ring. As previously described, blue lines indicate simulation results using the time shifted ACE data as input parameters. From top to bottom we present the average flux, inward flux, and the outward flux through the 6.6 R_e geocentric distance ring into the equatorial plane, expressed in units of $1/cm^2s$.

to the SYM-H index spectral power of CPCP suggests the existence of a ~ 5 hours periodicity but there is no indication of a 60 minutes periodicity. On the bottom two rows we present the modeled D_{st} and CPCPn results (run #1) and for these parameter too, the power is distributed over all frequencies showing no large peak at any frequency.

Similarly to Figure 6.4, Figure 6.5 shows the same quantities and their associated power spectra, only this time the Fourier transform was applied for each quantity on the time domain corresponding to the last day of the simulation (November 12 to 13). Since the 3 day period spans over both the CIR and high speed stream, we choose to take a closer look at the HSS region (November 12 to 13). Fourier transform of the IMF B_z reveals a larger peak in the frequency (at 0.245 mHz), corresponding to a 68 minute periodicity of the fluctuations (vertical bashed blue line). However, the power of the signal contained at this frequency is low, only double the background noise level. Similarly, the power spectrum of the observed SYM-H index shows a peak at the same frequency but once again, the power of the signal is low and about twice as large as the background noise. This frequency/periodicity of the Z component of the interplanetary magnetic field is not yet picked up by the AMIE transpolar potential, although a small peak is present at this frequency in the power spectrum of the CPCP within the last day sampling time. This might be due to the fact that the AMIE potential is a derived quantity and not a direct measurement, therefore the time cadence and the power of the signal might have been affected by the data processing. However, the modeled D_{st} (bottom row, blue line) does not show a large peak at the 0.245 mHz frequency. Furthermore, the simulated CPCP and averaged mass flux across geosynchronous orbit also show no periodicity, therefore the periodicity in the input (however weak) is not seen in the modeled magnetospheric response.

Since the power of the signal (observed IMF B_z and SYM-H) contained at the 0.245 mHz frequency (corresponding to a 68 minute periodicity) is low, it is uncertain

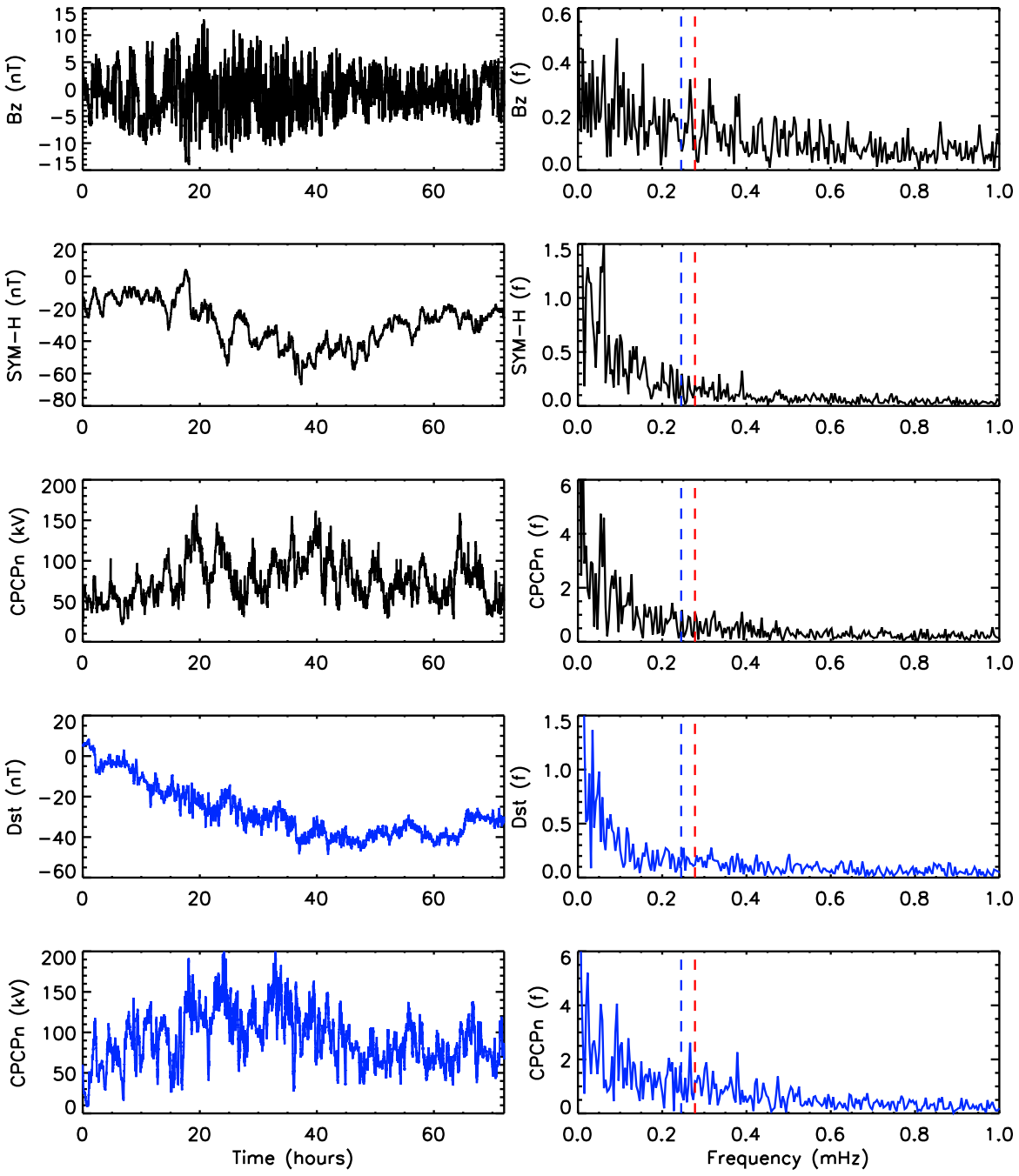

Figure 6.4: Power Spectra of the input versus system response. Left panels present from top to bottom the IMF B_z, Observed SYM-H index, northern hemisphere CPCP from AMIE, and the modeled D_{st} and CPCPn (run #1) for the November 10 -12 , 2003 time period. Panels on the right show their corresponding power spectra results for the specified time range. The red (blue) vertical dashed line shows the frequency corresponding to 60 (68) minute periodicity.

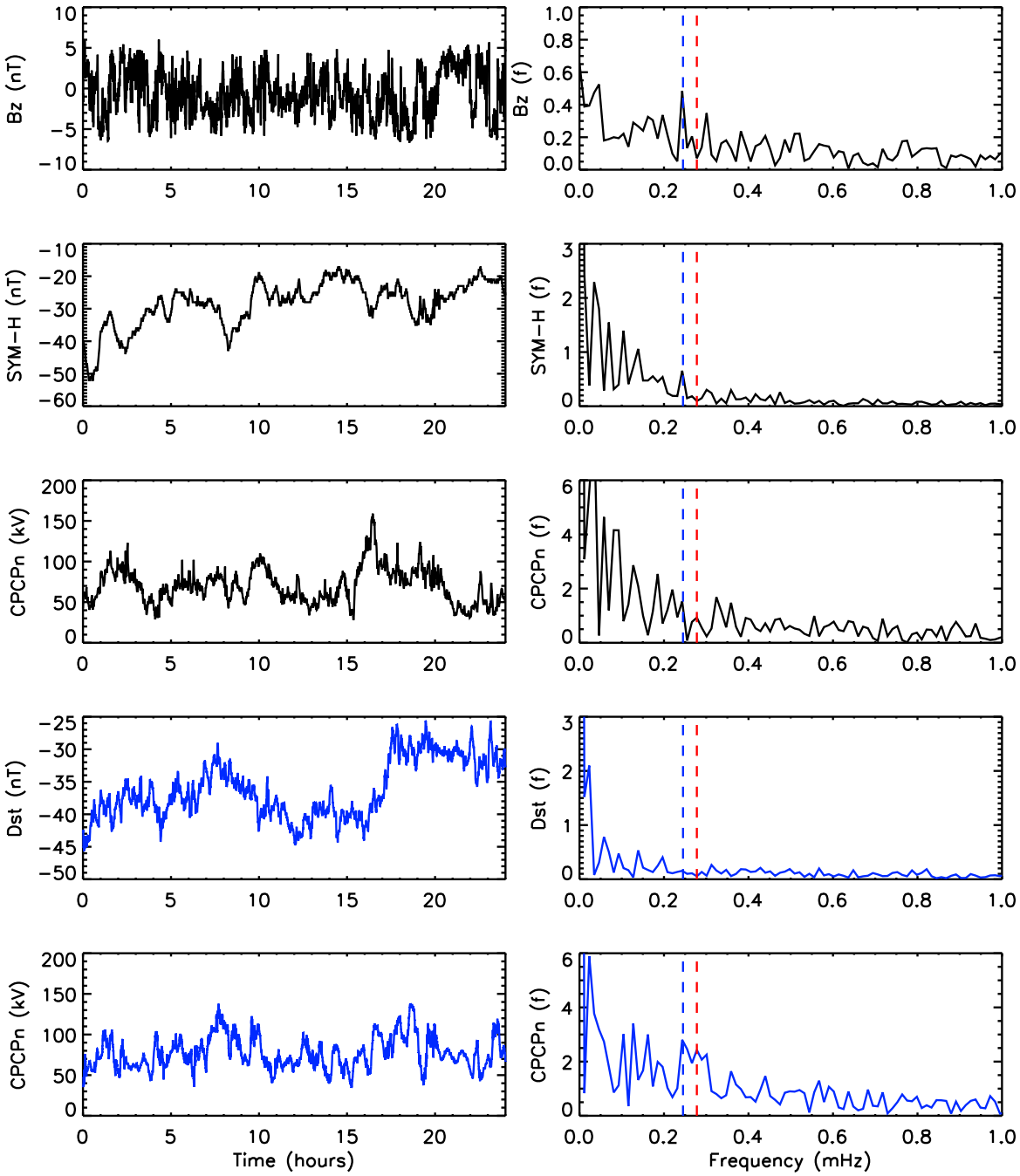

Figure 6.5: Similarly to Figure 6.4, only here the time period is the last day of the simulation, i.e. November 12, 2003.

if there is any correlation between the driver (IMF B_z) and the system response (SYM-H, CPCP) periodicities. The question is if the periodicity in the IMF B_z is not transmitted through the system (not really driving it) or is it just the model incapable to pick it up. To answer this question, we designed a simulation setup that involves idealized input as the upstream boundary conditions, and the results are described below.

6.3 Idealized Input Simulation 1: Results and Discussion

As an alternative scenario to the real measurements, we ran the code for two days using time shifted values of the ACE observations to 32 R_e as upstream boundary conditions, and on November 12, 2003, during the high speed stream period, we replaced the observationally based model input with an idealized version of it. Therefore, for run#2, the observed IMF B_z parameter was replaced by a simplified IMF B_z, a square wave for which the northward/southward turnings have a frequency of 1 hour and oscillates around the zero level from 5 nT to -5 nT. The periodicity choice, as well as the wave amplitude, were justified by *Hviuzova et al.* (2007) findings, as well as the observed periodicity in the real data (68 min), although the 1 hour periodic wave was selected for simplicity. In compliance with the observations during the HSS passage, all the other solar wind parameters were set as constants for simplicity. The X component of the solar wind velocity was set to v_x =$-$650 km/s, particle density n = 5.0 cm^{-3}, temperature $T = 2 \times 10^5$ K, while B_x , B_y , v_y , v_z were set to zero. A similar numerical study was carried out by *Gonzalez et al.* (2006) also using MHD simulations. The IMF B_z was set as a 40 minute periodic square wave with an amplitude alternating between -5 nT and 5 nT, and a constant solar wind speed of 600 km/s and density of 5 cm^{-3}. Their study shows that the response of pressure, eastward component of the convection electric field, and the X component of the plasma velocity in the plasma sheet responds to the imposed variation of the

IMF B_z. However, the response is delayed by 15 min from the IMF B_z.

6.3.1 D_{st} Index and Cross Polar Cap Potential

Figure 6.6 shows the model results only the last day of the simulation, during the high speed stream, for both real (blue lines - run #1) and idealized (red lines - run #2) input, for the same parameters as in Figure 6.2. The modeled CPCP for this idealized input case does not resemble the AMIE derived potential (black line) or the one obtained using the real data as input. The transpolar potential starts increasing as soon as the B_z becomes negative and reaches a maximum at the end of the 30 minute time interval of southward IMF. When B_z becomes positive, the magnetosphere starts to relax and the CPCP begins to decrease.

The northward/southward varying B_z field of run #2 produces similar variations in the modeled D_{st} time series to that in the CPCP, showing that the ring current responds to the changes in the IMF B_z. In a similar way, a decrease (increase) in the B_z field produces an intensification (weakening) of the ring current. We also note that the real and idealized input simulations produce similar D_{st} profiles, in the sense that the modeled D_{st} profiles are within the same slope and average values.

Similarly to the *Gonzalez et al.* (2006) study, the global simulation results presented here also suggest that the magnetosphere's reaction to the step like change in the Z component of the IMF is $\sim$ 18 minutes delayed.

6.3.2 Mass transport

In the same manner as Figure 6.3, Figure 6.7 shows only the last day of the simulation, where again, the red line presents the model results for the idealized input case (run #2) while the blue lines correspond to the run #1 simulation results. Mass fluxes through the geosynchronous orbit display great variability with the periodicity of the northward/southward turnings in the IMF B_z, displaying sporadic injections

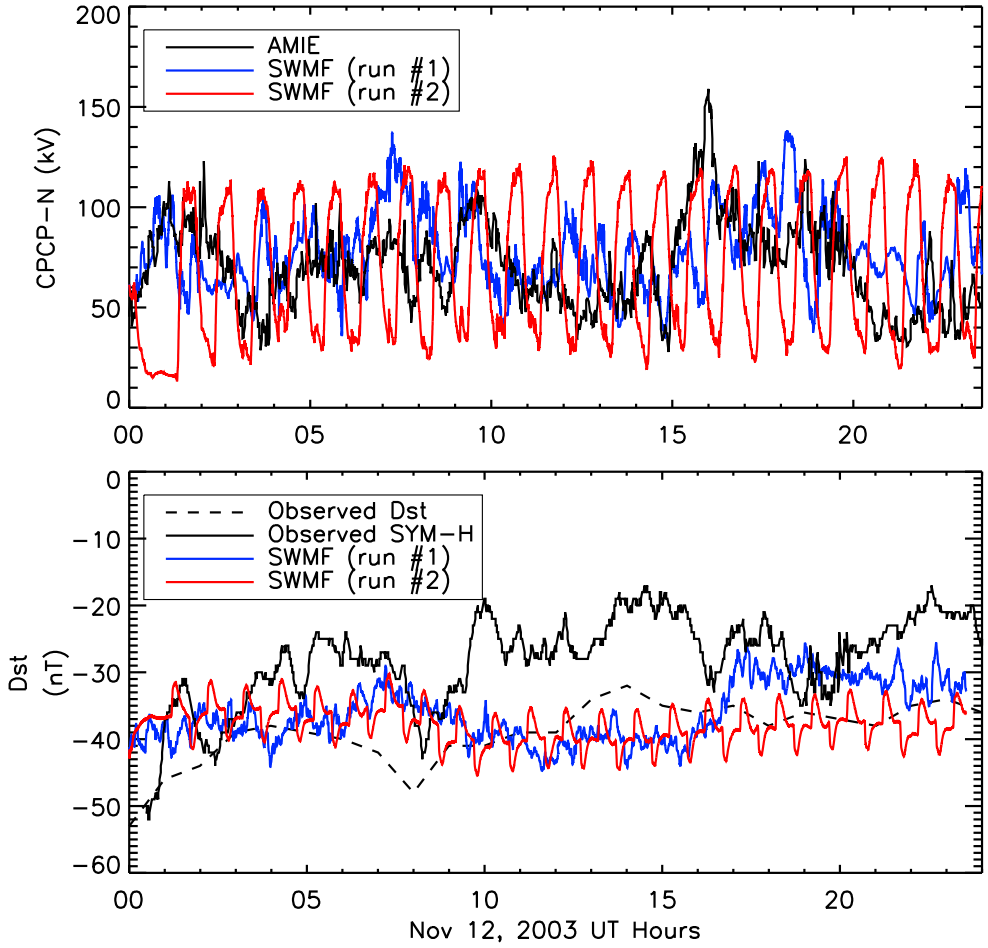

Figure 6.6: D_{st} and CPCP simulation results. Top panel: CPCP (kV). Blue line shows the SWMF simulation results using real data as upstream boundary conditions, red line denote the SWMF simulation results using idealized input parameters, while the black line shows the AMIE values. Bottom panel: D_{st}. Again the blue line shows the SWMF real data input simulation results, red line show the SWMF simulation results using idealized input parameters, while the black continuous line shows the 1 minute resolution SYM-H (nT) and the black dashed line represents the 1 hour temporal resolution D_{st} (nT) values.

into the inner magnetosphere that appear to be correlated with the variations in the IMF B_z amplitude. The trend between the two cases is similar, in both cases a decrease in the particle injection occurs in the afternoon interval of November 12th. We note that for the real input case, the decrease starts earlier (approx. 13:00 UT) than in the idealized input case (approx. 15:00 UT), but interestingly enough, the 'sine wave' like shape of the average flux is observed for both simulation cases. This might be due to some plasma sheet density internal feedback mechanism, captured even in the idealized input case.

6.3.3 Periodicity

The same Fourier transform technique is applied for the input parameters of run #2 as well as for the modeled D_{st}, transpolar potential, and inward and outward fluxes at geosynchronous orbit. The results are presented in Figure 6.8. For this case, the IMF B_z presents a strong peak at 60 minutes (how we designed this run), with a signal to noise ratio of about $\sim$10. Aside from the peak the the fundamental frequency (0.27 mHz), a new peak is seen at 0.92 mHz corresponding to a periodicity of 20 minutes. This is to be expected, since a square wave has the largest peak at the fundamental frequency and additional peaks at each odd harmonic of the fundamental frequency with a 25% reduction in the power contained at each of the subsequent frequencies. Therefore, the secondary peaks in the B_z power spectrum are just a consequence of the square wave profile of the input B_z.

However, this one hour periodicity in the northward/southward turning of the IMF B_z is reproduced in the magnetospheric response. The D_{st} index, transpolar potential, and mass flux, all show that the most of the signal power is contained at the 0.27 mHz frequency. The largest peak to noise ratio in the power is displayed by the cross polar cap potential ($\sim$9), while the same ratio for the modeled D_{st} and the inward/outward fluxes is of $\sim$6, $\sim$3 respectively. The peaks in the power

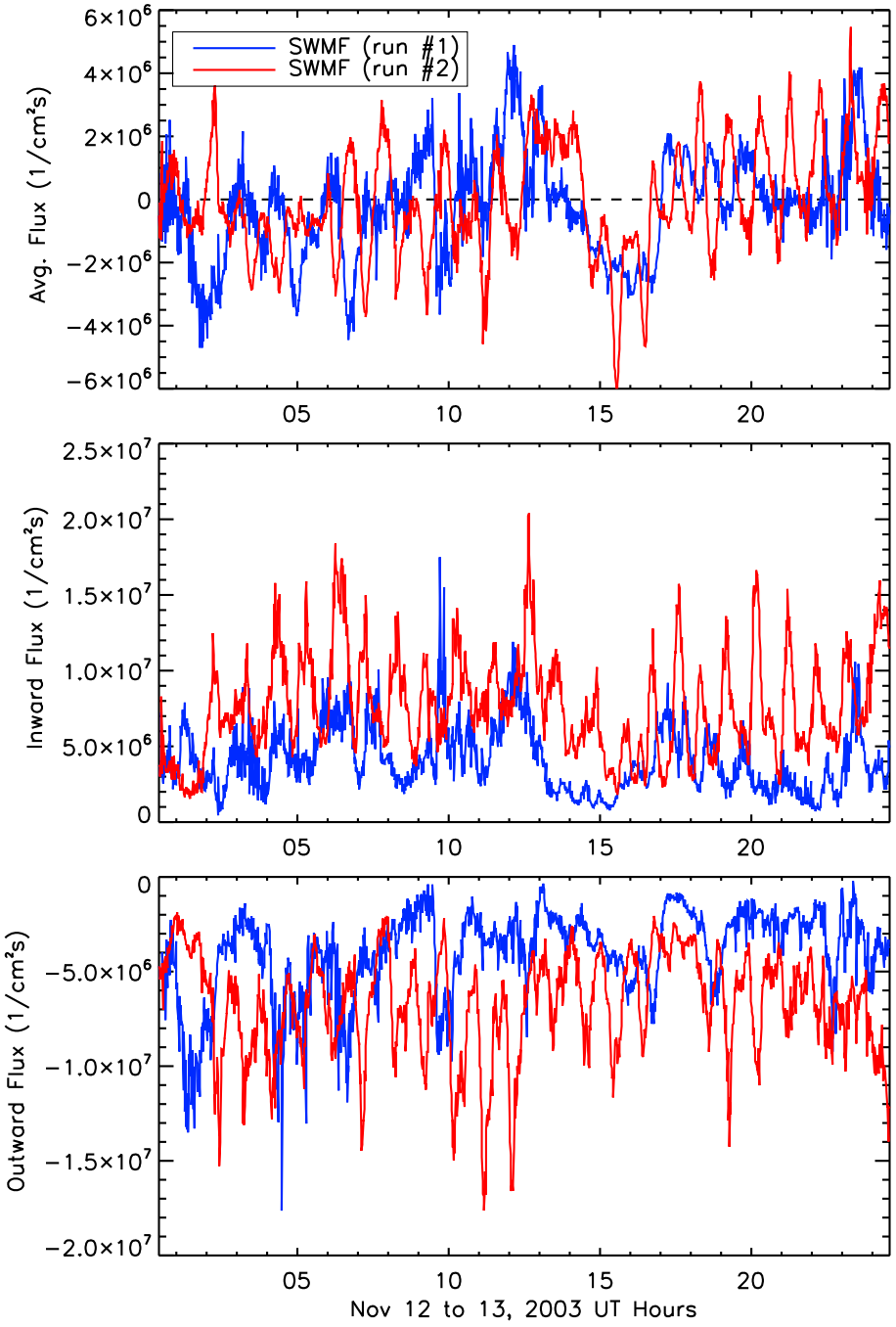

Figure 6.7: Simulation results for mass transport through the geosynchronous orbit ring. As previously described, blue lines indicate simulation results using the time shifted ACE data as input parameters while the red lines show the SWMF simulation results using the idealized input parameters. From top to bottom we present the average flux, inward flux, and the outward flux through the 6.6 R_e geocentric distance ring into the equatorial plane, expressed in units of $cm^{-3}km/s$.

spectra of the mass fluxes are the weakest but this is due to the fact that these are averaged quantities and the signal power was altered by the averaging across the 6.6 R_e boundary. However, the periodicity in the southward component of the IMF is best picked up upon by the CPCP, meaning that the transpolar potential is one quantity that quickly responds to the northward/southward turnings of the IMF.

6.4 Idealized Input Simulation 2: Results and Discussion

The results of the run #2 indicate that the periodicity in the IMF B_z is transmitted through the system and both the magnetosphere and the ionosphere are sensitive to the sudden changes in this parameter. However, for this case not only the Z component of the interplanetary field was changed, but all the other the solar wind parameters were greatly simplified (set to constant values). Because the solar wind-magnetosphere interaction is highly nonlinear, in order to assess the relative contribution of all the other solar wind parameters in the transfer of periodicity from IMF B_z to the magnetosphere, we designed an additional run (run #3) that takes as input the observed solar wind parameters and only the IMF B_z is set to a square wave as in run #2.

Moreover, the simulation results presented in the previous section appear to suggest that the signal to noise ratio in the input B_z power spectrum might be the controlling factor in transmitting this input periodicity to the magnetosphere. Therefore, 3 more runs were designed to help investigate this issue. To do so, the peak in the IMF B_z power spectrum contained at 0.245 mHz frequency (observed in the real data) was increased by a factor of 3 (run #4), 5 (run #5), 10 (run #5) and the IMF B_z signal was reconstructed by applying the inverse Fourier transform to the modified power spectra. All the other solar wind input parameters were set to the observed values. The input B_z parameters and their corresponding power spectra are presented in Figure 6.9 for all 4 runs described above. Increasing the peak in the

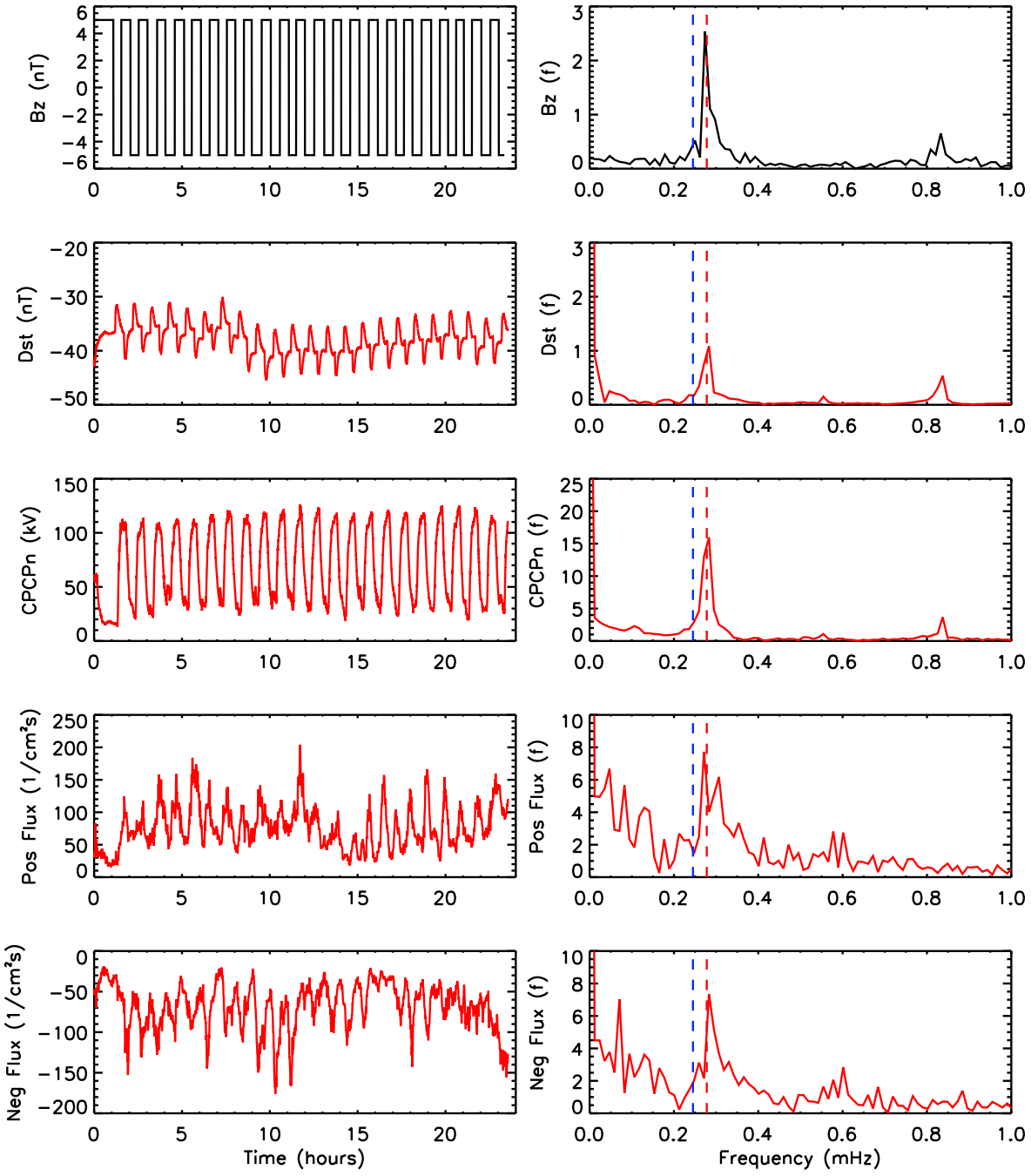

Figure 6.8: Power Spectra of the input versus system response. Left panels present from top to bottom the IMF B_z, modeled D_{st}, modeled CPCP, and the modeled inward and outward fluxes through geosynchronous orbit (run #2) for the November 12 , 2003 time period. Panels on the right show their corresponding power spectra results for the specified time range. The red (blue) vertical dashed line shows the frequency corresponding to 60 (68) minute periodicity.

observed IMF B_z power spectrum removes the high frequency spikes, yielding a less noisy reconstructed B_z as well as it changes the amplitude of the oscillations.

6.4.1 Periodicity

Figure 6.10 shows the model results for the disturbances in the geomagnetic field (left column) and their corresponding power spectra (right column), for all 4 input cases described above. We note that for run #3 (top row, orange lines), for which the model input contains observed solar wind parameters and the IMF B_z is a pure square wave, the magnetospheric response is very similar with the case of run #2, for which the IMF B_z is the same but all the other solar wind inputs are set to constant values. The power contained at the 0.27 mHz frequency by the modeled D_{st} is slightly lower for run #3, and a peak to noise ratio of about the same as in the case of run #2. Therefore the variations/fluctuations in all the other input parameters have very little to no contribution to the transfer of the field periodicity to the inner magnetosphere. However, the density, temperature and the X component of the solar wind velocity were steady during this time period, with little variation around the constant values that were set as an input for run #2.

The modeled D_{st} results from run #4 (purple line) reveal that, even though the peak in the power spectrum as increased by a factor of 3, IMF B_z periodicity is not seen in the magnetospheric response. The amplitude of the wave is smaller than in the observed B_z or the square wave, therefore this would decrease the amount of energy being transferred to the magnetosphere. Similarly, the modeled D_{st} results from run #5 (light blue line) shows no preferential frequency in the power spectrum, although for this case the frequency peak was increased by a factor of 5. Last row of Figure 6.10 presents the modeled D_{st} results for the case when the peak in the power spectrum of observed IMF B_z was increased by a factor of 10. For this case, the magnetosphere responds to this periodicity, and the peak to noise ratio in modeled

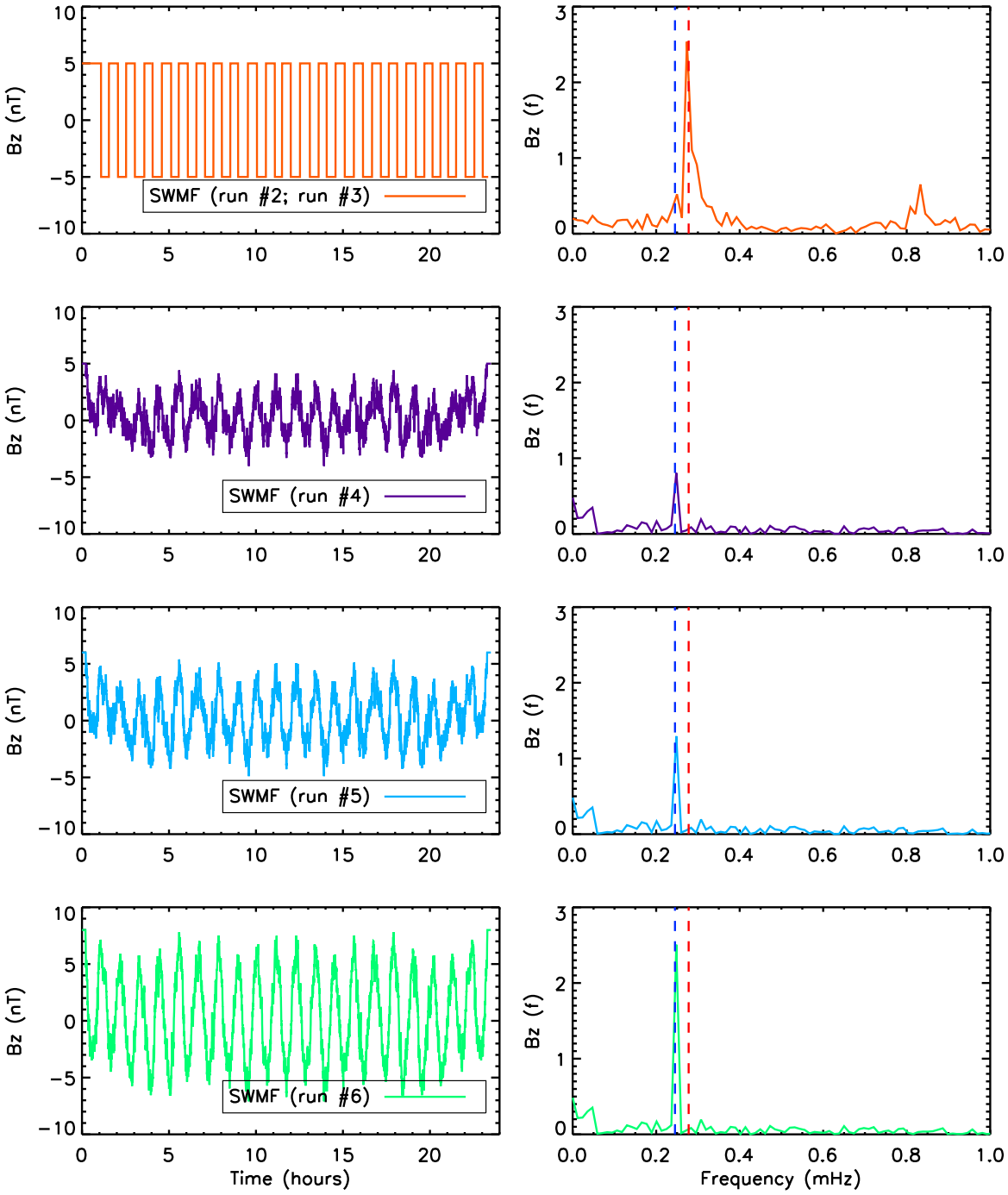

Figure 6.9: IMF B_z (left) and its corresponding power spectrum (right).From top to bottom are presented the input B_z for run #3 (orange line), run #4 (purple line), run #5 (light blue line), run #6 (green line). The red (blue) vertical dashed line shows the frequency corresponding to 60 (68) minute periodicity.

D_{st} power spectrum is about 3. Therefore, a peak to noise ratio of the input signal of about 10 is necessary in order for the magnetosphere to peak up on the periodicity of IMF B_z.

Similarly to Figure 6.10, Figure 6.11 shows the model results for the transpolar potential. Although no significant 68 minutes periodicity is observed in the AMIE derived cross polar cap potential, the model results indicate that this parameter requires a lower than 10 peak to noise ratio in the input B_z for it to respond to it. Furthermore, the peak to noise signal ratio in CPCP is proportional with the peak to noise signal ratio in the IMF B_z, meaning that the more power is contained at that specific frequency in the IMF B_z, more is going to be transmitted to the ionosphere. Therefore, for the magnetosphere to react to the periodicity in the input B_z, a threshold amount of power (peak to noise ratio) in the input signal is necessary while for the CPCP the threshold amount is significantly smaller.

The profiles of modeled CPCP and D_{st} of the 4 simulation cases are presented Figure 6.12. The cross polar cap potential looks similar for all runs, with the amplitude of the wave being altered by the amplitude of the IMF B_z input. Also, there is a phase shift of the signal by the end of the simulation time due to the fact that the period of the driver and the response is 68 minutes for run #4, #5, #6, while run #3 input B_z had a 60 minutes periodicity, therefore so they slowly shift out of phase over the day. D_{st} shows a similar phase shift. Moreover, the results from run #3 (orange line) are lower than those from run #4 (purple line), due to the B_z change in amplitude and the difference between the two can be as high as 10 nT.

6.5 Summary and Conclusions

For this study, the CIR driven storm of November 10, 2003 was examined using global magnetosphere simulations with both real and idealized solar wind upstream conditions. When using ACE observations as upstream conditions, the model repro-

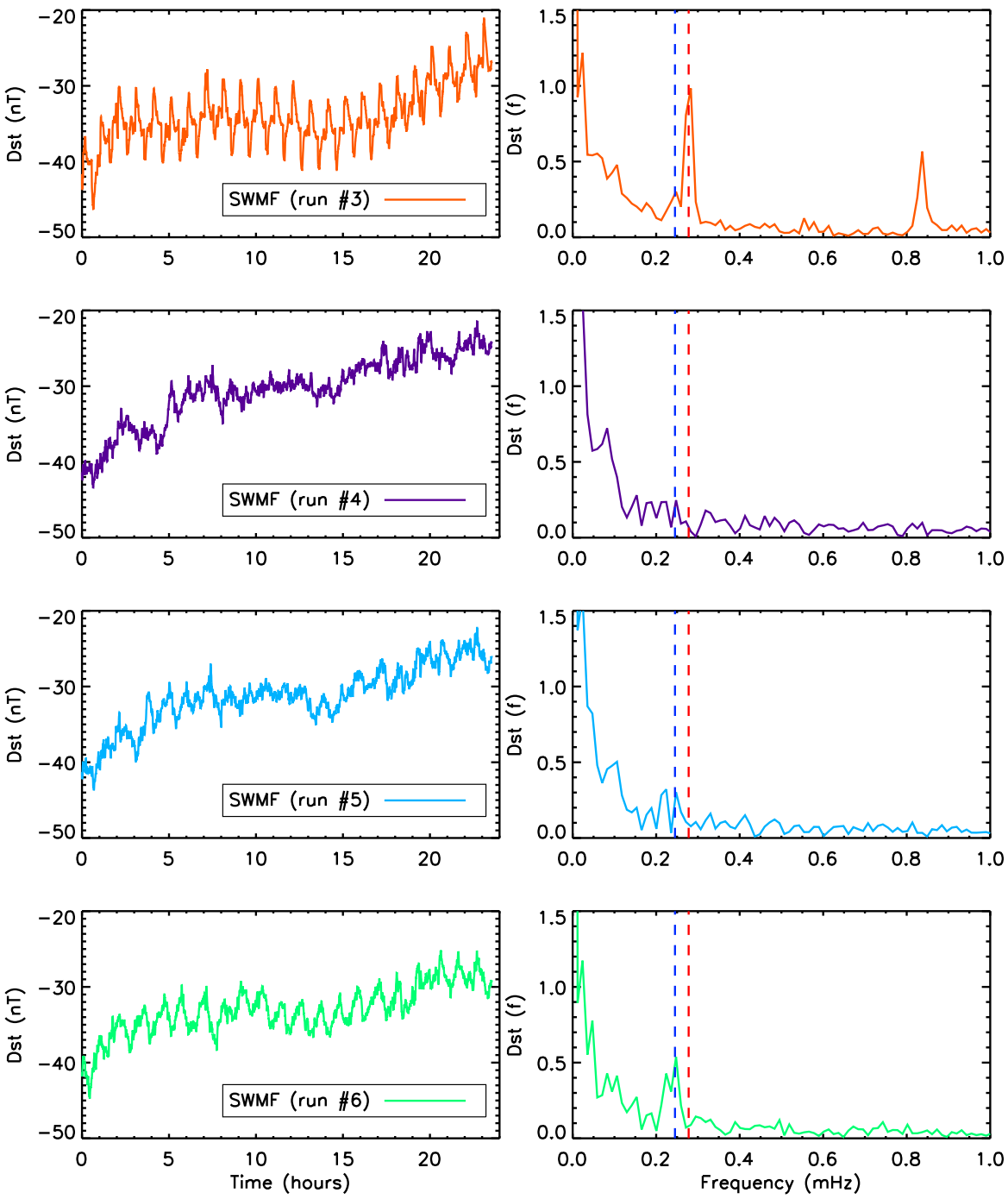

Figure 6.10: Modeled D_{st} (left) and its corresponding power spectrum (right).From top to bottom are presented the results from run #3 (orange line), run #4 (purple line), run #5 (light blue line), run #6 (green line). The red (blue) vertical dashed line shows the frequency corresponding to 60 (68) minute periodicity.

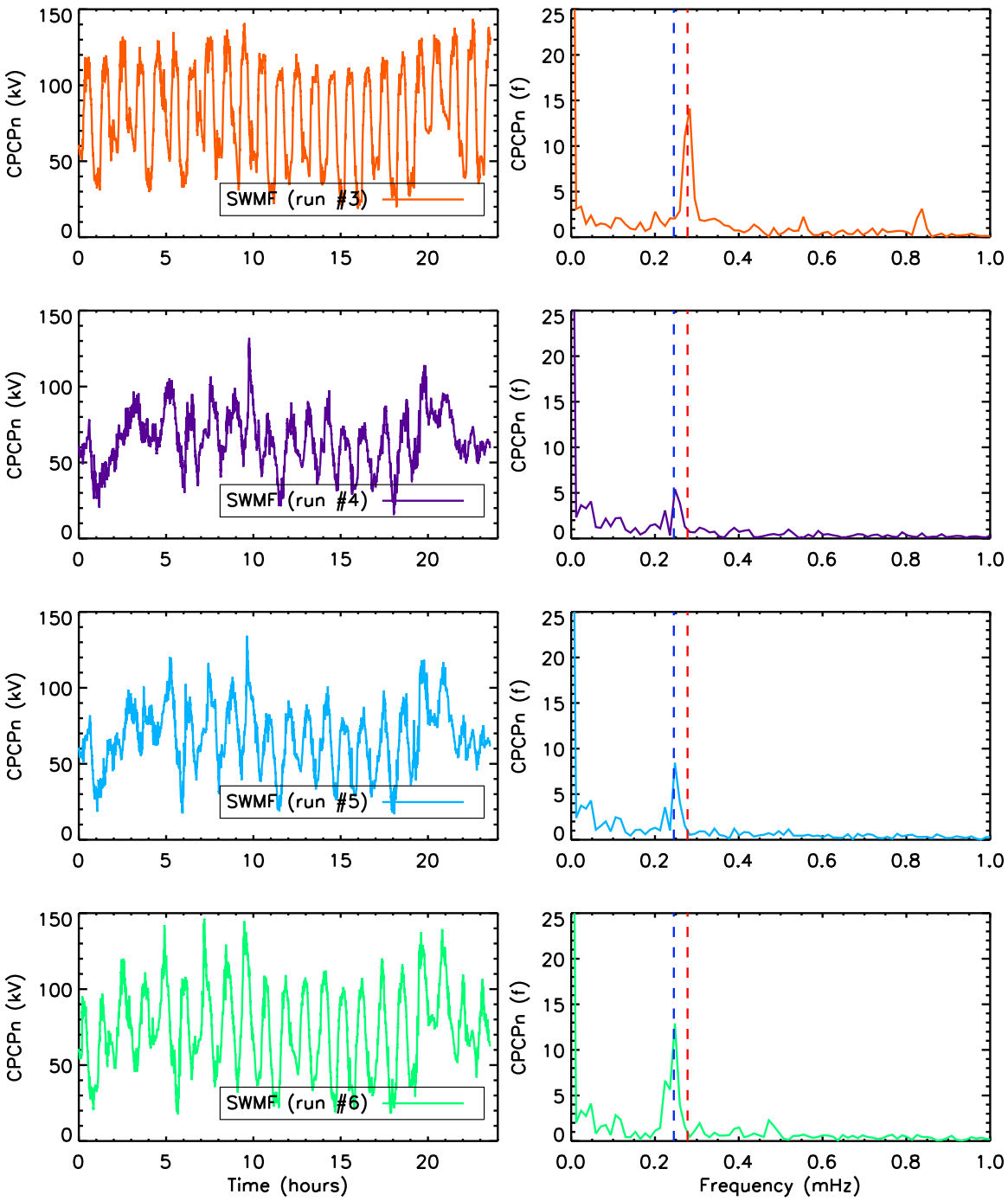

Figure 6.11: Modeled CPCP (left) and its corresponding power spectrum (right).From top to bottom are presented the results from run #3 (orange line), run #4 (purple line), run #5 (light blue line), run #6 (green line). The red (blue) vertical dashed line shows the frequency corresponding to 60 (68) minute periodicity.

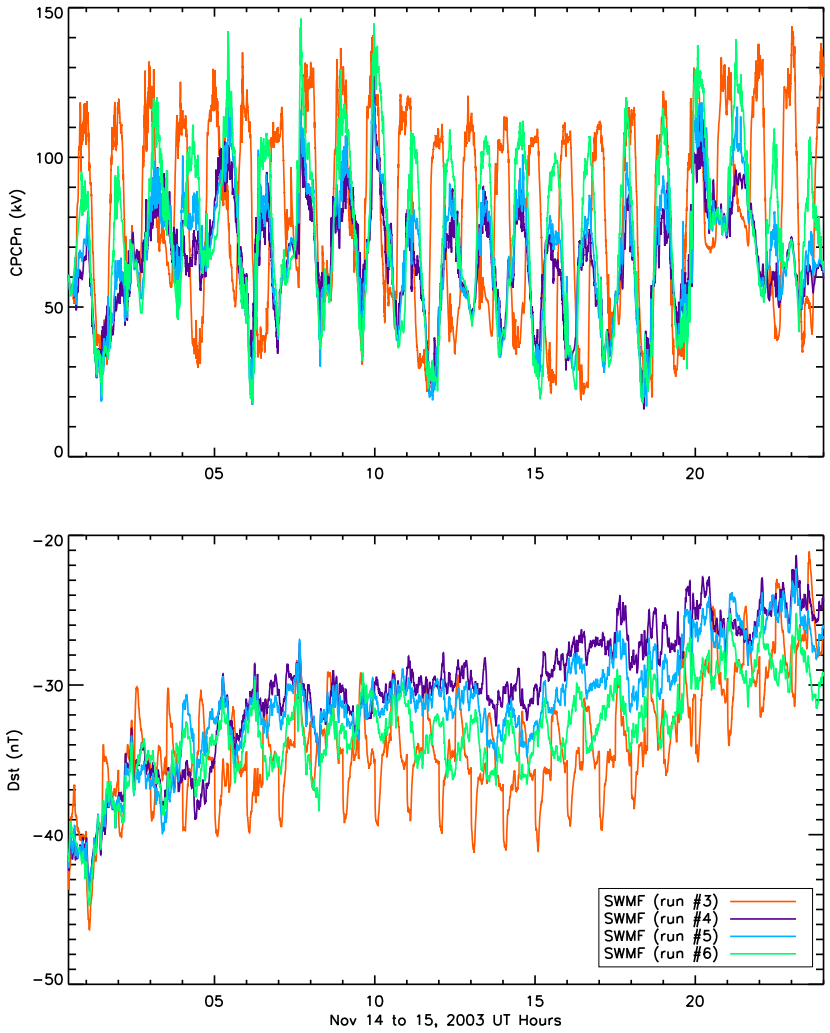

Figure 6.12: CPCP (kV) (top panel) and D_{st} (nT) (bottom panel) simulation results from run #3 (orange line), run #4 (purple line), run #5 (light blue line), run #6 (green line)

duces well the observed magnetospheric response, that is the modeled D_{st} profile is similar to the observed one, although it is underestimated. Nevertheless, discrepancies between the observed 1 hour resolution D_{st} and 1 minute resolution SYM-H also exists, with a difference in minimum values of about 15%. Furthermore, for this case, the model results for the transpolar potential illustrates very good agreement with the observationally based potential from AMIE.

Although a 68 minute periodicity is seen in the observed IMF B_z, and SYM-H during the high speed stream, the model results show no indication of this periodicity being carried through the system, that is, both the ionosphere and the magnetosphere are not sensitive to it. However, due to the fact that the average energy of the input signal (IMF B_z) contained in the frequency corresponding to 68 min periodicity is low (about twice the noise value) while most of it is spread out over the entire frequency range, it is uncertain if there is any correlation between the driver (IMF Bz) and the system response (SYM-H, CPCP) periodicities.

When using idealized input data as upstream conditions in the simulation setup, we find that the cross polar cap potential is more sensitive to the changes in the IMF orientation. The fast and abrupt changes in the IMF B_z control the variations in the CPCP, which in turn regulates the particle injection rate. The ring current intensifies and weakens as the IMF B_z changes sign. The transpolar potential starts increasing when the IMF B_z turns southward, reaching maximum at the end of the 30 min period of negative B_z. When the IMF turns northward, the magnetosphere starts to relax and the CPCP starts decreasing, and all of these responses are greatly correlated with the northward/southward turnings displayed in the IMF B_z profile. Furthermore, both the inward and the outward flux at geosynchronous orbit exhibits similar behaviour, indicating a intermittent injection of particles through this boundary, seen as well in the current density distribution.

Furthermore, the transfer of IMF B_z periodicity to the magnetosphere is unal-

tered by other solar wind parameters, although the size of the peak to noise ratio of the input signal is the controlling factor that determines this transfer. The global magnetosphere simulation suggest that a threshold amount of power (peak to noise ratio) of $\sim$10 in the input signal is needed for the magnetosphere to react to the periodicity in the input Bz, while for the CPCP the threshold amount is significantly smaller.

CHAPTER VII

Hot Electron Ion Drift Integrator Model

7.1 Motivation

Numerous studies, both data analysis and numerical simulations, have attempted to unravel the complex processes that control the nature, transport, and losses of the ring current population. Statistical studies involving large databases of in situ magnetic field measurements in the inner magnetosphere (*Lui*, 2003; *Tsyganenko et al.*, 2003; *Jorgensen et al.*, 2004; *Le et al.*, 2004) showed that under disturbed conditions, large depressions in the geomagnetic field strength (down to $\sim -400\ nT$) are associated with the ring current. *Borovsky et al.* (1997) suggested that the cold dense plasma sheet is the source of the superdense near Earth plasma sheet and as a consequence it enhances the ring current due to high diamagnetism of the near Earth super dense plasma sheet. *Thomsen et al.* (2003) showed that the access to geosynchronous orbit of the cold, dense plasma sheet particles happens under preferential northward IMF Bz conditions. Moreover, *Wygant et al.* (1998) and *Rowland and Wygant* (1998) report on the presence of bursty convection enhancements and reversed convection in the midnight sector that alter the morphology of the ring current.

The configuration of the storm time ring current depends entirely on storm epoch time and magnetic local time (MLT) (e.g. *Brandt et al.*, 2002). The ring current induced magnetic field alters the grad-B and curvature drift velocities of all the trapped

particles (e.g. *Ebihara and Ejiri*, 2000). Several empirical models of the ring current-induced magnetic field (e.g. *Kim and Chan*, 1997; *Nakamura et al.*, 1998) attempted to quantify the adiabatic changes of the ring current population using empirical magnetic field models that are a function of the geocentric distance and Dst.

The coupling between plasma and fields in the inner magnetosphere plays a key role in the overall behavior of the magnetosphere. In the inner magnetosphere, plasma does not behave like a fluid, therefore a kinetic description of this region is needed. While most kinetic models treat the plasma transport realistically, they lack a consistent treatment of the fields, that is, a dipolar assumption is used in the description of the magnetic field along with empirical formalisms for the electric fields. On the other hand, MHD numerical models have self consistency but they lack the ability to reproduce essential gradient curvature drifts and their description of the inner magnetosphere is overly simplified (*De Zeeuw et al.*, 2004).

A realistic time-varying magnetic field is crucial for understanding the ring current and plasma sheet dynamics, especially during magnetic activity. Several ring current simulations that incorporate a self-consistent magnetic field have been developed. One example is the Rice Convection Model (RCM) coupled with the Magneto-Friction (MF) code of *Toffoletto et al.* (2003), an inner magnetospheric model which self-consistently accounts for the inner magnetospheric currents in calculating the magnetospheric B-field configuration and also accounts for the coupling between these currents with ionospheric currents. Using this configuration, *Lemon et al.* (2004) obtained a force-balanced magnetic field by solving a set of ideal magnetohydrodynamic (MHD) equations with a frictional dissipation term. Their simulation results of the plasma transport from the plasma sheet to the ring current suggest that the perturbation associated with the injection of plasma sheet ions in the inner magnetosphere inhibits the formation of a significant ring current. Several models have been developed that use the T96 or T01 magnetic field model (*Tsyganenko*, 1995; *Tsyganenko*

and Stern, 1996; *Tsyganenko*, 2002), that take IMF and Dst as inputs (*Fok and Moore*, 1997; *Fok et al.*, 2001; *Vapirev and Jordanova*, 2007). *Fok et al.* (2001) solves the evolution of the phase space density of ions and the electric potential to incorporate a force-balanced magnetic field in a self-consistent manner. *Zaharia et al.* (2006) solved quasi-2-D elliptic equations to obtain a self-consistent magnetic field expressed by the Euler potentials. Comparison with a dipolar configuration shows that depressions of the plasma pressure on the nightside are lower (higher equatorial perpendicular pressure) when the magnetic field is consistently accounted for. Two way coupling between a ring current model (*Jordanova et al.*, 2006) and a 3-D plasma force-balance model also shows significant differences in the inner magnetosphere compared to the case when the ring current model is based on a dipolar approximation.

Another study by *Chen et al.* (2006) used a tracing method for the equatorially mirroring ions under a self-consistent magnetic field with an equatorial pitch angle distribution assumed to be sinusoidal and showed that the self-consistent feedback between the plasma pressure and the magnetic field is suppressing ring current energization. *Liu et al.* (2006) reported on the need of a consistent representation of the fields in an inner magnetosphere model and showed that their magnetically self-consistent model reasonably reproduced many of the general features of the storm time ring current.

Moreover, *Liemohn and Brandt* (2005) discussed electric field feedback as a limiter of future ring current enhancement. Numerical simulations of the ring current and plasmasphere indicate that an accurate description of the electric field is essential in reproducing their large-scale morphology and bulk parameters (*Liemohn et al.*, 2004, 2006).

On the other hand, *De Zeeuw et al.* (2004) presented initial results of self consistent RCM coupled with the BATS-R-US model within the SWMF. The authors report on

the inflation of the magnetic field in the tail due to the presence of the ring current. With a similar setup, *Zhang et al.* (2007) performed a real storm simulation using the coupled RCM-MHD code. Their simulation results are in good agreement with geosynchronous plasma and fields. Another study using RCM in conjunction with a realistic magnetic field from MHD model, shows that the global magnetosphere responds non-linearly to solar wind energy inputs (*Ilie et al.*, 2010).

Nevertheless, the RCM model has the disadvantage that it assumes an isotropic pitch angle distribution and charge exchange processes are not explicitly considered (at least not in the Space Weather Modeling Framework version of the RCM). Moreover, RCM assumes an isotropic particle pressure distribution. In this chapter we describe the Hot Electron Ion Drift Integrator model, that includes both charge exchange losses, as well as full pitch angle distributions therefore, pitch angle dependent drifts and losses, so it can handle arbitrary magnetic fields.

7.2 Governing Equations

7.2.1 The Kinetic Equation

The HEIDI model is the *Liemohn et al.* (2004) version of the Ring current - Atmosphere interaction Model (RAM) based on earlier versions by *Fok et al.* (1993) and *Jordanova et al.* (1996), developed at the University of Michigan. It computes the time-dependent, gyration- and bounce-averaged kinetic equation for the phase-space density of one or more ring current species (e, H^+, He^+, O^+) on an equatorial based grid.

The bounce-averaged kinetic equation

$$\frac{\partial Q}{\partial t} + \frac{1}{{R_0}^2}\frac{\partial}{\partial R_0}\left({R_0}^2\langle\frac{dR_0}{dt}\rangle Q\right) + \frac{\partial}{\partial\phi}\left(\langle\frac{d\phi}{dt}\rangle Q\right) + \frac{1}{\sqrt{E}}\frac{\partial}{\partial E}\left(\sqrt{E}\langle\frac{dE}{dt}\rangle Q\right) + \frac{1}{h(\mu_0)\mu_0}\frac{\partial}{\partial\mu_0}\left(h(\mu_0)\mu_0\langle\frac{d\mu_0}{dt}\rangle Q\right) = \langle\frac{\delta Q}{\delta t}\rangle_{collisions} \quad (7.1)$$

solves for the phase space distribution function $Q(R_0, \phi, E, \mu_0, t)$, where R_0 represents the radial distance in the equatorial plane, ϕ is the geomagnetic east longitude, E is the kinetic energy of the particle, $\mu_0 = cos\alpha_0$, where α_0 is the particle equatorial pitch angle. Note that the subscript '0' throughout this chapter indicates an equatorial value, unless specified otherwise. QdV represents the mean number of particles with kinetic energy between E and $E+dE$ and cosine of the equatorial pitch angle between μ_0 and $\mu_0 + d\mu_0$ at time t, for which the coordinates of the guiding center lie in a magnetic flux tube with equatorial area $R_0 dR_0 d\phi$. dV is the elementary volume in four dimensions (R_0, ϕ, E, μ_0) as defined by *Jordanova et al.* (1996):

$$dV = 8\pi\sqrt{2Em^3}R_0^2\mu_0 h\left(\mu_0\right) dR_0 d\phi dE d\mu_0 \tag{7.2}$$

where

$$h = \frac{1}{2R_0}\int_{s_m}^{s_{m'}} \frac{ds}{\sqrt{1-\frac{B(s)}{B_m}}} \tag{7.3}$$

is a quantity related to the half bounce path, and m is the particle's mass.

The relationship between the phase space distribution function $Q(R_0, \phi, E, \mu_0, t)$ and the velocity space distribution function $F(\vec{v}, \vec{R_0}, t)$ is given by $F = Qm^3$. The left hand side of Equation 7.1 describes the collisionless drift of charged particles and the right hand side describes changes in the distribution function due to loss processes. The brackets $\langle\rangle$ denote bounce - averaging and for a quantity χ as described in the following:

$$\langle\chi\rangle = \frac{1}{S_B}\int_{s_m}^{s_{m'}} \chi\frac{ds}{\sqrt{1-\frac{B(s)}{B_m}}} \tag{7.4}$$

where S_B represents the half-bounce path length, as defined by *Roederer* (1970).

$$S_B = \int_{s_m}^{s_{m'}} \frac{ds}{\sqrt{1 - \frac{B(s)}{B_m}}} = 2R_0 h \tag{7.5}$$

Equation 7.1 can be written in the conservative form by multiplying by $R_0^2 \mu_0 \sqrt{E} h\,(\mu_0)$, yielding an expression for the conservative function $Q^* = R_0^2 \mu_0 \sqrt{E} h\,(\mu_0)\, Q$ (*Jordanova et al.*, 1994, 1996):

$$\frac{\partial Q^*}{\partial t} + \frac{\partial}{\partial R_0}\left(\langle \frac{dR_0}{dt} \rangle Q^*\right) + \frac{\partial}{\partial \phi}\left(\langle \frac{d\phi}{dt} \rangle Q^*\right) + \frac{\partial}{\partial E}\left(\langle \frac{dE}{dt} \rangle Q^*\right) + \frac{\partial}{\partial \mu_0}\left(\langle \frac{d\mu_0}{dt} \rangle Q^*\right) = \langle \frac{\delta Q^*}{\delta t} \rangle_{collisions} \tag{7.6}$$

The various terms in Equation 7.6 account for the contribution from flow of plasma out to the dayside outer boundary, collisionless drifts, energy loss and pitch angle scattering due to Coulomb collisions with the thermal plasma, charge exchange loss with the hydrogen corona, and precipitative loss to the upper atmosphere. Time, geocentric distance in the equatorial plane, magnetic local time, kinetic energy, and cosine of the equatorial pitch angle are the five independent variables. The distribution function in both space and velocity space can be computed in HEIDI for all pitch angles and local times, with an energy range typically ranging from 10 eV to 400 keV and L shell values ranging from 2 to 6.5.

7.2.2 Particle Drifts

The magnetic gradient curvature along with the $\vec{E} \times \vec{B}$ drift velocities determine the particle's total drift at ring current energies. Since the current version of HEIDI assumes a dipolar magnetic field, the gradient curvature drift uses the analytical formulation from *Ejiri* (1978), valid only for dipolar configuration of the magnetic field:

$$\langle \vec{V_{GC}} \rangle = -\frac{3ER_0^2}{qM_e}\left(1 - \frac{I(\mu_0)}{6h(\mu_0)}\right)\hat{\phi} \tag{7.7}$$

where q is the charge of the particle and the dipole moment of the Earth is $M_e = 8.02 \times 10^{15}\ Tm^3$. $I(\mu_0)$ is a quantity related with the second adiabatic invariant and is defined by:

$$I = \frac{1}{R_0}\int_{s_m}^{s_m\prime} ds\sqrt{1 - \frac{B(s)}{B_m}} \tag{7.8}$$

The magnetospheric electric field is given by:

$$\vec{E} = -\nabla\left(\Phi_{convection} + \Phi_{corotation}\right) \tag{7.9}$$

where the corotation electric potential $\Phi_{corotation}$ is defined as

$$\Phi_{corotation} = -\frac{C}{R_0}, \tag{7.10}$$

with $C = 1.44 \times 10^{-2}\ R_e^2 V m^{-1}$. According to *Northrop* (1963) and *Roederer* (1970), provided that the fields vary slowly over a period comparable with the bounce period, only the equatorial electric field contributes to the bounce-averaged drift velocities of the guiding center:

$$\langle V_{drift} \rangle = \frac{\vec{E_0} \times \vec{B_0}}{B_0^2} \tag{7.11}$$

An accurate description of the convection electric field is very important for a complete description of the ring current. HEIDI includes a variety of electric field models: empirical Volland-Stern two-cell convection pattern (*Volland*, 1973; *Stern*, 1975; *Maynard and Chen*, 1975), modified McIlwain E5D model (*McIlwain*, 1986) along with a self consistent electric field described by *Liemohn et al.* (2004) and *Liemohn and Kozyra* (2005). The Volland-Stern model for the electric field is based

on the Kp index dependence with a shielding factor of $\gamma = 2$ as determined by *Korth et al.* (1999). The McIlwain model uses boundary conditions derived from the Defense Meteorological Satellites Program (DMSP) along with a Weimer model generated transpolar potential. The self consistent model for the electric field employs coupling with the Ridley Ionosphere Model (RIM), given that the field aligned currents calculated by HEIDI are used as source terms in the Poisson equation for the ionospheric potential, solved by RIM (*Ridley and Liemohn*, 2002; *Ridley et al.*, 2004).

7.2.3 Bounce-averaged Coefficients

In the absence of parallel electric fields and assuming the particles move in a dipolar magnetic field configuration, the bounce-averaged rate of change of the cosine of the equatorial pitch angle and the bounce-averaged rate of change of the particle's kinetic energy over a bounce period (*Ejiri*, 1978) are:

$$\langle \frac{d\mu_0}{dt} \rangle = \frac{1-\mu_0^2}{4R_0\mu_0} \frac{I(\mu_0)}{h(\mu_0)} \langle \frac{dR_0}{dt} \rangle \tag{7.12}$$

$$\langle \frac{dE}{dt} \rangle = -\frac{3E}{R_0} \left(1 - \frac{I(\mu_0)}{6h(\mu_0)} \right) \langle \frac{dR_0}{dt} \rangle \tag{7.13}$$

The $I(\mu_0)$ and $h(\mu_0)$ integrals, as defined in Equation 7.8 and Equation 7.3, are evaluated using the approximations of *Ejiri* (1978), valid only for a dipole magnetic field[1]:

$$h(\mu_0) = \alpha - \beta\,(\mu_0 + \sqrt{\mu_0}) + a_1{\mu_0}^{1/3} + a_2{\mu_0}^{2/3} + a_3\mu_0 + a_4{\mu_0}^{4/3} \tag{7.14}$$

[1] α here is not the pitch angle but rather a constant, defined in Equation 7.17

$$I(\mu_0) = 2\alpha\,(1-\mu_0) + 2\beta\mu_0 \ln(\mu_0) + 4\beta\,(\mu_0 - \sqrt{\mu_0}) + 3a_1\left({\mu_0}^{1/3} - \mu_0\right) + 6a_2\left({\mu_0}^{2/3} - \mu_0\right) + 6a_4\left(\mu_0 - {\mu_0}^{4/3}\right) - 2a_3\mu_0 \ln(\mu_0) \quad (7.15)$$

where the following coefficients were numerically determined.

$$a_1 + a_2 + a_3 + a_4 = 0 \quad (7.16)$$

$$\alpha = 1 + \frac{\ln\left(2+\sqrt{3}\right)}{2\sqrt{3}} \sim 1.38 \quad (7.17)$$

$$\beta = \frac{\alpha}{2} - \frac{\pi\sqrt{2}}{12} \sim 0.32 \quad (7.18)$$

$$a_1 = 0.055 \quad a_2 = -0.037 \quad a_3 = -0.074 \quad a_4 = 0.056 \quad (7.19)$$

Charge exchange with neutral hydrogen from the geocorona produces low energy protons as well as high energy neutral atoms. This charge exchange represents the main internal loss process for the ring current ions (*Dessler and Parker*, 1959). The loss rate due to charge exchange is:

$$\left\langle \left(\frac{\partial Q}{\partial t}\right)_{ce} \right\rangle = -\sigma\sqrt{\frac{2E}{m}}\langle n_H \rangle Q \quad (7.20)$$

where σ is the charge exchange cross section of the ion species colliding with the geocorona hydrogen with number density n_H.

Measurements of the exospheric hydrogen density from Dynamics Explorer 1 (DE1), based on observations of geocoronal emission due to solar Lyman alpha radiation scattered in the Earth's exosphere, provided by *Rairden et al.* (1986) are used.

The reported exponential behaviour (*Rairden et al.*, 1986; *Østgaard et al.*, 2003) between 2 and 6 Earth Radii of n_H is used to calculate this value at any radial distance. The bounce averaged values of the neutral hydrogen are calculated assuming a dipolar configuration of the magnetic field.

The HEIDI model is also coupled with the time dependent plasmasphere model of *Ober et al.* (1997) that solves the continuity equation for the total cold plasma content in a flux tube and provides HEIDI with the thermal electron density in the equatorial plane, needed to describe the Coulomb collisions with the plasmasphere. The bounce averaged plasmaspheric electron density n_{pe} is

$$\langle n_{pe} \rangle = \frac{n_{pe0}}{S_B B_0} \int_{s_m}^{s_m\prime} ds \frac{B(s)}{\mu} = \frac{n_{pe0}}{1-\mu_0^2} \left(1 - \frac{I(\mu_0)}{2h(\mu_0)} \right) \tag{7.21}$$

For simplicity, the ratio $n_{pe}(s)/B(s)$ is assumed to be constant along the magnetic field line. Then a simpler analytical expression is obtained for the bounce averaged plasmaspheric electron density:

$$\left\langle n_{pe} \frac{B_0 \mu^2}{B(s)} \right\rangle = \frac{n_{pe0}}{S_B} \int_{s_m}^{s_m\prime} \mu ds = \frac{n_{pe0} I(\mu_0)}{2h(\mu_0)} \tag{7.22}$$

The source term for the phase space density equation is provided by the nightside outer boundary of the simulation domain. That is, geosynchronous observations of particle fluxes are used as input functions. The composition of the plasma sheet is assumed to have Kp dependence and is described using the empirical formulation of *Young et al.* (1982),

$$n(H^+) = 0.34 \cdot e^{(0.54 \cdot Kp)} \tag{7.23}$$

$$n(O^+) = 0.011 \cdot e^{(0.24 \cdot Kp + 0.011 \cdot F_{10.7})} \tag{7.24}$$

For more details about the numerical model see *Liemohn et al.* (1999, 2001b,

2004).

7.3 New formalism for bounce averages in an arbitrary magnetic field

Extensive modifications of HEIDI were carried out in order to accommodate for a non-dipolar magnetic field, including the development of new theoretical formulations for the bounced averaged coefficients, to replace the previously used analytical approximations of *Ejiri* (1978). Details of the derivations are described below.

In the presence of external forces which are perpendicular to the magnetic field lines at all times (equipotential field lines), the particle's momentum and the magnetic field at the mirror points are not conserved. However the magnetic moment and the second adiabatic invariant remain constants. The bounce average rate of change of the cosine of the particle's pitch angle is derived from the conservation of the magnetic moment μ_m

$$\mu_m = \frac{1}{2}\frac{mv_\perp^2}{B} = \frac{1}{2}\frac{mv^2 sin^2\alpha_0}{B_0} \tag{7.25}$$

and the second adiabatic invariant J

$$J = 2mv \int_{s_m}^{s_m\prime} ds \sqrt{1 - \frac{B(s)}{B_m}} \tag{7.26}$$

where B_0 represents the equatorial value of the magnetic field, $B(s)$ is the magnetic field along the field line, s is the distance from the ionospheric foot-point along the field line, B_m denotes the magnitude of the magnetic field at the mirror points s_m and $s_m\prime$ and v is the particle's velocity.

We eliminate the velocity of the particle by combining the two invariants,

$$\frac{\mu_m}{J^2} = constant \tag{7.27}$$

and letting $y = sin\alpha_0$ yields:

$$\frac{\mu_m}{J^2} = \frac{1}{2}\frac{mv^2 sin^2\alpha_0}{B_0}\frac{1}{4m^2v^2\left[\int_{s_m}^{s_{m'}} ds\sqrt{1-\frac{B(s)}{B_m}}\right]^2} \tag{7.28}$$

$$\frac{\mu_m}{J^2} = \frac{y^2}{8mB_0I^2R_0^2} \tag{7.29}$$

Differentiating with respect to time we get:

$$\frac{d}{dt}\left[\frac{y^2}{8mB_0I^2R_0^2}\right] = 0 \tag{7.30}$$

$$\frac{2}{y}\frac{dy}{dt} - \frac{1}{B_0}\frac{dB_0}{dt} - \frac{2}{R_0}\frac{dR_0}{dt} - \frac{2}{I}\frac{dI}{dt} = 0 \tag{7.31}$$

Equation 7.25 along with energy conservation yields a relationship between the magnetic field at the mirror point (B_m), magnetic field at the equator (B_0) and the particle's equatorial pitch angle (α_0):

$$B_m = \frac{B_0}{sin^2\alpha_0} \tag{7.32}$$

Therefore, using the expressions of I (Equation 7.8) and h (Equation 7.3) together with Equation 7.32 we can write:

$$I = \frac{1}{R_0}\int_{s_m}^{s_{m'}} ds\sqrt{1-\frac{B(s)y^2}{B_0}} \tag{7.33}$$

and

$$h = \frac{1}{2R_0} \int_{s_m}^{s_{m'}} \frac{ds}{\sqrt{1 - \frac{B(s)y^2}{B_0}}} \tag{7.34}$$

The last term in Equation 7.31 ($\frac{dI}{dt}$) needs further examination.

$$\frac{dI}{dt} = \left(\frac{1}{R_0} \sqrt{1 - \frac{B(s_{m'})y^2}{B_0}} \right) \frac{ds_{m'}}{dt} - \left(\frac{1}{R_0} \sqrt{1 - \frac{B(s_{m'})y^2}{B_0}} \right) \frac{ds_m}{dt} + \int_{s_m}^{s_{m'}} \frac{\partial}{\partial t} \frac{1}{R_0 \sqrt{1 - \frac{B(s)y^2}{B_0}}} ds \tag{7.35}$$

$$\left(\frac{1}{R_0} \sqrt{1 - \frac{B(s_{m'})y^2}{B_0}} \right) \frac{ds_{m'}}{dt} = \left(\frac{1}{R_0} \sqrt{1 - \frac{B(s_{m'})y^2}{B_0}} \right) \frac{ds_m}{dt} = = \frac{1}{R_0} \sqrt{1 - \frac{B_m y^2}{B_0}} = 0 \tag{7.36}$$

Therefore,

$$\boxed{\frac{dI}{dt} = \int_{s_m}^{s_{m'}} \frac{\partial}{\partial t} \frac{1}{R_0 \sqrt{1 - \frac{B(s)y^2}{B_0}}} ds = \frac{\partial I}{\partial t} + \frac{\partial I}{\partial y}\frac{\partial y}{\partial t} + \frac{\partial I}{\partial R_0}\frac{\partial R_0}{\partial t} + \frac{\partial I}{\partial \phi}\frac{\partial \phi}{\partial t}} \tag{7.37}$$

Second term in Equation 7.37 can be further simplified by solving for $\frac{d}{dy}\left(\frac{I}{y}\right)$ first and then relating the $\frac{\partial I}{\partial y}$ term with I and h quantities.

$$\frac{\partial}{\partial y}\left(\frac{I}{y}\right) = -\frac{I}{y^2} + \frac{1}{y}\frac{\partial I}{\partial y} \tag{7.38}$$

$$\frac{\partial I}{\partial y} = \frac{1}{R_0} \int_{s_m}^{s_{m'}} -\frac{B(s)y}{B_0} \frac{ds}{\sqrt{1 - \frac{B(s)y^2}{B_0}}} \tag{7.39}$$

$$\frac{\partial}{\partial y}\left(\frac{I}{y}\right) = -\frac{1}{R_0 y^2}\left(\int_{s_m}^{s_m'} ds\sqrt{1-\frac{B(s)y^2}{B_0}} + y\int_{s_m}^{s_m'}\frac{B(s)y}{B_0}\frac{ds}{\sqrt{1-\frac{B(s)y^2}{B_0}}}\right) \tag{7.40}$$

$$\frac{\partial}{\partial y}\left(\frac{I}{y}\right) = -\frac{1}{R_0 y^2}\int_{s_m}^{s_m'}\frac{ds}{\sqrt{1-\frac{B(s)y^2}{B_0}}} \tag{7.41}$$

So we obtain

$$\frac{\partial}{\partial y}(\frac{I}{y}) = -\frac{2h}{y^2} \tag{7.42}$$

From Equation 7.38 and Equation 7.42 we get

$$\frac{\partial I}{\partial y} = \frac{I-2h}{y} \tag{7.43}$$

Therefore, Equation 7.37 becomes:

$$\boxed{\frac{dI}{dt} = \frac{\partial I}{\partial t} + \frac{(I-2h)}{y}\frac{\partial y}{\partial t} + \frac{\partial I}{\partial R_0}\frac{\partial R_0}{\partial t} + \frac{\partial I}{\partial \phi}\frac{\partial \phi}{\partial t}} \tag{7.44}$$

Now, we evaluate the third term in Equation 7.37.

$$\frac{\partial I}{\partial R_0}\frac{\partial R_0}{\partial t} = -\frac{1}{R_0^2}\frac{\partial R_0}{\partial t}\int_{s_m}^{s_m'} ds\sqrt{1-\frac{B(s)y^2}{B_0}} + \frac{1}{R_0}\int_{s_m}^{s_m'}\frac{\partial}{\partial R_0}\sqrt{1-\frac{B(s)y^2}{B_0}}ds \tag{7.45}$$

$$\begin{aligned}\frac{\partial I}{\partial R_0}\frac{\partial R_0}{\partial t} = &-\frac{I}{R_0}\frac{\partial R_0}{\partial t} + \frac{1}{2R_0B_0}\frac{\partial B_0}{\partial R_0}\frac{\partial R_0}{\partial t}\left(\int_{s_m}^{s_m'}\frac{ds}{\sqrt{1-\frac{B(s)y^2}{B_0}}} - \int_{s_m}^{s_m'} ds\sqrt{1-\frac{B(s)y^2}{B_0}}\right) + \\ &\frac{1}{R_0}\frac{\partial R_0}{\partial t}\int_{s_m}^{s_m'}\sqrt{1-\frac{B(s)y^2}{B_0}}\frac{\partial(ds)}{\partial R_0} - \frac{y^2}{2R_0B_0}\frac{\partial R_0}{\partial t}\int_{s_m}^{s_m'} ds\frac{\frac{\partial B}{\partial R_0}}{\sqrt{1-\frac{B(s)y^2}{B_0}}}\end{aligned} \tag{7.46}$$

$$\frac{\partial I}{\partial R_0}\frac{\partial R_0}{\partial t} = \frac{\partial R_0}{\partial t}\left[-\frac{I}{R_0} + \frac{(2h-I)}{2B_0}\frac{\partial B_0}{\partial t} + \frac{1}{R_0}\int_{s_m}^{s_{m'}}\sqrt{1-\frac{B(s)y^2}{B_0}}\frac{\partial(ds)}{\partial R_0} - \frac{y^2 S_B}{2R_0 B_0}\langle\frac{\partial B}{\partial R_0}\rangle\right] \tag{7.47}$$

In the case of a dipolar magnetic field it can be shown that the $\frac{\partial I}{\partial R_0} = 0$ as well as $\frac{\partial I}{\partial \phi}\frac{\partial \phi}{\partial t} = 0$ and $\frac{\partial I}{\partial t} = 0$.

Returning to Equation 7.31, this yields:

$$\frac{dy}{dt} = \frac{Iy}{2h}\left(\frac{1}{2B_0}\frac{dB_0}{dt} + \frac{1}{R_0}\frac{dR_0}{dt} + \frac{1}{I}\frac{\partial I}{\partial t} + \frac{1}{I}\frac{\partial I}{\partial R_0}\frac{\partial R_0}{\partial t} + \frac{1}{I}\frac{\partial I}{\partial \phi}\frac{\partial \phi}{\partial t}\right) \tag{7.48}$$

Considering that B_0 is a function $B_0(t, R_0, \phi)$, the total derivative $\frac{dB_0}{dt}$ becomes:

$$\frac{dB_0}{dt} = \frac{\partial B_0}{\partial t} + \frac{\partial B_0}{\partial R_0}\frac{\partial R_0}{\partial t} + \frac{\partial B_0}{\partial \phi}\frac{\partial \phi}{\partial t} \tag{7.49}$$

The total velocity vector in the equatorial plane in spherical coordinates,

$$\vec{v_0} = \hat{R_0}\frac{\partial R_0}{\partial t} + \hat{\phi}R_0\frac{\partial \phi}{\partial t} \tag{7.50}$$

has its components defined as:

$$v_{0R} = \frac{\partial R_0}{\partial t} = \left\{\frac{m_t}{qB_0^4}\left(v_{||}^2 + \frac{v_\perp^2}{2}\right)\left[\left(\nabla\frac{B_0^2}{2}\right)\times\vec{B_0}\right] + v_{Convection}\right\}\hat{R_0} \tag{7.51}$$

$$v_{0\phi} = R_0\frac{\partial \phi}{\partial t} = \left\{\frac{m_t}{qB_0^4}\left(v_{||}^2 + \frac{v_\perp^2}{2}\right)\left[\left(\nabla\frac{B_0^2}{2}\right)\times\vec{B_0}\right] + v_{Corrotation}\right\}\hat{\phi} \tag{7.52}$$

Going back in Equation 7.48, we are able to obtain an expression for $\frac{dy}{dt}$ as a function of I, h, B_0 field magnitude and total drift components v_{0R} and $v_{0\phi}$:

$$\frac{dy}{dt} = \frac{Iy}{2h}\left\{ v_{0R}\left(\frac{1}{2B_0}\frac{\partial B_0}{\partial R_0} + \frac{1}{R_0} + \frac{1}{I}\frac{\partial I}{\partial R_0}\right) + v_{0\phi}\left(\frac{1}{2B_0 R_0}\frac{\partial B_0}{\partial \phi} + \frac{1}{I R_0}\frac{\partial I}{\partial \phi}\right) + \frac{1}{2B_0}\frac{\partial B_0}{\partial t} + \frac{1}{I}\frac{\partial I}{\partial t}\right\} \quad (7.53)$$

Transforming $\mu_0 = \sqrt{1-y^2}$ and taking into account that in the case of no parallel electric fields the equatorial pitch angle is conserved over a bounce period, we have:

$$\boxed{\begin{aligned}\langle\frac{d\mu_0}{dt}\rangle = -\frac{(1-\mu_0^2)I}{2h\mu_0}\left\{ v_{0R}\left(\frac{1}{2B_0}(\nabla B_0)_{\hat{R_0}} + \frac{1}{R_0} + \frac{1}{I}(\nabla I)_{\hat{R_0}}\right) + \right. \\ \left. v_{0\phi}\left(\frac{1}{2B_0}(\nabla B_0)_{\hat{\phi}} + \frac{1}{I}(\nabla I)_{\hat{\phi}}\right) + \frac{1}{2B_0}\frac{\partial B_0}{\partial t} + \frac{1}{I}\frac{\partial I}{\partial t}\right\}\end{aligned}} \quad (7.54)$$

Additionally, the bounce-averaged rate of change of the kinetic energy of the particle is derived from the conservation of the first adiabatic invariant:

$$\frac{d}{dt}\left(\frac{1}{2}\frac{mv_\perp^2}{B}\right) = \frac{d}{dt}\left(\frac{Ey^2}{B_0}\right) = 0 \quad (7.55)$$

$$\frac{dE}{dt} = \frac{E}{B_0}\frac{dB_0}{dt} - \frac{2E}{y}\frac{dy}{dt} \quad (7.56)$$

Substituting in Equations 7.53 and 7.49, Equation 7.56 becomes:

$$\frac{dE}{dt} = \frac{E}{B_0}\left(1-\frac{I}{2h}\right)\frac{\partial B_0}{\partial t} + Ev_{0R}\left[\frac{1}{B_0}\left(1-\frac{I}{2h}\right)\frac{\partial B_0}{\partial R_0} - \frac{1}{h}\left(\frac{I}{R_0} + \frac{\partial I}{\partial R_0}\right)\right] + Ev_{0\phi}\left[\frac{1}{B_0}\left(1-\frac{I}{2h}\right)\frac{1}{R_0}\frac{\partial B_0}{\partial \phi} - \frac{1}{hR_0}\frac{\partial I}{\partial \phi}\right] - \frac{E}{h}\frac{\partial I}{\partial t} \quad (7.57)$$

Again, bounce-averaging, for the case of no parallel electric fields, we obtain:

$$\boxed{\begin{array}{c}\langle\frac{dE}{dt}\rangle = \frac{E}{B_0}\left(1-\frac{I}{2h}\right)\frac{\partial B_0}{\partial t} + Ev_{0R}\left[\frac{1}{B_0}\left(1-\frac{I}{2h}\right)(\nabla B_0)_{\hat{R_0}} - \right. \\ \left.\frac{1}{h}\left(\frac{I}{R_0}+(\nabla I)_{\hat{R_0}}\right)\right] + Ev_{0\phi}\left[\frac{1}{B_0}\left(1-\frac{I}{2h}\right)(\nabla B_0)_{\hat{\phi}} - \frac{1}{h}(\nabla I)_{\hat{\phi}}\right] - \frac{E}{h}\frac{\partial I}{\partial t}\end{array}} \tag{7.58}$$

Substituting a dipolar magnetic field in Equation 7.54 and Equation 7.58 we obtain the *Ejiri* (1978) formulae (Equation 7.12 and Equation 7.13, respectively).

Moreover, the analytical approximation of *Ejiri* (1978) for the bounce-averaged gradient-curvature drift (Equation 7.7) is replaced by the bounce average of the following general formula:

$$\vec{V}_{GC} = -\frac{m_t}{qB^4}\left(v_{||}^2 + \frac{v_{\perp}^2}{2}\right)\left[\left(\nabla\frac{B^2}{2}\right)\times\vec{B}\right] \tag{7.59}$$

The bounce - averaged geocorona hydrogen density and plasmaspheric electron density are numerically calculated, for an arbitrary magnetic field:

$$\langle H_{density}\rangle = \frac{1}{S_B}\int_{m_1}^{m_2} n_H \frac{ds}{1-\frac{B(s)}{B_m}} \tag{7.60}$$

$$\langle n_{pe}\rangle = \frac{n_{pe0}}{S_B B_0}\int_{s_m}^{s_m{}'} ds\frac{B(s)}{\mu} \tag{7.61}$$

The details of the numerical implementation and testing are described in the following section.

7.4 Numerical Implementation and Testing

7.4.1 Implementation of numerical integrals of I and h

As previously stated, the first step was to replace the analytical formulae for I (Equation 7.8) and h (Equation 7.3) with numerical integrals along the field line.

To do so, the integration was performed assuming that the magnetic field varies linearly in between two consecutive grid points along the field line and the value of the integral was analytically estimated between any two neighboring grid points. That is:

$$I = \frac{1}{R_0} \sum_i \frac{2}{3} \frac{1}{\sqrt{B_m}} \frac{s_{i+1} - s_i}{B_i - B_{i+1}} \left((B_m - B_{i+1})^{3/2} - (B_m - B_i)^{3/2} \right) \tag{7.62}$$

$$h = \frac{1}{2R_0} \sum_i 2\sqrt{B_m} \frac{s_{i+1} - s_i}{B_i - B_{i+1}} \left((B_m - B_{i+1})^{1/2} - (B_m - B_i)^{1/2} \right) \tag{7.63}$$

where ds_i is the length of the field line element at the current grid point. At the mirror points I and h become

$$\Delta I_m = \frac{2}{3} \frac{1}{\sqrt{B_m}} \Delta s \sqrt{(B_m - B_i)} \tag{7.64}$$

$$\Delta h_m = 2\sqrt{B_m} \frac{\Delta s}{\sqrt{B_m - B_i}} \tag{7.65}$$

where

$$\Delta s = \frac{(B_m - Bi)\,(s_i - s_{i-1})}{B_{i-1} - B_i} \tag{7.66}$$

is the field line element at the end segments (at the mirror points).

This assumption allowed us to avoid the singularities occurring at the mirror

point in the calculation of h. The grid along the field line is uniform in latitude and symmetric with respect to the equatorial plane. Nevertheless, this means the grid is not uniform in the field line length, although HEIDI can accommodate non-uniform grids as well (e.g. field aligned grids that are more refined in the equatorial region, to better resolve the equatorially mirroring particles).

Figure 7.1 presents the integration results of $I = \frac{1}{R}\int_{s_m}^{s_{m'}} ds\sqrt{1-\frac{B(s)}{B_m}}$ for three choices of the particle's pitch angle: 30° (top panel), 60° (middle panel) and 88° (bottom panel) for a L shell value of 4. The choice of 88° pitch angle was made in order to illustrate the profile of these parameters for near equator mirroring particles. For easy reference, in each plot the blue, red and green lines have constant slopes of 1, 1.5 and 2 respectively. This is a proxy for the order of accuracy of the integration method. Note that the scale is logarithmic. The relative error was calculated in the following manner:

$$Relative\ \ Error = True\ \ Value\ \ of\ \ I - I(nPoint) \tag{7.67}$$

where the true value of I is set to be that of the integral for a very refined grid, in our case 100001 points, and I(nPoint) is the value of I for nPoint grid size. We note that the integration has a second order accuracy.

Similarly to Figure 7.1, Figure 7.2 shows the integration results for $h = \frac{1}{2R}\int_{s_m}^{s_{m'}} \frac{ds}{\sqrt{1-\frac{B(s)}{B_m}}}$. Since this expression contains a singularity at the mirror points, our method of linearizing the magnetic field in between two consecutive field line grid points, is less accurate than second order. The fluctuations seen in the behaviour of h are due to the fact that the integration on the last segment has a relatively large contribution to the total value of the integral and at the end points brings up a larger error than in the case of the I integral. However, this is a good method for the purpose of our work and both integrals are converging quite fast for a reasonably sized grid, that is 101 points.

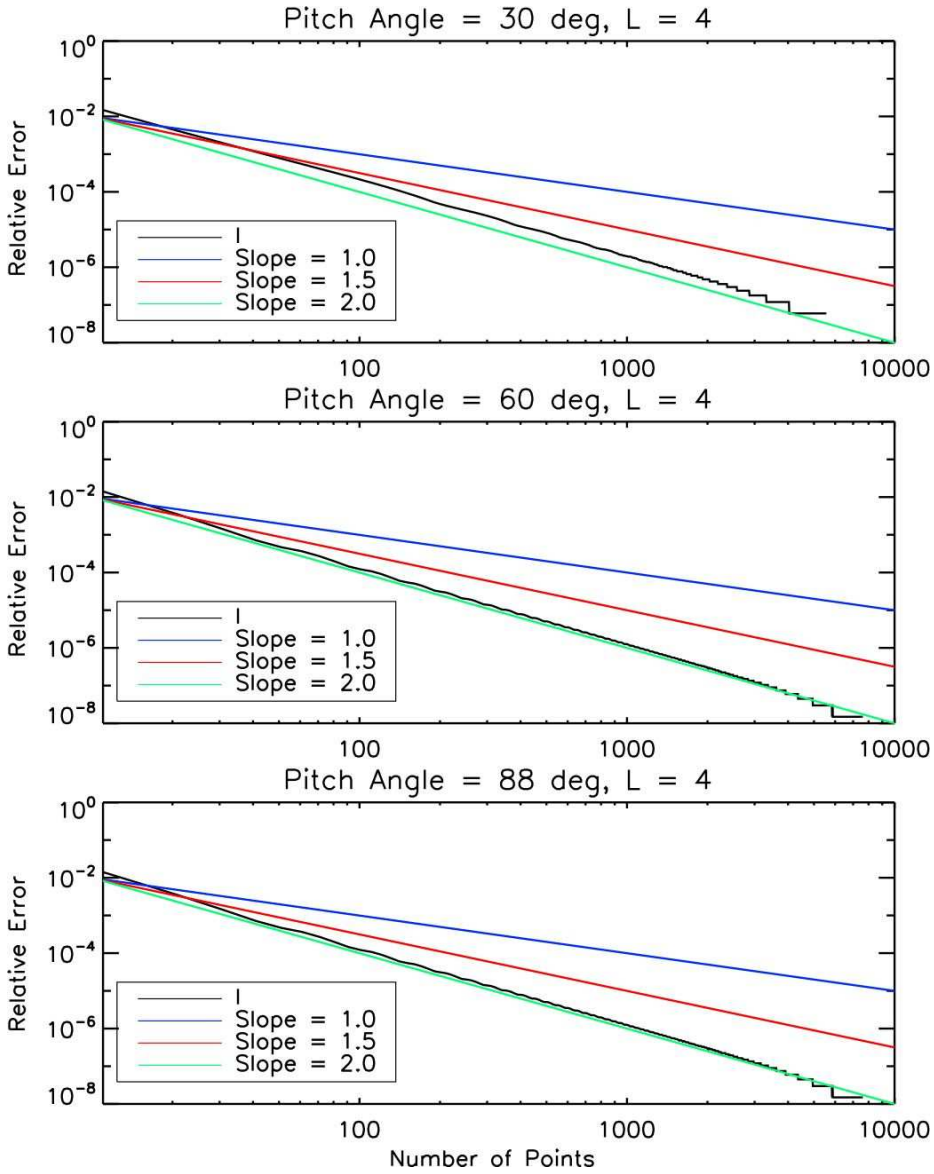

Figure 7.1: Relative error for I calculations versus number of points along a field line for three choices of pitch angle: 30° (top), 60° (middle) and 88° (bottom) for L shell = 4. Black line shows the results of the integral while the blue, red and green show lines with slopes of 1, 1.5 and 2 respectively.

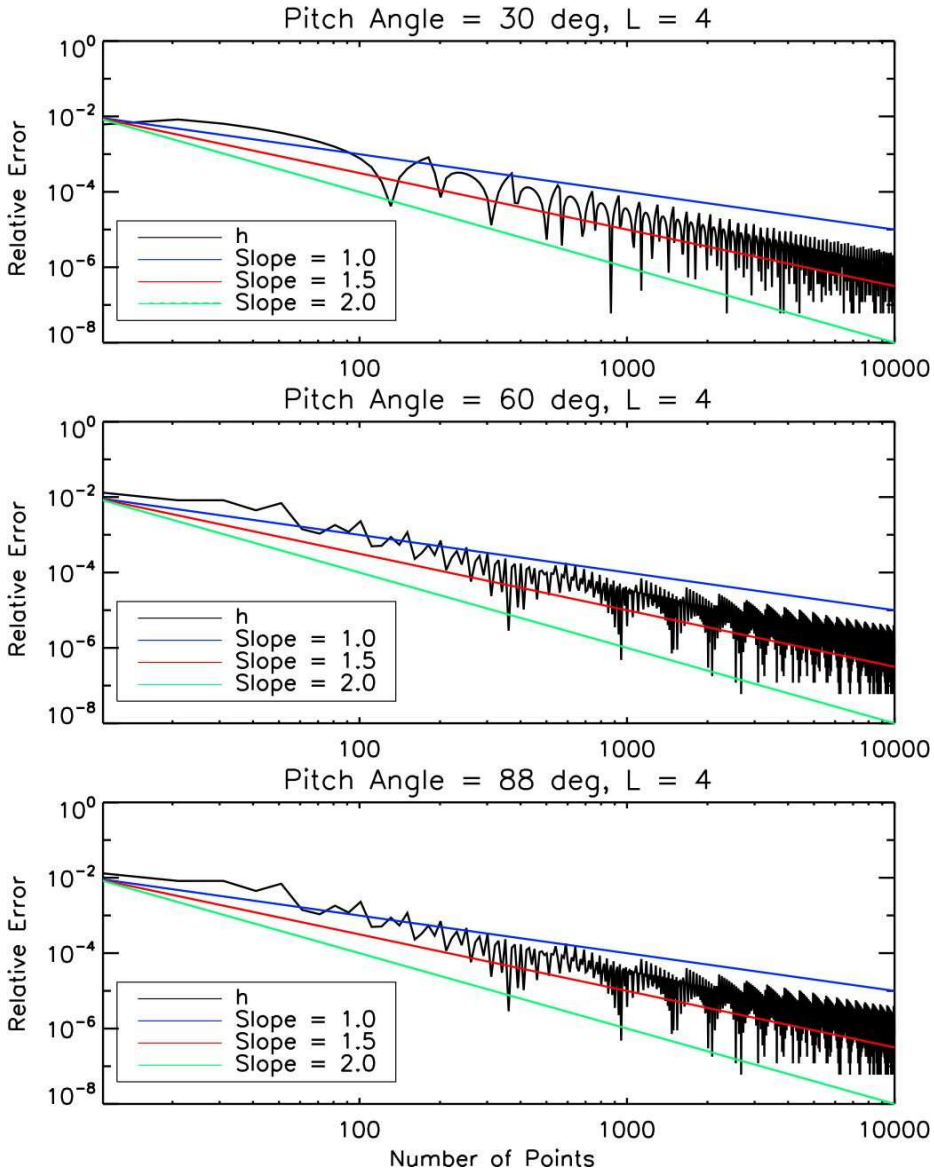

Figure 7.2: Relative error for h calculations versus number of points along a field line for three choices of pitch angle: 30° (top), 60° (middle) and 88° (bottom) for L shell = 4. Black line shows the results of the integral while the blue, red and green show lines with slopes of 1, 1.5 and 2 respectively.

To further reinforce our choice of 101 grid points, the left panels in Figure 7.3 show the relative error to the converged value (black line) and the relative error to the analytical value (the value as provided by *Ejiri* (1978) formula) for the three choices of pitch angle described above. On the right, we show a close-up of the same plots on the left. A dotted blue line marks the 101 point choice. Only the X axis is logarithmic for this plot. We note that the relative error for both comparisons is under 1%. However, the *Ejiri* (1978) expressions for I and h are numerical approximations as well and not analytical solutions (although for simplicity we refer to them as 'analytical', because they are expressed as a trigonometric polynomial function).

Figure 7.4 is a replica of Figure 7.3, only now for the h integration results. Again, the relative difference between both the converged and analytical values are under 1% for all pitch angles for 101 grid points along the magnetic field line.

7.4.2 Model Validation

To illustrate the differences between the dipolar and non-dipolar HEIDI, extensive tests were performed using an idealized magnetic field configuration, that is a stretched dipole in the dawn-dusk direction. The motivation behind this choice was that this configuration provides us with a simple, intuitive, non-dipolar solution for the magnetic field that can be easily tested. When the stretching was approaching zero, namely the magnetic field would approach the dipolar configuration, we were able to recover the dipole analytical solution. The HEIDI model was run including all 4 species, with the electric field provided by the Weimer model. The field aligned grid size was set to 101 points.

Moreover, this testing also enabled us with a measure of how much the distribution function changes when not only the magnetic field is not dipolar but also the bounced averaged coefficients are calculated consistently.

To do so, a dipolar magnetic field is being stretched in the Y and Z directions

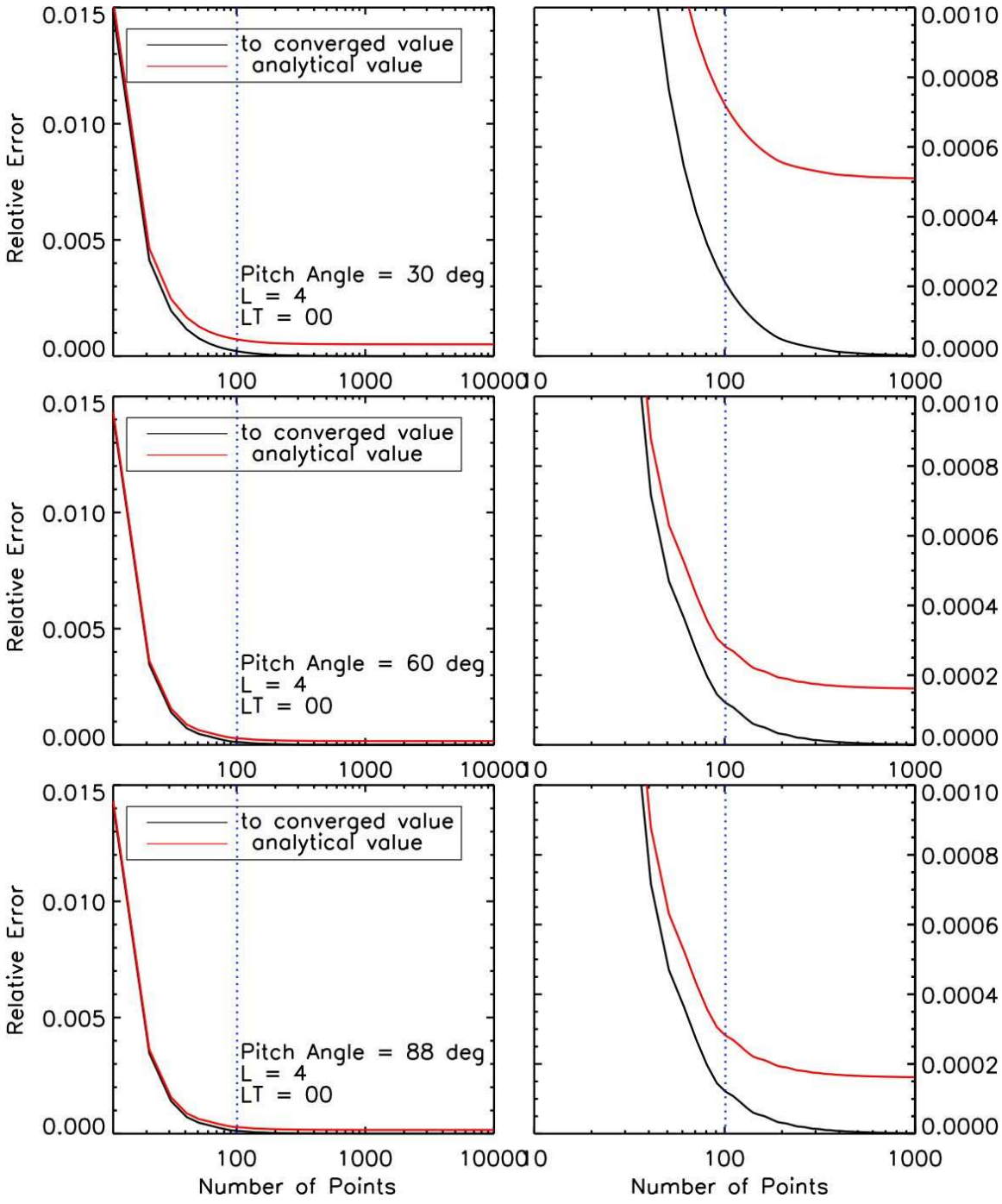

Figure 7.3: Relative error of the results of numerical integration of I for for three choices of pitch angle:30° (top), 60° (middle) and 88° (bottom) for L shell = 4 and Local Time (LT) = 0.0. Right panels show a close-up of the profile. Note that the x axis is logarithmic.

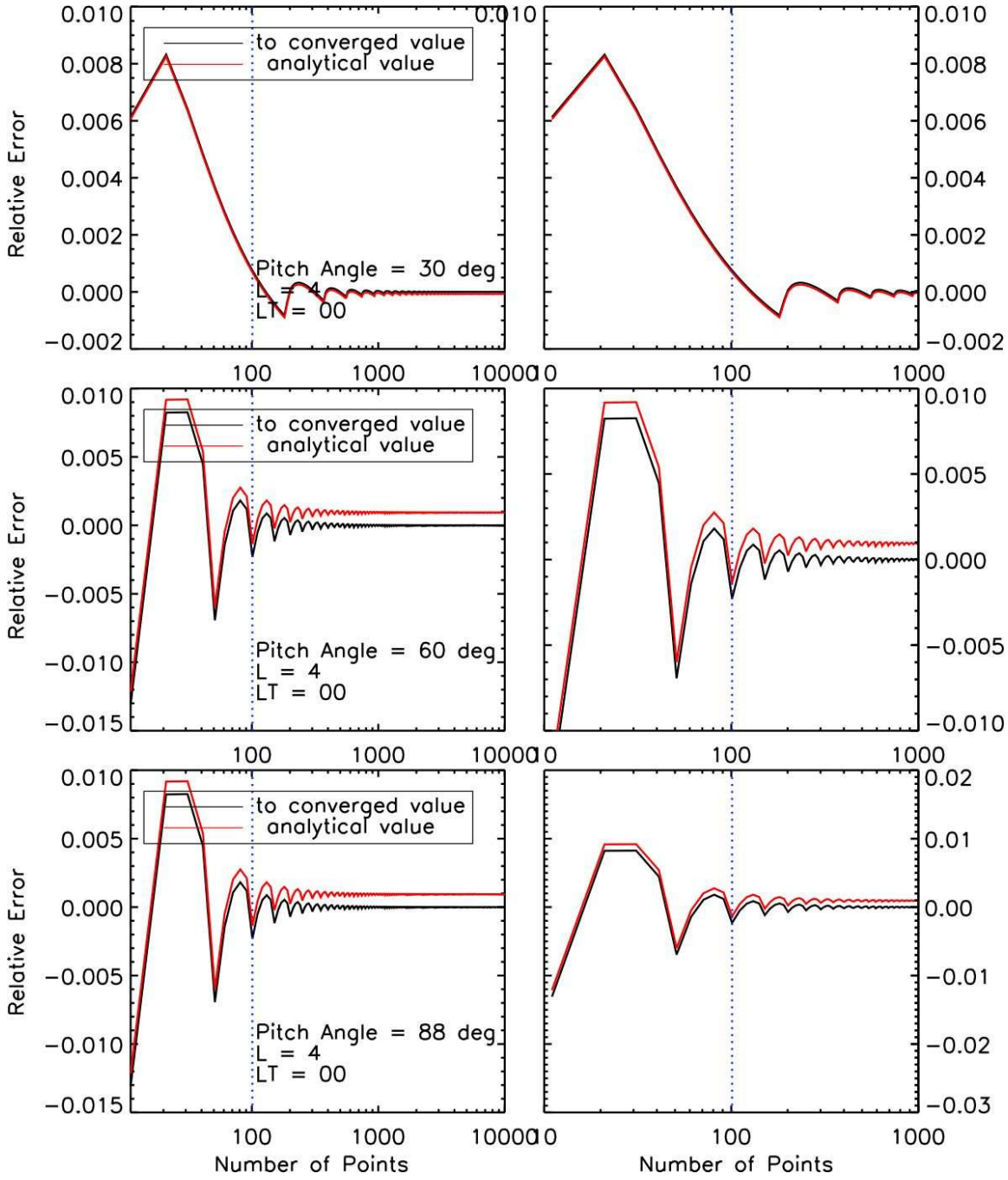

Figure 7.4: Relative error of the results of numerical integration of h for for three choices of pitch angle:30° (top), 60° (middle) and 88° (bottom) for L shell = 4 and Local Time (LT) = 0.0. Right panels show a close-up of the profile. Note that the x axis is logarithmic.

by a factor α and β, respectively. The stretched dipole radial distance $R_{stretched}$ is expressed similarly to the dipole radial distance $R_{dipole} = \sqrt{x^2 + y^2 + z^2}$ as:

$$R_{stretched} = \sqrt{x^2 + (\beta y)^2 + (\alpha z)^2} \tag{7.68}$$

Therefore the stretched magnetic dipole in Cartesian coordinates is defined as:

$$B = \frac{1}{R_{stretched}^{5/2}} \left[(3zx\alpha)\, \hat{e_x} + (3zy\alpha)\, \hat{e_y} + \frac{1}{\alpha} \left(2z^2\alpha^2 + x^2 + y^2\beta^2 \right) \hat{e_z} \right] \tag{7.69}$$

To find the latitude where the stretched field line crosses the $R = 1$ surface, we express the radial distance for the stretched dipole in spherical coordinates:

$${R_{stretched}}^2 = (LR_e cos^2\lambda)^2 [cos^2(\lambda)(cos^2(\phi) + \beta^2 sin^2(\phi)) + \alpha^2 sin^2(\lambda)] \tag{7.70}$$

where $R_{dipole} = LR_e cos^2\lambda$ is the distance to the unstretched dipole field line. For a given ϕ, we need so solve for λ.

$$1 = L^2 cos^4\lambda [cos^2(\lambda)(cos^2(\phi) + \beta^2 sin^2(\phi)) + \alpha^2 sin^2(\lambda)] \tag{7.71}$$

Letting

$$\zeta = cos^2(\lambda) \tag{7.72}$$

$$\gamma = cos^2(\phi) + \beta^2 sin^2(\phi) \tag{7.73}$$

The equation for the foot point latitude at the Earth surface is:

$$\zeta^3(\gamma - \alpha^2) + \zeta^2\alpha^2 - \frac{1}{L^2} = 0 \tag{7.74}$$

If we take $\alpha = \beta = 1$, which implies $\gamma = 1$, we recover the dipole solutions for latitude:

$$\zeta^2 = \frac{1}{L^2} \tag{7.75}$$

Which yields two symmetric solutions for latitude: $\lambda_1 = arccos\sqrt{\frac{1}{L}}$ and $\lambda_2 = -arccos\sqrt{\frac{1}{L}}$.

Figure 7.5 shows the magnitude of the magnetic field in the equatorial plane for a dipolar field (left) and the stretched dipole (right). The stretching factors we used were $\alpha = 1.1$ equivalent to a 10% stretching in the Z direction and $\beta = \frac{1}{\alpha}$, meaning that the dipole is actually compressed in the Y direction by about 9%. A black disk is drawn in the center with the radius 1.75 Re, which is the inner boundary in HEIDI. The X and Y axes are normalized to the radius of the Earth. The stretching can be seen from isocontours of magnitude that change from circles in the dipole case to ellipses for the stretched dipole. Comparing the values of the magnetic field magnitude for the stretched versus non-stretched configuration, we note that at a fixed radial distance, the stretched dipole field values are higher in regions close to the X axis. Conversely, close to the Y axis, the dipole field values are higher. This is consistent with Equation 7.69.

Figure 7.6 shows dial plots of the I results for 30° (top), 60° (middle) and 88° (bottom) pitch angles for the dipole field (left) and the stretched dipole field (right). For the case of the dipole, the values of I are relatively constant, in agreement with the analytical formula (Equation 7.15), which is only dependent on the pitch angle and predicts a constant value, independent of the radial distance. Nevertheless, the plots display small gradients with azimuthal symmetry that are due to numerical

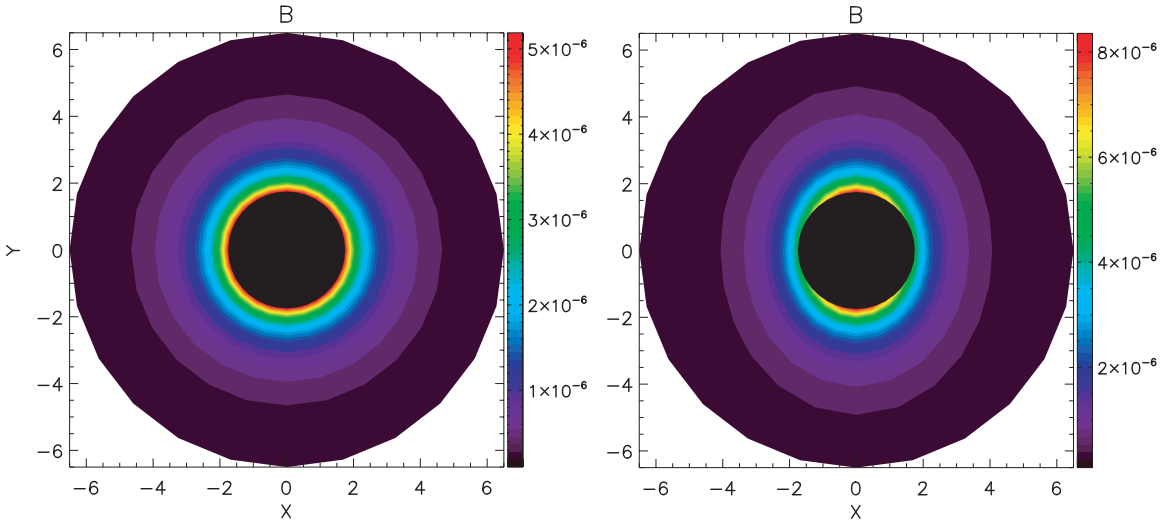

Figure 7.5: Dial plots of magnetic field magnitude on the equatorial plane. On the left is presented the dipolar field magnitude while on the right, the stretched dipole values.

artifacts on the integration. We also note an inverse proportionality between the values of I and those of pitch angle. This is to be expected since for lower pitch angles, field line length between mirror points is greater and therefore the integration is done over a larger domain. Nevertheless, the relative errors to the 'analytical' solution are small (see Figure 7.3). For the case of a stretched dipole magnetic field, the configuration changes dramatically. At a fixed radial distance, the values of I are smaller in the vicinity of the Y axis and increase as we move towards the X axis. This is due to the fact that the magnetic field magnitude at these locations displays the exact opposite behaviour (remember that the I is proportional with the integral of $\sqrt{1-\frac{B(s)}{B_m}}$ between the mirror points). Moreover, as opposed to the case of a dipole where the values of I are relatively constant for a given pitch angle, in the case of the stretched dipole the values of I range over a larger domain. However, the maximum values are smaller than for the dipole case and this is due to the geometry of the field line. For the case of 88° pitch angle, that is near equator mirroring particles, the numerical values of I span over the greatest range. This is because the integration

domain is the smallest and therefore the numerical errors are largest for our uniform grid. Also, the density of points along the field line decreases with increasing radial distance and therefore the solution is less accurate the farther away we go from the inner boundary (i.e. we expect that 6.0×10^{-4} at $L = 2$ is a better estimate than 4.0×10^{-4} at $L = 6$ for $I(88°)$; see Figure 7.6 bottom left plot).

Similarly to Figure 7.6, Figure 7.7 shows the distribution of h values for dipole configuration (left panels) and stretched dipole (right panels) for the three choices of pitch angle described above. Again, for the dipole case and for a fixed pitch angle, the values are relatively constant and similar to the analytical solution. The gradients that are apparent in the corresponding plots are due to the oscillatory nature in the error from the integration on the end segments, near the mirror points. To understand the behaviour of h we need to remember that it is defined as $h = \frac{1}{2R}\int_{s_m}^{s_{m'}} \frac{ds}{\sqrt{1-\frac{B(s)}{B_m}}}$. So the profile of h would be given by the interplay between the two terms in the integrand. Although the $\frac{1}{\sqrt{1-\frac{B(s)}{B_m}}}$ in increasing with increasing magnetic field (i.e. for a fixed radial distance it is larger in regions close to the Y axis), the ds term has the opposite behaviour due to the field compression along the Y axis. When the equatorial magnetic field becomes depressed, the distance between the mirror points can be shortened by the ring current in order to conserve the first adiabatic invariant. Just as in the case of I, h values for near equator mirroring particles span over a larger range for the same reasons explained above.

To illustrate the profile of the bounce-averaged rate of change in the particle's energy, Figure 7.9 presents the distribution of $\langle \frac{dE}{dt} \rangle$ (Equation 7.58) for a dipole configuration (left panels) and a stretched dipole (right panels) for all three choices of pitch angle aforementioned. We note that the distribution is similar for all the pitch angles but the values are slightly decreasing with decreasing pitch angle for both stretched and non-stretched dipole cases. The asymmetry of the distribution is due to the asymmetric electric potential generated by the Weimer model (Figure 7.8).

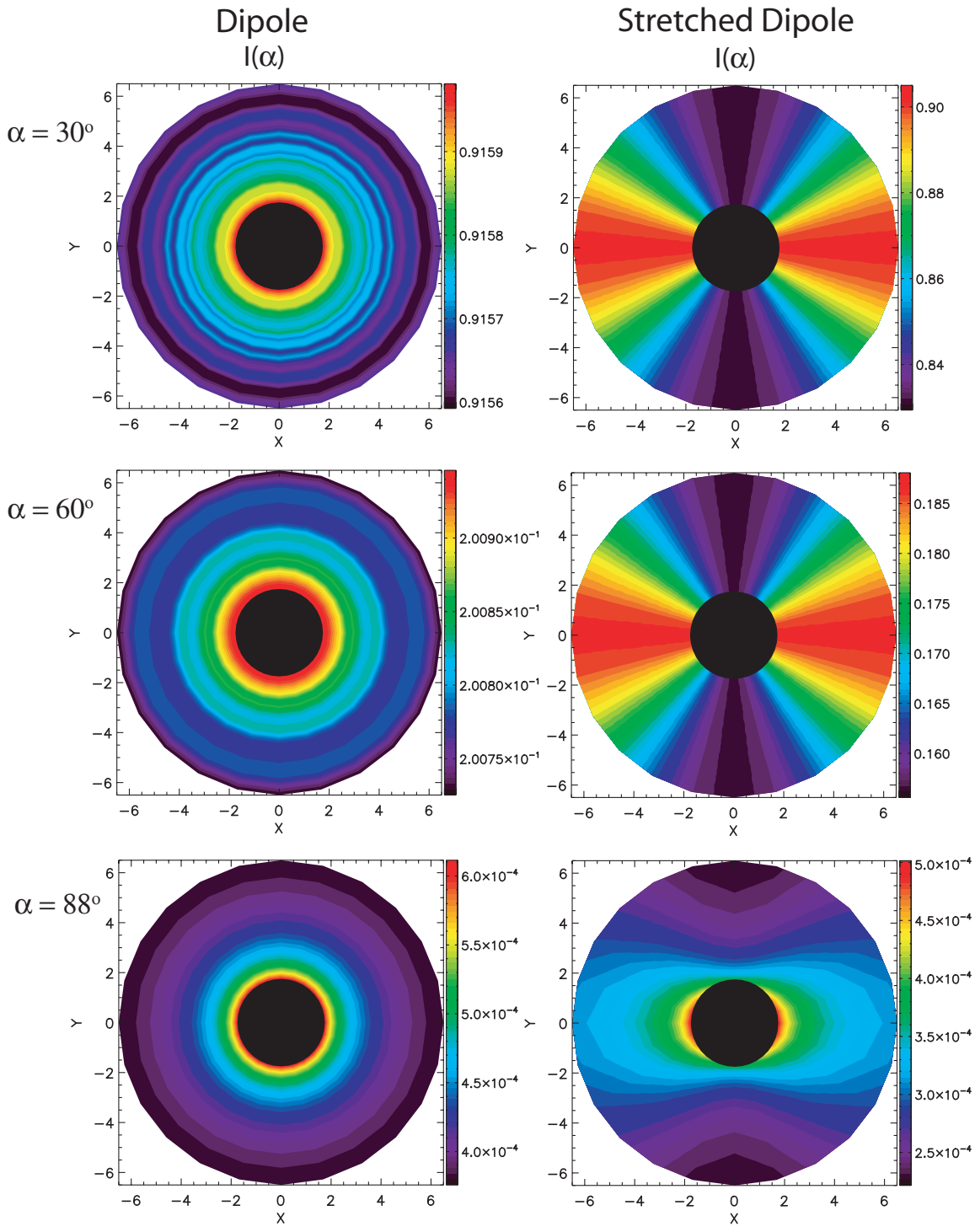

Figure 7.6: The distribution of I for dipole configuration (left panels) and stretched dipole (right panels). From top to bottom are presented the results for three choices of pitch angles: 30° (top), 60° (middle) and 88° (bottom).

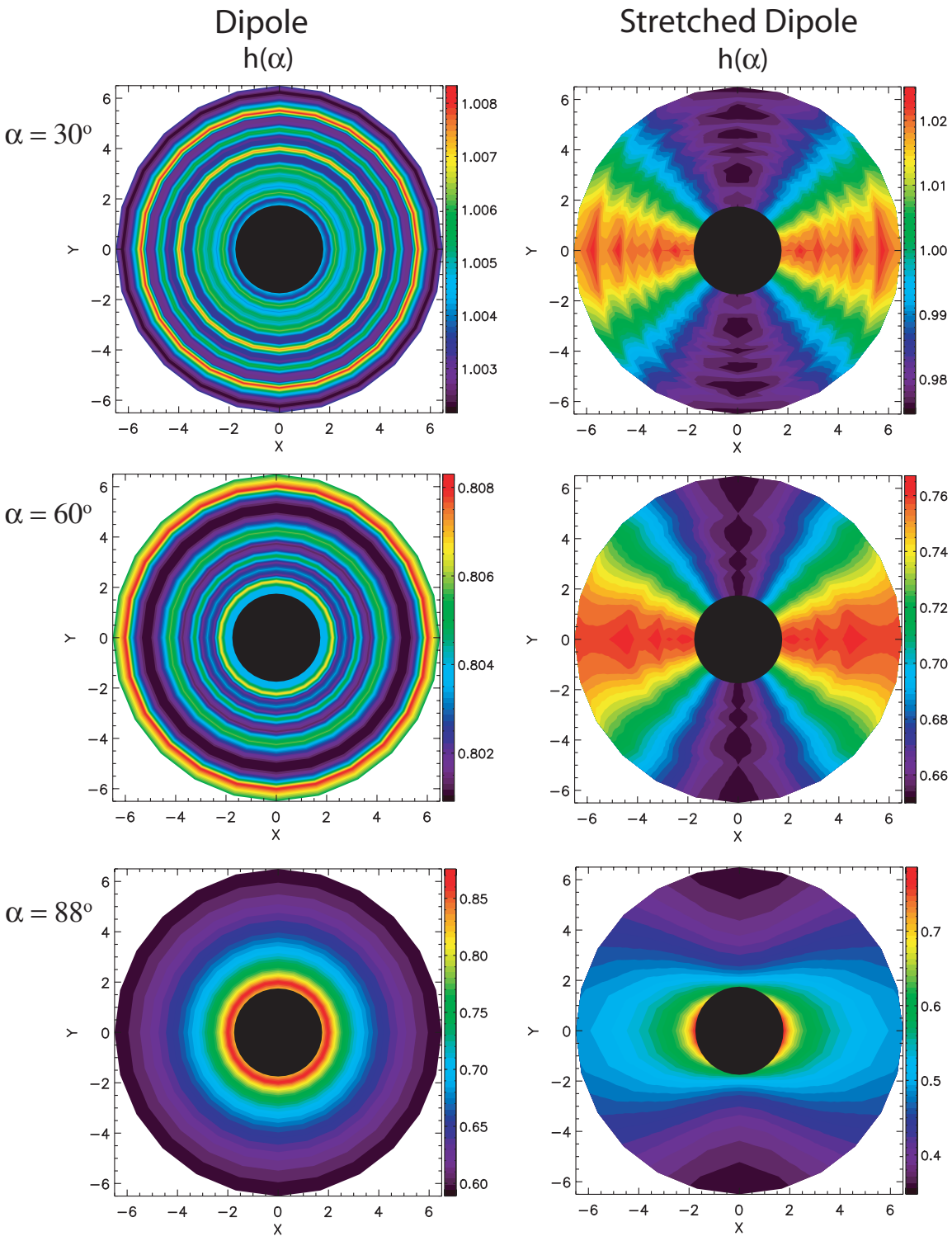

Figure 7.7: The distribution of h for a dipole configuration (left panels) and stretched dipole (right panels). From top to bottom are presented the results for three choices of pitch angles: 30° (top), 60° (middle) and 88° (bottom).

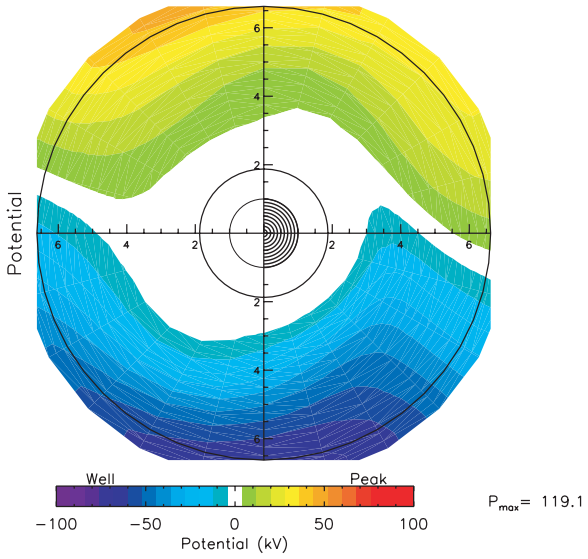

Figure 7.8: Convection electric potential contours generated by the Weimer model. The view is over the northern hemisphere and the distances are expressed in Earth radii (R_e).

The topology varies significantly from the dipolar configuration even when the dipole field is distorted by only 10% which causes the values to increase by about 25%. A positive change in the particles energy is seen in the evening sector (1800 LT - 0000LT quadrant) while the afternoon sector (0600 and 1200 magnetic local time) is dominated by negative change in energy for the dipole case. However, when the magnetic field is compressed in the Y direction and stretched in the Z direction (right panels), the whole dayside becomes dominated by negative $\langle \frac{dE}{dt} \rangle$. This is due to the change in the magnetic field, with a stronger field on the dawn and dusk side at the same radial distance as compared to the dipole magnetic field, which in turn changes the gradient curvature drift, altering the particles total radial drift.

Similarly to Figure 7.9, Figure 7.10 presents the distribution of $\langle \frac{d\mu_0}{dt} \rangle$ (Equation 7.54) for the dipole configuration (left panels) and the stretched dipole (right panels) for all three choices of pitch angle. We note the in this case, the values of $\langle \frac{d\mu_0}{dt} \rangle$ are increasing with decreasing pitch angle for both magnetic field configurations. Again, the asymmetry is due to the electric potential generated by the Weimer model. For

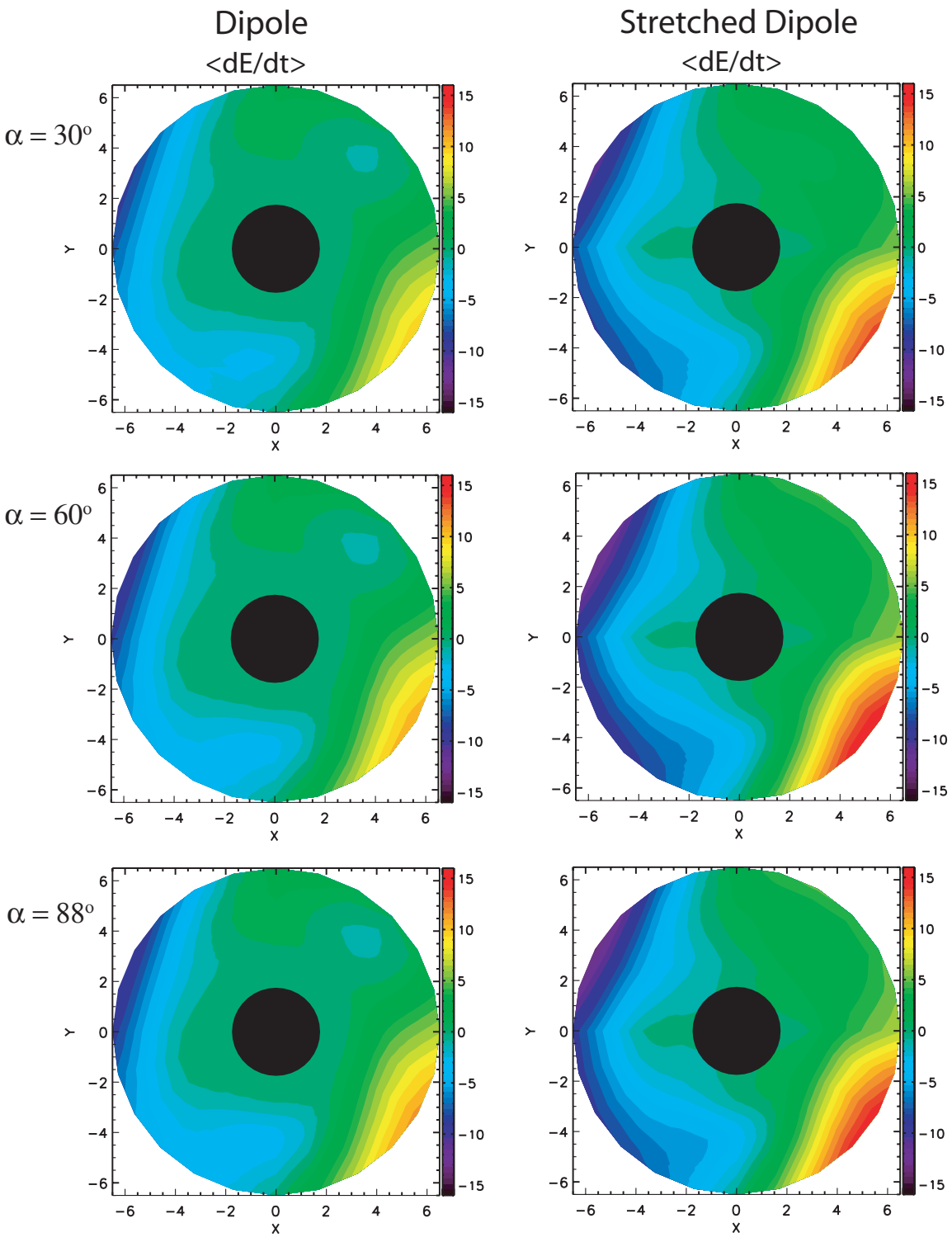

Figure 7.9: The distribution of $\frac{dE}{dt}$ for a dipole configuration (left panels) and stretched dipole (right panels). From top to bottom are presented the results for three choices of pitch angles: 30° (top), 60° (middle) and 88° (bottom).

$\langle \frac{d\mu_0}{dt} \rangle$, the locations of minima and maxima are the opposite of those in the case of $\langle \frac{dE}{dt} \rangle$.

In the dipolar magnetic field configuration, the change in particle's pitch angle is now negative in the evening sector and positive in the afternoon sector. When the magnetic field is non-dipolar (right panels), the topology changes significantly and the values are only slightly higher. This change in the distribution is due to not only the change in the magnetic field strength but also due to asymmetry in the field line length between the mirror points. For a certain equatorial pitch angle in a dipole field at a fixed equatorial distance, the magnetic field strength as well as the field line length are the same in all local times. Therefore the change in the particle's equatorial pitch angle is mainly due to the convection drift. This is no longer true for a non-dipolar field.

To illustrate such drifts, Figure 7.11 shows the drift in the $\hat{\phi}$ direction for a analytical dipole (Equation 7.7) and the stretched dipole configuration for a particle with kinetic energy 107 keV. We note that V_ϕ due to a stretched dipole field has a higher value compared with the V_ϕ dipole field. Also, due to azimuthal symmetry of the dipolar magnetic field, the drift is constant at all local times. However, for a particle mirroring in the vicinity of the equatorial plane, the stretched dipole produces a V_ϕ that displays an oscillatory behaviour, as expected.

Finally, we ran an idealized event simulation, and the results are presented in Figure 7.12. We note that there are not large differences between the left (HEIDI with a dipole field and *Ejiri* (1978) formulations for the bounce averaged coefficients) and center plots (HEIDI with a dipole field and the new formulations and numerical integrations for the bounce averaged coefficients), that is, our new formulations can recover the dipolar analytical solution of *Ejiri* (1978). The right hand side of Figure 7.12 shows that the stretched dipole configuration produces a significant increase in the maximum pressure. This is due to the dawn to dusk stretching of the dipole, the

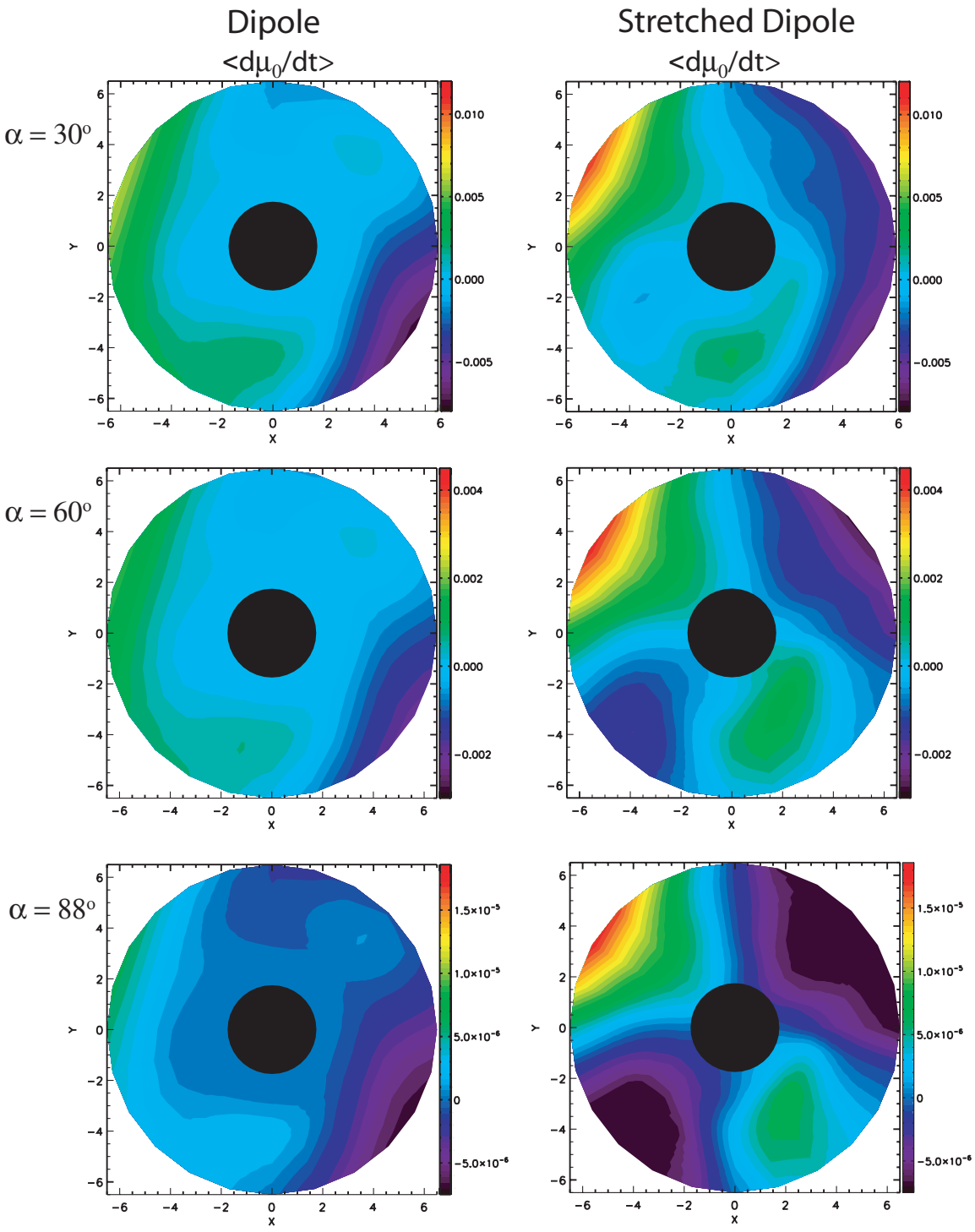

Figure 7.10: The distribution of $\frac{d\mu_0}{dt}$ for dipole configuration (left panels) and stretched dipole (right panels). From top to bottom are presented the results for three choices of pitch angles: 30° (top), 60° (middle) and 88° (bottom).

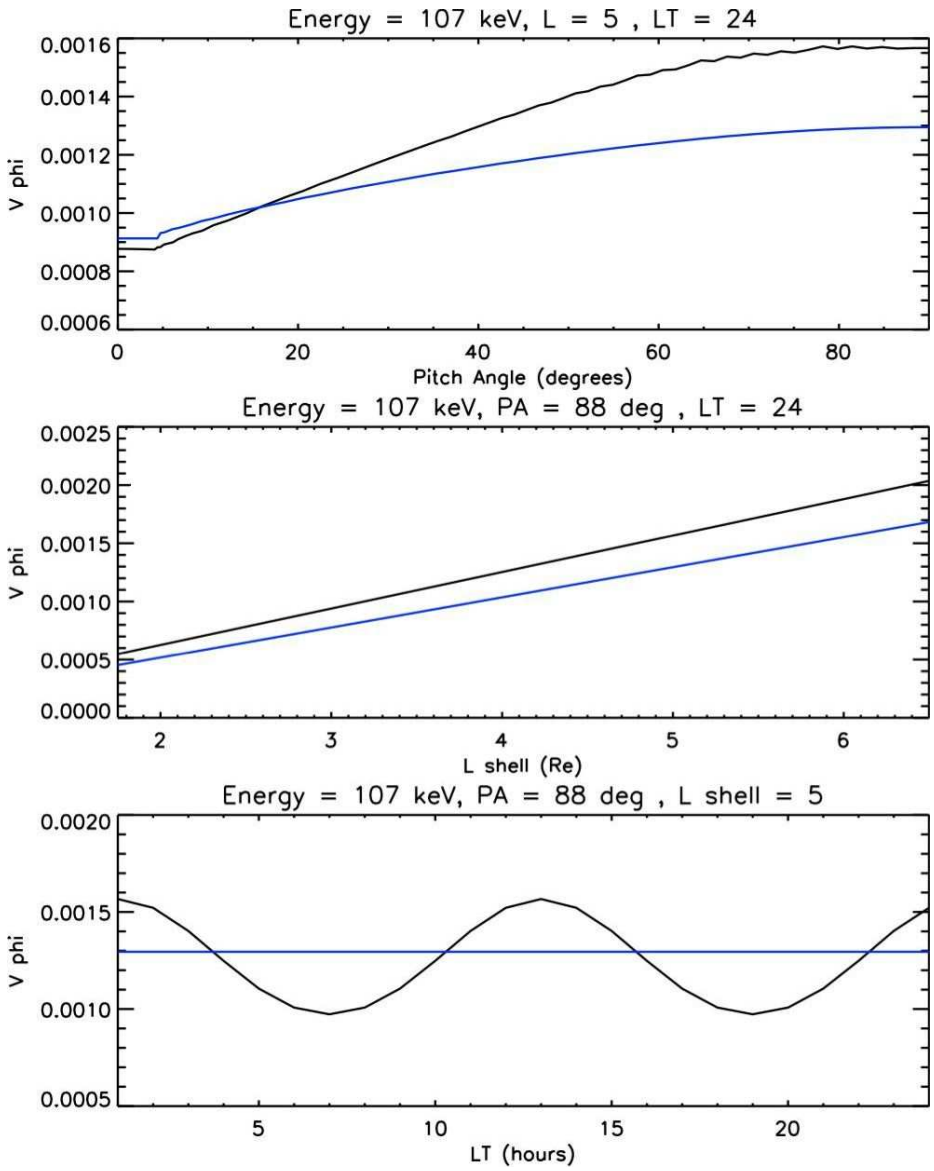

Figure 7.11: Particle drift in the $\hat{\phi}$ direction for a dipole (blue lines) and the stretched dipole configuration (black lines). From top to bottom we present the V_ϕ versus pitch angle, V_ϕ versus radial distance and V_ϕ versus local time. Please note the V_ϕ is in units of (L shells/sec)

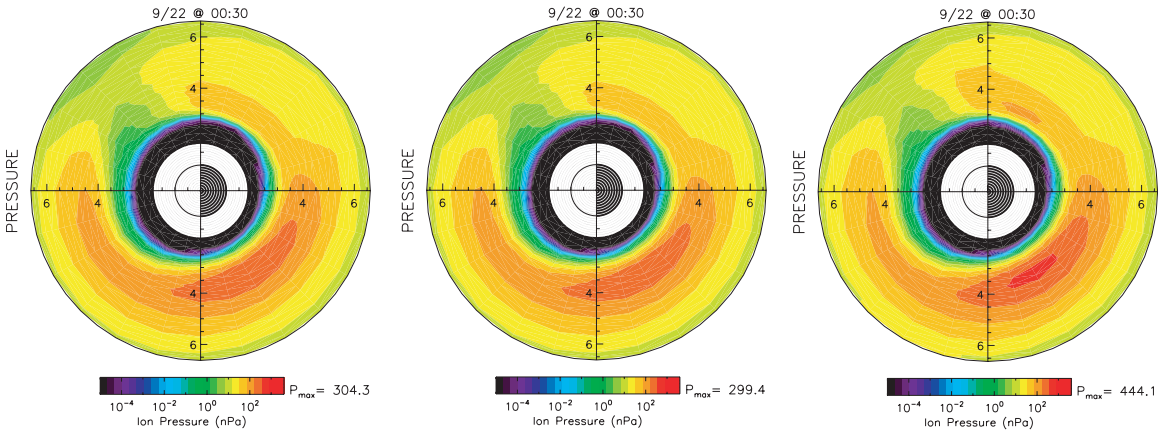

Figure 7.12: Pressure distribution for HEIDI with dipole field and *Ejiri* (1978) formulations for the bounce averaged coefficients (left), HEIDI with dipole field and new formulations for the bounce averaged coefficients (center), HEIDI with stretch dipole magnetic field (right)

nightside injected particles drift in different regions of magnetic field.

7.5 Conclusions and Future Work

We now have a new version of HEIDI that is capable of accommodating arbitrary magnetic fields. A new formalism for the bounce-averaged coefficients has been developed, implemented and tested within HEIDI.

However, additional improvements are necessary for a more comprehensive model. Electric fields in the magnetosphere have both potential and inductive components. For instance, the inclusion of inductive electric fields that arise due to the time varying nature of the magnetic field are believed to play an important role in a realistic description of the convection. Previous models that included such fields (*Fok and Moore*, 1997) were based on ionospheric grids and used the assumption that the ionospheric foot-point of the magnetic field is fixed in the ionosphere for the process of magnetic reconfiguration. Therefore a measure of the field displacement can be used as a proxy for the inductive component of the electric field. On the other

hand, inclusion of inductive electric fields can be quite a challenging task when using equatorial based grids, since it requires a Biot Savart like integration over the whole domain. As an alternative, the convection velocity provided by BATSRUS can be used. Nevertheless, a quantitative comparison between the two solutions can be performed.

CHAPTER VIII

Conclusions and Future Work

8.1 Conclusions

Throughout this dissertation, the nature of the relationship between the storm-time ring current and the solar wind parameters is examined via extensive data analyses and global modeling of the magnetosphere. Results presented in Chapters II, IV, V and VI improve our understanding of the storm time ring current formation and decay and the its global magnetospheric feedback under different solar wind conditions. Chapter IV motivates the need for a new inner magnetospheric model, described in detail in Chapter VII. All of the outstanding problems stated in Chapter I, Section 1.7 have been addressed.

Chapter II addressed the first goal by examining a statistical study of intense storms occurring at solar maximum, employing the Superposed Epoch Analysis technique on both the solar wind data from ACE and geosynchronous observations by the MPA instruments from the LANL satellites. Our study clearly demonstrates that certain parameters require a particular epoch time in order to reproduce an accurate behavior, while others are less sensitive to the epoch time choice and exhibit less spatial and temporal variation. We show that the *Gonzalez et al.* (1994) convention commonly used to illustrate intense storm behavior is met by superposed storm profiles, only if the superposition of the data is done no earlier than about 6 hours before

the storm peak for an average length storm. In addition, when the zero epoch time is set near the minimum Dst index, the storm sudden commencement features are lost. Therefore, a distinct epoch time is needed to accurately resolve particular solar wind features in the observations.

Close examination of the characteristics and the temporal evolution of geosynchronous plasma parameters as a function of local and epoch time reveals an eastward motion of the particle peak density with different local time densities, peaking at different moments during the development of the storm. This motion describes the inflow of fresh plasma sheet particles into the inner magnetosphere. Conversely, flow-out of the preexisting ring current is seen best with early epoch times. Thus the noon temperature is one of the bulk ion parameters that requires a time stamp closer to the start of the storm in order to be resolved in the averaging. However, the choice of the epoch time primarily matters in accurately depicting the size of the peak in all averaged quantities while the presence and shape of the peaks is unaltered by the time stamp used in the analysis.

In addition, our work indicates that, in the case of intense storms at solar maximum, the average duration of the main phase is found to be 13.2 hours, the ring current takes about 7.2 hours on average to reach maximum enhancement while the Late Main Phase lasts for approximately 6 hours, in agreement with the findings of *Pulkkinen et al.* (2007).

In light of the results obtained from the data analysis on Chapter II, global magnetosphere simulations using the Space Weather Modeling Framework were performed in order to evaluate the relationship between a simulated event driven by averaged solar wind upstream conditions with the results of the Superposed Epoch Analysis of the same set of individual storm simulations. The technique of Superposed Epoch Analysis smooths the data, therefore using averaged solar wind input in our simulations would allow for an examination of the role that transient spikes in the solar

wind play in the development of the storm. However, in spite of the similar nature of all events selected for this study, the model was unable to consistently reproduce their observed profile. Only for one of the five events (September 1999) the simulated D_{st} index reached an 'intense storm-like' value. Therefore, it was unprofitable to continue the superposed input study. Nevertheless, we can focus our attention on a single event rather than a series of events, and perform smoothing of the input parameters for just that particular storm.

The work outlined in Chapter V follows just this procedure. The assessment of the geoeffectiveness of transient spikes in the solar wind parameters was examined through global magnetospheric simulations of the September 22, 1999 event using a variety of different solar wind upstream conditions. Smoothing all solar wind parameters in the input data with windows of 1, 2 and 3 hours as well as just smoothing selected parameters (i.e., IMF B_z and density) reduced the energy input into the magnetosphere and therefore allowed us to quantify the role each of them played in the enhancement of the ring current. Our results indicate that a weaker ring current forms (a less intense storm develops) when the energy input is reduced by more than 13%. However, averaging longer than 60 minutes changes the plasma sheet characteristics as well as the entire magnetosphere and reduces the plasma sheet density and pressure. Small scale variations of the electric and magnetic field alter the inner magnetosphere energy density, while rapid small scale variations produce a more dynamic tail. On the other hand, removing only the high frequency spikes (smoothing up to 60 minutes time resolution) in the upstream input data produces essentially the same D_{st} time series, regardless of the averaging window length.

In addition, a two-phase, fast and then slow, recovery phase is seen in our model results, even though the observations only shows a one phase recovery of the observed event. Our findings suggest that the two phase recovery phase is due to a large cross polar cap potential combined with a low plasma sheet density, similar to the results

of *Liemohn et al.* (1999).

However, empirical prediction of the D_{st} index shows a linear relationship with the energy input as well as reveals a one phase recovery D_{st} profile, as expected (the empirical model has linear dependence on the solar wind parameters). Furthermore, the global simulation results based on this storm in September of 1999 indicate that varying the energy input produces variations in the magnetic field topology and strength. These changes reveal a magnetic field that is less stretched with a weaker ring current, therefore the particle orbits are altered and new loss processes are induced.

Moreover, we observe a non-linear relationship between the energy input and the response of the magnetosphere. We suggest that, while the short time fluctuations in the solar wind parameters did not have a significant contribution, a threshold in the energy input is necessary for a ring current to develop. Furthermore, while initial increase in the energy input enhances the magnetospheric response, as the power transferred to the system is increased, a saturation limit is reached and the growth of ring current is suspended. This implies that the energy flow in the magnetosphere is limited by an internal feedback mechanism as the magnetosphere acts as a low-pass filter on the interplanetary magnetic field.

Based on the results of Chapter IV, as a next step we examined a different type of solar wind driver. Therefore, the study presented in Chapter VI focuses on CIR driven storms. Again, using global simulations with both real and idealized solar wind upstream conditions for the CIR driven storm of November 10, 2003, we investigate the role of IMF B_z fluctuation periodicity in the transfer of solar wind mass and energy to the magnetosphere. Fast Fourier transforms of both input to and the response of the magnetosphere reveals that, although a 68 minute periodicity is seen in the data during the high speed stream, the model results show no indication of this periodicity being carried through the system. We suggest that this is possibly due to very low average energy of the input signal (IMF Bz) contained in the frequency corresponding

to 68 min periodicity (about twice the noise value) while most of it is spread out over the entire frequency range.

However, idealized upstream conditions in our simulation setup (with abrupt and periodic changes in the IMF B_z orientation) produce a highly sensitive cross polar cap potential to the changes in the IMF orientation. Moreover, both the inward and the outward flux at geosynchronous orbit as well as the current density distribution, exhibits similar behaviour. The fast and abrupt changes in the IMF Bz control the particle injection rate resulting in intermittent injection of particles seen in the simulations at the geosynchronous orbit. In this case most of the energy in the input signal is carried over to the same frequency in the geospace quantities. The input shows a peak in the power spectrum of more than 10 times the noise, meaning that most of the energy of the signal is contained at the frequency corresponding to 1 hour periodicity. However, it seems that the magnetosphere is sensitive to this frequency and quickly responds to it. Therefore, we suggest that a peak in the input power spectrum of at least 2 times larger that the background noise is needed in order to trigger a similar periodicity in the magnetosphere response.

Moreover, the outcome of Chapter IV is indicative of the need for a new model for the Inner Magnetosphere to be included into the SWMF. The HEIDI model has the advantage that it can solve the kinetic distribution function for all pitch angles, as opposed to the current version of RCM that is part of the SWMF, which assumes an isotropic pitch angle distribution. However, a new version of HEIDI was needed in order to consistently accommodate arbitrary magnetic fields. Therefore, a new formalism for the bounce-averaged coefficients has been developed, implemented and tested within HEIDI. Now we have a consistent model of the ring current, capable of treating arbitrary magnetic field configurations.

8.2 Implications

The results outlined in Chapter II have important implications for the interpretation of the results when doing statistical studies of magnetic storms. The technique of Superposed Epoch Analysis is widely used for investigations of common characteristics of magnetic storms. However, the new contribution of this work is a detailed scrutinise of the effect of the epoch time choice on the averaged profile of the storm temporal evolution is being scrutinized. As we described above, the selection of a particular time stamp when doing Superposed Epoch Analysis has significant repercussions on the overall features reproduced by using this statistical tool. One needs to be extremely careful when interpreting statistical results obtained in this manner since a single time stamp cannot fully capture all storm characteristics.

Strong discrepancies between model results and observations could have important implications for the interpretation of the model results as well as for the choice of model to represent certain regions of geospace, as shown in Chapter IV. This seemingly unfruitful exercise led us to revise the simulation strategy to reach new and interesting conclusions.

Close examination of the response of the magnetosphere and in particular, of the ring current, to various solar wind conditions revealed a non-linear relationship between them. This implies that the short-lived peaks present in the solar wind parameters do not have a significant contribution in the development of a magnetic storm. Nevertheless, an additional loss mechanism might be responsible of the saturation limit in the energy input that stalls the development of the ring current. On the other hand, average energy contained in the frequency of the short-lived spikes has to be much larger than the noise value in order for the magnetosphere to respond.

The results of Chapter VII may have important implications in the modelling of the inner magnetosphere. For storms, the inner magnetospheric drift physics model is one of the key elements of the code. Therefore, it is useful to incorporate a new

drift physics model into SWMF. Coupling of the new HEIDI model with BATS-R-US will allow a realistic magnetic field representation and therefore for a more accurate description of the ring current. This will enable us not only to study the ring current as a stand alone problem but also to retrieve the ring current solution as part of a larger system.

8.3 Future Work

Even though significant progress has been done so far, much work needs to be done for a better understanding of the morphology and leading mechanisms that control the storm time ring current.

As mentioned in Chapter VII, the inclusion of inductive electric fields that arise due to the time varying nature of the magnetic field, are necessary for an accurate description of geospace. However, this can be a challenging task for models based equatorial grids. Nevertheless, the convection velocity provided by BATS-RU-S can be used as a proxy for the inductive electric field.

With this in mind, an interesting next step is to examine how the inner magnetosphere responds in a coupled system. For that we can use the Hot Electron and Ion Drift Integrator (HEIDI) ring current model coupled to a global magnetosphere model. That is the BATS-R-US, RIM and HEIDI models working together via SWMF. Coupling with the Ridley Ionosphere Model (RIM), which is a combination of an electric potential solver and a model of the electron precipitation (*Ridley and Liemohn*, 2002), assures that the electric field is self consistently calculated and provided to HEIDI, through couplers inside the SWMF. A realistic magnetic field solution can be provided by the BATSRUS global magneto-hydrodynamic (MHD) model.

Furthermore, in order to accurately account for the ionospheric outflow in our simulations, is is possible to incorporate the Polar Wind Outflow Model (PWOM)

(*Gombosi et al.*, 1992; *Glocer et al.*, 2007). This model solves the gyrotropic continuity, momentum and energy equations for supersonic field aligned flow, in one dimension. Through couplers, the PWOM model provides the Global Magnetosphere (BATS-R-US code) component mass and velocity corrections at the inner boundary, while the electric potential and the locations of the field aligned currents are received from the Ionosphere Electrodynamics (RIM code) module. While there is no direct coupling with the inner magnetosphere component (HEIDI), ionospheric mass is being convected through the system and the Inner Magnetosphere solution is being altered. *Glocer et al.* (2009) shows through data-model comparison that the inclusion of ionospheric outflow improved the MHD solution significantly, altering the cross polar cap potential and the ring current formation.

The model setup described above will allow us to examine how the changes in the magnetosphere affect the ring current and plasma sheet dynamics in a self consistent manner.

In order to assess the response of the inner magnetosphere in a coupled system numerical studies including various levels of coupling within the SWMF and close examine the data-model comparison goodness of fit are necessary. Many data sets are available be used for the data-model comparisons and model assessment. Observations from ACE, WIND, POLAR, GEOTAIL, THEMIS, LANL, and GOES geosynchronous spacecraft are extremely valuable for this type of study. For instance, examining the magnetic field configuration and topology, the convection pattern, the inner magnetosphere pressure and their subsequent comparison with the observed quantities will help not only validate the model but also give insight on the dominant physical processes that dominate this regions.

Also, the purpose of these data in study is to quantify the accuracy of a particular simulation, revealing where and when the code performed well (and, conversely, where it did not). By doing this we can determine what mechanisms are controlling the

development and evolution of a particular magnetic storm event.

The selection of the events can be a key component to this study. Therefore re-evaluating the magnetic storms selected in Chapter IV and comparison with the results presented in this study will give us some insight into the relative importance of pitch angle anisotropy, for instance.

BIBLIOGRAPHY

BIBLIOGRAPHY

Akasofu, S. (1983), Solar-wind disturbances and the solar wind-magnetosphere energy coupling function, *Space Science Reviews*, *34*, 173–183, doi:10.1007/BF00194625.

Anderson, B. J., K. Takahashi, R. E. Erlandson, and L. J. Zanetti (1990), Pc1 pulsations observed by AMPTE/CCE in the earth's outer magnetosphere, *Geophys. Res. Lett.*, *17*, 1853–1856, doi:10.1029/GL017i011p01853.

Axford, W. I., and C. O. Hines (1961), A unifying theory of high-latitude geophysical phenomena and geomagnetic storms, *Canadian Journal of Physics*, *39*, 1433–+.

Baker, D. N., and R. L. McPherron (1990), Extreme energetic particle decreases near geostationary orbit - A manifestation of current diversion within the inner plasma sheet, *J. Geophys. Res.*, *95*, 6591–6599, doi:10.1029/JA095iA05p06591.

Baker, D. N., E. W. Hones, Jr., J. B. Payne, and W. C. Feldman (1981), A high time resolution study of interplanetary parameter correlations with AE, *Geophys. Res. Lett.*, *8*, 179–182, doi:10.1029/GL008i002p00179.

Bame, S. J., B. E. Goldstein, J. T. Gosling, J. W. Harvey, D. J. McComas, M. Neugebauer, and J. L. Phillips (1993), ULYSSES observations of a recurrent high speed solar wind stream and the heliomagnetic streamer belt, *Geophys. Res. Lett.*, *20*, 2323–2326, doi:10.1029/93GL02630.

Bargatze, L. F., D. N. Baker, and R. L. McPherron (1986), Magnetospheric Response to Solar Wind Variations, in *Solar Wind Magnetosphere Coupling*, *Astrophysics and Space Science Library*, vol. 126, edited by Y. Kamide & J. A. Slavin, pp. 93–+.

Baumjohann, W. (1993), The Near Earth Plasma Sheet - an AMPTE / IRM Perspective, *Space Science Reviews*, *64*, 141–163, doi:10.1007/BF00819660.

Birn, J., M. Hesse, and K. Schindler (2006), Entropy conservation in simulations of magnetic reconnection, *Physics of Plasmas*, *13*(9), 092,117–+, doi:10.1063/1.2349440.

Bishop, J. (1996), Multiple charge exchange and ionization collisions within the ring current-geocorona-plasmasphere system: Generation of a secondary ring current on inner L shells, *J. Geophys. Res.*, *101*, 17,325–17,336, doi:10.1029/95JA03468.

Boris, J. P. (1970), A physically motivated solution of the Alfven problem. Internal report at Naval Research Laboratory, *NRL Memorandum Report*.

Borovsky, J. E., and M. H. Denton (2006), Differences between CME-driven storms and CIR-driven storms, *Journal of Geophysical Research (Space Physics)*, *111*(A10), 7–+, doi:10.1029/2005JA011447.

Borovsky, J. E., M. F. Thomsen, and D. J. McComas (1997), The superdense plasma sheet: Plasmaspheric origin, solar wind origin, or ionospheric origin?, *J. Geophys. Res.*, *102*, 22,089–22,106, doi:10.1029/97JA02469.

Borovsky, J. E., M. F. Thomsen, and R. C. Elphic (1998), The driving of the plasma sheet by the solar wind, *J. Geophys. Res.*, *103*, 17,617–17,640, doi:10.1029/97JA02986.

Borrini, G., J. T. Gosling, S. J. Bame, and W. C. Feldman (1982), Helium abundance enhancements in the solar wind, *J. Geophys. Res.*, *87*, 7370–7378, doi:10.1029/JA087iA09p07370.

Brandt, P. C. ., D. G. Mitchell, Y. Ebihara, B. R. Sandel, E. C. Roelof, J. L. Burch, and R. Demajistre (2002), Global IMAGE/HENA observations of the ring current: Examples of rapid response to IMF and ring current-plasmasphere interaction, *Journal of Geophysical Research (Space Physics)*, *107*, 1359–+, doi:10.1029/2001JA000084.

Burlaga, L., E. Sittler, F. Mariani, and R. Schwenn (1981), Magnetic loop behind an interplanetary shock - Voyager, Helios, and IMP 8 observations, *J. Geophys. Res.*, *86*, 6673–6684, doi:10.1029/JA086iA08p06673.

Burton, R. K., R. L. McPherron, and C. T. Russell (1975), An empirical relationship between interplanetary conditions and Dst, *J. Geophys. Res.*, *80*, 4204–4214, doi:10.1029/JA080i031p04204.

Chamberlain, J. W. (1963), Planetary coronae and atmospheric evaporation, *Planet. Space Sci.*, *11*, 901–+, doi:10.1016/0032-0633(63)90122-3.

Chapman, S., and V. C. A. Ferraro (1929), The electrical state of solar streams of corpuscles, *MNRAS*, *89*, 470–+.

Chappell, C. R., T. E. Moore, and J. H. Waite, Jr. (1987), The ionosphere as a fully adequate source of plasma for the earth's magnetosphere, *J. Geophys. Res.*, *92*, 5896–5910, doi:10.1029/JA092iA06p05896.

Chen, M. W., M. Schulz, and L. R. Lyons (1993), Energy content of stormtime ring current from phase space mapping simulations, *Geophys. Res. Lett.*, *20*, 1727–1730, doi:10.1029/93GL01252.

Chen, M. W., L. R. Lyons, and M. Schulz (1994), Simulations of phase space distributions of storm time proton ring current, *J. Geophys. Res.*, *99*, 5745–5759, doi:10.1029/93JA02771.

Chen, M. W., S. Liu, M. Schulz, J. L. Roeder, and L. R. Lyons (2006), Magnetically self-consistent ring current simulations during the 19 October 1998 storm, *Journal of Geophysical Research (Space Physics)*, *111*(A10), 11–+, doi: 10.1029/2006JA011620.

Christon, S. P., M. I. Desai, T. E. Eastman, G. Gloeckler, S. Kokubun, A. T. Y. Lui, R. W. McEntire, E. C. Roelof, and D. J. Williams (2000), Low-charge-state heavy ions upstream of Earth's bow shock and sunward flux of ionospheric O^{+1}, N^{+1}, and O^{+2} ions: Geotail observations, *Geophys. Res. Lett.*, *27*, 2433–2436, doi: 10.1029/2000GL000039.

Coleman, I. J., G. Chisham, M. Pinnock, and M. P. Freeman (2001), An ionospheric convection signature of antiparallel reconnection, *J. Geophys. Res.*, *106*, 28,995–29,008, doi:10.1029/2001JA900084.

Daglis, I. A. (1997), The Role of Magnetosphere-Ionosphere Coupling in Magnetic Storm Dynamics, in *Magnetic Storms, Geophysical Monograph Series, Vol. 98*, edited by Tsurutani, B. T., Gonzalez, W. D., Kamide, Y., & Arballo, J. K. , pp. 107–+, AGU.

Daglis, I. A., and W. I. Axford (1996), Fast ionospheric response to enhanced activity in geospace: Ion feeding of the inner magnetotail, *J. Geophys. Res.*, *101*, 5047–5066, doi:10.1029/95JA02592.

Daglis, I. A., R. M. Thorne, W. Baumjohann, and S. Orsini (1999), The terrestrial ring current: Origin, formation, and decay, *Reviews of Geophysics*, *37*, 407–438, doi:10.1029/1999RG900009.

Davis, C. J., M. N. Wild, M. Lockwood, and Y. K. Tulunay (1997), Ionospheric and geomagnetic responses to changes in IMF B Z : a superposed epoch study, *Annales Geophysicae*, *15*, 217–230, doi:10.1007/s005850050435.

De Zeeuw, D. L., T. I. Gombosi, C. P. T. Groth, K. G. Powell, and Q. F. Stout (2000), An adaptive MHD method for global space weather simulations, *IEEE Transactions on Plasma Science*, *28*, 1956–1965, doi:10.1109/27.902224.

De Zeeuw, D. L., S. Sazykin, R. A. Wolf, T. I. Gombosi, A. J. Ridley, and G. Toth (2004), Coupling of a global mhd code and an inner magnetospheric model: Initial results, *J. Geophys. Res.*, *109*, doi:10.1029/2003JA010,366.

Denton, M. H., M. F. Thomsen, H. Korth, S. Lynch, J. C. Zhang, and M. W. Liemohn (2005), Bulk plasma properties at geosynchronous orbit, *Journal of Geophysical Research (Space Physics)*, *110*(A9), 7223–+, doi:10.1029/2004JA010861.

Denton, M. H., J. E. Borovsky, R. M. Skoug, M. F. Thomsen, B. Lavraud, M. G. Henderson, R. L. McPherron, J. C. Zhang, and M. W. Liemohn (2006), Geomagnetic storms driven by ICME- and CIR-dominated solar wind, *Journal of Geophysical Research (Space Physics)*, *111*(A10), 7–+, doi:10.1029/2005JA011436.

Dessler, A. J., and E. N. Parker (1959), Hydromagnetic Theory of Geomagnetic Storms, *J. Geophys. Res.*, *64*, 2239–2252, doi:10.1029/JZ064i012p02239.

Diego, P., M. Storini, M. Parisi, and E. G. Cordaro (2005), AE index variability during corotating fast solar wind streams, *Journal of Geophysical Research (Space Physics)*, *110*(A9), 6105–+, doi:10.1029/2004JA010715.

Dungey, J. (1961), Interplanetary magnetic field and the auroral zones, *Phys. Rev. Lett.*, *93*, 47.

Dungey, J. W. (1963), Loss of Van Allen electrons due to whistlers, *Planet. Space Sci.*, *11*, 591–+, doi:10.1016/0032-0633(63)90166-1.

Ebihara, Y., and M. Ejiri (1998), Modeling of solar wind control of the ring current buildup: A case study of the magnetic storms in April 1997, *Geophys. Res. Lett.*, *25*, 3751–3754, doi:10.1029/1998GL900006.

Ebihara, Y., and M. Ejiri (2000), Simulation study on fundamental properties of the storm-time ring current, *J. Geophys. Res.*, *105*, 15,843–15,860, doi:10.1029/1999JA900493.

Ebihara, Y., M.-C. Fok, R. A. Wolf, M. F. Thomsen, and T. E. Moore (2005), Nonlinear impact of plasma sheet density on the storm-time ring current, *J. Geophys. Res.*, *110*, in press, doi:10.1029/2004JA010435.

Ejiri, M. (1978), Trajectory traces of charged particles in the magnetosphere, *J. Geophys. Res.*, *83*, 4798–4810, doi:10.1029/JA083iA10p04798.

Elphic, R. C., L. A. Weiss, M. F. Thomsen, D. J. McComas, and M. B. Moldwin (1996), Evolution of plasmaspheric ions at geosynchronous orbit during times of high geomagnetic activity, *Geophys. Res. Lett.*, *23*, 2189–2192, doi:10.1029/96GL02085.

Fairfield, D. H., and L. J. Cahill, Jr. (1966), Transition Region Magnetic Field and Polar Magnetic Disturbances, *J. Geophys. Res.*, *71*, 155–+.

Feldstein, I. I. (1992), Modelling of the magnetic field of magnetospheric ring current as a function of interplanetary medium parameters, *Space Science Reviews*, *59*, 83–165, doi:10.1007/BF01262538.

Feldstein, Y. I., A. E. Levitin, S. A. Golyshev, L. A. Dremukhina, U. B. Vestchezerova, T. E. Valchuk, and A. Grafe (1994), Ring current and auroral electrojets in connection with interplanetary medium parameters during magnetic storm, *Annales Geophysicae*, *12*, 602–611, doi:10.1007/s005850050087.

Feldstein, Y. I., L. A. Dremukhina, U. Mall, and J. Woch (2000), On the two-phase decay of the Dst-variation, *Geophys. Res. Lett.*, *27*, 2813–2816, doi:10.1029/2000GL003783.

Feynman, J. (1980), Implications of solar cycles 19 and 20 geomagnetic activity for magnetospheric processes, *Geophys. Res. Lett.*, *7*, 971–973, doi: 10.1029/GL007i011p00971.

Fite, W. L., T. R. Brackman, and W. R. Snow (1958), Charge transfer in proton-hydrogen atom collisions, *Phys. Rev.*, *112*, 1161.

Fok, M., and T. E. Moore (1997), Ring current modeling in a realistic magnetic field configuration, *Geophys. Res. Lett.*, *24*, 1775–1778, doi:10.1029/97GL01255.

Fok, M., J. U. Kozyra, A. F. Nagy, and T. E. Cravens (1991), Lifetime of ring current particles due to Coulomb collisions in the plasmasphere, *J. Geophys. Res.*, *96*, 7861–7867, doi:10.1029/90JA02620.

Fok, M., J. U. Kozyra, A. F. Nagy, C. E. Rasmussen, and G. V. Khazanov (1993), Decay of equatorial ring current ions and associated aeronomical consequences, *J. Geophys. Res.*, *98*, 19,381–+, doi:10.1029/93JA01848.

Fok, M., P. D. Craven, T. E. Moore, and P. G. Richards (1995), Ring Current-Plasmasphere Coupling Through Coulomb Collisions, in *Cross-Scale Coupling in Space Plasmas, Geophysical Monograph 93*, edited by J. L. Horwitz, N. Singh, & J. L. Burch, pp. 161–+.

Fok, M., R. A. Wolf, R. W. Spiro, and T. E. Moore (2001), Comprehensive computational model of Earth's ring current, *J. Geophys. Res.*, *106*, 8417–8424, doi: 10.1029/2000JA000235.

Friedel, R. H. W., H. Korth, M. G. Henderson, M. F. Thomsen, and J. D. Scudder (2001), Plasma sheet access to the inner magnetosphere, *J. Geophys. Res.*, *106*, 5845–5858, doi:10.1029/2000JA003011.

Galvin, A. B., F. M. Ipavich, G. Gloeckler, D. Hovestadt, and B. T. Tsurutani (1987), Solar wind iron charge states preceding a driver plasma, *J. Geophys. Res.*, *92*, 12,069–12,081, doi:10.1029/JA092iA11p12069.

Ganushkina, N. Y., T. I. Pulkkinen, V. F. Bashkirov, D. N. Baker, and X. Li (2001), Formation of intense nose structures, *Geophys. Res. Lett.*, *28*, 491–494, doi:10.1029/2000GL011955.

Ganushkina, N. Y., T. I. Pulkkinen, A. Milillo, and M. Liemohn (2006), Evolution of the proton ring current energy distribution during 21-25 April 2001 storm, *Journal of Geophysical Research (Space Physics)*, *111*(A10), 11–+, doi: 10.1029/2006JA011609.

Ganushkina, N. Y., et al. (2000), Entry of plasma sheet particles into the inner magnetosphere as observed by Polar/CAMMICE, *J. Geophys. Res.*, *105*, 25,205–25,220, doi:10.1029/2000JA900062.

Glocer, A., G. Toth, and T. Gombosi (2007), Modeling Ionospheric Outflow During a Geomagnetic Storm, *AGU Fall Meeting Abstracts*, pp. B521+.

Glocer, A., G. Tóth, T. Gombosi, and D. Welling (2009), Modeling ionospheric outflows and their impact on the magnetosphere, initial results, *Journal of Geophysical Research (Space Physics)*, *114*(A13), 5216–+, doi:10.1029/2009JA014053.

Goldstein, J., B. R. Sandel, W. T. Forrester, and P. H. Reiff (2003), IMF-driven plasmasphere erosion of 10 July 2000, *Geophys. Res. Lett.*, *30*(3), 030,000–1, doi:10.1029/2002GL016478.

Gombosi, T. I. (1999), *Physics of the Space EnvironmenT*, Cambridge.

Gombosi, T. I., L. K. Kerr, A. F. Nagy, and R. W. Cannata (1992), Helium in the polar wind, *Advances in Space Research*, *12*, 183–186, doi:10.1016/0273-1177(92)90054-2.

Gombosi, T. I., D. L. de Zeeuw, K. G. Powell, and et al. (2003), Adaptive Mesh Refinement for Global Magnetohydrodynamic Simulation, in *Space Plasma Simulation*, *Lecture Notes in Physics, Berlin Springer Verlag*, vol. 615, edited by J. Büchner, C. Dum, & M. Scholer, pp. 247–274.

Gonzalez, W. D., and B. T. Tsurutani (1987), Criteria of interplanetary parameters causing intense magnetic storms (Dst of less than -100 nT), *Planet. Space Sci.*, *35*, 1101–1109, doi:10.1016/0032-0633(87)90015-8.

Gonzalez, W. D., A. L. C. Gonzalez, B. T. Tsurutani, E. J. Smith, and F. Tang (1989), Solar wind-magnetosphere coupling during intense magnetic storms (1978-1979), *J. Geophys. Res.*, *94*, 8835–8851, doi:10.1029/JA094iA07p08835.

Gonzalez, W. D., J. A. Joselyn, Y. Kamide, H. W. Kroehl, G. Rostoker, B. T. Tsurutani, and V. M. Vasyliunas (1994), What is a geomagnetic storm?, *J. Geophys. Res.*, *99*, 5771–5792, doi:10.1029/93JA02867.

Gonzalez, W. D., B. T. Tsurutani, and A. L. Clúa de Gonzalez (1999), Interplanetary origin of geomagnetic storms, *Space Science Reviews*, *88*, 529–562, doi:10.1023/A:1005160129098.

Gonzalez, W. D., F. L. Guarnieri, A. L. Clua-Gonzalez, E. Echer, M. V. Alves, T. Ogino, and B. T. Tsurutani (2006), Magnetospheric Energetics During HILDCAAs, in *Recurrent Magnetic Storms: Corotating Solar Wind*, *Washington DC American Geophysical Union Geophysical Monograph Series*, vol. 167, edited by R. McPherron, W. Gonzalez, G. Lu, H. A. José, & S. Natchimuthukonar Gopalswamy , pp. 175–+.

Gopalswamy, N. (2006), Properties of Interplanetary Coronal Mass Ejections, *Space Science Reviews*, *124*, 145–168, doi:10.1007/s11214-006-9102-1.

Gosling, J. T. (1990), Coronal mass ejections and magnetic flux ropes in interplanetary space, *Washington DC American Geophysical Union Geophysical Monograph Series*, *58*, 343–364.

Gosling, J. T., D. J. McComas, J. L. Phillips, and S. J. Bame (1991), Geomagnetic activity associated with earth passage of interplanetary shock disturbances and coronal mass ejections, *J. Geophys. Res.*, *96*, 7831–7839, doi:10.1029/91JA00316.

Greenspan, M. E., and D. C. Hamilton (2000), A test of the Dessler-Parker-Sckopke relation during magnetic storms, *J. Geophys. Res.*, *105*, 5419–5430, doi:10.1029/1999JA000284.

Hamilton, D. C., G. Gloeckler, F. M. Ipavich, B. Wilken, and W. Stuedemann (1988), Ring current development during the great geomagnetic storm of February 1986, *J. Geophys. Res.*, *93*, 14,343–14,355, doi:10.1029/JA093iA12p14343.

Harel, M., R. A. Wolf, P. H. Reiff, R. W. Spiro, W. J. Burke, F. J. Rich, and M. Smiddy (1981), Quantitative simulation of a magnetospheric substorm. I - Model logic and overview, *J. Geophys. Res.*, *86*, 2217–2241, doi:10.1029/JA086iA04p02217.

Horwitz, J. L., and N. Singh (1991), Refilling of the earth's plasmasphere, *EOS Transactions*, *72*, 399–+.

Horwitz, J. L., C. J. Pollock, T. E. Moore, W. K. Peterson, J. L. Burch, J. D. Winningham, J. D. Craven, L. A. Frank, and A. Persoon (1992), The polar cap environment of outflowing O(+), *J. Geophys. Res.*, *97*, 8361–8379, doi:10.1029/92JA00147.

Hundhausen, A. J. (1972), *Coronal Expansion and Solar Wind*, Springer-Verlag Berlin Heidelberg New York.

Huttunen, E. (2005), Geoeffectiveness of CMEs in the Solar Wind, in *Coronal and Stellar Mass Ejections*, *IAU Symposium*, vol. 226, edited by K. Dere, J. Wang, & Y. Yan, pp. 455–456, doi:10.1017/S1743921305001031.

Huttunen, K., and H. Koskinen (2004), Importance of post-shock streams and sheath region as drivers of intense magnetospheric storms and high-latitude activity, *Annales Geophysicae*, *22*, 1729–1738.

Huttunen, K. E. J., H. E. J. Koskinen, and R. Schwenn (2002), Response of magnetic indices to different solar wind disturbances, in *Solspa 2001, Proceedings of the Second Solar Cycle and Space Weather Euroconference*, *ESA Special Publication*, vol. 477, edited by H. Sawaya-Lacoste, pp. 339–342.

Huttunen, K. E. J., H. E. J. Koskinen, A. Karinen, and K. Mursula (2006), Asymmetric development of magnetospheric storms during magnetic clouds and sheath regions, *Geophys. Res. Lett.*, *33*, 6107–+, doi:10.1029/2005GL024894.

Hviuzova, T. A., S. V. Tolochkina, and V. L. Zverev (2007), Variations in the IMF vertical component in isolated solar wind streams, *Geomagnetism and Aeronomy/Geomagnetizm i Aeronomiia*, *47*, 149–155, doi:10.1134/S0016793207020028.

Ilie, R., M. W. Liemohn, and A. Ridley (2010), The effect of smoothed solar wind inputs on global modeling results, *J. Geophys. Res.*, *115*, doi:10.1029/2009JA014443.

Jordanova, V. K., J. U. Kozyra, G. V. Khazanov, A. F. Nagy, C. E. Rasmussen, and M. Fok (1994), A bounce-averaged kinetic model of the ring current ion population, *Geophys. Res. Lett.*, *21*, 2785–2788, doi:10.1029/94GL02695.

Jordanova, V. K., L. M. Kistler, J. U. Kozyra, G. V. Khazanov, and A. F. Nagy (1996), Collisional losses of ring current ions, *J. Geophys. Res.*, *101*, 111–126, doi:10.1029/95JA02000.

Jordanova, V. K., L. M. Kistler, M. F. Thomsen, and C. G. Mouikis (2003), Effects of plasma sheet variability on the fast initial ring current decay, *Geophys. Res. Lett.*, *30*(6), 060,000–1, doi:10.1029/2002GL016576.

Jordanova, V. K., Y. S. Miyoshi, S. Zaharia, M. F. Thomsen, G. D. Reeves, D. S. Evans, C. G. Mouikis, and J. F. Fennell (2006), Kinetic simulations of ring current evolution during the Geospace Environment Modeling challenge events, *Journal of Geophysical Research (Space Physics)*, *111*(A10), 11–+, doi:10.1029/2006JA011644.

Jordanova, V. K., et al. (1998), Effect of wave-particle interactions on ring current evolution for January 10-11, 1997: Initial results, *Geophys. Res. Lett.*, *25*, 2971–2974, doi:10.1029/98GL00649.

Jorgensen, A. M., M. G. Henderson, E. C. Roelof, G. D. Reeves, and H. E. Spence (2001), Charge exchange contribution to the decay of the ring current, measured by energetic neutral atoms (ENAs), *J. Geophys. Res.*, *106*, 1931–1938, doi:10.1029/2000JA000124.

Jorgensen, A. M., H. E. Spence, W. J. Hughes, and H. J. Singer (2004), A statistical study of the global structure of the ring current, *Journal of Geophysical Research (Space Physics)*, *109*(A18), 12,204–+, doi:10.1029/2003JA010090.

Keika, K., M. Nose', K. Takahashi, S. Ohtani, P. C:Son Brandt, D. G. Mitchell, S. P. Christon, and R. W. McEntire (2003), Contribution of ion flow-out and charge exchange processes to the decay of the storm-time ring current, *AGU Fall Meeting Abstracts*, pp. A565+.

Keika, K., M. Nosé, S. Ohtani, K. Takahashi, S. P. Christon, and R. W. McEntire (2005), Outflow of energetic ions from the magnetosphere and its contribution to the decay of the storm time ring current, *Journal of Geophysical Research (Space Physics)*, *110*(A9), 9210–+, doi:10.1029/2004JA010970.

Keika, K., M. Nosé, P. C. Brandt, S. Ohtani, D. G. Mitchell, and E. C. Roelof (2006), Contribution of charge exchange loss to the storm time ring current decay: IMAGE/HENA observations, *Journal of Geophysical Research (Space Physics)*, *111*(A10), 11–+, doi:10.1029/2006JA011789.

Khazanov, G. V., M. W. Liemohn, M. Fok, T. S. Newman, and A. J. Ridley (2004), Stormtime particle energization with high temporal resolution AMIE potentials, *Journal of Geophysical Research (Space Physics)*, *109*(A18), 5209–+, doi:10.1029/2003JA010186.

Kim, H., and A. A. Chan (1997), Fully adiabatic changes in storm time relativistic electron fluxes, *J. Geophys. Res.*, *102*, 22,107–22,116, doi:10.1029/97JA01814.

Kivelson, M. G., and C. T. Russell (1995), *Introduction to Space Physics*, Cambridge University Press.

Klimas, A. J., D. N. Baker, D. Vassiliadis, and D. A. Roberts (1994), Substorm recurrence during steady and variable solar wind driving: Evidence for a normal mode in the unloading dynamics of the magnetosphere, *J. Geophys. Res.*, *99*, 18,855–+.

Korth, H., M. F. Thomsen, J. E. Borovsky, and D. J. McComas (1999), Plasma sheet access to geosynchronous orbit, *J. Geophys. Res.*, *104*, 25,047–25,062, doi:10.1029/1999JA900292.

Kozyra, J. U., and M. W. Liemohn (2003), Ring Current Energy Input and Decay, *Space Science Reviews*, *109*, 105–131, doi:10.1023/B:SPAC.0000007516.10433.ad.

Kozyra, J. U., A. F. Nagy, and D. W. Slater (1997), High-altitude energy source(s) for stable auroral red arcs, *Reviews of Geophysics*, *35*, 155–190, doi:10.1029/96RG03194.

Kozyra, J. U., M. Fok, E. R. Sanchez, D. S. Evans, D. C. Hamilton, and A. F. Nagy (1998a), The role of precipitation losses in producing the rapid early recovery phase of the Great Magnetic Storm of February 1986, *J. Geophys. Res.*, *103*, 6801–6814, doi:10.1029/97JA03330.

Kozyra, J. U., V. K. Jordanova, J. E. Borovsky, M. F. Thomsen, D. J. Knipp, D. S. Evans, D. J. McComas, and T. E. Cayton (1998b), Effects of a high-density plasma sheet on ring current development during the November 2-6, 1993, magnetic storm, *J. Geophys. Res.*, *103*, 26,285–26,306, doi:10.1029/98JA01964.

Kozyra, J. U., M. W. Liemohn, C. R. Clauer, A. J. Ridley, M. F. Thomsen, J. E. Borovsky, J. L. Roeder, V. K. Jordanova, and W. D. Gonzalez (2002), Multistep Dst development and ring current composition changes during the 4-6 June 1991 magnetic storm, *Journal of Geophysical Research (Space Physics)*, *107*, 1224–+, doi:10.1029/2001JA000023.

Lavraud, B., M. F. Thomsen, S. Wing, M. Fujimoto, M. H. Denton, J. E. Borovsky, A. Aasnes, K. Seki, and J. M. Weygand (2006), Observation of two distinct cold, dense ion populations at geosynchronous orbit: local time asymmetry, solar wind dependence and origin, *Annales Geophysicae*, *24*, 3451–3465.

Le, G., C. Russell, and K. Takahashi (2004), Morphology of the ring current derived from magnetic field observations, *Annales Geophysicae*, *22*, 1267–1295.

Lemon, C., R. A. Wolf, T. W. Hill, S. Sazykin, R. W. Spiro, F. R. Toffoletto, J. Birn, and M. Hesse (2004), Magnetic storm ring current injection modeled with the Rice Convection Model and a self-consistent magnetic field, *Geophys. Res. Lett.*, *31*, 21,801–+, doi:10.1029/2004GL020914.

Lennartsson, O. W. (2001), Ion composition aspects of magnetotail plasma flows, *J. Geophys. Res.*, *106*, 15,621–15,634, doi:10.1029/2000JA000427.

Liemohn, M. W., and P. C. Brandt (2005), Small-Scale Structure in the Storm Time Ring Current, *Magnetic Storms, Geophys. Monogr. Ser*, *159*.

Liemohn, M. W., and J. U. Kozyra (2003), Lognormal form of the ring current energy content, *Journal of Atmospheric and Solar-Terrestrial Physics*, *65*, 871–886, doi: 10.1016/S1364-6826(03)00088-9.

Liemohn, M. W., and J. U. Kozyra (2005), Testing the Hypothesis That Charge Exchange Can Cause a Two-Phase Decay, in *The Inner Magnetosphere: Physics and Modeling*, *Washington DC American Geophysical Union Geophysical Monograph Series*, vol. 155, edited by T. I. Pulkkinen, N. A. Tsyganenko, & R. H. W. Friedel, pp. 211–+.

Liemohn, M. W., J. U. Kozyra, V. K. Jordanova, G. V. Khazanov, M. F. Thomsen, and T. E. Cayton (1999), Analysis of early phase ring current recovery mechanisms during geomagnetic storms, *Geophys. Res. Lett.*, *26*, 2845–2848, doi: 10.1029/1999GL900611.

Liemohn, M. W., J. U. Kozyra, C. R. Clauer, and A. J. Ridley (2001a), Computational analysis of the near-Earth magnetospheric current system during two-phase decay storms, *J. Geophys. Res.*, *106*, 29,531–29,542, doi:10.1029/2001JA000045.

Liemohn, M. W., J. U. Kozyra, M. F. Thomsen, J. L. Roeder, G. Lu, J. E. Borovsky, and T. E. Cayton (2001b), Dominant role of the asymmetric ring current in producing the stormtime Dst^*, *J. Geophys. Res.*, *106*, 10,883–10,904, doi: 10.1029/2000JA000326.

Liemohn, M. W., A. J. Ridley, D. L. Gallagher, D. M. Ober, and J. U. Kozyra (2004), Dependence of plasmaspheric morphology on the electric field description during the recovery phase of the 17 April 2002 magnetic storm, *Journal of Geophysical Research (Space Physics)*, *109*(A18), 3209–+, doi:10.1029/2003JA010304.

Liemohn, M. W., A. J. Ridley, J. U. Kozyra, D. L. Gallagher, M. F. Thomsen, M. G. Henderson, M. H. Denton, P. C. Brandt, and J. Goldstein (2006), Analyzing electric field morphology through data-model comparisons of the Geospace Environment Modeling Inner Magnetosphere/Storm Assessment Challenge events, *Journal of Geophysical Research (Space Physics)*, *111*(A10), 11–+, doi:10.1029/2006JA011700.

Liemohn, M. W., J. Zhang, M. F. Thomsen, J. E. Borovsky, J. U. Kozyra, and R. Ilie (2008), Plasma properties of superstorms at geosynchronous orbit: How different are they?, *Geophys. Res. Lett.*, *35*, 6–+, doi:10.1029/2007GL031717.

Liemohn, M. W., M. Jazowski, J. U. Kozyra, N. Ganushlina, M. F. Thomsen, and J. E. Borovsky (2010), CIR vs. CME Drivers of the Ring Current During Intense Magnetic Storms, submitted.

Liu, S., M. W. Chen, M. Schulz, and L. R. Lyons (2006), Initial simulation results of storm-time ring current in a self-consistent magnetic field model, *Journal of Geophysical Research (Space Physics)*, *111*(A10), 4225–+, doi:10.1029/2005JA011194.

Loewe, C. A., and G. W. Prölss (1997), Classification and mean behavior of magnetic storms, *J. Geophys. Res.*, *102*, 14,209–14,214, doi:10.1029/96JA04020.

Lu, G. (2006), High-Speed Streams, Coronal Mass Ejections, and Interplanetary Shocks: A Comparative Study of Geoeffectiveness, in *Recurrent Magnetic Storms: Corotating Solar Wind*, *Washington DC American Geophysical Union Geophysical Monograph Series*, vol. 167, edited by R. McPherron, W. Gonzalez, G. Lu, H. A. José, & S. Natchimuthukonar Gopalswamy , pp. 97–+.

Lu, G., P. H. Reiff, T. E. Moore, and R. A. Heelis (1992), Upflowing ionospheric ions in the auroral region, *J. Geophys. Res.*, *97*, 16,855–+, doi:10.1029/92JA01435.

Lu, G., T. E. Holzer, D. Lummerzheim, J. M. Ruohoniemi, P. Stauning, O. Troshichev, P. T. Newell, M. Brittnacher, and G. Parks (2002), Ionospheric response to the interplanetary magnetic field southward turning: Fast onset and slow reconfiguration, *Journal of Geophysical Research (Space Physics)*, *107*, 1153–+, doi:10.1029/2001JA000324.

Luhmann, J. G., R. J. Walker, C. T. Russell, N. U. Crooker, J. R. Spreiter, and S. S. Stahara (1984), Patterns of magnetic field merging sites on the magnetopause, in *Neilsen Eng. and Res., Inc. Appl. of a Global Solar Wind/Planetary Obstacle Interaction Computational Model 10p (SEE N84-26509 16-88)*, edited by C. T. Russell, J. G. Luhmann, J. R. Spreiter, & S. S. Stahara .

Lui, A. T. Y. (2003), Inner magnetospheric plasma pressure distribution and its local time asymmetry, *Geophys. Res. Lett.*, *30*(16), 160,000–1, doi:10.1029/2003GL017596.

Mann, G., A. Klassen, C. Estel, and B. J. Thompson (1999), Coronal Transient Waves and Coronal Shock Waves, in *8th SOHO Workshop: Plasma Dynamics and Diagnostics in the Solar Transition Region and Corona*, *ESA Special Publication*, vol. 446, edited by J.-C. Vial & B. Kaldeich-Schü, pp. 477–+.

Mayaud, P. N. (1980), *Derivation, meaning, and use of geomagnetic indices / P. N. Mayaud*, vi, 154 p. : pp., American Geophysical Union, Washington :.

Maynard, N. C., and A. J. Chen (1975), Isolated cold plasma regions - Observations and their relation to possible production mechanisms, *J. Geophys. Res.*, *80*, 1009–1013, doi:10.1029/JA080i007p01009.

McComas, D. J., S. J. Bame, B. L. Barraclough, J. R. Donart, R. C. Elphic, J. T. Gosling, M. B. Moldwin, K. R. Moore, and M. F. Thomsen (1993), Magnetospheric plasma analyzer - Initial three-spacecraft observations from geosynchronous orbit, *J. Geophys. Res.*, *98*, 13,453–+, doi:10.1029/93JA00726.

McIlwain, C. E. (1986), A Kp dependent equatorial electric field model, *Advances in Space Research*, *6*, 187–197, doi:10.1016/0273-1177(86)90331-5.

Meinel, A. B. (1951), Doppler-Shifted Auroral Hydrogen Emission., *ApJ*, *113*, 50–+, doi:10.1086/145375.

Mitsakou, E., G. Babasidis, and X. Moussas (2009), Interplanetary coronal mass ejections during the descending cycle 23: Sheath and ejecta properties comparison, *Advances in Space Research*, *43*, 495–498, doi:10.1016/j.asr.2008.08.003.

Miyoshi, Y. S., and R. Kataoka (2005), Ring current and radiation belt during geomagnetic storms driven by CMEs and CIRs, *AGU Fall Meeting Abstracts*, pp. A426+.

Moebius, E., D. Hovestadt, B. Klecker, M. Scholer, and F. M. Ipavich (1986), A burst of energetic O(+) ions during an upstream particle event, *Geophys. Res. Lett.*, *13*, 1372–1375, doi:10.1029/GL013i013p01372.

Moen, J., and A. Brekke (1993), The solar flux influence on quiet time conductances in the auroral ionosphere, *Geophys. Res. Lett.*, *20*, 971–974, doi:10.1029/92GL02109.

Murr, D. L., and W. J. Hughes (2007), The coherence between the IMF and high-latitude ionospheric flows: The dayside magnetosphere ionosphere low-pass filter, *Journal of Atmospheric and Solar-Terrestrial Physics*, *69*, 223–233, doi:10.1016/j.jastp.2006.07.019.

Mursula, K., and B. Zieger (1996), The 13.5-day periodicity in the Sun, solar wind, and geomagnetic activity: The last three solar cycles, *J. Geophys. Res.*, *101*, 27,077–27,090, doi:10.1029/96JA02470.

Nakamura, R., K. Kamei, Y. Kamide, D. N. Baker, J. B. Blake, and M. Looper (1998), SAMPEX observations of storm-associated electron flux variations in the outer radiation belt, *J. Geophys. Res.*, *103*, 26,261–26,270, doi:10.1029/97JA02873.

Neugebauer, M., R. Goldstein, and B. E. Goldstein (1997), Features observed in the trailing regions of interplanetary clouds from coronal mass ejections, *J. Geophys. Res.*, *102*, 19,743–19,752, doi:10.1029/97JA01651.

Northrop, T. G. (1963), Adiabatic Charged-Particle Motion, *Reviews of Geophysics and Space Physics*, *1*, 283–304.

Ober, D. M., J. L. Horwitz, and D. L. Gallagher (1997), Formation of density troughs embedded in the outer plasmasphere by subauroral ion drift events, *J. Geophys. Res.*, *102*, 14,595–14,602, doi:10.1029/97JA01046.

O'Brien, T. P., and R. L. McPherron (2000), An empirical phase space analysis of ring current dynamics: Solar wind control of injection and decay, *J. Geophys. Res.*, *105*, 7707–7720, doi:10.1029/1998JA000437.

Ohtani, S., M. Nosé, G. Rostoker, H. Singer, A. T. Y. Lui, and M. Nakamura (2001), Storm-substorm relationship: Contribution of the tail current to Dst, *J. Geophys. Res.*, *106*, 21,199–21,210, doi:10.1029/2000JA000400.

Orsini, S., A. Milillo, and M. Candidi (1998), Charge-Exchange Process in the Inner Magnetosphere and Energetic Neutral Atoms, in *Substorms-4*, *Astrophysics and Space Science Library*, vol. 238, edited by S. Kokubun & Y. Kamide, pp. 791–+.

Østgaard, N., S. B. Mende, H. U. Frey, G. R. Gladstone, and H. Lauche (2003), Neutral hydrogen density profiles derived from geocoronal imaging, *Journal of Geophysical Research (Space Physics)*, *108*, 1300–+, doi:10.1029/2002JA009749.

Palmroth, M., T. I. Pulkkinen, P. Janhunen, and C. Wu (2003), Stormtime energy transfer in global MHD simulation, *Journal of Geophysical Research (Space Physics)*, *108*, 1048–+, doi:10.1029/2002JA009446.

Parker, E. N. (1957), Newtonian Development of the Dynamical Properties of Ionized Gases of Low Density, *Physical Review*, *107*, 924–933, doi:10.1103/PhysRev.107.924.

Parker, E. N. (1958), Dynamics of the Interplanetary Gas and Magnetic Fields., *ApJ*, *128*, 664–+, doi:10.1086/146579.

Pizzo, V. J. (1985), Interplanetary shocks on the large scale - A retrospective on the last decade's theoretical efforts, *Washington DC American Geophysical Union Geophysical Monograph Series*, *35*, 51–68.

Posner, A., N. A. Schwadron, T. H. Zurbuchen, J. U. Kozyra, M. W. Liemohn, and G. Gloeckler (2002), Association of Low-Charge-State Heavy Ions up to 200 R_e upstream of the Earth's bow shock with geomagnetic disturbances, *Geophys. Res. Lett.*, *29*(7), 070,000–1, doi:10.1029/2001GL013449.

Powell, K. G., P. L. Roe, T. J. Linde, T. I. Gombosi, and D. L. De Zeeuw (1999), A Solution-Adaptive Upwind Scheme for Ideal Magnetohydrodynamics, *Journal of Computational Physics*, *154*, 284–309, doi:10.1006/jcph.1999.6299.

Pulkkinen, T. I., N. Partamies, K. E. J. Huttunen, G. D. Reeves, and H. E. J. Koskinen (2007), Differences in geomagnetic storms driven by magnetic clouds and ICME sheath regions, *Geophys. Res. Lett.*, *34*, 2105–+, doi:10.1029/2006GL027775.

Rairden, R. L., L. A. Frank, and J. D. Craven (1986), Geocoronal imaging with Dynamics Explorer, *J. Geophys. Res.*, *91*, 13,613–13,630, doi:10.1029/JA091iA12p13613.

Richardson, I. G., and H. V. Cane (2003), What fraction of interplanetary coronal mass ejections in the near-Earth solar wind are magnetic clouds?, in *EGS - AGU - EUG Joint Assembly*, pp. 6603–+.

Richardson, I. G., E. W. Cliver, and H. V. Cane (2001), Sources of geomagnetic storms for solar minimum and maximum conditions during 1972-2000, *Geophys. Res. Lett.*, *28*, 2569–2572, doi:10.1029/2001GL013052.

Richmond, A. D., G. Lu, B. A. Emery, and D. J. Knipp (1998), The AMIE procedure: prospects for space weather specification and prediction, *Advances in Space Research*, *22*, 103–112, doi:10.1016/S0273-1177(97)01108-3.

Ridley, A., T. Gombosi, and D. Dezeeuw (2004), Ionospheric control of the magnetosphere: conductance, *Annales Geophysicae*, *22*, 567–584.

Ridley, A. J., and C. R. Clauer (1996), Characterization of the dynamic variations of the dayside high-latitude ionospheric convection reversal boundary and relationship to interplanetary magnetic field orientation, *J. Geophys. Res.*, *101*, 10,919–10,938, doi:10.1029/JA101iA05p10919.

Ridley, A. J., and E. A. Kihn (2004), Polar cap index comparisons with AMIE cross polar cap potential, electric field, and polar cap area, *Geophys. Res. Lett.*, *31*, 7801–+, doi:10.1029/2003GL019113.

Ridley, A. J., and M. W. Liemohn (2002), A model-derived storm time asymmetric ring current driven electric field description, *Journal of Geophysical Research (Space Physics)*, *107*, 1151–+, doi:10.1029/2001JA000051.

Ridley, A. J., G. Lu, C. R. Clauer, and V. O. Papitashvili (1998), A statistical study of the ionospheric convection response to changing interplanetary magnetic field conditions using the assimilative mapping of ionospheric electrodynamics technique, *J. Geophys. Res.*, *103*, 4023–4040, doi:10.1029/97JA03328.

Ridley, A. J., G. Crowley, and C. Freitas (2000), An empirical model of the ionospheric electric potential, *Geophys. Res. Lett.*, *27*, 3675–3678, doi:10.1029/1999GL011161.

Roederer, J. G. (1970), *Dynamics of geomagnetically trapped radiation*, Springer-Verlag, New York.

Rowland, D. E., and J. R. Wygant (1998), Dependence of the large-scale, inner magnetospheric electric field on geomagnetic activity, *J. Geophys. Res.*, *103*, 14,959–14,964, doi:10.1029/97JA03524.

Ruohoniemi, J. M., and R. A. Greenwald (1998), The response of high-latitude convection to a sudden southward IMF turning, *Geophys. Res. Lett.*, *25*, 2913–2916, doi:10.1029/98GL02212.

Russell, C. T., and R. L. McPherron (1973), The Magnetotail and Substorms, *Space Science Reviews*, *15*, 205–266, doi:10.1007/BF00169321.

Sandholt, P. E., and C. J. Farrugia (2003), Does the aurora provide evidence for the occurrence of antiparallel magnetopause reconnection?, *Journal of Geophysical Research (Space Physics)*, *108*, 1466–+, doi:10.1029/2003JA010066.

Sazykin, S. (2000), Theoretical studies of penetration of magnetospheric electric fields to the ionosphere, Ph.D. thesis, UTAH STATE UNIVERSITY.

Sckopke, N. (1966), A General Relation between the Energy of Trapped Particles and Disturbance Field near Earth, *J. Geophys. Res.*, *71*(13).

Sheeley, N. R., Jr., and J. W. Harvey (1978), Coronal holes, solar wind streams, and geomagnetic activity during the new sunspot cycle, *Sol. Phys.*, *59*, 159–173.

Shue, J., et al. (1998), Magnetopause location under extreme solar wind conditions, *J. Geophys. Res.*, *103*, 17,691–17,700, doi:10.1029/98JA01103.

Siscoe, G. L., R. L. McPherron, and V. K. Jordanova (2005), Diminished contribution of ram pressure to Dst during magnetic storms, *Journal of Geophysical Research (Space Physics)*, *110*(A9), 12,227–+, doi:10.1029/2005JA011120.

Slinker, S. P., J. A. Fedder, J. M. Ruohoniemi, and J. G. Lyon (2001), Global MHD simulation of the magnetosphere for November 24, 1996, *J. Geophys. Res.*, *106*, 361–380, doi:10.1029/2000JA000603.

Smith, P. H., and N. K. Bewtra (1978), Charge exchange lifetimes for ring current ions, *Space Science Reviews*, *22*, 301–318, doi:10.1007/BF00239804.

Song, P., and C. T. Russell (1992), Model of the formation of the low-latitude boundary layer for strongly northward interplanetary magnetic field, *J. Geophys. Res.*, *97*, 1411–1420, doi:10.1029/91JA02377.

Søraas, F., K. Aarsnes, D. V. Carlsen, K. Oksavik, and D. S. Evans (2005), Ring Current Behavior as Revealed by Energetic Proton Precipitation, in *The Inner Magnetosphere: Physics and Modeling*, *Washington DC American Geophysical Union Geophysical Monograph Series*, vol. 155, edited by T. I. Pulkkinen, N. A. Tsyganenko, & R. H. W. Friedel, pp. 237–+.

Speiser, T. W. (1965), Acceleration of particles in the neutral sheet of the geomagnetic tail., in *International Cosmic Ray Conference*, *International Cosmic Ray Conference*, vol. 1, pp. 147–+.

Spjeldvik, W. N. (1977), Equilibrium structure of equatorially mirroring radiation belt protons, *J. Geophys. Res.*, *82*, 2801–2808, doi:10.1029/JA082i019p02801.

Spjeldvik, W. N., and T. A. Fritz (1978), Theory for charge states of energetic oxygen ions in the earth's radiation belts, *J. Geophys. Res.*, *83*, 1583–1594, doi:10.1029/JA083iA04p01583.

St. Cyr, O. C., et al. (2000), Properties of coronal mass ejections: SOHO LASCO observations from January 1996 to June 1998, *J. Geophys. Res.*, *105*, 8169–+, doi:10.1029/1999JA000381.

Stern, D. P. (1975), The motion of a proton in the equatorial magnetosphere, *J. Geophys. Res.*, *80*, 595.

Stuart, G. W. (1959), Satellite-measured radiation, *Phys. Rev. Lett.*, *2*, 417.

Sugiura, M., and T. Kamei (1991), Equatorial dst index 1957 - 1986, edited by a. berthelier and m. menvielle, *IAGA Bull.*, *40*.

Takahashi, S., T. Iyemori, and M. Takeda (1990), A simulation of the storm-time ring current, *Planet. Space Sci.*, *38*, 1133–1141, doi:10.1016/0032-0633(90)90021-H.

Takalo, J., K. Mursula, and J. Timonen (2000), Role of the driver in the dynamics of a coupled-map model of the magnetotail: Does the magnetosphere act as a low-pass filter?, *J. Geophys. Res.*, *105*, 27,665–27,672, doi:10.1029/2000JA900114.

Temerin, M., and X. Li (2002), A new model for the prediction of Dst on the basis of the solar wind, *Journal of Geophysical Research (Space Physics)*, *107*, 1472–+, doi:10.1029/2001JA007532.

Temerin, M., and X. Li (2006), Dst model for 1995-2002, *Journal of Geophysical Research (Space Physics)*, *111*(A10), 4221–+, doi:10.1029/2005JA011257.

Thomsen, M. F. (2004), Why Kp is such a good measure of magnetospheric convection, *Space Weather*, *2*, 11,004–+, doi:10.1029/2004SW000089.

Thomsen, M. F., J. E. Borovsky, D. J. McComas, and M. R. Collier (1998), Variability of the ring current source population, *Geophys. Res. Lett.*, *25*, 3481–3484, doi:10.1029/98GL02633.

Thomsen, M. F., J. E. Borovsky, R. M. Skoug, and C. W. Smith (2003), Delivery of cold, dense plasma sheet material into the near-Earth region, *Journal of Geophysical Research (Space Physics)*, *108*, 1151–+, doi:10.1029/2002JA009544.

Thorne, R. M., E. J. Smith, R. K. Burton, and R. E. Holzer (1973), Plasmaspheric hiss, *J. Geophys. Res*, *78*, 1581–+.

Toffoletto, F., S. Sazykin, R. Spiro, and R. Wolf (2003), Inner magnetospheric modeling with the Rice Convection Model, *Space Science Reviews*, *107*, 175–196, doi: 10.1023/A:1025532008047.

Tóth, G., D. L. De Zeeuw, T. I. Gombosi, and K. G. Powell (2006), A parallel explicit/implicit time stepping scheme on block-adaptive grids, *Journal of Computational Physics*, *217*, 722–758, doi:10.1016/j.jcp.2006.01.029.

Tóth, G., D. L. De Zeeuw, T. I. Gombosi, W. B. Manchester, A. J. Ridley, I. V. Sokolov, and I. I. Roussev (2007), Sun-to-thermosphere simulation of the 28-30 October 2003 storm with the Space Weather Modeling Framework, *Space Weather*, *5*, 6003–+, doi:10.1029/2006SW000272.

Tóth, G., et al. (2005), Space Weather Modeling Framework: A new tool for the space science community, *Journal of Geophysical Research (Space Physics)*, *110*(A9), 12,226–+, doi:10.1029/2005JA011126.

Tsurutani, B. T. (2000), Solar/interplanetary plasma phenomena causing geomagnetic activity at Earth, in *Proceedings of International School of Physics Enrico Fermi*, edited by F. A. Coppi B. and S. E., IOS Press, p. 273.

Tsurutani, B. T., and W. D. Gonzalez (1987), The cause of high-intensity long-duration continuous AE activity (HILDCAAS) - Interplanetary Alfven wave trains, *Planet. Space Sci.*, *35*, 405–412, doi:10.1016/0032-0633(87)90097-3.

Tsurutani, B. T., and W. D. Gonzalez (1997), The interplanetary causes of magnetic storms, *Magnetic Storms, Geophys. Monogr. Ser*, *98*, 77–+.

Tsurutani, B. T., E. J. Smith, W. D. Gonzalez, F. Tang, and S. I. Akasofu (1988), Origin of interplanetary southward magnetic fields responsible for major magnetic storms near solar maximum (1978-1979), *J. Geophys. Res.*, *93*, 8519–8531, doi: 10.1029/JA093iA08p08519.

Tsurutani, B. T., B. E. Goldstein, M. Sugiura, T. Iyemori, and W. D. Gonzalez (1990), The nonlinear response of AE to the IMF Bs driver - A spectral break at 5 hours, *Geophys. Res. Lett.*, *17*, 279–282, doi:10.1029/GL017i003p00279.

Tsurutani, B. T., W. D. Gonzalez, A. L. C. Gonzalez, F. Tang, J. K. Arballo, and M. Okada (1995), Interplanetary origin of geomagnetic activity in the declining phase of the solar cycle, *J. Geophys. Res.*, *100*, 21,717–21,734, doi: 10.1029/95JA01476.

Tsurutani, B. T., G. S. Lakhina, J. S. Pickett, F. L. Guarnieri, N. Lin, and B. E. Goldstein (2005), Nonlinear Alfvén waves, discontinuities, proton perpendicular acceleration, and magnetic holes/decreases in interplanetary space and the magnetosphere: intermediate shocks?, *Nonlinear Processes in Geophysics*, *12*, 321–336.

Tsurutani, B. T., et al. (2006), Corotating solar wind streams and recurrent geomagnetic activity: A review, *Journal of Geophysical Research (Space Physics)*, *111*(A10), 7–+, doi:10.1029/2005JA011273.

Tsyganenko, N. A. (1995), Modeling the Earth's magnetospheric magnetic field confined within a realistic magnetopause, *J. Geophys. Res.*, *100*, 5599–5612, doi:10.1029/94JA03193.

Tsyganenko, N. A. (2002), A model of the near magnetosphere with a dawn-dusk asymmetry 1. Mathematical structure, *Journal of Geophysical Research (Space Physics)*, *107*, 1179–+, doi:10.1029/2001JA000219.

Tsyganenko, N. A., and D. P. Stern (1996), Modeling the global magnetic field of the large-scale Birkeland current systems, *J. Geophys. Res.*, *101*, 27,187–27,198, doi:10.1029/96JA02735.

Tsyganenko, N. A., H. J. Singer, and J. C. Kasper (2003), Storm-time distortion of the inner magnetosphere: How severe can it get?, *Journal of Geophysical Research (Space Physics)*, *108*, 1209–+, doi:10.1029/2002JA009808.

Turner, N. E., E. J. Mitchell, D. J. Knipp, and B. A. Emery (2006), Energetics of Magnetic Storms Driven by Corotating Interaction Regions: A Study of Geoeffectiveness, in *Recurrent Magnetic Storms: Corotating Solar Wind*, *Washington DC American Geophysical Union Geophysical Monograph Series*, vol. 167, edited by R. McPherron, W. Gonzalez, G. Lu, H. A. José, & S. Natchimuthukonar Gopalswamy , pp. 113–+.

Vapirev, A. E., and V. K. Jordanova (2007), Calculation of bounce-averaged velocities and hydrogen densities for a storm-time magnetic field, *Geophys. Res. Lett.*, *34*, 10,103–+, doi:10.1029/2007GL029380.

Vasyliunas, V. M. (1970), Mathematical Models of Magnetospheric Convection and Its Coupling to the Ionosphere, in *Particles and Field in the Magnetosphere*, *Astrophysics and Space Science Library*, vol. 17, pp. 60–+.

Volland, H. (1973), A semiempirical model of large-scale magnetospheric electric fields, *J. Geophys. Res.*, *78*, 171.

Wang, C. B., J. K. Chao, and C. Lin (2003), Influence of the solar wind dynamic pressure on the decay and injection of the ring current, *Journal of Geophysical Research (Space Physics)*, *108*, 1341–+, doi:10.1029/2003JA009851.

Weimer, D. R. (2004), Correction to "Predicting interplanetary magnetic field (IMF) propagation delay times using the minimum variance technique", *Journal of Geophysical Research (Space Physics)*, *109*(A18), 12,104–+, doi:10.1029/2004JA010691.

Weimer, D. R., D. M. Ober, N. C. Maynard, M. R. Collier, D. J. McComas, N. F. Ness, C. W. Smith, and J. Watermann (2003), Predicting interplanetary magnetic field (IMF) propagation delay times using the minimum variance technique, *Journal of Geophysical Research (Space Physics)*, *108*, 1026–+, doi:10.1029/2002JA009405.

Wentworth, R. C. (1963), Pitch angle diffusion in a magnetic mirror geometry, *Phys. Fluids*, *3*, 341.

Wing Ho, C., J. L. Horwitz, and T. E. Moore (1994), DE1 observations of polar O(+) stream bulk parameters and comparison with a model of the centrifugally-accelerated polar wind, *Geophys. Res. Lett.*, *21*, 2459–2462, doi: 10.1029/94GL02340.

Wolf, R. A. (1983), The Quasi-Static / Slow-Flow / Region of the Magnetosphere, in *SOLAR-TERRESTRIAL PHYSICS: BOSTON COLLEGE: 82AUG P.303, 1983*, edited by R. L. Carovillano & J. M. Forbes, pp. 303–+.

Wolf, R. A., R. W. Spiro, and F. J. Rich (1991), Extension of convection modeling into the high-latitude ionosphere - Some theoretical difficulties, *Journal of Atmospheric and Terrestrial Physics*, *53*, 817–829.

Wygant, J., D. Rowland, H. J. Singer, M. Temerin, F. Mozer, and M. K. Hudson (1998), Experimental evidence on the role of the large spatial scale electric field in creating the ring current, *J. Geophys. Res.*, *103*, 29,527–29,544, doi: 10.1029/98JA01436.

Yeh, H., and J. C. Foster (1990), Storm time heavy ion outflow at mid-latitude, *J. Geophys. Res.*, *95*, 7881–7891, doi:10.1029/JA095iA06p07881.

Young, D. T., H. Balsiger, and J. Geiss (1982), Correlations of magnetospheric ion composition with geomagnetic and solar activity, *J. Geophys. Res.*, *87*, 9077–9096, doi:10.1029/JA087iA11p09077.

Zaharia, S., V. K. Jordanova, M. F. Thomsen, and G. D. Reeves (2006), Self-consistent modeling of magnetic fields and plasmas in the inner magnetosphere: Application to a geomagnetic storm, *Journal of Geophysical Research (Space Physics)*, *111*(A10), 11–+, doi:10.1029/2006JA011619.

Zhang, J., M. W. Liemohn, J. U. Kozyra, B. J. Lynch, and T. H. Zurbuchen (2004), A statistical study of the geoeffectiveness of magnetic clouds during high solar activity years, *Journal of Geophysical Research (Space Physics)*, *109*(A18), 9101–+, doi:10.1029/2004JA010410.

Zhang, J., M. W. Liemohn, J. U. Kozyra, M. F. Thomsen, H. A. Elliott, and J. M. Weygand (2006a), A statistical comparison of solar wind sources of moderate and intense geomagnetic storms at solar minimum and maximum, *Journal of Geophysical Research (Space Physics)*, *111*(A10), 1104–+, doi:10.1029/2005JA011065.

Zhang, J., M. W. Liemohn, M. F. Thomsen, J. U. Kozyra, M. H. Denton, and J. E. Borovsky (2006b), A statistical comparison of hot-ion properties at geosynchronous orbit during intense and moderate geomagnetic storms at solar maximum and minimum, *Journal of Geophysical Research (Space Physics)*, *111*(A10), 7206–+, doi: 10.1029/2005JA011559.

Zhang, J., et al. (2007), Solar and interplanetary sources of major geomagnetic storms during 1996-2005, *Journal of Geophysical Research (Space Physics)*, *112*(A11), 10,102–+, doi:10.1029/2007JA012321.

Zong, Q., B. Wilken, S. Y. Fu, T. A. Fritz, A. Korth, N. Hasebe, D. J. Williams, and Z. Pu (2001), Ring current oxygen ions escaping into the magnetosheath, *J. Geophys. Res.*, *106*, 25,541–25,556, doi:10.1029/2000JA000127.